Complex hydrocarbons in the Saturn system

A Dissertation
Presented in Partial Fulfillment of the Requirements for the
Degree of Doctorate of Philosophy
with a
Major in Physics
in the
College of Graduate Studies
University of Idaho
by
Shannon M. MacKenzie

Major Professor: Jason W. Barnes, Ph.D.
Committee Members: Gwen Barnes, Ph.D.; Matthew Hedman, Ph.D.; Brian Jackson, Ph.D.
Department Administrator: Ray von Wandruszka, Ph.D.

December 2017

Authorization to Submit Dissertation

This dissertation of Shannon M. MacKenzie, submitted for the degree of Doctorate of Philosophy with a Major in Physics and titled "Complex hydrocarbons in the Saturn system," has been reviewed in final form. Permission, as indicated by the signatures and dates below is now granted to submit final copies for the College of Graduate Studies for approval.

Advisor:	Jason W. Barnes, Ph.D.	Date
Committee Members:	Gwen Barnes, Ph.D.	Date
	Matthew Hedman, Ph.D.	Date
	Brian Jackson, Ph.D.	Date
Department Chair:	Ray von Wandruszka, Ph.D.	Date

Abstract

The *Cassini-Huygens* mission discovered hydrocarbons–molecules and compounds made of carbon and hydrogen–of various sizes throughout the Saturn system, from the simple (methane and ethane) to the very complex (observed but not identifiable ions of up to 400x the mass of methane). In this dissertation, I discuss hydrocarbons at two of Saturn's moons, Titan and Enceladus, whose availability of chemical species, liquid water, and energy sources make them prime targets for investigating habitable environments within our own solar system. In Chapter 2, I identify evaporites via their unique spectral properties and explore what their distribution might tell us about the global availability of liquid carbons in Titan's past. I show that *Cassini* data are not sufficient to definitively identify or distinguish between evaporite deposits in Chapter 3. The data do support the findings of theoretical models, namely that the solid hydrocarbons deposits differ in composition and grain size, further evidence that the plethora of organic species in the atmosphere is mirrored and further modified on the surface. I discuss in Chapter 4 how observations of lakes at Titan's north pole may hint at the rates of such modification. An orbiter mission architecture to identify the larger carbon species present in Enceladus' plume is presented in Chapter 5. Together, these works represents an improvement in our knowledge on the location and diversity of carbon-bearing compounds in the Saturnian system.

Acknowledgments

A PhD, like most science, isn't done in a vacuum–or at least mine wasn't. Without the support of many, but especially the following, this journey would not have been as productive, successful, or down-right enjoyable.

First and foremost, I must thank my advisor, Jason Barnes. From pushing me to get out of the classroom and into the field (be it southwestern California, the Arabian desert, or the western edge of the Erg Chebbi), to bringing me to numerous VIMS team meetings and Titan surface workshops, to involving me in grant writing and reviewing, Jason made sure to round out my physics education with what I'd actually be expected to do as a career planetary scientist. I will forever be grateful for the number of opportunities he facilitated during my time at UI. Jason's frank critiques, enthusiastic discussions, and honest advice have made me an infinitely better scientist and communicator. I will miss being able to just wander down the hall for a conversation about everything from the philosophy of doing science to the latest science fiction.

I also wish to thank the other members of my committee, Gwen Barnes, Matt Hedman, and Brian Jackson. Gwen's mentorship came at a much needed time when the pressures of our male-dominated-field seemed insurmountable. Her wisdom and friendship have helped me create a more realistic and healthy mindset both at work and at home. Matt's office door was always open whether I stopped by to discuss the prospects of Enceladus' plumes or for an impromptu lesson on Mie theory. His patience and enthusiasm were contagious enough to inspire confidence in one who walked into the conversation without any. Brian's voice of experience supported our first forays into radiative transfer, giving us confidence in our attempts to validate the earliest results.

I am forever indebted to the Cassini VIMS team, especially Bob Brown, Roger Clark, and Christophe Sotin. It's so easy to grow attached these instruments when they act as our sensory organs out in the outer solar system. For me this easy with VIMS, not because of our poetic milestone entanglements (VIMS first team meeting was the same year as my birth; VIMS' "death" coincided with the end of my PhD), but because of the welcome and support of the team members. Their patience with my naive questions and frequent challenging of my assumptions has made me a better scientist. And of course, without their efforts the data on which I cut my analysis teeth would not exist. I hope I can live up to their legacy and help those that come after me.

The Titan community is small but mighty. Sure, we study the most interesting moon in the solar system, but there is also an established culture that welcomes and fosters new scientists, new ideas, and new collaborations. I'd especially like to thank Jani Radebaugh for her patient tutelage in the field, from which I learned both the wonders of studying dunes and excellent teaching tactics. Between enabling this physicist to play geologist in various deserts and long conversations about careers and trajectories, I am honored to consider myself one of Jani's unofficial students. Zibi Turtle and Ralph Lorenz too were excellent field instructors, though they've played a larger role in molding me as a scientist by inviting my participation on Dragonfly. From the earliest days of the mission proposal's conception, they not only allowed me to observe, but also encouraged and listened to what I had to contribute. Similarly, Christophe Sotin, Alex Hayes, and Mike Malaska engaged me and other Titan students in Oceanus, valuing our input despite the greenness around our ears.

The next generation VIMS team members further exemplify the Titan community at its best. Jason Soderblom was the first VIMS person I talked to, right after a particularly intense first presentation to the group. Then and ever since, Jason has been an excellent sounding board and source of advice. Sébastien Rodriguez and Stéphane Le Mouélic were first to respond with feedback on manuscripts and abstracts, even before we had met and I was simply an anonymous "Barnes student" emailing about evaporites. In particular, Chapter 3 would not have been the same without the constructive feedback from Sébastien's review. (They, along with Daniel Cordier and Christophe Sotin, are also incredibly patient when I attempt to send them emails en français.)

Other Titanites that merit mention include Catherine Neish, Mike Malaska, and Alex Hayes for their honest feedback and discussions. I am especially indebted to Alex for encouraging his students to attend the surface workshops and VIMS team meetings–I like to think of Jason Hofgartner, Sam Birch, Paul Corlies, and Nic Kutsop as my Cornellian cohort. Thanks to each of these excellent young scientists for many delightful conversations from the various remaining mysteries surrounding Titan's surface, to the next missions in the outer solar system, to questions of faith and science. I hope we all have many fruitful years of collaboration ahead of us.

Not represented in this thesis are the two years Jason and I spent developing a radiative transfer code in C++ at the behest of Eliot Young. I want to thank Eliot for prodding us to take on this challenge, as well as graciously offering his time, insight, and support on the project. Mate Ádámkovics came aboard later and kindly answered many of our ignorant questions (including making k coefficients approachable rather than intimidating!).

And finally, I want to thank that special group of individuals who ensured my success at the University of Idaho. My academic forebears were indispensable for navigating my first years. Casey Cook and Emily Martin were gracious enough to share both their successes and pitfalls when I asked for their advice, saving me some headaches! My thanks also goes to my cohort and academic brother, Johnathon Ahlers. I cannot imagine surviving classes (let alone the quals!) without his patience and contagious laugh. My fellow Titanite, Rajani Dhingra, was an invaluable sounding board for all things Titan, remote sensing, paratha-making, and work/life balance. I'll never forget our adventures in the field, at workshops, and trying to make r5d4 behave. Rob Chancia's unapologetic discussions and quick wit were the best start to many a day in the lab or the best end of the week over a pint. I will greatly miss our banter, be it science-, career-, garden-, or trivia-related. Chase Chivers was the first undergrad I mentored and he made my job pretty easy. I wish him the best of luck but am confident he won't need it. Joseph A'Hearn took on the astronomy lab and eclipse planning like the expert observer he is; many thanks for discussions on how to improve curriculum and for the making sure our first total eclipse was such a success! I am also grateful to my friends in biology–especially Roxie Hickey, Kenetta Nunn, Sarah Jacobs, Andy Kraemer, and Amy Worthington–for answering all my naive questions about their subject, discussing careers, and generally being an incredible group to share the highs and lows of graduate school.

Dedication

To my parents–Ann and Kirk–who first instilled in me a love for learning,
To my in-laws–Tim and Gayle–who supported me like their own,
To my old friends–Mara, Adria, Megan, Zoe, Kyle, and Ashleigh–
who kept me sane despite the hour or thousands of kilometers,

And most importantly,

To my husband Michael,

who pours the best cup of coffee,
who taught me all the biology and stats I've ever used,
who makes the journey worthwhile,
and who started all this when he confessed to me in 2011,
"I'm thinking about grad school at the University of Idaho..."

Table of Contents

List of Tables

List of Figures

Chapter 1: Introduction

The search for life elsewhere in our solar system has long focused on "following the water" (Hubbard et al., 2002). Liquid water is necessary for biology that resembles Earth's. Here H_2O serves as the solvent that facilitates biochemical processes and the electron source for oxygenic photosynthesis. But water is not, by itself, sufficient. Jones and Lineweaver (2010) estimate that 88% of Earth's water volume is uninhabited due to a variety of factors including limited energy or nutrient sources. Our best estimate for what determines an environment's degree of habitability therefore depends not only on the presence of liquid water–or a solvent in general–but also energy sources and essential elements (e.g. Domagal-Goldman et al., 2016).

Furthermore, unlike on the surface of Mars, liquid water is not in short supply in the outer solar system (e.g. Grasset et al., 2017). We now know that Titan, Enceladus, Europa, Ganymede, and Callisto all harbor vast oceans beneath their icy crusts (e.g. Kivelson et al., 1996; Carr et al., 1998; Khurana et al., 1998; McCord et al., 2001; Iess et al., 2012; Iess et al., 2014; Čadek et al., 2016). These moons of Saturn and Jupiter may not even be the only examples: more "ocean worlds" may be identified with further exploration of bodies like Pluto, Triton, and the Uranian satellites (e.g. Hussmann et al., 2006, 2010; Robuchon and Nimmo, 2011; Nimmo et al., 2016). We've already found the water–it's time to follow the carbon.

Carbon's abundance and chemical affinity make it one of the most commonly used elements in biochemical processes. Carbon chains serve as the backbone for amino acids, lipids, and carbohydrates, the basic biomolecules on which our metabolism and very cellular structure are based. Hydrocarbons like methane and formaldehyde function as oxidation agents (electron donors) in the redox reactions of metabolic pathways. Understanding these metabolic networks and the molecular building blocks that drive them is critical for investigating the very origins of life because despite a diversity of sizes, evolutionary histories, and environments, life on Earth employs common chemical processes to grow and proliferate.

Though the recent explosion of exoplanet identification indicates that solar system formation processes are likely more complicated than originally thought (e.g. Ahlers et al., 2015), some proposed histories for carbon do make sense for our own solar system. CO and CH_4 condensed in the outer portions of the solar nebula according to the condensation sequence, a function of temperature and thus not tied to a single "ice line" throughout solar system formation (Lodders, 2003). Regions hotter than the condensation temperatures could not accrete the gaseous volatiles. Thus, inner planets may have gained their carbon later when migration events may have flung carbon-enhanced planetesimals inward (Marty et al., 2013).

Today, carbon can be found across the solar system, from the carbon dioxide of Venus' atmosphere (Adams and Dunham, 1932; Von Zahn et al., 1983), to the CO_2 snows of Mars (e.g. Head et al., 2005), to the carbonate deposits observed on Ceres (De Sanctis et al., 2016), to the amino acids found in meteorites (e.g. Engel and Macko, 1997), to the trace hydrocarbon species in the atmospheres of the gas giants (e.g. Strobel, 1983; Gladstone et al., 1996; Fouchet et al., 2000; Moses et al., 2000, 2005), to the condensing methane of the ice giant atmospheres (e.g. Lindal et al., 1987; Baines and Smith, 1990; Bishop et al., 1992; Lunine, 1993), to the carbon dioxide on icy moons (Hibbitts et al., 2003; Cruikshank et al., 2010;

Clark et al., 2012), and even the higher altitudes of Pluto (e.g. Cruikshank et al., 1976; Douté et al., 1999; Grundy et al., 2016; Protopapa et al., 2017).

Data from the *Cassini-Huygens* mission has allowed us to start following the carbon at the Saturn system, revealing that two of Saturn's moons are priority targets for following carbon to prebiotic chemistry: Titan and Enceladus.

Titan, Saturn's largest moon, has long stood out as the only moon with an atmosphere. Much like Earth, nitrogen dominates the atmospheric composition, followed by methane and other trace species (see Table 1 of Hörst (2017)). Methane participates in the equivalent of Earth's hydrological cycle, raining down onto the surface and evaporating back into the atmosphere. Unlike Earth, UV-driven photolysis initiates a sequence of organic chemistry where molecular hydrogen escapes to space while species like methane, ethane, acetylene, and even cyanide condense to form aerosols, particles suspended within the gas (e.g. Strobel, 1983; Vuitton et al., 2014). As we only have measurements of the molecular precursors, laboratory studies and theoretical models offer the best insight into the composition of the haze, involatile aerosols produced via photochemical processes. The haze begins as spheres 0.05 $\pm$0.02 μm in size formed hundreds of kilometers above the surface, the exact altitude depending on composition. Eventually, thousands of spherules aggregate into fractals a few microns in size (Tomasko et al., 2008c) that settle onto Titan's surface.

There, a multitude of processes act to chemically or physically alter the haze fallout. The haze particles may directly sinter together to form saltatable particles (Barnes et al., 2015). Winds organize these organic sands into fields of longitudinal dunes that almost entirely encircle Titan's equator (Radebaugh et al., 2008; Barnes et al., 2008a; Lorenz and Radebaugh, 2009; Rodriguez et al., 2014). Perhaps the sands become buried to form Titan sandstone, which may then be reworked by other processes (Barnes et al., 2015).

Fluvial activity carves the surface and subsequently transports eroded material. *Huygens* glimpsed rounded cobbles at its landing site, morphologically consistent with fluvial transport, perhaps in the channels imaged during the probe's descent (Tomasko et al., 2005). *Cassini* observed channels (Lorenz et al., 2008; Burr et al., 2013; Burr et al., 2013) emerging from mountainous terrains (Barnes et al., 2007c; Burr et al., 2009; Radebaugh et al., 2011) and terminating at fans (Radebaugh et al., 2016; Birch et al., 2016; Cartwright and Burr, 2017). Liquid-filled channels feeding into Ligeia Mare, the second largest sea, lie at the bottom of deep (up to 570 m) canyons, suggesting extensive carving into the surface (perhaps enhanced by uplift) and transport of eroded material (Poggiali et al., 2016). Titan's crust should be mostly water ice based on its bulk density (Elliot et al., 1975). Thus we might anticipate any bedrock incision to create water ice sediments–if not for the photochemical haze products. Models of photochemical production predict that if the current benzene production alone were consistent over the age of the solar system (4.5 x 10^9 years), 3 m of benzene would cover the surface (Vuitton et al., 2008). The *Cassini* Visual and Infrared Mapping Spectrometer observed no pure water ice deposits (Clark et al., 2010), only materials with an enhanced water ice component (Rodriguez et al., 2006; Barnes et al., 2007b,c; Soderblom et al., 2007; Le Mouélic et al., 2008; Soderblom et al., 2010; Rodriguez et al., 2014; Brossier, under review). Furthermore, while the radiometer data show that organics generally make up the top few meters of crust, the low emissivity and low dielectric constant observed at 2.18 cm suggests

some water ice is also present (Janssen et al., 2016). Thus, fluvial erosion and transport likely operate on whatever mixture of organics and water ice make up the local crust.

Lacustrine processes are also at work at Titan's poles, though most of Titan's surface liquids are presently sequestered at the north (Stofan et al., 2007; Sotin et al., 2012; Hayes, 2016; Birch et al., 2017). Birch et al. (2017) infer a blanket of lacustrine sediments could have been deposited by a previous epoch of regional seas. Titan's organic sands could also form via flocculation within the sea (Barnes et al., 2015), though subsequent transport from the poles uphill to the equator would be difficult. The "cookie cutter" morphology of the smaller lakes has been interpreted as similar to karstic terrain on Earth where water eats into bedrock by dissolving soluble material in limestone (Malaska and Hodyss, 2014; Cornet et al., 2015). As the liquids on Titan are chemically nonpolar, the solutes must also be nonpolar; thus it is the organic sediment rather than water ice bedrock that would be dissolved.

Theoretical models (Cordier et al., 2013; Glein and Shock, 2013; Cordier et al., 2016) and laboratory experiments (Malaska and Hodyss, 2014; Diez-y Riega et al., 2014; Singh et al., 2017) confirm that species observed in Titan's atmosphere like benzene (Vuitton et al., 2008; Waite et al., 2007; Coustenis et al., 2007), naphthalene (Waite et al., 2007), acetylene (Coustenis et al., 2010), acetonitrile (Vuitton et al., 2006), and biphenyl (Delitsky and McKay, 2010) dissolve in hydrocarbon liquids at Titan surface conditions ($\sim$90K, 1.5 bar; Fulchignoni et al. (2005)). When lakes are saturated with solute and have no other outlet to draining, the sediments fall out of solution as the lake liquid evaporates leaving behind a record of previous fill states. These 'evaporite' deposits may represent some of the most concentrated deposits on Titan's surface. Sediments deposition is a function of solubility and thus composition (Barnes et al., 2011; Cordier et al., 2013). Evaporites on Titan represent both an excellent target for identifying chemical species on Titan as well as an indicator of past presence of hydrocarbon liquids because their formation requires liquid (MacKenzie et al., 2014).

Cassini has thus revealed Titan to be a sedimentary world akin to Earth in complexity and diversity of surface processes and their products. And yet, the importance of sedimentological processing of Titan's organics extends beyond the interests of geologists. Laboratory experiments show that Titan haze analogs, "tholins" (Sagan and Khare, 1978; Cable et al., 2011), react in liquid water to create biologically relevant molecules like amino acids. While Titan's surface temperature is much too cold for liquid water, there are some very near surface environments where water can remain liquid for long periods: impact melt and cryovolcanic flows. The kinetic energy imparted by an impact of craters melts the ice crust, which refreezes over timescales 10-10^6 years based on the impact scale (crater diameter) (O'Brien et al., 2005). Similarly, cryovolcanic flows of liquid water (probably mixed with ammonia to make the lava buoyant) sourced from the subsurface ocean would cool over timescales tens of hours to tens of years based on the thickness of flow and amount of ammonia dissolved (Davies et al., 2016). In either case, the suddenly liquid water would mix with the organic sediments that previously sat on the surface. Even at low temperatures (253 K), tholin hydrolysis happens much faster than the refreezing timescales of impact melts and thick cryovolcanic flows (tens of hours) (Neish et al., 2008, 2009, 2010). Thus, the search for water-based life on Titan need not wait until technologies allow us to drill through Titan's $>$ 100 km thick ice shell to the subsurface ocean. Near surface ephemeral liquid water environments like impact melt pools and cryovolcanic flows make much more approachable targets.

What sediments are mixed into the melted water directly affects what kind of chemistry can take place within these cooling oases similar to those of the Miller-Urey experiment. Thus, Titan's organic cycle, the processing of carbon species from the atmosphere to and across the surface, is intimately linked with the potential for habitable environments for Earth-like life on Titan (e.g. Schulze-Makuch and Grinspoon, 2005). Furthermore, the organic cycle also affects the likelihood of "weird life", biology that uses liquid hydrocarbons instead of liquid water as a solvent (e.g. McKay and Smith, 2005; Stevenson et al., 2015; McKay, 2016), by controlling the availability of nutrients or constituent molecules.

Cassini also identified intriguing evidence for interesting carbon chemistry at Enceladus. Enceladus's unusually bright albedo as determined from ground-based and Voyager observations suggested some kind of recent resurfacing (e.g. Smith et al., 1982; Hanel et al., 1982; Buratti and Veverka, 1984). *Cassini* revealed the process responsible: linear vents at the south pole spout water vapor and ice particles, ultimately sourced from a global subsurface ocean. As *Cassini* flew through the plumes of erupted material the two mass spectrometers, Ion-Neutral Mass Spectrometer (INMS, Waite et al. (2006)) and Cosmic Dust Analyzer (CDA, Srama et al. (2004)), sampled the vapor and particles respectively. These instruments detected methane, ethane, pentane, and other hydrocarbons (C_2H_x-C_6H_6) (Waite et al., 2009). Sodium chloride (Hsu et al., 2015) and molecular hydrogen (Waite et al., 2017) observed in the plume indicate that the ocean is warm (>360 K at the ocean-core boundary) and interacts with a rocky core to produce a chemical disequilibrium within the ocean waters similar to that which Earth's deep sea dwellers leverage for metabolism (Kelley et al., 2005). Thanks to the high velocities of *Cassini*'s treks through the plumes, molecules larger than the INMS sensitivity range (i.e. $>$ 100 atomic mass units) fragmented in the instrument. The result, an unusual increase in carbon products observed only in samples taken at higher velocities, supported the existence of more complex species (Perry et al., 2015). Thus Enceladus too meets both requirements of liquid water and carbon and makes a unique target for future study with subsurface ocean material available for *in situ* sampling via remote sensing instruments.

Saturn's moons Titan and Enceladus represent the next logical destinations in our search for life in the solar system. Liquid water is readily available and evidence from *Cassini-Huygens* suggests complex carbon species are too. In Chapter 2 I identify and characterize what may be some of the most concentrated hydrocarbon deposits on Titan, the evaporites. I constrain the extent to which *Cassini* infrared spectra can discern compositional or grain size differences between evaporite deposits in Chapter 3. Chapter 4 investigates the timescale for removal of hydrocarbon liquids at Titan's north pole. Chapter 5 discusses a concept architecture for returning to Enceladus to follow up on the discoveries of *Cassini*.

Chapter 2: Evidence of Titan's Climate History from Evaporite Distribution

"Evidence of Titan's Climate History from Evaporite Distribution" *Icarus, vol. 243, 2014, pp. 191-207*

In this chapter, I build on the work of Barnes et al. (2011), who first identified the presence of evaporite on the surface of Titan. Evaporites are the solutes dissolved in the lakes that precipitate out when the liquids evaporate; a formation process similar to Earth's evaporites though the chemistry is quite difference. Salts and carbonates that dissolve in Earth's solvent, water, do not in Titan's solvent, liquid methane and ethane. Instead, Titan's hydrocarbons must be some kind of hydrocarbon. Because they require liquid to form, however, we use the presence of evaporite to map out where liquids have been in Titan's past in this chapter.

Evaporite deposits are located around the shores of currently filled lakes, and at the bottoms of dry lake beds, easily identifiable thanks to their unique signature in VIMS data. The evaporites are bright at 5 mum and have a low ratio of reflectance at 2.7 μm / 2.8 μm suggesting that the surface material has a larger grain size and little water ice in its composition.

I found that liquids had to be in Titan's currently desert equatorial region in order to create the 5 μm bright material observed at Tui and Hotei, corroborated by the lacustrine morphology of landforms discussed by Moore and Howard (2010). The lack of evaporites at the south pole places a constraint on models of liquid transport from pole to pole; some mechanism must be at work to bury or remove the 5 μm bright signature or the proposed south polar seas might not have had conditions suitable for evaporite formation (no closed basins, not enough dissolved sediment, etc). Thus, in this project I found that the evaporites suggest that the distribution of lakes and seas across the surface has changed throughout Titan?s history. Since lakes are sediment sinks and create new deposits (like evaporites), tracing where liquids have been in the past helps us understand the availability of both simple (the liquids) and complex (the sediments) across the Titan surface.

2.1 abstract

Water-ice-poor, 5-μm-bright material on Saturn's moon Titan has previously been geomorphologically identified as evaporitic. Here we present a global distribution of the occurrences of the 5-μm-bright spectral unit, identified with *Cassini*'s Visual Infrared Mapping Spectrometer (VIMS) and examined with RADAR when possible. We explore the possibility that each of these occurrences are evaporite deposits. The 5-μm-bright material covers 1% of Titan's surface and is not limited to the poles (the only regions with extensive, long-lived surface liquid). We find the greatest areal concentration to be in the equatorial basins Tui Regio and Hotei Regio. Our interpretations, based on the correlation between 5-μm-bright material and lakebeds, imply that there was enough liquid present at some time to create the observed 5-μm-bright material. We address the climate implications surrounding a lack of evaporitic material at the south polar basins: if the south pole basins were filled at some point in the past, then

where is the evaporite?

2.2 Introduction

Titan, unique among other satellites in our solar system, has a thick atmosphere in which a volatile (methane, though ethane is thought to also play an important role) precipitates and evaporates in the same fashion as water in Earth's hydrological cycle (Roe, 2012). Our understanding of Titan's surface and climate has evolved from the once widely expected global surface ocean thought to sustain the photolytic processes in the atmosphere (e.g., Lunine et al., 1983; Flasar, 1983) to a world only sparsely covered by liquid deposits but hosting a collection of strikingly Earth-like surface morphologies (e.g., dunes and channels) thanks to data now available from *Cassini-Huygens*. These observations reveal Titan to be generally wet at the poles and dry at the equator.

At the poles, Titan's liquid bodies range from seas (surface area greater than 100,000 km^2, only in the north) to smaller lakes (Stofan et al., 2007; Hayes et al., 2008; Sotin et al., 2012), to fluvial features thought to be drainage networks (e.g., Lorenz et al., 2008; Lunine et al., 2008; Burr et al., 2009; Langhans et al., 2012; Burr et al., 2013). The equatorial region, however, is characterized by expansive dune fields (e.g. Elachi et al., 2006; Soderblom et al., 2007; Lunine et al., 2008; Radebaugh et al., 2008; Rodriguez et al., 2014), intermittent mountain chains (e.g., Radebaugh et al., 2007; Cook-Hallett et al., 2015), and a noticeable lack of permanent surface liquid (but see Griffith et al. (2012)). Rain has been observed to wet the midlatitude and near-equatorial surface (Turtle et al., 2011b), but standing bodies similar in extent and stability to the polar lakes have yet to be conclusively identified. The most equator-ward lake candidates, Sionscaig and Urmia, are located between 39°S and 42°S and, while hypothesized to have standing liquid, are yet to be confirmed as either long-lived or ephemeral (Vixie et al., 2015). Mitchell (2008) were able to reproduce a dry equatorial climate with a global circulation model (GCM) where a limited reservoir of methane exchanges between the atmosphere and surface.

And yet, sizable volumes of liquid are still thought to have played an important role in forming the equatorial region. As Huygens discovered during its descent to the Titanian surface on January 14, 2005, fluvial features such as rounded cobbles, channels, and valleys also dot the equatorial landscape (Tomasko et al., 2005). The subsurface structure controlling fluvial drainage networks in southwestern Xanadu (Burr et al., 2009) agrees with the wind flow derived from aeolian driven dune morphology (Lorenz and Radebaugh, 2009). Rainfall has been proposed as the source the liquid responsible for carving fluvial features (Lorenz and Lunine, 2005; Turtle et al., 2011c). While storms have been observed in the equatorial region (Turtle et al., 2011b), *Cassini* has yet to directly observe actively flowing channels. The average global rainfall on Titan has been suggested to be $\sim$ 1 cm/yr (Lorenz and Lunine, 1996; Rannou et al., 2006), but such a low rate could be reconciled with the observed fluvial features if precipitation were to occur in intense but infrequent storms ("methane monsoons" akin to what terrestrial deserts experience though an order of magnitude smaller (Jaumann et al., 2008; Schneider et al., 2012)).

Clouds have been frequently observed in the active atmosphere of Titan, ranging from the enormous winter polar vortex, to bands of tropospheric clouds around certain latitudes (e.g. Griffith, 2009; Hirtzig et al., 2009; Rodriguez et al., 2009; Brown et al., 2010; Rodriguez et al., 2011; Le Mouélic et al., 2012b), to

the low lying fog (Brown et al., 2009). Stratospheric and high tropospheric clouds have been deduced to be composed of methane and ethane, but fog is necessarily made of methane alone (Brown et al., 2009). Precipitation has been indirectly observed after cloud coverage via the surface darkening, brightening, and subsequent return to the original spectrum by *Cassini*'s Visual Infrared Mapping Spectrometer (VIMS) (Barnes et al., 2013a) and Imaging Science Subsystem (ISS) (Turtle et al., 2009, 2011b; Barnes et al., 2013a).

The present distribution of Titan's lakes is asymmetric: there are more in number and extent at the north pole than at the south (Aharonson et al., 2009a). In the north, for example, the largest body is Kraken Mare, a sea covering 400,000 km^2 (Turtle et al., 2009), while in the south, the largest is Ontario Lacus which covers only 15,000 km^2 (Hayes et al., 2010). Global Circulation Models (GCMs) have found that some kind of seasonal exchange or link between the north and south poles may be taking place (e.g., Tokano, 2005; Mitri et al., 2007; Rannou et al., 2006; Mitchell et al., 2009; Tokano, 2009). While changes in the size of the northern lakes and seas were not observed before equinox (Hayes et al., 2011; Sotin et al., 2012), *Cassini* has begun to witness signs of seasonal transport as Titan approaches northern summer. The Composite Infrared Spectrometer (CIRS) has recorded evidence that subsidence has just started above the south pole (Teanby et al., 2012) while the cloud distribution observed by VIMS is indicative of a pole-to-pole meteorological turnover (Rodriguez et al., 2011; Le Mouélic et al., 2012b).

On a longer than seasonal timescale, it has been proposed that the observed dichotomy actually reverses every $\sim$ 50,000 years with a Titanian Milankovitch cycle (Aharonson et al., 2009a). This cycle would be driven by changes in solar insolation as to which hemisphere receives a more intense summer. A GCM by Schneider et al. (2012) shows that an asymmetry in solar insolation can explain the difference in liquid distribution between the north and the south poles. That work, however, assumes a static amount of methane in the surface-atmosphere system, which may not be the case on Titan, as indicated by other models (Nixon et al., 2012) and empirical estimates for the age of the atmosphere (Niemann et al., 2005; Mandt et al., 2012).

Dry and partially filled lakes have been identified with the *Cassini* RADAR mapper (RADAR) (Hayes et al., 2008; Barnes et al., 2011) both in isolation and near filled lakes. Hayes et al. (2011) also observed ephemeral lakes in the south polar region. These dry beds imply that the distribution of Titan's liquid is not static. Moore and Howard (2010) propose that the landscape elements with crenulated margins and small lacustrine features similar to those identified by Hayes et al. (2008, 2011) observed in RADAR images of Tui and Hotei Regiones indicate that the previous presence of liquid, i.e. that the two equatorial features may be fossil seas. Thus, because the small lacustrine features observed within Tui and Hotei would require long-lived surface liquid for their creation, there seems to be evidence for a previous global liquid distribution that differs from what is presently observed.

The 5-μm-bright VIMS spectral unit has been observed on Titan since the first *Cassini* flybys where Tui Regio was clearly differentiated from other surface features (Barnes et al., 2005). However, from observations of a region of small lakes and dry lake beds by VIMS during T69 (2010 June 5), Barnes et al. (2011) established the connection between lakebeds and 5-μm-bright material: this unique spectral unit coincided with the shores of filled lakes and the bottoms of dry lakes identified by RADAR (Hayes et al., 2008). Within this small region, there are also examples of dry and filled lakes that do not exhibit

a 5-μm-bright signature. Barnes et al. (2011) demonstrated how evaporite formation would be consistent with these observations of the water-ice poor, uniquely 5-μm-bright material: the compounds making up the deposits would have re-crystalized upon solute evaporation (accounting for the uniquely bright, water-ice poor spectrum) and the formation process would only occur in saturated solutions (explaining the spectral differences between such geographically close lakes and lakebeds). While we prefer this evaporitic interpretation for 5-μm-bright material formation, other, lacustrine-related explanations could be possible, such as sedimentary deposits forming at the bottom of lakebeds. Thus, we discuss the 5-μm-bright material as "evaporite candidates" to reinforce the connection between lakebeds and 5-μm-bright material for ease of comprehension.

In this paper, we identify all other examples of the 5-μm-bright spectral unit in the VIMS data. While brightness at 5 μm alone is not diagnostic enough to say definitively that an observed signature is from specifically evaporitically formed material, the strength of the geomorphological correlation between lakebeds and this spectral unit (first demonstrated by Barnes et al. (2011) and bolstered in this work with available RADAR images) gives us enough ground to explore the implications for the global liquid distribution on Titan if each localized 5-μm-bright signature were indeed indicative of some previous presence of surface liquid. Isolating the specific chemical compounds of evaporite is beyond the scope of this paper. In Section 2.3, we describe the 5-μm-bright spectral unit, define our candidate selection criteria, and detail the mapping process. Our results are given in Section 2.4 and their implications on the past climate on Titan are discussed in Section 2.5. We conclude with a summary of our interpretations, scenarios inspired by the evaporite candidate distribution for GCMs to consider, and propositions for future study.

2.3 Methods

2.3.1 Selection Criteria

In a hydrological cycle[1], surface liquid evaporates into the atmosphere where it eventually condenses and rains down onto the surface. There the liquid can dissolve surface material if the solvent is in contact with the solute long enough. For liquid reservoirs that are saturated, the evaporation of the liquid will cause the solute to precipitate out and deposit as evaporite either onto the surface exposed after the liquid has left or at the bottom of the bed of saturated liquid.

On Titan, the surface liquid is a predominately methane-ethane mixture (Brown et al., 2008). It is expected that while the formation processes of evaporite on Titan are similar to those on Earth, the composition will be different because, unlike water, methane and ethane are non-polar. Most of the suggested candidates for compounds that would be soluble in such a mixture are organic (Cordier et al., 2009; Barnes et al., 2011; Cordier et al., 2013). It could be that the organic compound has a finite vapor pressure such that it could itself evaporate and condense nearby. However, we build upon the geomorphological evidence of Barnes et al. (2011) and use this 5-μm-bright spectral unit to identify possible evaporitic deposits.

[1]Here we refer to any cycle similar to that of water on Earth as "hydrological" to avoid clumsy and somewhat inaccurate terminology; "methanological" would seem to belie the role of liquid ethane, for example.

In Figure 2.1, we show examples of the 5-μm-bright spectral unit (red line, all panels) in the context of other surface spectral units: the dark brown dunes (brown line, panel a), the bright terrain of Xanadu (green, panel a), the liquid of Kraken Mare (blue, panel b), the non-Xanadu equatorial bright material (light blue, panel b), the dark blue material (dark blue, panel b). We also show the spectral correlation between shoreline evaporite and Hotei Regio (black) in panel c. To compare individual spectra, it is necessary to take into account viewing geometry which necessarily has an effect on the observed signal intensity (as discussed in Solomonidou et al. (2014)). Spectra of the same region taken near the limb will look different from one at nadir as the former's signal must travel through more atmosphere, for example. Thus, in Figure 2.1, we group the data based on viewing angles, which are summarized in panel d, along with the ratio of I/F at 2.8 and 2.7 μm (affected by the presence of pure water ice (Rodriguez et al., 2006)). For the behavior of the 5-μm-bright material in the 5 μm window, we refer the reader to Section 7.2 and Figure 27 of McCord et al. (2008), where outlying pixels are compared to the scene average of Tui Regio.

The 5-μm-bright unit is named after its most dramatic characteristic: material of this composition is brighter than all other spectral units at 5 μm. However, the titular spectral feature is not the unit's only distinction. 5-μm-bright material has a high ratio of I/F at 2.8 μm / 2.7 μm. Generally, in the wavelength windows greater than 2 μm, the 5-μm-bright unit is brighter than any other surface unit. The I/F of the 5-μm-bright unit is on the order of other spectral units (and even darker than Xanadu) in the shortest wavelength windows. Instead of working in the spectral domain, we consider the data spatially by assigning to the VIMS data a color scheme that exploits the spectral characteristics of the 5-μm-bright unit. With R = 5 μm, G = 2 μm, and B = 1.3 μm, the evaporite-correlated unit appears as a very bright, reddish-orange color. This method facilitates quick identification of 5-μm-bright material in VIMS maps, enabling our search to encompass the breadth of available data.

Titan's clouds also appear bright at 5 μm but can be generally distinguished from evaporite. Clouds exhibit a distinctive spectral signature in the wings of the 2 μm peak due to their altitude (Griffith et al., 1998; Griffith et al., 2006, 2005; Rodriguez et al., 2011), allowing for identification of tropospheric and stratospheric clouds (that is, at least 40 km above Titan's surface). Additionally, clouds demonstrate a simultaneous increase in all windows, particularly evident at the 2.75 μm and 5 μm windows (Rodriguez et al., 2009) and are ephemeral.

Low lying vapor, what we broadly refer to as fog, does not demonstrate the 2 μm wing signature but otherwise has the spectral signature of a cloud. Hence, to identify fog and check the longevity of an evaporite candidate, we compare between VIMS coverage of the same area at different flybys. For each case we ask: Is the 5-μm-bright material present? Does it change shape and extent? Admittedly, such criteria are less robust than the spectral characteristic of higher altitude clouds. After all, it could be that an evaporitic deposit is no longer seen (or no longer has the same shape) at a different time because the surface has been wetted; the evaporite is either submerged or even dissolved again into the covering liquid. The persistence of an evaporitic deposit is more telling than any "sudden" disappearance. Low altitude clouds would not statically endure for long timescales, thus the persisting signature would seem to be evaporite. Indeed, if no disappearances were observed over a long enough time scale, for example, one could surmise something about the lack of sufficient rainfall to re-dissolve the evaporite into solution.

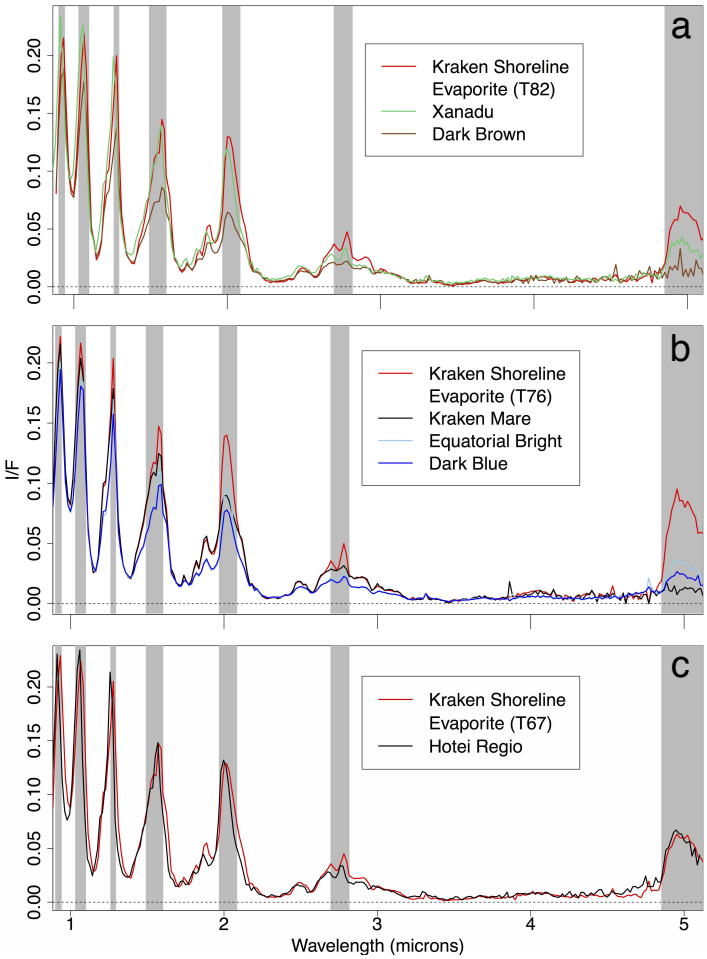

Unit	Flyby	Phase	Incidence	Emission	2.8 / 2.7μm
Kraken Evaporite	T82	63	47	65	1.28
Xanadu	T12	70	46	65	1.16
Dark Brown	T88	59	46	65	1.04
Kraken Evaporite	T76	42	51	60	1.40
Kraken Mare	T76	42	52	62	1.10
Equatorial Bright	T28	45	52	58	1.19
Dark Blue	T28	45	52	62	1.14
Kraken Evaporite	T67	13	53	58	1.26
Hotei Regio	T8	25	49	71	1.18

Figure 2.1: The unique spectrum of 5-μm-bright material found on the shorelines of Kraken Mare (red in each panel) compared to those of other identified surface feature VIMS spectral units (listed in Barnes et al. (2007a)): dark brown (brown, panel a), Xanadu (green, panel a), liquid (black, panel b), non-Xanadu equatorial bright (light blue, panel b), dark blue (dark blue, panel b). In panel c, we also show the correlation between shoreline evaporite and the spectral signature of Hotei Regio (black). We have broken up the spectra into different plots based on viewing geometry in order to make appropriate comparisons. The viewing angles and ratio of the I/F at 2.8 and 2.7 μm is listed in the table of panel d. The grey boxes indicate the wavelength windows in which VIMS can observe Titan's surface. The 5-μm-bright material is also bright in the 2 μm windows, though not as distinctly as in the 5 μm window. The spectrum of Kraken Mare is rather bright in T76 which may be due to specular reflections of the sky reflecting off the surface of the liquid (Vixie et al., 2015).

Realistically, however, such a measurement would require coverage more extensive and more frequent than currently available. We therefore require that a 5-μm-bright feature be seen at the same location and of the same shape in at least two flybys in order to be considered an evaporite candidate. The grey polygons of Figure 2.2 represent surface features that could not be identified as candidates due to lack or repeat data of sufficient quality.

2.3.2 Mapping

To identify evaporite candidates, we searched through images taken by VIMS from T0-T94 (July 3, 2004 - January 1, 2014). The spectroscopic data were reduced using the VIMS pipeline detailed in Barnes et al. (2007a) and geometrically projected with software developed for Barnes et al. (2008a). Color images were then created by assigning individual wavelengths the RGB= 5, 2, 1.3 μm color scheme to capitalize on the unique spectral characteristics of the 5-μm-bright unit as discussed above. (This color scheme was also used by Barnes et al. (2007a) and Barnes et al. (2011)). For topographical and geological context, we use data from the RADAR instrument taken in either Synthetic Aperture RADAR (SAR) or high altitude Synthetic Aperture RADAR (HiSAR) modes that spatially coincide with 5-μm-bright material observed by VIMS.

In Table 1, we list the locations of each evaporite deposit that is mapped in this work, as well as the calculated surface area. Polygons representing the outline of each evaporite candidate are plotted as a global distribution in the bottom half of Figure 2.2. We also include a cylindrical map of Titan as seen by VIMS in Figure 2.2 to provide global context for each candidate's location. From the surface areas, we estimate the volumes of liquid bodies, as well as the hypothetically filled liquid bodies corresponding to evaporite deposits. The depths are estimated from the assumption that depth is proportional to surface area using the measured values for Ligeia Mare (Mastrogiuseppe et al., 2014).

2.4 Results

We identify new evaporite candidates in the north polar region, the northern midlatitudes, the equatorial band, and the south polar region, listed in Table 2.1 and shown in Figure 2.2. If the connection between 5-μm-bright material and lakebeds in the north pole holds for other regions, then the areas outlined in Figure 2.2 would have been covered with enough liquid at least once to have created the 5-μm-bright deposits. Interestingly, the largest evaporite candidates are not located in the poles, where the largest amount of surface liquid currently resides, but rather in the equatorial band (Figure 2.3). The following subsections discuss the deposits in detail by region.

2.4.1 North Pole

In Figure 2.4, the best VIMS coverage (panel a) of the north pole is compared to the RADAR coverage (panel c) and our mapped evaporite deposits (pink polygons of panels b and d). As Titan enters northern spring, VIMS has begun to explore the previously night-covered, near-polar surface. In addition, the dense cloud cover above the north pole that was present during northern winter has progressively vanished since

Table 2.1: 5-μm-bright deposits identified as evaporite in order of decreasing latitude. Coordinates are given in the positive-west longitudinal convention. Areas were calculated by summing over the area of each pixel spanned by a polygon outlined with software first designed for Barnes et al. (2008a). Data obtained in flybys before T86 are publicly available on the Planetary Data System. The best resolution given below is an average of the best latitudinal and longitudinal resolution available. The listed emission angle is also from the best resolution image. Evaporite deposits cover 1% of the surface of Titan.

	Central Latitude	Central Longitude (Positive west)	Total Evaporite Area (km^2)	Best VIMS Flyby	Best Resolution (km/pixel)	Emission Angle (°)
90 N - 80 N			21,500	T90-T94		
Punga Mare	88	150	1,220	T93, T94	6	16 - 22
Kutch	88	222	13,800	T93, T94	7	17 - 22
Ligeia Mare	75	170	4,250	T69, T94	1	14 - 60
Kivu Lacus	87.02	118	88	T85, T93, T94	1	47
Muggel Lacus	83	170	30,000	T93, T94	7	15 - 34
80 N - 70 N			16,800			
MacKay Lacus	77	96	14,600	T94	8	5 - 21
Lake District	64-83	183 - 125	55,900	T97	15	5
70 N - 60 N			18,300			
Cardiel Lacus	68	203	7,100	T90	62	70
Woytchugga Lacuna	69	110	66,700	T97	13	9
Nakuru Lacuna	65.5	92.38	2,580	T97	13	18
Vanern Lacus	69.9	223.2	7,060	T69	14	63
Towada Lacus	69.3	242	782	T69	10	63
Atacama Lacuna	67.6	226.1	799	T69	13	62
Djerid Lacuna	65.8	219.7	808	T69	13	59
Uyuni Lacuna	65.7	223.8	700	T69	13	59
Ngami Lacuna	67.2	211.2	1,020	T69	13	60
60 - 50			6,020			
Kraken Shores	60	305	32,300	T76	20	73
South of Kraken			42,000	T76		
50 N - 40 N			2,810	T76		
Hammar Lacus	47	313.49	18,600	T76	31	55
40 N - 30 N			17,200			
West Fensal	15	52	18,300	T5	9	22-37
East Fensal	17.4	39.5	3,660	T5	37	18
West Belet North	-1.5	284.9	1,160	T61	15	48
West Belet South	-8.2	283.9	3,650	T61	15	48
Southwest Belet	-18.2	276.6	3,930	T61	22	57
Hotei Regio	-25.8	81.2	211,000	T48	14	73
Tui Regio	-25.8	122	296,000	T12	43	
North Yalaing Terra	-15.2	322.46	2,300	T58	20	16
Ontario Lacus	-72	180	2,610	T38, T51	1	28 - 75
Arrakis Planitia	-78.1	110.5	27,500	T51	6	
78 S - 82 S			16,400	T23		
		Total	**998,000**			

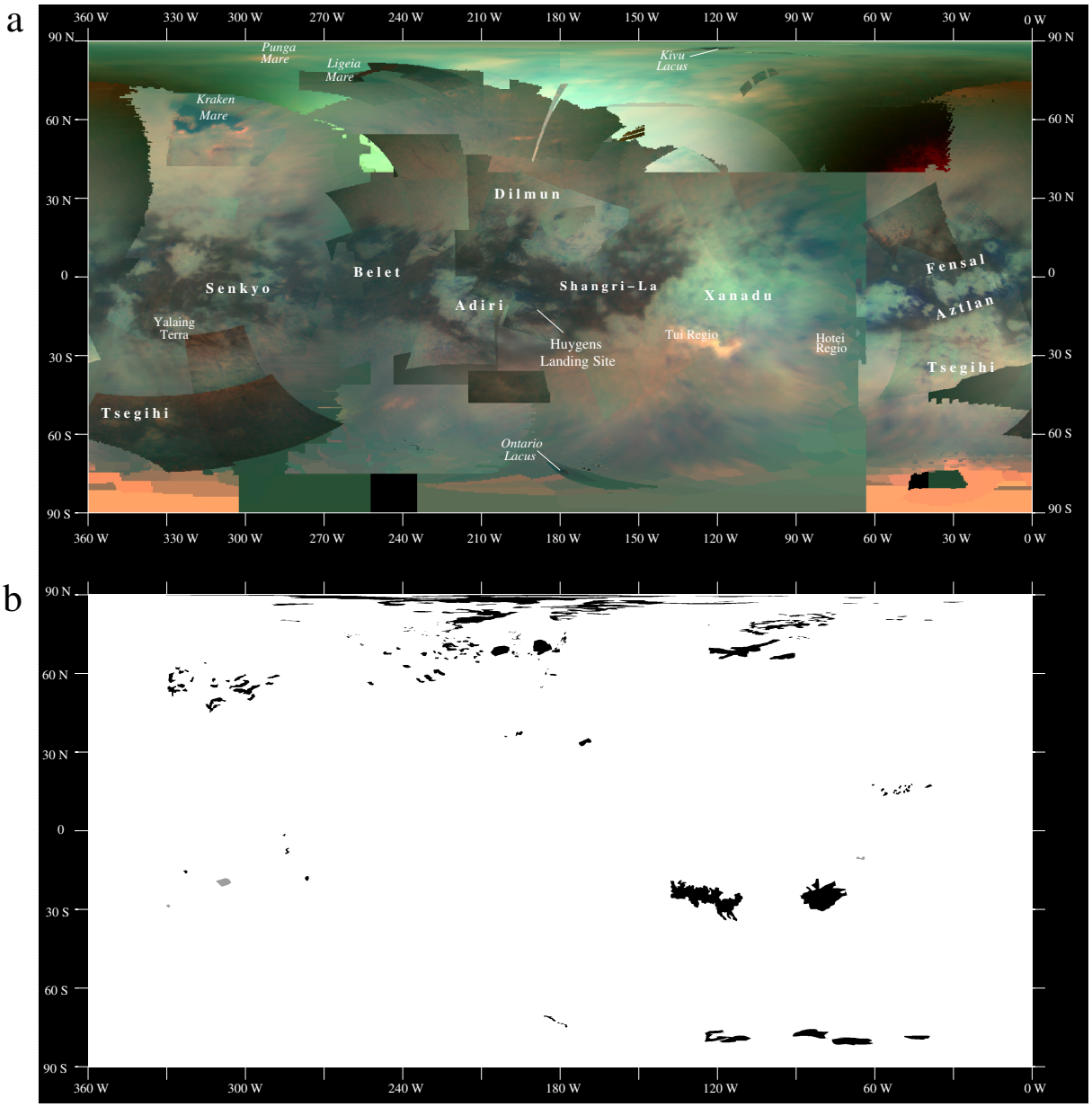

Figure 2.2: (a) Global cylindrical map of Titan as seen by *Cassini* VIMS using the color scheme of Barnes et al. (2007a): R = 5 μm, G = 2 μm, and B = 1.3 μm. This VIMS base map uses data from T8-T90. (b) Global distribution of evaporitic deposits in black (listed in Table 2.1) as well as several 5-μm-bright areas that did not meet sufficient criteria (e.g. not observed twice, no data of high enough resolution) to be considered evaporite candidates in grey. The polygons shown here, created with software designed for the analysis of Barnes et al. (2008a), were used to calculate the area covered by evaporite. While many of the new deposits identified in this study are located near liquid (on or near the shores or empty bottoms of polar lakes and seas), the existence of 5-μm-bright material in the equatorial region is evidence for the presence of large scale tropical seas in this area sometime in Titan's past.

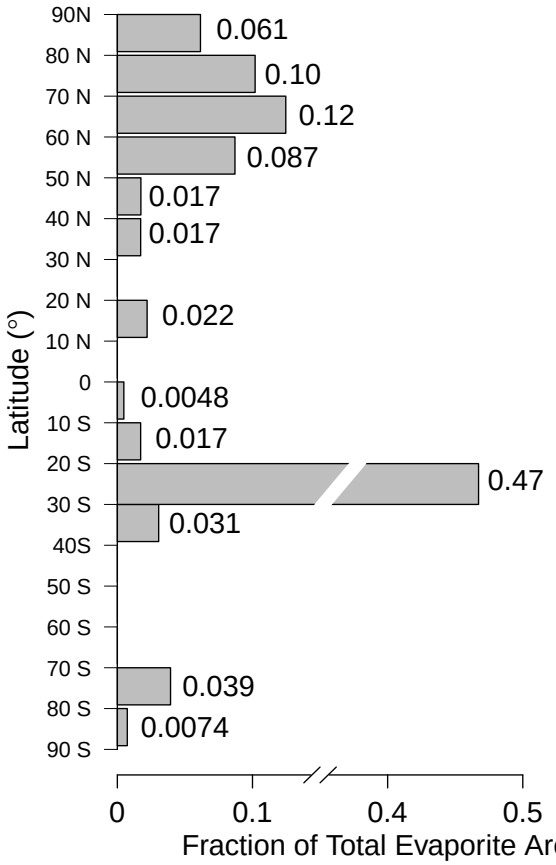

Figure 2.3: Fraction of total surface area covered by evaporite candidates binned by 10° in latitude (fraction listed for each bin by the number to the right of each column). In total, 5-μm-bright deposits cover a little more than 1% of Titan's surface. Though the north polar region has the largest amount of known surface liquid, it is the southern equatorial basins Tui Regio and Hotei Regio (located in the 10°S - 40°S) that contain the most 5-μm-bright material. The north pole (latitude $>$ 60°N) is the region with the next greatest evaporite occurrence. This is unsurprising in light of the formation scenario proposed by Moore and Howard (2010): if Tui Regio and Hotei Regio are fossil sea beds, then all possible compounds precipitated out when the liquid evacuated. The seas of the north pole, the only bodies capable of producing a comparable amount of evaporite, are still covered by liquid and therefore have either not precipitated out the maximum amount of material or some evaporite has fallen to sit on the seafloor. The south pole, notably, is as devoid of evaporite as the northern midlatitudes.

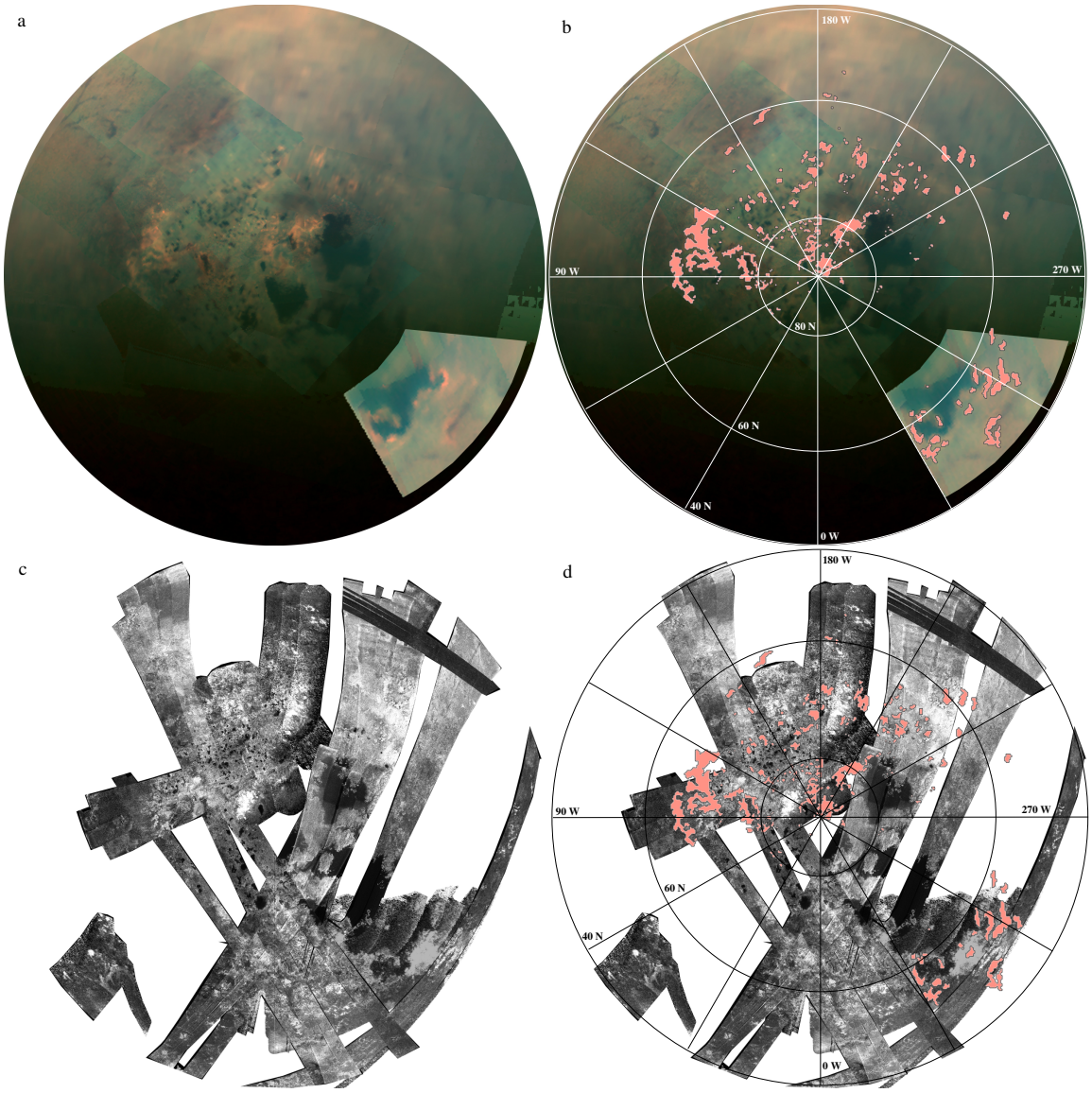

Figure 2.4: VIMS (T76, T93, T94, T96,T97) and RADAR (T16, T18, T19, T21, T25, T28-T30, T55, T56, T69, T83, T84, T86, and T91) coverage of Titan's north pole projected into an orthographic view from above the north pole: (a,c) without annotation and (b,d) with labeled coordinates and the polygons used to calculate the areas listed in Table 2.1. While there is an observational bias towards the western half of the pole with regard to smaller lakes as seen by VIMS, it is interesting to note that there is a real discrepancy in the distribution of large seas; that is, Punga, Kraken, and Ligeia are all in the western hemisphere. On the eastern side, there are no maria, but we do see two large evaporite deposits, Woytchugga and Nakuru.

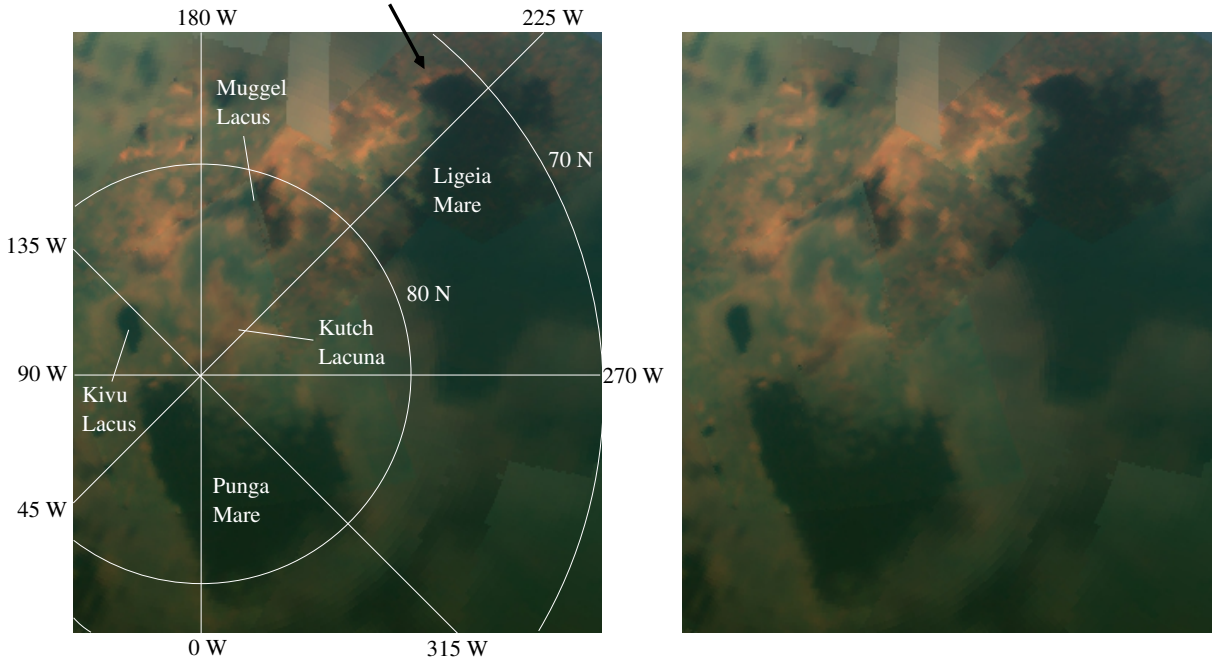

Figure 2.5: VIMS coverage of Titan's north pole from T93 and T94 projected into an orthographic view from above the equator with labeled coordinates (left) and unannotated (right). The "strip" of evaporite along the shore of Ligeia that seems to connect to Muggel Lacus's evaporite is pointed to by a black arrow. It may be that Muggel Lacus, unlike Kutch Lacunae, is not an isolated system, but rather a remnant of a time when Ligeia Mare extended further north.

equinox, allowing observations of the underlying lakes (Rodriguez et al., 2011; Le Mouélic et al., 2012b). Notably, with flybys T90 and later, we were able to investigate the anti-Saturn half of the north polar region, including the extent of Punga Mare and a variety of yet unnamed lakes.

In the latest VIMS data, we see that Punga Mare and Kivu Lacus are not the only features surrounding the exact North Pole: a distinct evaporitic feature, Kutch Lacuna, exists independently. Shown in Figure 2.5, Kutch does not lie along the shorelines of either the lake or sea nearby. Interestingly, Punga has small evaporite deposits only visible in the high resolution shot of T93 (best sampling of ~ 5 km/pixel). This is unusual, as the other three largest bodies (Kraken Mare, Ligeia Mare, and Ontario Lacus) have both small deposits and larger shoreline coverage of 5-μm-bright material. Perhaps Punga's liquid level is currently at its "high water" mark, or the sea could have steeper shores than its counterparts.

The southeastern shore of Kivu Lacus was seen at a fine sampling (roughly 1 km/pixel) by VIMS in the T85 flyby. In T85 (zoom in of Figure 2.6 a), 5-μm-bright material hugs the south eastern shoreline. In panel b, we use a hue-saturation-value (HSV) scheme to combine RADAR and VIMS data. The RADAR data provide the combined image's brightness (value), while VIMS data determine the color (hue) and degree of color (saturation) relative to the value. We also identify some non-shoreline 5-μm-bright material (orangey-red in the color stretch of Figure 2.6) as deposits though no RADAR features are discernible. These deposits near the lake were observed in both T85 and T93, forming a half ring about 150 km wide a few kilometers from Kivu's southern shore.

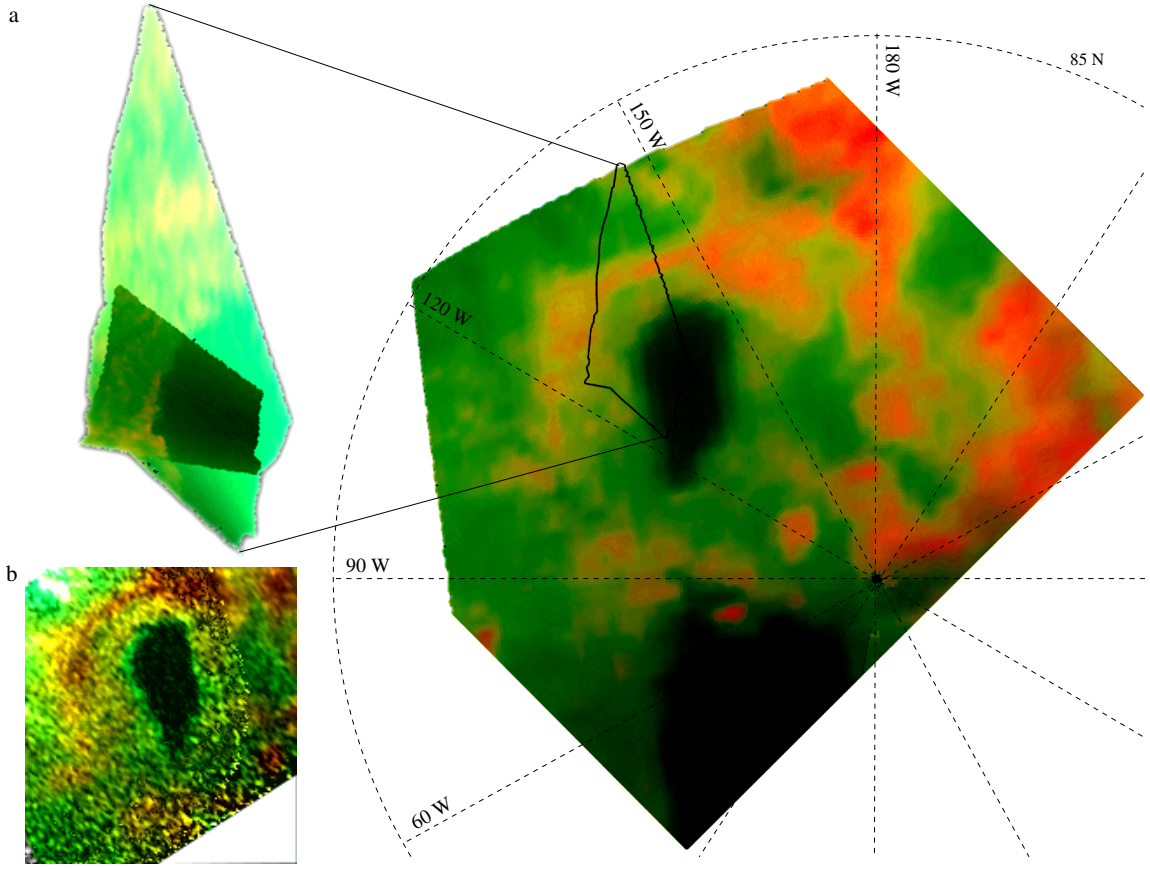

Figure 2.6: Orthographic projection of Kivu Lacus. (a) Annotated VIMS data from T93 is shown on the right with the outline of the high resolution image from T85, a zoom in of which is shown on the left. (b) RADAR data (HiSAR T25) combined such that the VIMS data provides hue and saturation while RADAR provides the value (HSV). We see that 5-μm-bright material (bright orange and red in this HSV) is geomorphologically consistent with evaporite. As with Titan's other lakes, evaporite is not found along the entirety of the shoreline, though we do not have the resolution around the entire shore to be certain that the evaporite is truly absent. There are some non-shoreline 5-μm-bright areas (a semicircle a few kilometers from Kivu's southern shore, seen in both T93 and T85) though no RADAR features are discernible in the low signal of available data.

North of Ligeia, a large distribution of 5-μm-bright material surrounds the uniquely shaped, VIMS dark blue lacustrine feature known as Muggel Lacus, shown in Figure 2.5. The morphology suggests either a paleo shoreline of Ligeia Mare or a previously more extensively filled lacustrine feature. In the former case, Ligeia would extend over an area of 136,000 km^2, an increase of about 9%. Muggel Lacus was covered by what we assume to be fog in T91, but returned to the morphology seen in T90 by T93 and T94. The most northern extension of Muggel Lacus (near Kivu) was covered by a cloud in T93, but is cloud free in T94. We interpret Muggel to be a shallow evaporitic basin with a very shallow lake at its bottom– shallowness would be consistent with why the feature is difficult to see in RADAR.

In Figure 2.7, we again combine VIMS and RADAR data and see that the expansive 5-μm-bright region indicated by arrow *a*, Woytchugga Lacuna, is similar to Kutch. Neither are located in conjunction with currently filled liquid bodies. To the right of Woytchugga is another not-lake-bordering 5-μm-bright deposit, Nakuru Lacuna, indicated by arrow *d*. The 5-μm-bright signature of both candidates is consistent in shape between T90 through T97– they are thus unlikely to be patches of fog. The northeastern-most corner of Woytchugga even appears 5-μm-bright in a small hi-res shot from T88. Smaller deposits identified from T88 also agree with the deposits identified in this T93 image, *b* and *c*. Arrow *b* points to a streak that does not seem to correspond with SAR-identifiable lacustrine features, though in VIMS data it borders the dark material typical of liquid filled lakes (blue in our color scheme) in the north pole. Arrow *c*, however, shows the often observed evaporite-covered shores of MacKay Lacus.

The region dense with small lakes identified by Hayes et al. (2008) around 80N, 140W was seen by VIMS during T96 and T97. Figure 2.8 shows the VIMS data on the left, and a VIMS-RADAR composite on the right. With few exceptions, the 5-μm-bright material corresponds to the shores of filled lakes or the bottoms of dried lakebeds as discerned from RADAR. Thus, evaporite is found on the largest liquid bodies on Titan (notably, the large deposits along the shores of Kraken Mare), as well as lakes at the limit of detectability for VIMS. There seems to be a higher number of evaporite deposits in this region than elsewhere in the north pole, though we caution that this statement is observationally biased until the sub-Saturn half of the north pole has better VIMS coverage.

While we will show in this section that much of the correlation between RADAR and VIMS data is geomorphologically consistent with evaporite formation along lakebed bottoms or liquid filled shorelines, the remaining diversity of RADAR features corresponding to VIMS 5-μm-bright material, especially in the liquid-abundant north pole region, is evidence for complex processes that are not yet understood. Woytchugga and Nakuru Lacunae, for example, are not located near current lacustrine features. Instead, the 5-μm-bright areas seem to be located along a boundary between varying intensities in the RADAR signal (perhaps similar to Arrakis Planitia, discussed below).

The geomorphological interpretation by Wasiak et al. (2013) of the RADAR coverage of Ligeia Mare complements the evaporite candidates that we map in the region. The deposits are located in the kinds of terrains one would expect evaporite to form. Evaporites dotting the southern shoreline of Ligeia (identified in T69), for example, are small, isolated, and coincide with bays (possibly flooded) and mottled (erosion pattern lacking) landscapes. In the area between Kraken and Ligeia, where we identify evaporite along the shore of Kraken, Wasiak et al. (2013) interpret a dome structure to establish a watershed between

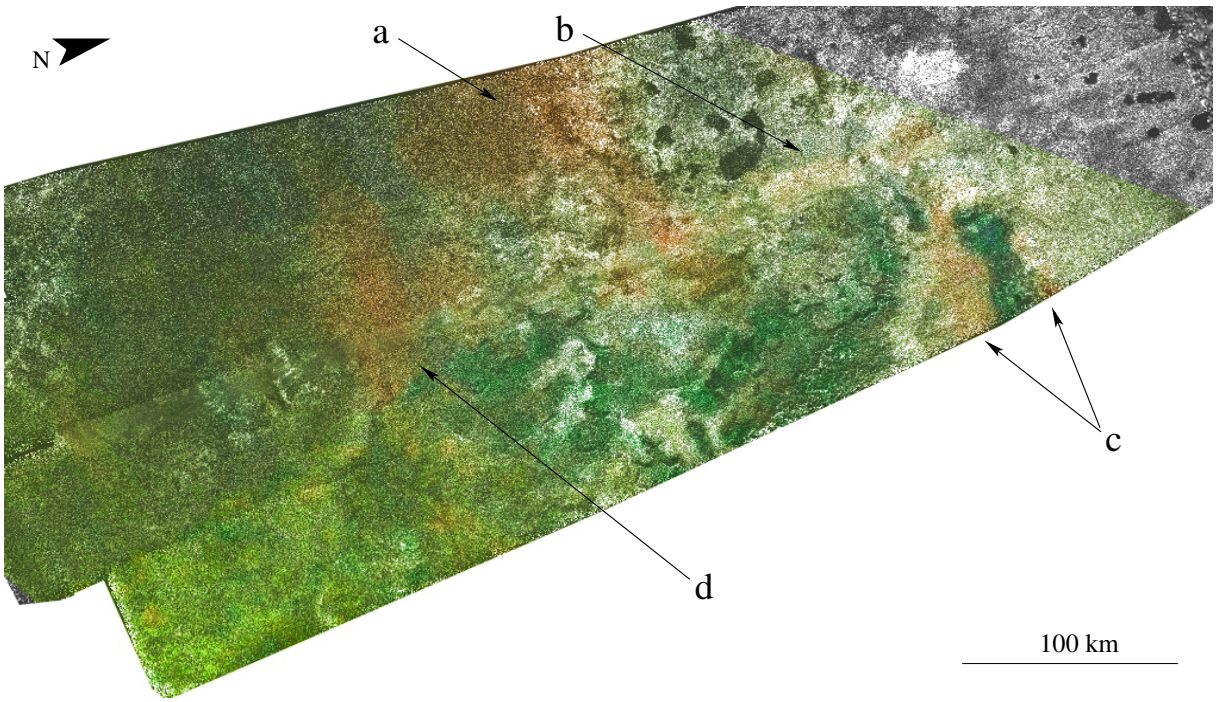

Figure 2.7: VIMS images of the eastern north pole evaporites from T93 overlaid atop RADAR HiSAR from T91 with an HSV color-stretch. Arrows *a* and *b* point to evaporite candidates, Woytchugga and Nakuru respectively, that are partially seen in a small, high resolution image from T88 (and appear 5-μm-bright there). Woythchugga is located at 69°N, 110°W; Nakuru is at 65.5°N, 92.38°W. Evaporite surrounding MacKay Lacus is indicated by the *c* arrows (77°N, 96°W). The deposit pointed to by arrow *d* is seen in T90-T97 as a 5-μm-bright feature of static morphology. To date, the best resolution images of Woytchugga and Nakuru (arrows *a* and *d*) are from T97.

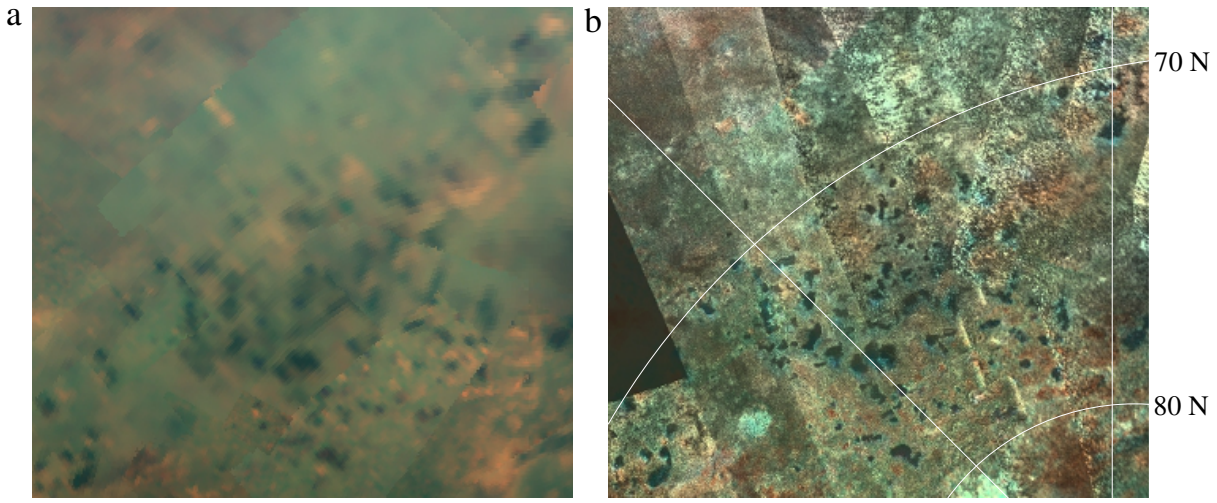

Figure 2.8: Titan's north polar lake district as seen by VIMS in T96 and T97 (a) and RADAR (b, colored with VIMS) in a HiSAR swath from T25. Despite VIMS' comparatively coarse resolution, the agreement between the 5-μ-bright material in dry beds and around lake shores is geomorphologically consistent with evaporite.

the three seas. The "strip" of evaporite along the easternmost southern shore of Ligeia (viewed in T94 and pointed to by a black arrow in Figure 2.5) is located in a lower lying region than the hummocky terrain directly east.

North of the region Dilmun, evaporite deposits continue eastward from those south of Ligeia identified by Barnes et al. (2011), shown in Figure 2.9. The two northern deposits indicated with black arrows appear in T69 as well as T90 and T97. The correlation between RADAR and VIMS data for this general area is ambiguous, as the HiSAR swath of T29 is noisy along the seams. The data do, however, provide enough qualitative context for the evaporite deposits outlined in *b* to again confirm that the 5-μm-bright material coincides with a region in which lakes exist. Clouds are also active in this region: the white arrows of Figure 2.9 point to clouds that exhibit the specific 2 μm wing, 2.75 μm, and 5 μm window signatures. Whether the lake desiccation process drives the clouds or the clouds drive the precipitation is beyond our present ability to determine.

Kraken Mare, Titan's largest body of liquid, extends farther south than any other sea. In fact, the highest resolution VIMS imaging of the liquid body covers its southernmost shore. In Figure 2.10 we again use HSV to compare VIMS and RADAR data. The difference in quality (mostly spatial resolution) between the middle RADAR swaths and those at the top and bottom is the difference between HiSAR and SAR modes, respectively. As with Ontario Lacus (Barnes et al., 2009a, 2011), evaporite is not detected along the entirety of the shoreline seen at VIMS resolution. If the RADAR-bright material of the southwest is a mountain chain, then the steep shoreline could explain the apparent absence of evaporite along the middle of the southern coast. This would be a scenario similar to the northwest shore of Ontario, where mountain chains have been identified (Wall et al., 2010; Hayes et al., 2011; Turtle et al., 2011c; Cornet et al., 2012a). On the northwest shoreline above 60°N, there is neither extensive evaporite coverage (only an isolated deposit viewed in T69) nor RADAR-bright material to explain the absence of 5-μm-bright material, similar to the other mare shorelines. Unless there are small deposits beyond presently available VIMS resolution, some other process, like steeper shorelines or frequent flooding for example, could be responsible for preventing large scale evaporite formation there.

South of Kraken, there are several evaporite deposits not located along the sea's shoreline. In the middle of the shoreline mountains, what may be a valley is seen to be 5-μm-bright. To the east, the 5-μm-bright material that appears to be separate from the very bright deposits on Kraken's southeastern-most shore extends from 58°N down to 50°N. At the lower latitudes, where SAR data is available, this material is coincident with some discernible RADAR features. Hammar Lacus, indicated by the white arrow of Figure 2.10 is about 11,000 km^2 in area with 5-μm-bright material delineating all but its eastern shores. The lake itself is RADAR-dark and the evaporite is RADAR-neutral to the west, as expected. To the northeast of Hammar Lacus, however, evaporite extends into the increasingly RADAR-bright area, probably indicative of mountains or very rough terrain. Mountains typically appear dark blue in our VIMS color scheme (Barnes et al., 2007c). Thus, if the RADAR-bright features are mountains, then one mechanism for them to appear 5-μm-bright would be if some erosional process was exhuming evaporite. If Kraken were to cover all these non-shoreline deposits (difficult if the RADAR-bright material is indeed mountainous), the sea would need to increase in area by about 10%.

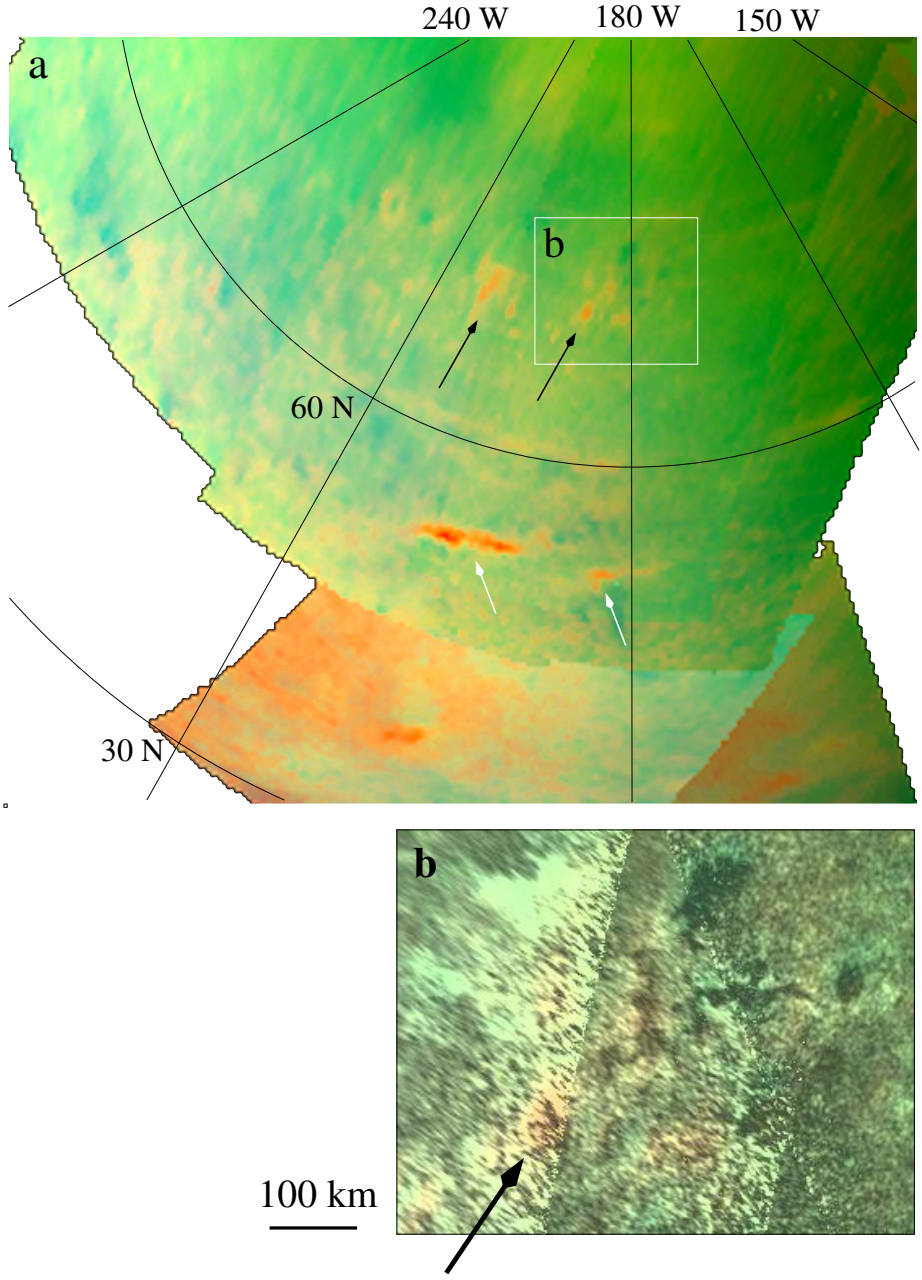

Figure 2.9: (a) VIMS image from T69 of the lake dotted region located north of Dilmun. The white arrows point out clouds (identified via their 2 μm window signature). The other 5-μm-bright isolated areas are evaporite candidates. (b) HSV composite of RADAR data from T29 colored according to VIMS. Most of the HiSAR mode RADAR swath covering this region is of too poor resolution to make a comparison to VIMS. However, the section shown in (b) has high enough signal-to-noise to give, at least qualitatively, more geomorphological evidence that 5-μm-bright signatures correspond to lake features in RADAR.

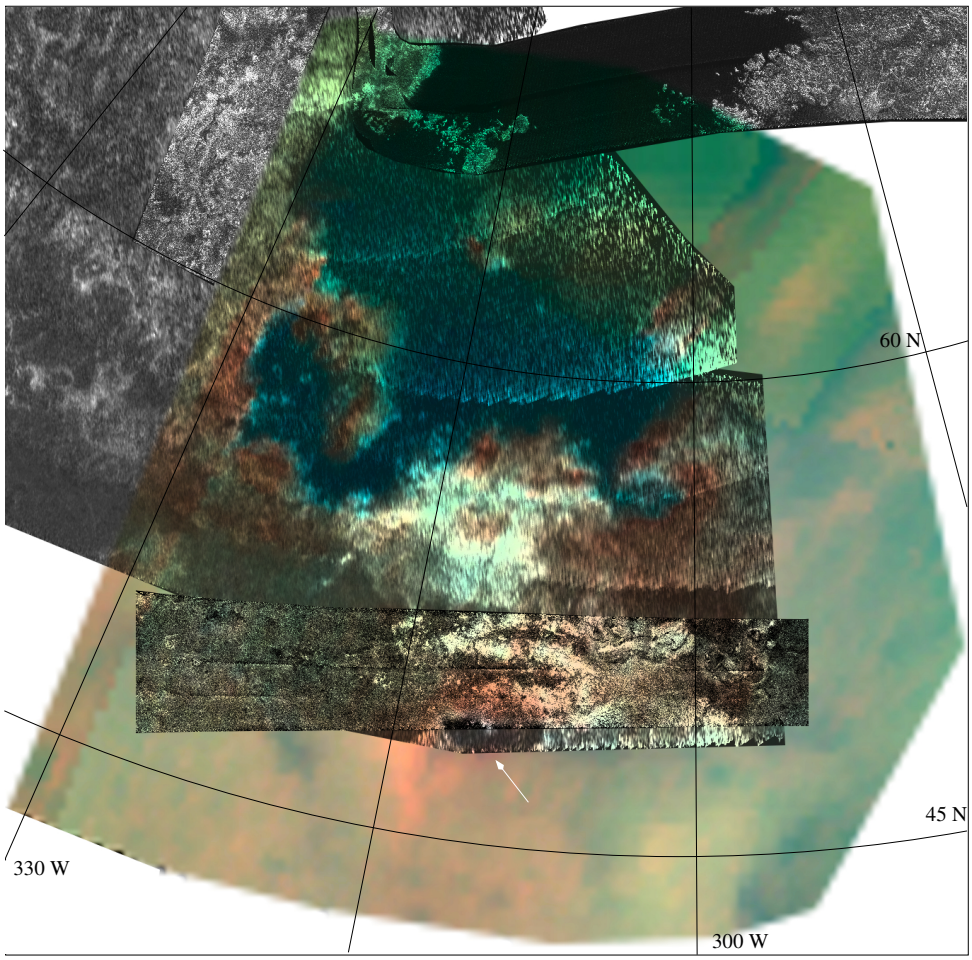

Figure 2.10: (a) Best resolution VIMS coverage of the southern shoreline of Kraken Mare from T76 overlaid with SAR and HiSAR data from T84 in HSV space. The evaporite deposits (explicitly outlined in Figure 2.4b) correlate well with the sea's shoreline, as well as with the boundary of the RADAR-dark feature to the south and a depression-like area to the east. The white arrow points to Hammar Lacus; the RADAR-dark material indicates a smooth surface coinciding with dark VIMS material typical of liquid-filled lakes.

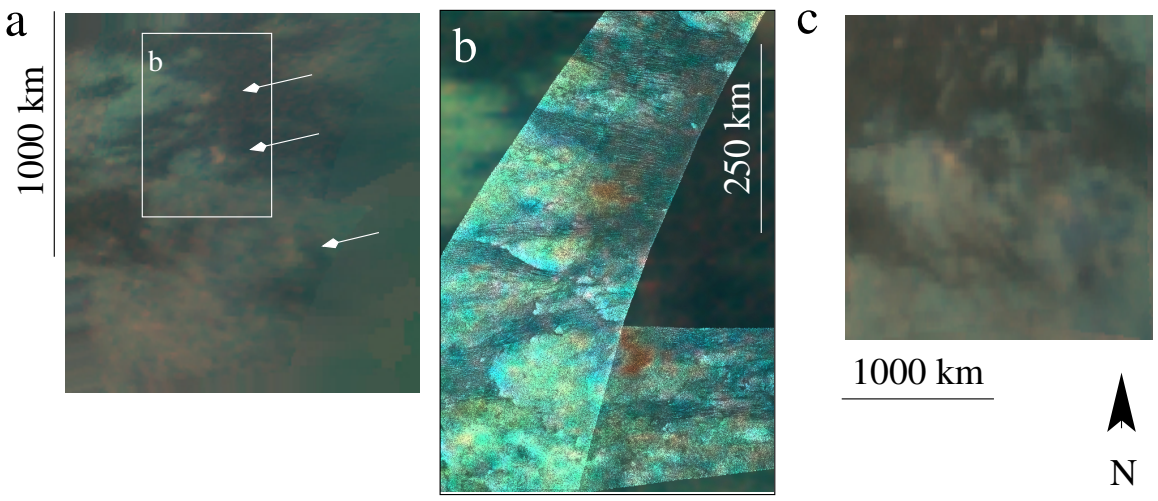

Figure 2.11: Best VIMS images of the smaller tropical evaporite deposits: (a) west Belet north (top; 1.5°S, 284.9 W), south (middle; 8.2°S, 283.9°W), and southwest (bottom; 18.2°S, 276.6°W) from T61; (b) RADAR images from T8 and T21 for west Belet north and south colored according to the VIMS data; and (c) north (left) and east (right) Yalaing from T67. All of the evaporite deposits seem to be located at the border between VIMS dark brown and VIMS equatorial bright spectral units. Where RADAR coverage exists, these VIMS boundaries coincide with RADAR dark and bright boundaries.

2.4.2 Midlatitudes and Tropics

In the non-polar regions, despite the present-day lack of filled lakes or seas, we identify several evaporite candidates. West of Belet, there are three distinct deposits seen in VIMS data from T61, indicated by white arrows in Figure 2.11a: from top to bottom, West Belet North, West Belet South, and Southwest Belet. Each deposit seems to be located on the border between (non-Xanadu) equatorial bright and dark brown spectral units. In the equatorial band, the dark brown spectral unit, ascribed to water-ice-poor material and associated with organic material (atmospheric aerosol-like particles), corresponds to dunes (Soderblom et al., 2007; Barnes et al., 2007b; Le Mouélic et al., 2008; Rodriguez et al., 2014). When the RADAR image is colored according to the VIMS data (Figure 2.11b), the spectroscopic boundaries correspond to those in the RADAR data and West Belet North and South are located along such a boundary. It could be that lacustrine or fluvial features are present in the region, but beyond the resolution limit of SAR, VIMS, or ISS (as is the case for the Huygens Landing Site, where probe data reveal such features while *Cassini* instruments do not). On the other hand, the lack of fluvial features may be indicative of distinct processes responsible for creating or exhuming evaporite along the border of the two spectral units (perhaps dune induced convecting clouds, for example (Barth, 2010)).

Unique among 5-μm-bright deposits not found at the poles, the evaporite candidate located on the north end of the land mass Yalaing Terra has been observed by VIMS several times. This evaporite candidate does not always appear 5-μm-bright: for over a year, the surface experienced brightening in the shorter wavelengths that correspond to the Equatorial Bright spectral unit, then reverted to

its original spectrum, which is shown Figure 2.11c. Based on the long time scale of reversion and the relative reflectivity behavior (between the brightened area and nearby unchanged dark and bright areas), this phenomenon was suggested by Barnes et al. (2013a) to be due to the rainfall from the 2010 September cloudburst. Similar brightening/darkening was seen at locations of similar latitude: Heptet Regio, Concordia Regio, and Adiri. Turtle et al. (2011b) also attribute observed surface darkenings to a change in surface wetness. If rainfall is the cause for surface brightening, the evaporite may have dissolved, then precipitated out again as the liquid evaporated. Alternatively, there may have been just enough liquid accumulation to effectively mask the brightness at 5 μm, without actual dissolution of the solute. In either case, this observation is evidence against short-term evaporite volatility, for the deposit reappears in the exact location where it was previously observed. Such behavior would be unusual for a vapor. As of yet there are no RADAR data to provide further evidence as to whether this 5-μm-bright signature coincides with lacustrine or fluvial morphologies or is located along a RADAR bright/dark border in the same fashion as the other not-polar evaporite candidates.

There is a particularly bright outcropping of 5-μm-bright material north of the western part of the region known as Fensal, best seen by VIMS in T5 and encapsulated by a black box in Figure 2.12a. To the furthest west of this box, two deposits are located on the border between equatorial bright and dark brown material, similar to what we see in West Belet (Figure 2.11a). East of these features, there are a number of 5-μm-bright patches nestled amongst VIMS dark blue spots. The VIMS dark blue unit, unlike the dark brown unit, is suspected to be water-ice rich (Rodriguez et al., 2006, 2014; Soderblom et al., 2007; Barnes et al., 2007b; Le Mouélic et al., 2008). Comparison between the VIMS and RADAR data in panel b is hindered by the high level of photon shot noise; that is, the low signal of this flyby is highly affected by random photon fluctuations. While the composite is not very useful for distinguishing the RADAR features corresponding to 5-μm-bright deposits, we can discern that the dark blue VIMS unit coincides with RADAR bright material. These dark blue spots have a lacustrine-like morphology; liquid lakes could appear RADAR bright if there were enough waves to roughen the surface. However, SARtopo inferred relative altimetry (Stiles et al., 2009) indicates that peaks in this region correspond to the RADAR-bright and VIMS dark blue spots. While such altimetric evidence does not rule out the possibility of lakes (there are mountain lakes on Earth, such as tarns and cirques, that are formed in the basins excavated by glaciers and filled with rainwater or snow melt), the prevalence of the VIMS dark blue unit coinciding with mountains in the equatorial region as well as the putative absence of equatorial lakes makes such an explanation less likely. Thus, we prefer an interpretation in which the peaks are mountainous and evaporite candidates are either exhumed by crustal activity or is the remnant of liquid that pooled in slight depressions at the base of the mountains, where the mass of the peaks could deform the surface crust enough to create very localized basins.

Further east we see a larger but fainter 5-μm-bright region (pointed to by the white arrow in Figure 2.12) once again bordering equatorial bright and dark brown VIMS spectral units. The spatial resolution of this part of the VIMS composite image is not as good as that of the smaller west Fensal deposits discussed above. SARtopo indicates that this region is of lower altitude than the RADAR bright spot bordering on the east– the topography expected for an evaporitic deposit as liquid could pool in the depression. If there was once enough liquid to form this evaporite candidate along the edges of this basin,

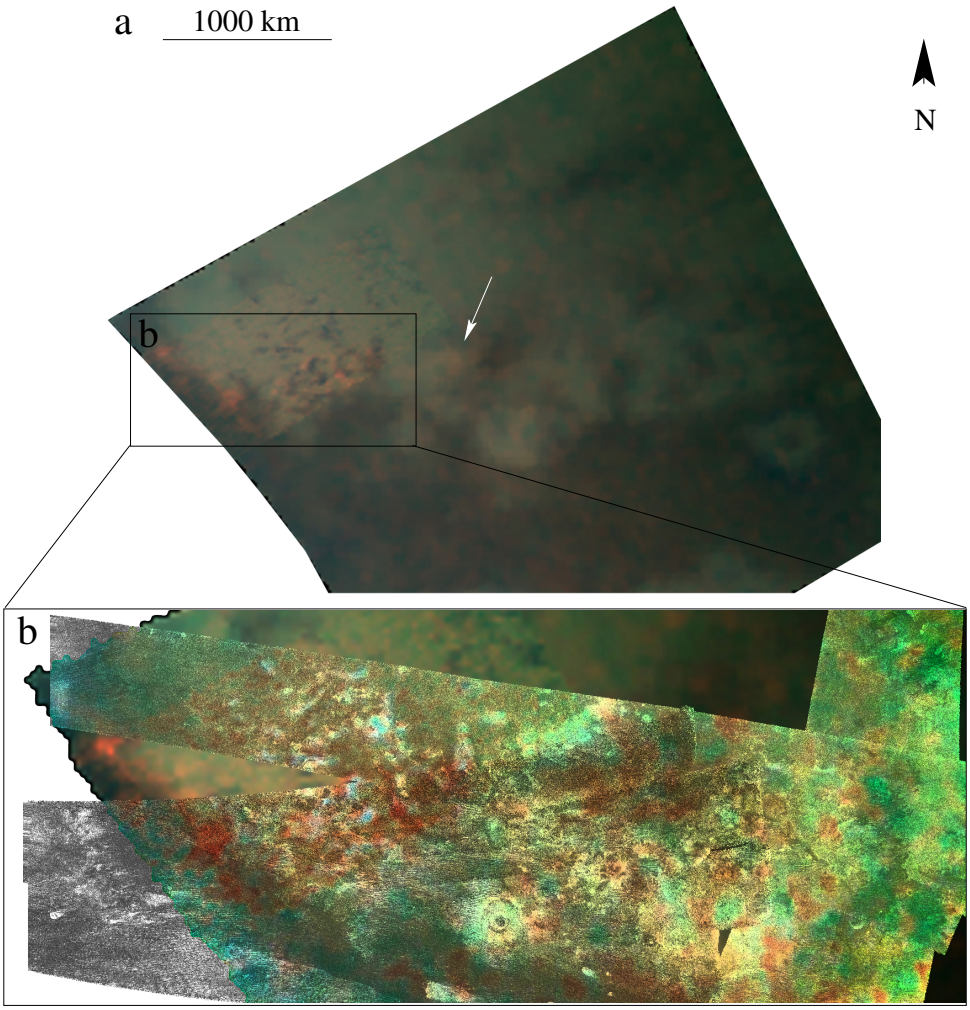

Figure 2.12: (a) VIMS image from T5 for west and east Fensal (centered at 1°5 N, 52°W and 17.4 N, 39.5°W respectively). West Fensal is enclosed in the black box while east Fensal is indicated by the white arrow. (b) RADAR images from T5, T28, and T29 overlaid with VIMS in HSV space. While the evaporite candidates are easily discernible in the VIMS data alone, the high photon shot noise makes comparison to RADAR difficult. However, the VIMS dark blue material that the evaporite deposits border are seen to correlate with RADAR bright areas identified as peaks in SARtopo.

perhaps there was also enough to wet the surface at the base of the VIMS dark blue mountains nearby.

2.4.3 Tui and Hotei Regiones

Recent work by Lopes et al. (2013) reestablishes the evidence for possible cryovolcanic features around Hotei from the most recent VIMS and RADAR data. While we maintain the hypothesis of Moore and Howard (2010) that the basins Tui Regio and Hotei Regio are 5-μm-bright because they are fossil seabeds that were once filled with enough liquid from which evaporite could form, we note that cryovolcanic activity and a fossil seabed are not mutually exclusive. Isla Incahuasi, for example, is an ancient volcano in the middle of the Salar de Uyuni, Earth's largest salt flat. However, since the 5-μm-bright spectral unit is water-ice-poor, the *formation* of the 5-μm-bright material is not consistent with cryovolcanism.

As shown in Figure 2.3, Tui and Hotei are the largest single outcroppings of 5-μm-bright material on the surface of Titan, comprising 30% and 21% of the total area of mapped 5-μm-bright material respectively. (For VIMS observations of the regiones, we refer to Figures 1 and 2 of Barnes et al. (2006) for Tui and Figure 1 of Soderblom et al. (2009) for Hotei.) We estimated the volume that the basins could hold by a simple approximation similar to Lorenz et al. (2008) and Lorenz et al. (2014): we assumed that the depth/area ratio is constant for large bodies and scaled this ratio to the recently measured depth value for Ligeia Mare (Mastrogiuseppe et al., 2014). From this, the total volume in the seas was found to be $\approx$ 42,000 km^3, a value within the range of those found independently by Lorenz et al. (2014) and Hayes et al. (2014) ($\approx$ 32,000 km^3 and $\approx$ 70,000 km^3, respectively). Our total volume for Tui (ratio depth of 370 m) and Hotei (200 m) was 57,000 km^3. To first order, there is enough liquid currently in the north pole to fill Tui and Hotei.

2.4.4 South Pole

Cassini's RADAR has revealed Titan's south pole to have a geomorphology as complex as the north: hummocky terrain thought to be topographic highs (Lopes et al., 2010), fluvial networks (Burr et al., 2013), and lacustrine features both persistent and ephemeral (Hayes et al., 2011). Unlike the north pole, however, where lacustrine and evaporitic features are widely distributed and vary greatly in size, the southern polar region is dotted with only a handful of evaporite candidates large enough for VIMS to spectrally identify. Shown in Figure 2.13, these deposits are found along the shorelines of Ontario Lacus, isolated in the eastern half of the region, and on the edges of Arrakis Planitia.

The 5-μm-bright material along the eastern shore of Ontario Lacus, the largest and most long-lived liquid filled body in the region (Brown et al., 2008; Turtle et al., 2009), has been well documented (Barnes et al., 2009b; Wall et al., 2010; Turtle et al., 2011c; Cornet et al., 2012a,b)). The general geomorphological interpretation is that this area is an evaporite covered (Barnes et al., 2009b) alluvial plain (Wall et al., 2010; Turtle et al., 2011c; Wall et al., 2010), though Cornet et al. (2012a) also propose lunette dunes. We estimate that evaporite covers an area equivalent to 17% of Ontario's liquid filled portion and would require an increase in liquid volume of about 30% to cover it (using the same method described in Section 2.4.3).

A darkening of Arrakis Planitia was observed from T0 (2004 July 3) to Rev009 (2005 June 6) by ISS

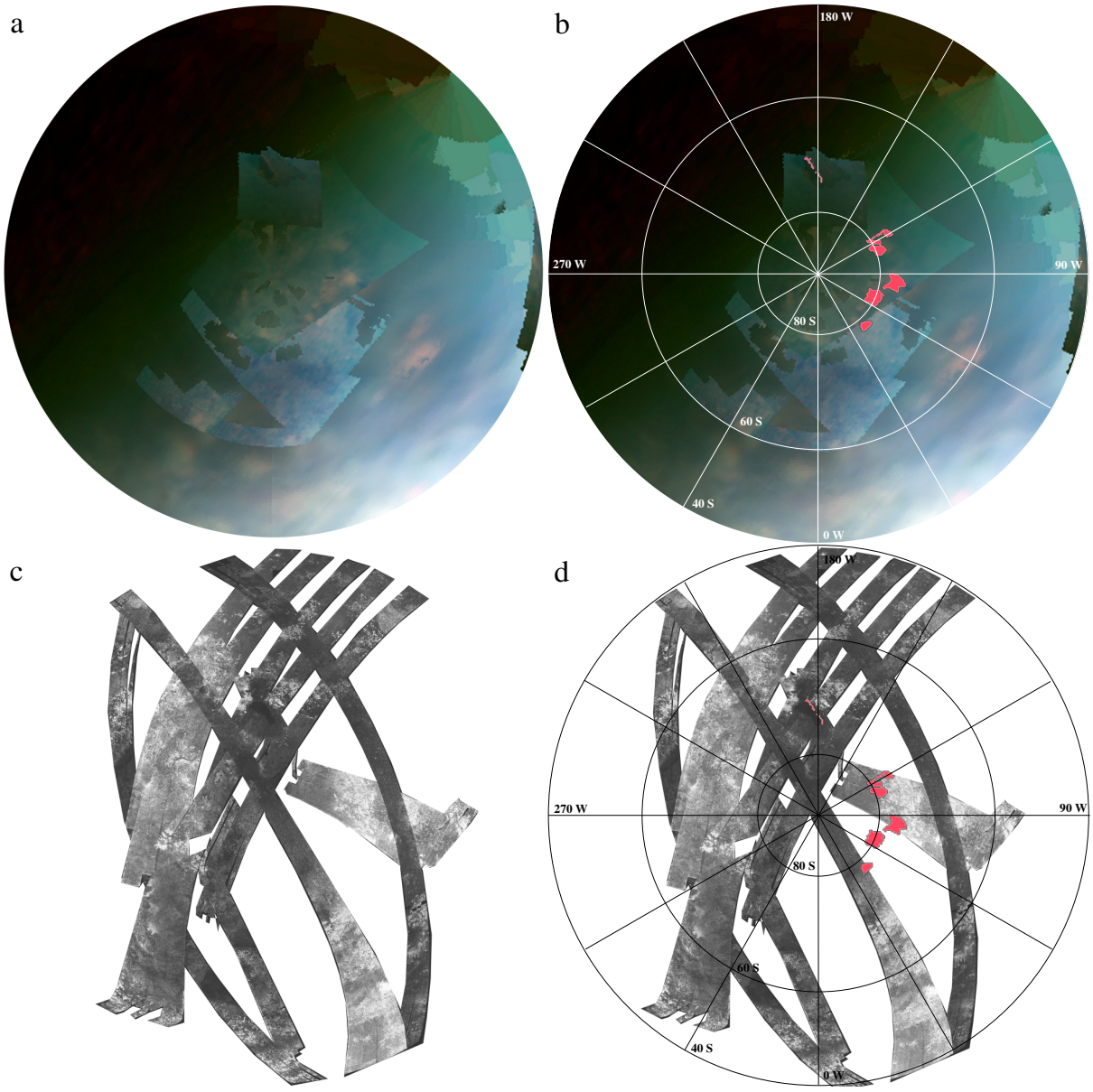

Figure 2.13: Orthographic projections of Titan's South Pole as seen by VIMS in panel a (T20, T23, T24, T28, and T51), by RADAR in panel c (T36, T39, T49, T55, T56, T57, T58, T59, T65, and T71), and annotated with polygon outlines of evaporite candidates in panels b and d. Clouds have been removed from this VIMS composite to increase surface visibility. Fewer lacustrine features are present in this region in comparison to the north pole, as are evaporite candidates. Ontario Lacus, seen along the 180°W line, is the region's only known long-lived liquid body with evaporite. Deposits on the edge of Arrakis Planitia, however, are seen by VIMS after an ISS identified surface wetting event (Turtle et al., 2009). (There are no VIMS observations of the area before those of ISS.) The other evaporite candidates, though they lack RADAR data with which to correlate, are observed in multiple VIMS flybys, in the midst of frequent cloud activity.

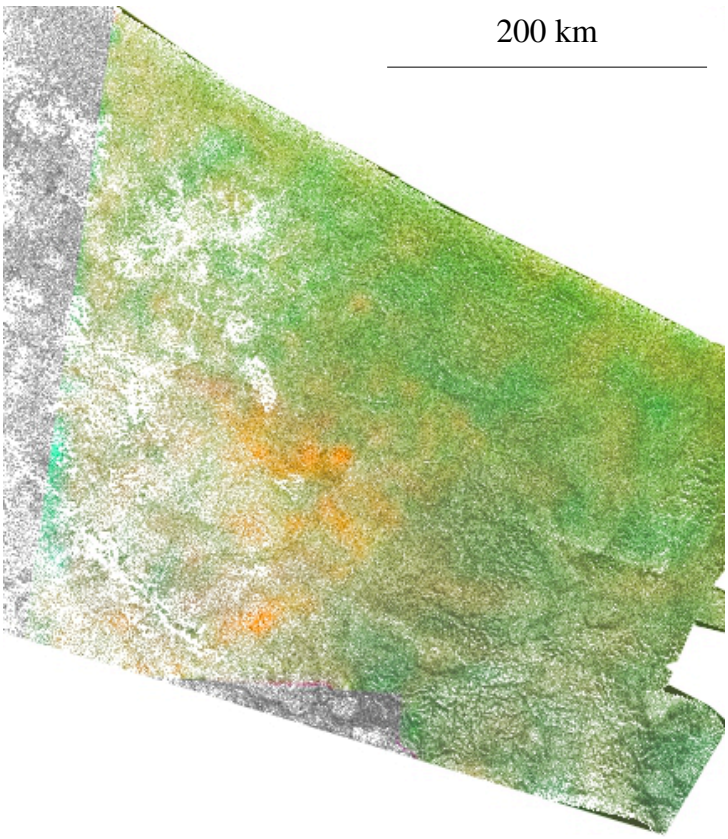

Figure 2.14: RADAR image of Arrakis Planitia (78.1°S, 110°W) from T49 orthographically projected and colored according to VIMS data from T51. The 5-μm-bright material is coincident with the edges of the low plain whose albedo was observed to darken after presumed rainfall from earlier cloud coverage. ISS detected a return to the original albedo in T50 (Turtle et al., 2011b). VIMS observes the 5-μm-bright signature in several flybys, but only after the darkening period.

coincident with cloud coverage in Ta (2004 October 6) (Turtle et al., 2009). The area was then seen to return to the lighter albedo observed in 2004 in ISS data procured in T50 (2009 February 6) (Turtle et al., 2011b). This surface change was interpreted by Turtle et al. (2009) and Turtle et al. (2011b) as precipitation driven wetting and subsequent drying by infiltration or evaporation. VIMS observed Arrakis Planitia in T20 (2006 October 25), T22 (2006 December 28), T23 (2007 January 13), T24 (2007 January 29), and T51 (2009 March 27), revealing some 5-μm-bright signatures in the same area. In T20, the signature is small and faint. In T22, the area is covered by low altitude clouds, which seem to move or dissipate by T23. The 5-μm-bright feature looks the same in T23 and T24, but by T51 extends over a somewhat larger area. We interpret these observations as complementary to the processes observed by ISS–the increase in 5-μm-bright signature could be due to surface liquid (either still present from Ta or in connection to the cloud activity of T22) evaporating and leaving the 5-μm-bright material behind. This would be similar to the scenarios explored by Barnes et al. (2013a), where the evaporite deposit north of Yalaing Terra disappears after a rainfall event and reappears when (presumably) the surface liquid has evaporated again. Figure 2.14 shows the correlation between RADAR coverage from T49 and the VIMS data from T51. The evaporitic material lies along the border of the low plain. (The T24 coverage of Arrakis Planitia is shown in the VIMS composite of Figure 2.13.)

The other two candidates in the south pole do not coincide with any RADAR data, but are seen to be 5-μm-bright in more than one flyby. We note that the locations of our evaporite candidates, except for that around Ontario Lacus, do not coincide with the pole's large basins (Stofan et al., 2012; Lorenz et al., 2013) proposed by Wood et al. (2013) as large enough to be seas if they were filled. If the surface liquid transport were mostly seasonal, we would expect to see these basins filled to some extent during *Cassini*'s observations of southern summer. The absence of such filling in addition to the lack of evaporite would point to some longer than seasonal process of liquid exchange, if any ever occurred. The small lakes of the south pole (Hayes et al., 2011) could have a more seasonal cycle, though we anticipate that such a relatively short period of fill would not be enough to accumulate enough solute for evaporite formation.

2.4.5 Topography

To date, the available topographic data for Titan cover only 11% (Lorenz et al., 2013) of the surface area. Recent work by Lorenz et al. (2013) interpolates a global topographic map for Titan based on these data from RADAR SAR, altimetry, and SARtopo (Stiles et al., 2009). To investigate the relative topography of our evaporite candidates, we transform the data of Lorenz et al. (2013) into altitudes relative to the degree-three geoid of Iess et al. (2012) by using the ellipsoid defined by $(a, b, c) = 2575 + (230, -68, -171)/1000$. The results are shown in Figure 2.15: panel a shows the frequency of altitudes while panel b shows the global distribution of evaporite candidates binned by altitude.

The Gaussian shape of the histogram shows that the 5-μm-bright material is not always at the overall lowest points on Titan. This is perhaps unsurprising in the case of evaporite formation. Liquid pools in *local* topographic lows, not necessarily global lows. After all, the largest salt basin on Earth today, Salar de Uyuni, was once a filled lake at 3,600 m above sea-level in the Andes Mountains. Additionally, salt deposits on Earth can be buried and later exhumed by tectonic activity. Comparing our evaporite candidate locations to the immediate vicinity indicates that the deposits are locally low-lying, at least at

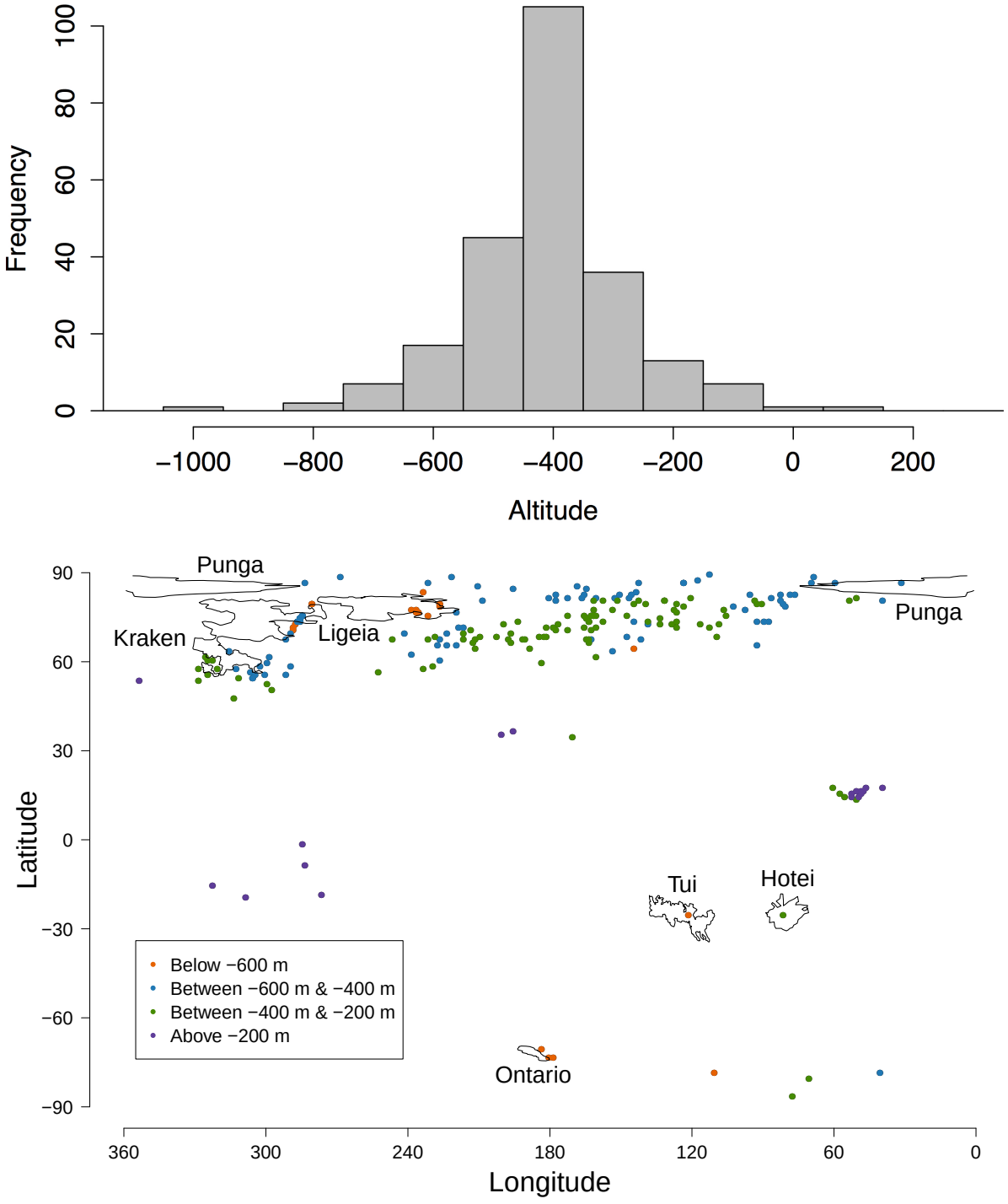

Figure 2.15: Altitudes of the evaporite candidates from the topographic map of Lorenz et al. (2013) relative to the degree 3 geoid of Iess et al. (2012) shown in (a) a histogram and (b) in cylindrical projection with contours of major bodies of liquid drawn from VIMS data. The average altitude is about -400m with σ=140m.

the resolution of the interpolated map. Further investigation and quantification of our proposed evaporite covered topography will therefore have to wait for a more conclusive topographic data set.

2.5 Discussion

Based on the correlation between 5-μm-bright material and lakebeds shown in this work and by Barnes et al. (2011), we explore the implications of liquid having been present at some time in Titan's history at the locations now covered with 5-μm-bright material (with the caveat that more of this material may be present but buried under a thick enough layer to mask its spectral signature.) In this section, we begin with a discussion of explicitly evaporation-formed deposits, as the geomorphological evidence for 5-μm-bright material on the shores of lakes in the north pole strongly suggests such a process has taken place on the surface (regardless of whether all our 5-μm-bright deposits are formed in this exact manner or not). We then discuss the different scenarios implied by the absence of evaporite deposits in the south pole and the presence of such material in the equatorial basins Tui and Hotei. We conclude with a comment on the seasonality of these processes.

2.5.1 Evaporite Formation

The drying-up of a liquid body does not always involve the creation of evaporite: evaporite only forms when a solution becomes saturated and the dominant mechanism for liquid removal is evaporation. This is more likely to happen in closed systems where solute can't be washed downstream or the solution can't percolate through a porous regolith. In our discussion we describe such systems as long-lived, i.e. having been closed systems of surface liquid long enough to enable saturation of the solution. Short-lived surface liquids, such as those left after a rainfall, may come into contact with a large amount of dissolvable material as they flow across the surface. However, maintaining saturation and evaporation-dominant removal is probably more difficult, especially if the flow is fairly fast or in contact with other streams of liquid. We note that "short-lived" is an ambiguous term, referring to an amount of time that is simply less than that required for saturation to take place– the latter is a function of the chemical nature of both solute and solvent, as well as the terrain over which these surface processes are happening. For example, Malaska and Hodyss (2014) suggest that an ethane-rich Ontario Lacus should have reached saturation with benzene falling from the atmosphere within 3-20 million years.

Due to the yet-unknown exact chemical composition of Titan's evaporites, we cannot definitively exclude the possibility that the deposits are themselves volatile. As *Cassini* has yet to capture even one full Titan year and data for particular regions are not continuous, it is difficult to observationally determine the rates of such processes. We expect, however, that they would have to operate on geological timescales based on the relative stability observed of the evaporite candidates: the shoreline deposits around Ontario Lacus are seen in T38 and T51 (a little over one terrestrial year); Kraken Mare's shoreline deposits are observable from T61-T82 (two years); and Tui Regio is 5-μm-bright from Ta-T51 (four and a half years). The evaporite deposit at the north end of Yalaing Terra did disappear for some time following a rain induced surface wetting event, but then returned to its original, 5-μm-bright spectral signature. This would seem to imply that if the 5-μm-bright material is volatile, it either recondenses onto

the surface in the exact same location (within 3-11 months after the first observation of the evaporite's disappearance) or is only volatile on longer time scales. There is no evidence from the *Cassini* data that the 5-μm-bright material is volatile on a less than seasonal time scale, though we cannot rule out longer time scales without a better definition of the material's chemical makeup.

2.5.2 South Polar Basins

Aharonson et al. (2009a) argue that the periodicity of which pole receives the greater summer insolation (according to the behavior of Saturn's orbit) is responsible for the migration of liquid between the north and south poles (a Milankovitch cycle). Thus orbital influence driving the evaporation-to-precipitation ratio assumes that the south will at some time look like the north does today: the region where the majority of the surface liquid is concentrated. Why then, if the south at one time housed enough liquid to make seas from the dry basins observed today (Wood et al., 2013; Lorenz et al., 2013) are there no evaporite deposits similar in extent to the north pole? We offer two categories of answers to this question: either (1) evaporite formed but is no longer visible or (2) conditions were never suitable for evaporite formation.

The southern basins could be closed systems; they are probably the lowest points (Lorenz et al., 2013) in the region, so liquid would tend to pool there. Thus, evaporite formed at the south pole would have either been covered up since the liquid moved north or was itself volatile. If the evaporite is simply covered by settling atmospheric aerosols, a 0.15 -1.5 mm thick layer could build up over the 45 kyr period predicted for a Milankovitch cycle. This is an upper limit– the time required to completely empty the southern seas is not taken into account. As VIMS only probes a few microns into the surface, this could be enough to mask an evaporite layer. It could also be that the 5-μm-bright material is ephemeral: eroded away by weather, volatile enough to sublimate, or chemically altered while exposed on the surface. All of these processes could occur on Milankovitch cycle timescales to remove 5-μm-bright material.

And yet, another explanation for the lack of evaporites is that they never formed. Perhaps the basins were not filled long enough for the liquid to reach saturation. Or, some other mechanism may have been more dominant in removing liquid from the system– a porous regolith or connection to a subsurface reservoir could empty the basins without any evaporite deposition. These scenarios are inconsistent with Milankovitch cycles, as there is no evidence of a subsurface connection to allow the liquid to get back to the north pole (Sotin et al., 2014).

Evaporite also wouldn't form if the basins have never been filled (clearly not in agreement with a Milankovitch cycle as described above). For example, if the total methane volume in Titan's atmosphere and surface is not constant, then there might not have been enough methane available to fill the south seas at the periods of greatest solar insolation (i.e. heaviest rainfall). In one of the possible cases for Titan's methane abundance modeled by Nixon et al. (2012), the supply increases over time, a process that is probably driven by the brightening of the Sun over time (Ribas et al., 2005) warming Titan's crust (Nixon et al., 2012). In such a scenario, there may not have been enough liquid to fill the north pole lakes and seas, the equatorial basins, and the south polar basins.

2.5.3 Equatorial Basins

In light of the discussion above, what does the presence of 5-μm-bright material imply for the histories of Tui and Hotei? Based on Earth analogs, we assume that such a large areal extent of evaporite lying at the bottom of a basin is more consistent with a long-lived body of liquid, where a saturated solution has been in a closed system long enough to undergo a few cycles of evaporite formation to deposit the material we observe today. While Xanadu is a neighboring, low-lying region, its paucity of 5-μm-bright material is consistent with the requirement that liquid systems be sufficiently closed to form evaporite (at least on the order of the large scale deposits observable by VIMS): Xanadu is riddled with channels (Burr et al., 2009) that (probably) drain liquid into Tui and Hotei. Burr et al. (2013) and Burr et al. (2013) discuss a variety of possible flow mechanisms that may be happening in Xanadu based on the observed fluvial features.

Assuming evaporite did form at the south pole and has subsequently been buried, why haven't the deposits covering Tui and Hotei suffered the same fate? As noted by Sotin et al. (2012), the haze production rates of Rannou et al. (2003),Rannou et al. (2004); Rannou et al. (2006), and Wahlund et al. (2009) span a range of values as do possible particle densities. If we use the lower estimate of the deposition rate of atmospheric particles to be about 0.1 μm per Titan year, it would take a few thousand Earth years to build up a layer of atmospheric particles on the surface of Tui and Hotei thick enough to mask the signal from any 5-μm-bright material. However, with higher estimates of haze production, on the order of 1 μm per Titan year, deposition would sufficiently build up after only a few hundred Earth years. Either Tui and Hotei were filled more recently than this (and thus also more recently than the proposed south polar seas) or the basins experience enough rainfall to dissolve and reprecipitate the evaporite deposits on timescales comparable to those predicted for equatorial storms. However, there is as yet no observational evidence for rainfall reaching Tui and Hotei.

It is also unlikely that a single storm of the present climate could have created the amount of liquid necessary to create Tui and Hotei's evaporites. The evaporites extend to the RADAR-identified boundaries of Tui and Hotei, thus the basins would have had to be completely filled to deposit evaporite at those farthest edges. According to the calculations of Section 2.4.3, we show that this is a sizable volume of liquid. Comparisons between possible flooding mechanisms on Earth, Mars, and Titan led Burr (2010) to conclude that monsoonal flooding of the equatorial region (and thus the resulting carving of fluvial features) could be linked to a methane cycle. Periods of heavy rainfall would deplete the atmosphere, creating a more arid climate that would slowly be replenished until saturation in the atmosphere triggered another monsoon event. Pluvial events like these are responsible for some of the largest salt pans on Earth: Devil's Golf Course (Arizona, USA), Bonneville Salt Flats (Utah, USA), and the Lake Eyre (South Australia, Australia).

2.5.4 Seasonality

The most likely candidates for evaporitic compounds on Titan are the hydrocarbons that originate in the atmosphere that have been dissolved in the surface liquid. Titan's surface liquid is probably a complex mixture of methane, ethane, nitrogen, and small amounts of alkanes (e.g. propane) (Cordier et al., 2013;

Glein and Shock, 2013) (but see Mastrogiuseppe et al. (2014)). Experimental studies (Luspay-Kuti et al., 2012) and thermodynamic models (Glein and Shock, 2013) indicate that organic molecules have a higher solubility with liquid ethane than methane. While this affects the composition of the solution itself, it has less influence on the actual formation of evaporite. Evaporite can only form if the solution is saturated. Thus, regardless of the solubilities of the individual constituent solvents, solute will deposit when one evaporates.

The composition of the solution filling the lakes does raise questions concerning the seasonality of evaporation and evaporite formation. Methane is thought to be the only compound volatile enough to undergo evaporation over reasonable timescales; ethane has been proposed to be volatile on larger-than-seasonal timescales. Hence, if evaporation were the sole mechanism for evacuating both methane and ethane (as we expect for evaporite-bottomed lakes), the lake desiccation processes would take longer than methane evaporation alone. Alternatively, if an over-saturated, ethane-dominated lake were emptied of liquid via a regolith porous enough for the solution but not the undissolved solute to percolate through, then evaporite formed when the methane evaporated could be left behind. It is also possible to envision scenarios where different liquid-removing mechanisms have been dominant at different times. Infiltration could drain out some of the liquid and evaporation became the dominant mechanism after the subsurface liquid reaches the water-table, for example.

Thus, the evaporite formation timescale could be complex: formation associated with the evaporation of methane occurring seasonally and evaporation of the entire liquid body's contents occurring over large enough timescales for ethane to evaporate, with allowances for rain influx. Presumably, such mechanisms would work faster with shallower bodies of liquid, such as those identified by Barnes et al. (2011), where the local timescales of evaporation would contribute to the observed dichotomy in surface liquid distribution on Titan. In the case that evaporation is the only liquid removal process in the lifetime of the lake, seasonal exchange of methane alone, as discussed above, is *not* enough to explain the observation of dry lakebeds with 5-μm-bright bottoms.

2.6 Conclusion

Operating under the hypothesis put forth by Barnes et al. (2011) that coherent, 5-μm-bright signatures on Titan's surface are evaporitic in origin, we map the global distribution of 5-μm-bright material and thus present newly-identified evaporite candidates. These evaporite candidates cover a little over 1% of Titan's surface area and are mostly concentrated in Tui and Hotei Regiones (proposed fossil seas of the equatorial region) and at the north pole (around the giant seas and dry, filled, or wetted lakebeds). Unlike those at their northern counterparts, the south polar basins are noticeably void of 5-μm-bright material, prompting the following possible explanations: evaporite deposits at the south pole have been subsequently covered or removed, or conditions were never suitable for evaporite formation. In these two scenarios, Tui and Hotei were then either filled more recently than the south polar basins or the processes responsible for making evaporite in the north pole also took place at the equatorial basins (but not at the south). As climate models seek to address the currently observed asymmetry in surface liquid distribution between the north and south polar regions, we encourage the consideration of each of these

scenarios and their implications, including the more active role of the equatorial region implied by the evaporitic evidence for Tui and Hotei having once been filled seas.

Without the benefit of a lander, Titan's surface composition must be constrained through other, less direct means. We present this distribution of evaporite candidates as the first in a series of works investigating the 5-μm-bright spectral unit. Having now cataloged the total and best occurrences of each isolated deposit, we will next be able to construct spectra of high enough signal-to-noise to facilitate inter-flyby comparison. In particular, we will look for the absorption feature at 4.92 μm exhibited by Tui and Hotei in the spectra of other evaporite candidates (McCord et al., 2008). Especially in comparison to the spectra of 5-μm-bright deposits observed on the shores of filled lakes or dried lake beds, a sharing of this absorption feature would strengthen the case of the 5-μm-bright unit as diagnostic of material of evaporitic-origin.

2.7 Acknowledgments

The authors would like to thank an anonymous reviewer for constructive suggestions to the manuscript. This work was supported by NASA *Cassini* Data Analysts and Participating Scientists (CDAPS) grant #NNX12AC28G to JWB. CS acknowledges support from the NASA Astrobiology Institute. Part of this work was conducted at JPL/Caltech under contract with NASA.

Chapter 3: Compositional Similarities and Distinctions between Titan's Evaporitic Terrains

"Compositional Similarities and Distinctions between Titan's Evaporitic Terrains" *The Astrophysical Journal* 821.1 (2016): 17.

In the previous chapter, I mapped out evaporite deposits without identifying their composition beyond the general statement that they are hydrocarbons. I sought to establish in this work what the evaporites are made of. Unfortunately, Titan surface spectroscopy is complicated by the atmosphere. Even within the infrared "windows" where gas absorption is weakest, surface spectra are not immune to the effects of the atmosphere. Titan's haze particles are highly scattering at the shorter wavelengths: only 17% of the photons that make it the surface at 1.3 μm make it back out of the atmosphere to Cassini *unscattered. At 2 μm, 40% of the photons are unscattered. The 5 μm window has the least scattering (75% photons unscattered) and a plethora of potential organic absorption features to identify (Clark et al., 2010).*

Following the discovery of McCord et al. (2008) of an absorption feature in Tui Regio at 4.92 μm in the earliest Cassini *data, I used Principal Component Analysis to determine whether the absorption feature is present (1) in every observation of Tui Regio; (2) in observations of the other equatorial paleobasin, Hotei Regio; and (3) in other evaporite deposits. Unfortunately, the results were somewhat ambiguous. The presence of the absorption feature was not correlated with time, viewing geometry, or deposit morphology.*

However, the differences in reflectance between the deposits can be interpreted as heterogeneity between evaporite deposit composition and/or grain size (the properties that control reflectance). This makes sense in comparison to Earth. Even with only one solvent at work, Earth's evaporites exhibit a variety of compositions and morphologies (Figure 3.1). There are two solvents on Titan (methane and ethane) and a plethora of organic species thought to rain out from the atmosphere with various degrees of solubility within each liquid (e.g. Cordier et al., 2016).

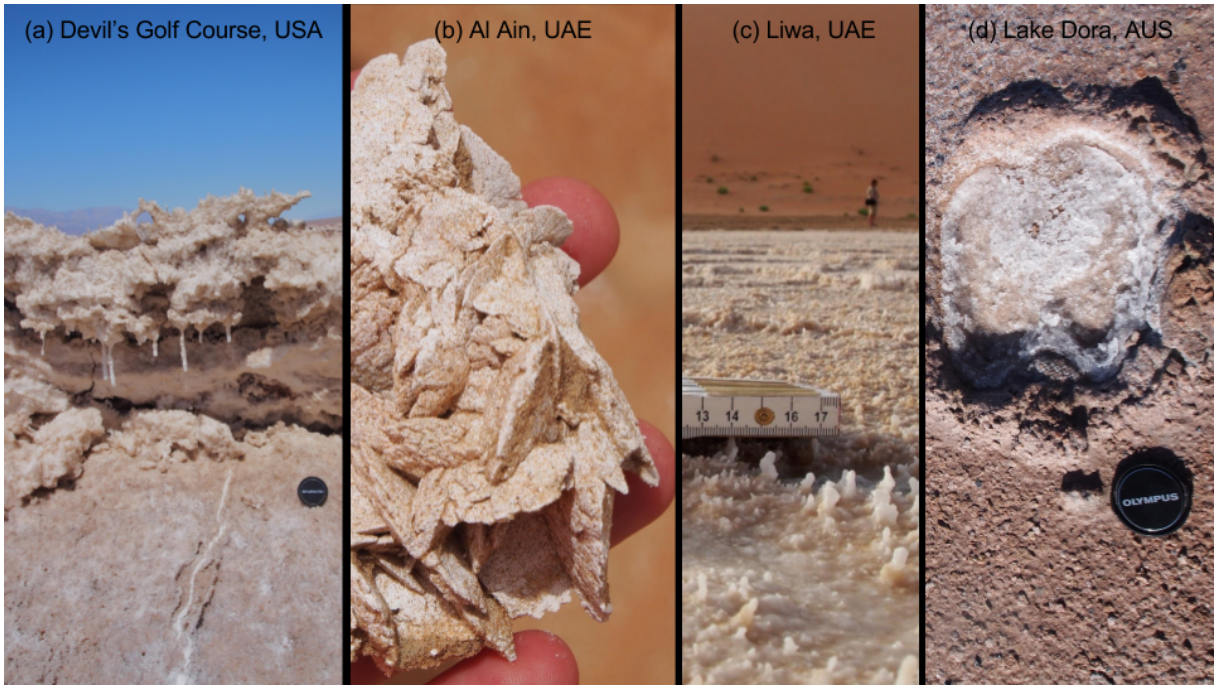

Figure 3.1: (a) Structures at Devil's Golf Course are tall and bladed thanks to erosive winds. (b) Rose gypsum has a unique plated structure. (c) Interdune evaporites in Liwa show both smooth and small columns growing a few mm high. (d) A sheet of thin, plated evaporites formed in this camel hoof print on the shores of Lake Dora, Western Australia.

3.1 ABSTRACT

We document the similarities in composition between the equatorial basins Tui Regio, Hotei Regio, and other 5-μm-bright materials, notably the north polar evaporites, by investigating the presence and extent of an absorption feature at 4.92 μm. In most observations, Woytchugga Lacuna, Ontario Lacus, MacKay Lacus, deposits near Fensal, some of the lakes and dry lake beds south of Ligeia, and the southern shores of Kraken Mare share the absorption feature at 4.92 μm observed in the spectra of Tui and Hotei. Besides Woytchugga and at Fensal, these 5-μm-bright deposits are geomorphologically-substantiated evaporites. Thus, the similarity in composition strengthens the hypothesis that Tui and Hotei once contained liquid. Other evaporite deposits, however, do not show the 4.92 μm absorption, notably Muggel Lacus and the shores of Ligeia Mare at the north pole. This difference in composition suggests that there are more than one kind of soluble material in Titan's lakes that can create evaporite and/or that the surface properties at the VIMS wavelength scale are not uniform between the different deposits (crystal size, abundance, etc). Our results indicate that the surface structure, composition, and formation history of Titan's evaporites may be at least as dynamic and complex as their Earth counterparts.

3.2 Introduction

Titan, Saturn's largest moon, is swathed in a thick atmosphere with haze that is highly scattering and gas that absorbs at visible wavelengths. Several wavelengths of light in the near infrared penetrate the atmosphere to reach the surface, however, with varying degrees of interference from the atmosphere (e.g. Griffith et al., 1991; Lellouch et al., 2003; Gibbard et al., 2004). Since *Cassini*'s arrival at the Saturnian system in 2004, the Visual and Infrared Mapping Spectrometer (VIMS) has been observing Titan's surface at these seven spectral windows where methane gas absorption is weakest in the IR (Brown et al., 2004; Baines et al., 2005; Sotin et al., 2005). The visible channels can be also be used to look at the surface, but to a more limited extent (Vixie et al., 2012).

Even through these windows, however, observing the surface is complicated by the properties of Titan's atmosphere. The haze particles of are highly forward scattering (e.g. Porco et al., 2004; Tomasko et al., 2008c). This effect is seen across the IR-spectrum, increasing the reflectance of both windows and methane-saturated bands, and is stronger at the shorter wavelengths than at longer ones. Analyses of solar occultations (Hayne et al., 2014) and specular reflections (Barnes et al., 2013b) have measured the decreasing total optical depth (both haze and gas opacities) as a function of increasing wavelength. The haze distribution changes with latitude (e.g. Flasar et al., 2005; Rannou et al., 2010), altitude (e.g. Young et al., 2002), and season (e.g. Lebonnois et al., 2001; Vinatier et al., 2015). Scattering properties of the haze particles change with altitude and wavelength (Tomasko et al., 2005, 2008c). Despite this wealth of new insight into Titan's atmosphere in the *Cassini* era, the details of the atmosphere's effects on emergent spectra are still far from understood.

Thus, as VIMS IR data only sample seven parts of Titan's surface spectrum, it is difficult to identify which specific chemical species are present to create the observed signal. And yet, there are three cases where this has been done. Clark et al. (2010) identified a feature in Titan's global spectrum at 5.05 μm,

which the authors suggest is indicative of benzene. Brown et al. (2008) identified ethane in the VIMS data from Ontario Lacus.

McCord et al. (2008) identified an absorption feature in the spectrum of Tui Regio at 4.92 μm using some of the earliest VIMS data. Their method used deviance from the scene average as the criteria for absorption. CO_2 ice was originally proposed as a candidate material, as it demonstrates an absorption feature near 4.92 μm. Clark et al. (2010), however, point out that the wavelength shift necessary to match CO_2 ice to the 4.92 μm feature is unphysical and the expected CO_2 feature in the 2.7 μm region is not observed. Clark et al. (2010) also list several species from their laboratory survey with spectral features near 4.92, including a predominately potassium ferricyanide mixture, acrylonitrile, and cyanonaphthalene. However, as we cannot yet even specify exactly *where* this 4.92 μm absorption occurs, let alone consider other coincident spectral features, the specific attribution of a chemical species to the 4.92 μm absorption has not yet been made.

Generally, however, VIMS data are used to classify surface material into spectral units, groups of material that share overall spectral characteristics. Spectral units define the unique characteristics of the "dark brown" dunes (Barnes et al., 2007b; Soderblom et al., 2007; Rodriguez et al., 2014), "dark blue" terrains including mountains (Rodriguez et al., 2006; Barnes et al., 2007b,c; Le Mouélic et al., 2008; Rodriguez et al., 2014), and the mountainous, channel-ridden Xanadu region (Barnes et al., 2007b).

Titan's lakes and seas are also spectrally distinct: in the near infrared, they are darker than their surroundings at all wavelengths (Brown et al., 2008; Sotin et al., 2012). These liquid bodies seem to be restricted to the polar regions, though see Griffith et al. (2012) and Vixie et al. (2015). At the north pole, the lakes and seas are of a variety of shapes and sizes: from Kraken Mare, the largest sea covering 400,000 km^2 (Turtle et al., 2009), to the Lake District, a region of "cookie-cutter lakes"(Hayes et al., 2008) which are just resolvable in VIMS data. The south pole, however, looks quite different. The south has just one substantial body of liquid, Ontario Lacus, which is about 15,000 km^2 in size (Hayes et al., 2008).

Thermodynamic models (e.g. Cordier et al., 2009; Cordier et al., 2012; Glein and Shock, 2013) and laboratory experiments (e.g. Diez-y Riega et al., 2014; Mitchell et al., 2015; He and Smith, 2015; Luspay-Kuti et al., 2015) explore and observations with the RADAR instrument constrain some of the liquid's composition and properties (e.g. Hayes et al., 2010; Ventura et al., 2012; Hofgartner et al., 2014). Besides the ethane detection of Brown et al. (2008), VIMS data is difficult to use to confirm the bulk composition of the liquid as the methane in the atmosphere obfuscates detection of liquid methane on the surface and VIMS can only sample a depth of a few microns. The ethane absorption in Ontario Lacus's spectrum is not sensitive to abundance. No other absorption features have been observed in VIMS lake spectra.

Some of the lakes and seas on Titan have evaporite along their shorelines, as do some dry lakebeds (Barnes et al., 2011; MacKenzie et al., 2014). Evaporite is solid material redeposited on the surface after the liquid in which it was dissolved evaporates. On Titan, these deposits demonstrate a unique spectral behavior such that they are referred to as the 5-μm-bright spectral unit–so named because it is significantly brighter than any other surface units in the eponymous window. At 2.8 μm, this material is relatively brighter than other surface units, but at shorter wavelengths, 5-μm-bright material is similar in reflectivity to other bright units like Xanadu or the equatorial bright unit (Barnes et al., 2005).

The first evaporitic deposits were identified just south of Ligeia Mare where RADAR identified small (10-200 km in diameter) lakes (Barnes et al., 2011) and dry lake beds (Hayes et al., 2008). The same region also has lakes and dry lake beds without the 5-μm-bright signature: evidence that the bright deposits are evaporite, the material left over when liquid (presumably methane or ethane) evaporates. Evaporite only forms once the liquid is saturated with solute (on Titan, probably some kind of hydrocarbon) and if evaporation is the dominant mechanism for removing the liquid. An evaporitic deposit therefore indicates a location where liquid has ponded on the surface at some point in the past.

MacKenzie et al. (2014) conducted a survey of then-available VIMS data to locate all deposits of this 5-μm-bright material on Titan's surface. The authors found that while more separate instances of evaporite deposits appear at the north pole, where the majority of Titan's surface liquid is now located, the largest single deposits by surface area are located in Titan's presently desert equatorial region at Tui and Hotei Regio. Moore and Howard (2010) interpreted lacustrine and fluvially carved features in the RADAR coverage of these two basins as indicative of Tui and Hotei being paleo seas. Observing the 4.92 μm absorption feature in the spectra of the north polar evaporites would be further evidence for this hypothesis as it would compositionally link the basins Tui and Hotei with the clearly lacustrine-associated deposits south of Ligeia.

In this work, we determine the degree of similarity between the compositions of the 5-μm-bright material at different latitudes by documenting all observations of the 4.92 μm absorption in spectra of Tui Regio, Hotei Regio, and the evaporite candidates of MacKenzie et al. (2014). We compare the relative depths of the absorption feature with time and flyby geometries in an effort to distinguish what controls the absorption depth. In Section 3.3, we describe the VIMS data and in Section 3.4 we describe the principal component analysis (PCA) technique that we use to analyze them. Section 3.5 presents our results for each 5-μm-bright deposit. We discuss our findings in Section 3.6 and conclude with a summary of our work and its implications.

3.3 Observations

We use data from the Visual Infrared and Mapping Spectrometer on-board *Cassini* from 2004-2014. These were processed with the VIMS pipeline described in Barnes et al. (2007b) which converts the raw data into I/F, the observed reflectance divided by the incident solar flux. All geometric projections are done with software developed for Barnes et al. (2008b). In Table 3.1 we summarize the geometries and average resolutions of the data from each flyby. Tui and Hotei Regiones were imaged during 2004-2009 (Barnes et al., 2009c), but the north pole evaporites were not fully visible until 2013-2015. The viewing geometries between equatorial and polar deposits are therefore unavoidably different. In fact, the spread of viewing geometries over just the Tui and Hotei observations differ enough as to make comparison of uncorrected I/F between flybys difficult. We describe how we address this problem in Section 3.4.

We investigate a select subset of the deposits identified by MacKenzie et al. (2014), including evaporites found along the shores of the seas and lakes of the north pole as well as some evaporite candidates from the equatorial regions. Figure 3.2 shows the relative locations of Tui Regio, Hotei Regio, Xanadu, and the evaporites studied here (white arrows) on a cylindrically projected VIMS map. For the coordinates

Table 3.1: Summary of characteristics for flybys used in this work. The incidence and emission angle ranges listed span those of the images used for the features listed. Note that shoreline evaporite deposits are listed by the name of the lake or sea they border.

Flyby	Date	Features Covered	Phase (°)	Inc (°)	Emis (°)	Best Resolution (km/pixel)
Ta	24-Oct-04	Hotei, Tui, Xanadu	10	10-70	20-80	43
Tb	13-Dec-04	Tui, Xanadu	10	10-40	20-40	8
T3	15-Feb-05	Hotei, Tui, Xanadu	30	0-70	20-80	94
T4	31-Mar-05	Hotei, Xanadu	50	0-20	60	74
T5	16-Apr-05	Fensal, Hotei, Xanadu	50-60	0-40	20-70	9
T6	22-Aug-05	Fensal	50	40	20	40
T7	7-Sept-05	Fensal	50	30	30	56
T8	28-Oct-05	Hotei, Tui, Xanadu	20	0-50	20-70	43
T9	26-Dec-05	Fensal, Hotei, Xanadu	20	20-40	30-60	50
T10	15-Jan-06	Hotei, Tui, Xanadu	35	0-40	20-70	17
T12	18-Mar-06	Hotei, Tui, Xanadu	65	0-40	20-80	17
T14	20-May-06	Hotei, Tui, Xanadu	90	10-70	20-80	66
T38	5-Dec-07	Ontario	40	60	60	0.6
T44	28-May-08	Hotei, Tui, Xanadu	90	10-70	10-70	100
T46	3-Nov-08	Hotei, Tui, Xanadu	80	10-70	0-60	36
T47	19-Nov-08	Hotei, Tui, Xanadu	80	10-80	0-70	83
T48	5-Dec-08	Hotei, Tui, Xanadu	70	10-60	10-60	64
T49	21-Dec-08	Hotei, Tui, Xanadu	70	10-70	10-40	95
T50	7-Feb-09	Hotei, Tui, Xanadu	70	10-70	20-60	65
T51	27-Mar-09	Hotei, Ontario, Tui, Xanadu	70	10-70	20-60	39
T61	25-Aug-09	Kumbaru, Walvis, Yalaing	10	10-50	10-70	20
T67	5-Apr-10	Kumbaru, Walvis, Yalaing	10	20-50	10-60	30
T69	5-Jun-10	Atacama, Atitlan, Djerid, Ligeia, Uvs, Vanern	30	60-70	50-60	10
T76	8-May-11	South of Kraken, Walvis, Kumbaru, Yalaing	40	30-50	20-60	19
T82	19-Feb-12	South of Kraken, Walvis, Kumbaru, Yalaing	60	40-50	20-60	24
T90	5-Apr-13	Muggel, Woytchugga	110	60-70	40-50	35
T93	26-July-13	Muggel, Vanern,Woytchugga	80-90	50-70	20-50	7
T94	12-Aug-13	Ligeia, MacKay, Muggel	70	60-70	0-20	4
T96	1-Dec-13	Ligeia, MacKay, Muggel, Woytchugga	60	60	0-30	6
T97	1-Jan-14	Ligeia, Muggel, Woytchugga	50	60	0-20	13
T98	2-Feb-14	MacKay, Muggel, Woytchugga	50	60	0-20	74
T100	7-Apr-14	Ligeia, Muggel, Vanern, Woytchugga	30	50-60	20-40	19
T103	20-Jul-14	Kumbaru, South of Kraken, Walvis	100	40-70	40-50	95
T104	21-Aug-14	Flensborg, Gabes, Kumbaru,	100	40-70	20-60	29
T104	21-Aug-14	South of Kraken, Walvis, Woytchugga	100	40-70	20-60	29

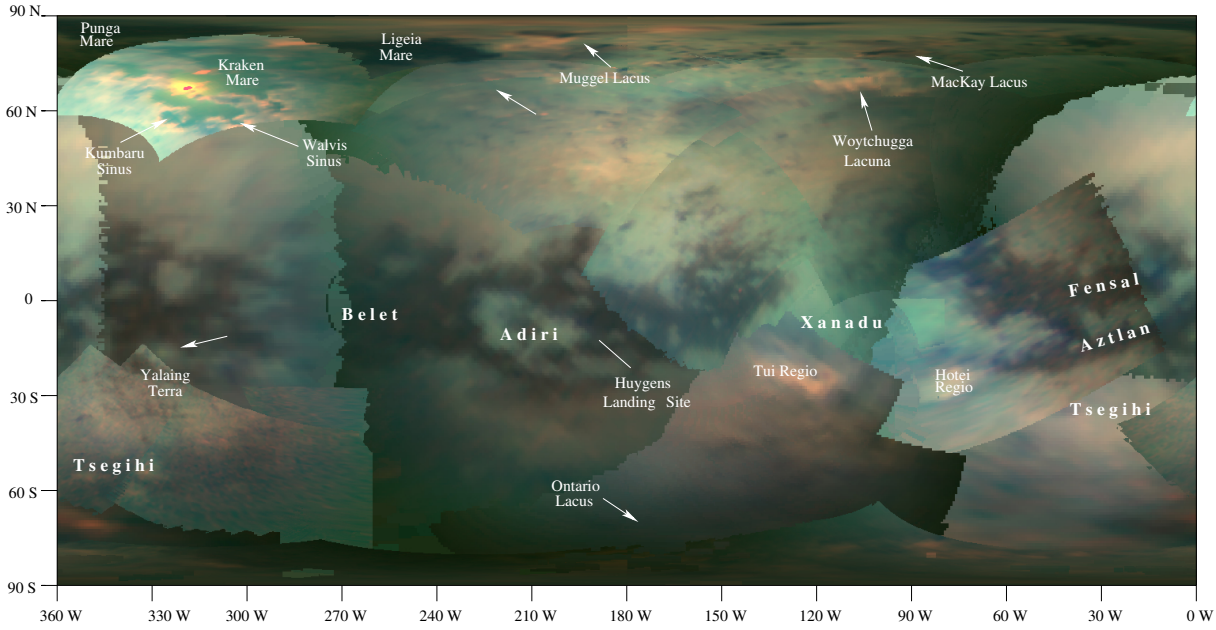

Figure 3.2: Cylindrically projected VIMS map of Titan's surface with R = 5 μm, G = 2 μm, and B = 1.3 μm. White arrows point to the areas studied in this paper (though see Figure 3.12 for a better projection for the north polar deposits). Tui and Hotei Regiones are the largest 5-μm-bright deposits on Titan's surface and are easy to see at the global scale; some of the smaller evaporites are harder to distinguish in this global view.

and best VIMS observations of each deposit, we refer the reader to Table 1 of MacKenzie et al. (2014).

3.4 Methods

The 4.92 μm absorption feature shows a very shallow depth ($\sim$ 2% difference in I/F from the scene average in Figure 27a of McCord et al. (2008)) and thus is challenging to distinguish in raw VIMS data. Although the Sun is darker at 5 μm than at shorter wavelengths, Titan's haze scatters less at this wavelength than at the shorter windows (Rodriguez et al., 2006). Thus, a higher percentage of those incident photons make it to the VIMS detector unimpeded. This means that the problem in detecting the 4.92 μm absorption lies not in correcting for atmospheric interference but in building up enough signal relative to the inherent noise (dark, read, and shot). We tried several approaches to identify the 4.92 μm absorption. In the end, the most effective method was to subtract the albedo component of the spectrum and then coadd all corrected pixels from an individual flyby that cover a certain surface feature.

3.4.1 Principal Component Analysis

The albedo subtraction approach that we use involves principal component analysis (PCA). In PCA, an initial spectrum $\vec{v}$, an n-dimensional vector where each entry corresponds to a VIMS wavelength channel, gets reprojected into a new space spanned by a new set of n orthogonal and linearly independent basis vectors, $\vec{b_n}$. The new basis vectors $\vec{b_n}$ are effectively individual spectra that represent combinations

of the original channels that tend to vary in concert. The strategic purpose behind this reprojection is to simplify what can be a large n-dimensional spectrum into component spectra that better represent the inherent variability across a dataset.

PCA has a long history of use in planetary science. On the Moon, for example, PCA has been used to determine relative composition (e.g. Johnson et al., 1985; Pieters et al., 2002) and to create compositional maps of similar spectral units (e.g. Bellucci et al., 1998; Chevrel et al., 1999). Similarly, different spectral units and compositions have been identified on Mars using PCA (e.g Noe Dobrea et al., 2006; Dobrea et al., 2008; Gasnault et al., 2010; Farrand et al., 2013). In the outer solar system, PCA has been used to help increase the signal-to-noise ratio in Galileo data for Ganymede (Stephan et al., 2008) and VIMS data for Titan (Le Mouélic et al., 2012a). Recently, PCA has been used with VIMS data for Titan by Solomonidou et al. (2014) to infer the spectral surface diversity of features in Titan's equatorial region.

A drawback of PCA approaches is that given the abstract and subjective nature of the results, it can be difficult to ascribe particular meaning to individual components. For instance, when we trained PCA using the full 256-channel VIMS wavelength range (0.89-5.12 μm), the resulting high-power components are non-trivial combinations of surface reflectivity, atmospheric scattering, and solar illumination. Solomonidou et al. (2014) found similar behavior.

Given the concentration on the 4.92 μm feature in this work, we consider only the last 16 VIMS channels (4.84 - 5.12 μm). The total haze optical depth in Titan's atmosphere decreases strongly as a function of wavelength due to the particle size of individual aerosols ($\sim$ 1 μm) (Tomasko et al., 2008c; Doose et al., 2016). Thus the haze influence is minimized in the 5 μm window (Rodriguez et al., 2006; Brown et al., 2008). We find that using only the sixteen 5 μm channels yields more interpretable principal components.

We show spectra of the first five of these components in Figure 3.3. The shape of the first component (red line) generally matches that of the overall 5 μm window as seen in VIMS (see, for example, Barnes et al. (2007b)). Therefore, we interpret the first component to represent the overall surface reflectivity that, in general, varies concurrently with all channels of the 5 μm window. We refer to this as the "albedo" component, and show this component as an image at the center of Figure 3.4. The left hand graph in Figure 3.4 shows a representation of the relative magnitudes ascribed to each principal component. The first component carries over two orders of magnitude more power than subsequent principal components.

In the first component image (Figure 3.4, center), the different spectral units are distinguishable. Their relative brightnesses at different wavelengths—a function of viewing geometry, surface roughness, etc—are the dominant control on the shape of the added pixels' cumulative spectrum. The dunes are dark while Tui, Hotei, and Xanadu are relatively bright.

The second component (green line of Figure 3.3, image shown at right of Figure 3.4) may correspond with instrumental artifacts, particularly given the high signal in the third to last VIMS channel which is known to be unreliable. Individually, however, the second component and higher orders are more inscrutable: we don't know what any of the components beyond the first truly mean. For the purpose of this analysis, interpretation of these higher-order components is in fact irrelevant.

If the first component represents the relative differences in albedo between different spectral units, then the remaining components should collectively be differences from the general albedo. Presumably,

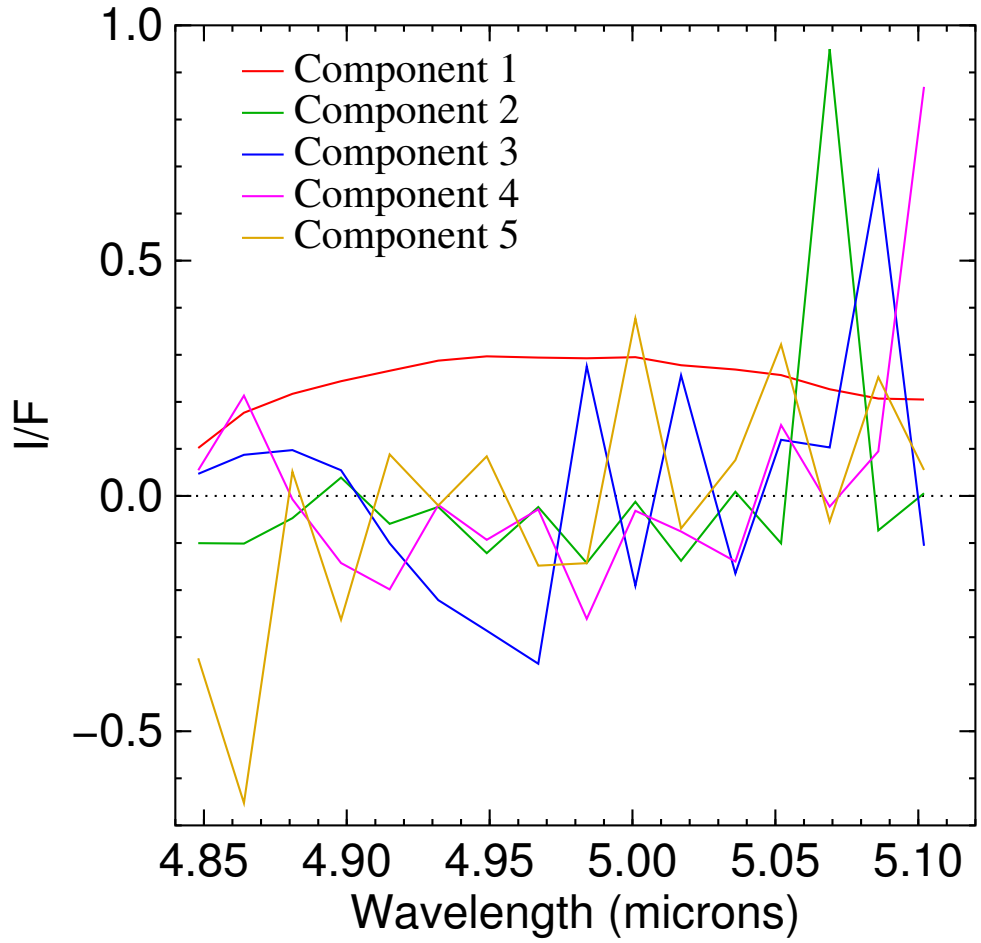

Figure 3.3: Principal components' spectra from a principal components analysis (PCA) trained on a coadded VIMS map from T8. The first component reproduces the overall shape of the 5 μm window and is thus interpreted to represent the "albedo" of the surface. The other components are more difficult to interpret individually, but taken together and reprojected into image space, are better for identifying shallow depth spectral features that are difficult to detect in the original VIMS spectra.

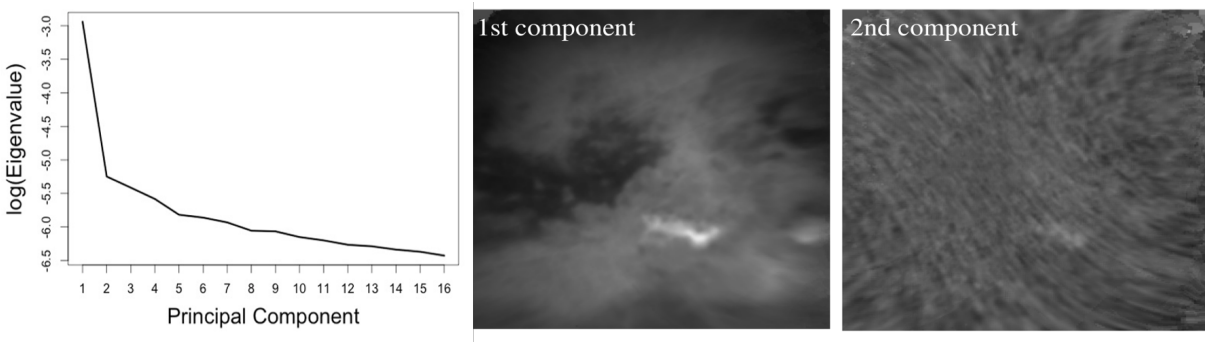

Figure 3.4: Results of the principal component analysis for T8: (left) eigenvalues produced using the eigenvectors from T8; (middle) the first component, which we interpret to be differences in reflectance albedo; and (right) the second component. The eigenvalues describe how much variation from the mean pixel spectrum each component describes: the first component's eigenvalue is two orders of magnitude more than the next component's. Because the 4.92 μm absorption feature is so shallow, it can easily get overwhelmed by changes in the reflectance albedo due to different illumination conditions, making inter-flyby comparison difficult. Thus, to calculate the depth of the 4.92 μm absorption, we zero out off the first component from each pixel's spectrum before coadding the signal.

these differences represent compositional variation. To isolate that compositional signal, we remove the "albedo" component to create what we refer to as "color-only" images.

Functionally, we generate the color-only images by resetting the albedo component (the first principal component) to zero. We then perform an inverse principal components transformation to convert the signal back into wavelength space. In so doing, we revert back to VIMS channels ($\vec{v}$) from the more complex combinations of channels represented by the principal components ($\vec{b_n}$).

So in summary, we use a training dataset to infer a set of principal components. We then transform any given set of VIMS observations (the observation dataset) into the principal component space. To focus on spectral variation, we set the first component, the albedo, to zero, and then transform back into a VIMS spectrum, resulting in a color-only image cube.

To construct the training datasets, we coadd images from a single flyby to create a global mosaic from which we remove the signal of 5-μm-bright material. Removing the surface features of interest ensures that the first component is not controlled by the unique features of the 5-μm-bright unit. We then perform PCA on the mosaic to calculate the eigenvectors (i.e. the principal component spectra shown in Figure 3.3) for a particular flyby; the eigenvalues and two primary components for T8 are shown in Figure 3.4.

The principal components from any one flyby or VIMS cube can then be used to decompose new VIMS cubes in the same principal component space. The choice of eigenvectors affects the resulting spectrum because the eigenvectors necessarily contain some information specific to a flyby (geometry, illumination, etc). We therefore use three sets of eigenvectors for each flyby to obtain the general behavior of the spectra: eigenvectors from regional maps from T8 (because of its good views of Tui known to exhibit absorption feature and decent SNR for Hotei), T49 (best views of Hotei), and the flyby in question (i.e. the observation dataset itself).

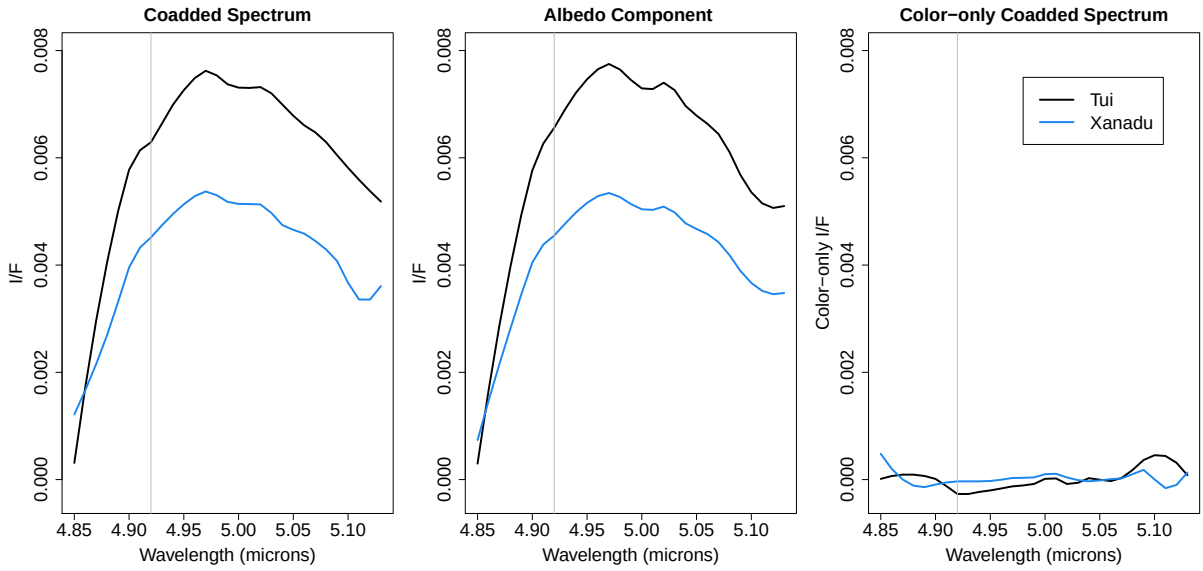

Figure 3.5: Example of subtracting the primary component identified by our principal component analysis from a coadded spectrum to better observe spectral features in the spectra of Tui (black) and Xanadu (blue): (left) raw coadded spectrum from T8, (middle) the albedo component shown in Figure 3.4, and (right) the resulting color-only spectrum. The first component of PCA explains the vast majority of the variance of the spectral data, so when we subtract it from the original spectrum, a fraction of the signal is left. In this color-only spectrum, it is much easier to distinguish differences in the shape of the spectra of Tui and Xanadu.

3.4.2 Processing the color-only data

To obtain the necessary signal-to-noise ratio, we coadd pixels from images within the same flyby, weighting by number of pixels from each image as well as their exposure times, and calculate the standard deviation of the mean of all selected pixels. These pixels come from the color-only images, which is why the corrected I/F values plotted here can be negative–we've subtracted out the common albedo component. Figure 3.5 demonstrates this effect: the first component explains the largest percentage of the observed spectrum, so subtracting it yields an overall smaller signal. Variances from the spectral mean due to absorptions–that is, chemical composition– are, however, easier to distinguish in this color-only space. At the far right of Figure 3.5, the difference in the spectrum of Tui Regio (black) stands out from the relative flatness of Xanadu's (blue) after the albedo subtraction.

An algorithm reads in the color-only image, selects pixels whose center latitude and longitude are within the feature of interest (e.g. Tui, Hotei, Xanadu, etc.), weights the color-only I/F appropriately, and returns the average spectrum for each flyby.

We quantify the depth of an absorption feature using the equivalent width metric, the width of a rectangle whose height is unity and whose area is equal to the area between the continuum and the observed spectrum. For Titan's noisy 5 μm surface spectra, we define the continuum to be a straight line drawn between the two endpoints of the 4.92 μm feature. There are three possible cases for identifying the feature, shown in Figure 3.6: (1) a dip or peak with extrema two VIMS channels wide, (2) a dip

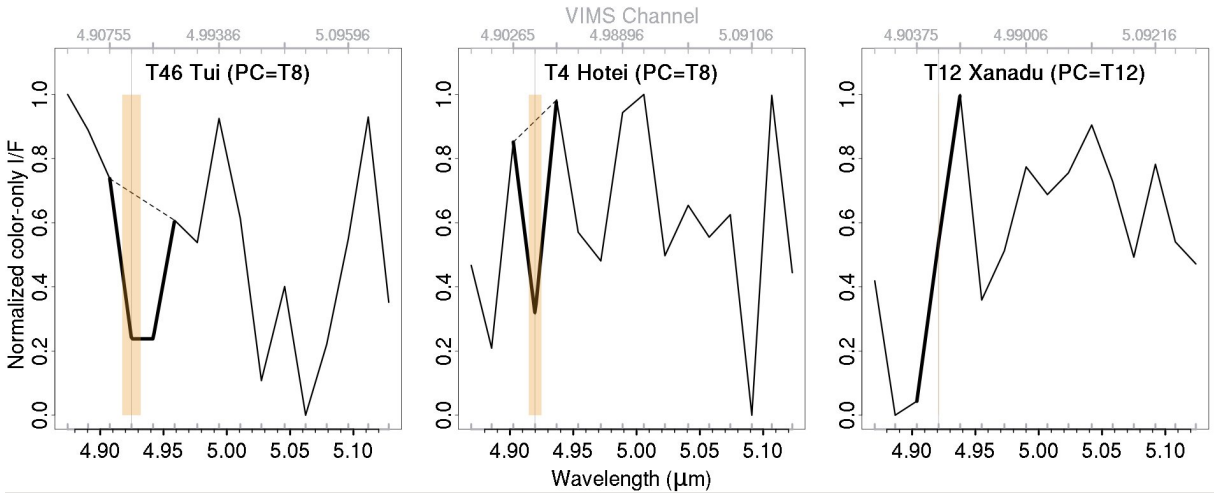

Figure 3.6: Calculating equivalent widths from color-only I/F as a function of wavelength for Tui, Hotei, and Xanadu with data from T12. The thick dashed line represents the continuum estimation while the thick, bolded line represents the analyzed part of the spectrum. These spectra are offset by the value of the spectra at 4.92 μm and normalized to the maximum. The vertical grey line is drawn at the VIMS channel closest to 4.92 μm. The orange box represents the area between the continuum and observed spectra; thus its width is the equivalent width. For Xanadu, which does not have a minimum at or near 4.92 μm, the equivalent width is zero. The right-most panel represents case (1) where the "dip" of the 4.92 μm feature is calculated from four spectral points, the center panel is an example of case (2) where it is calculated from three, and the right-most panel is representative of case (3) where there is no feature at 4.92 μm.

or peak with extrema at one VIMS channel, and (3) no peak or dip. For the first and second cases, we define the feature by either three or four points and the third case by two or three (depending on the center criteria, discussed below). We employ this uniformity to reduce the subjectivity of our analysis.

We do not know the exact center of the absorption feature at 4.92 μm and the wavelengths sampled by the VIMS channels shift long ward as a function of time[1]. We thus calculate the equivalent width twice over the entire dataset: (1) identifying the center of the absorption feature at 4.92 μm and (2) identifying the center at whatever VIMS channel is closest to 4.92 μm. This distinction only significantly affects flybys in our dataset after T14, where the shift in wavelength from the original channel (4.91983 μm) becomes greater than 0.0019 μm ($\sim$ 0.1 spectels). For congruency and ease of comparison between the different flybys, we display the results from method (1) in Figures 3.9-3.11, though the results of the two methods do not differ enough to affect our conclusions.

The criteria for a dip in the spectrum to be an absorption are two-fold. First, the equivalent width must be positive; that is, the observed spectrum values at 4.92 μm must be smaller than those of the continuum spectrum. Second, the equivalent width of Tui or Hotei's spectrum must be larger than that of Xanadu, calculated in the same manner. Xanadu, an equatorial region known for its river networks and mountains, has its own unique spectral unit: bright short of 5 μm with a low 2.7/2.8 ratio (Barnes et al., 2007b). Because it is not expected to exhibit the absorption at 4.92 μm, we use Xanadu's equivalent width as our control. Examples of these calculations from T10 are shown in Figure 3.6. The control region, Xanadu, sometimes has a negative correlation (i.e. a peak at 4.92 μm) or, as shown in Figure 3.6, no feature at 4.92 μm.

3.5 Results

3.5.1 Behavior of the Absorption at Tui and Hotei

In Figure 3.7, we show an example of the color-only 5 μm spectra for Tui Regio using the data from T12. As described in Section 3.4.1, the color-only spectrum is independently calculated with the three different sets of principal components generated from different training sets: from the T12 flyby (solid line), from T8 (dashed), and from T49 (dotted). The absorption at 4.92 μm is present in each spectra, though the equivalent width differs with eigenvector to varying degrees. Plotting raw VIMS spectra from different flybys reveals the same problem: the overall amplitude of the 5 μm window (indeed of all Titan's spectral windows) is a complicated function that relies, in part, on viewing geometry.

To demonstrate the spatial correlation between the 4.92 μm absorption feature and the spectrum of Tui Regio, we independently calculate the equivalent width for each pixel of a map of coadded images from a single flyby (rather than creating a coadded spectrum from all pixels within a region as described in Section 3.4.1). The signal-to-noise ratio is still too low to observe the absorption feature in a single pixel's spectrum, even for pixels from maps created with multiple images from a single flyby. We therefore run this analysis with spectra coadded from multiple flybys. The map shown in Figure 3.8 is the coadded spectra of Ta, Tb, and T8 coverage of Tui Regio and Xanadu. These three flybys have similar viewing

[1]Documentation of this phenomenon can be found at
http://atmos.nmsu.edu/data_and_services/atmospheres_data/Cassini/vims.html

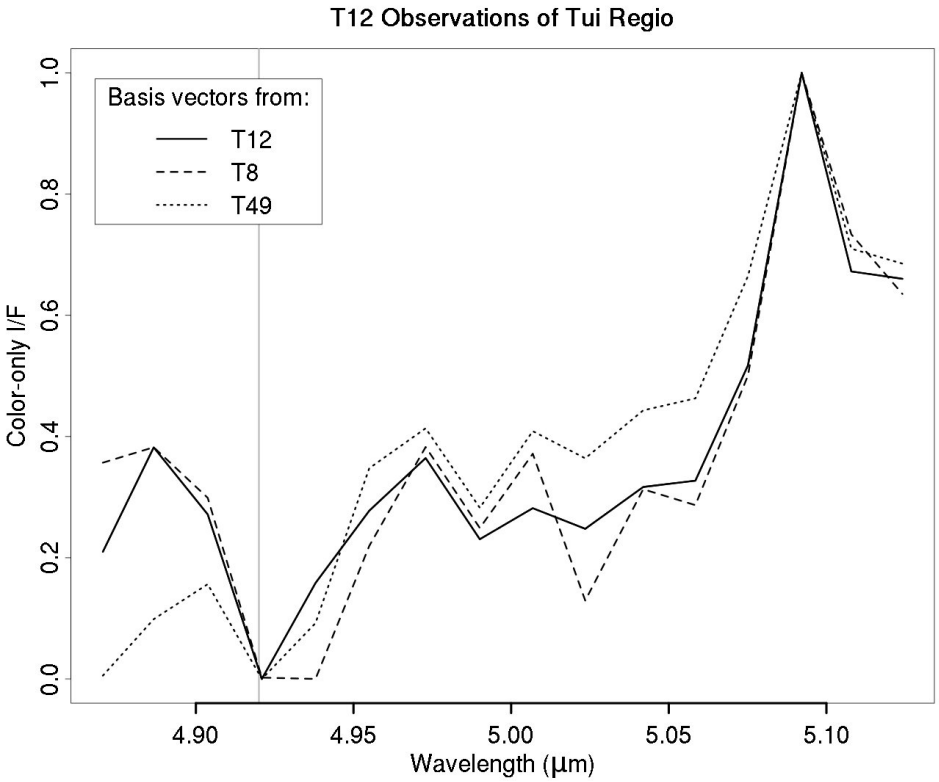

Figure 3.7: VIMS data for Tui Regio from T12 shown as spectra created by adding all pixels that span Tui Regio in the color-only image using principal components from T12 itself (solid), T8 (dashed), and T49 (dotted). The color-only I/F are normalized to the average coadded I/F of Tui Regio. The grey line of the spectra lies at 4.92. The choice of basis vectors affects the depth of the absorption feature as the principal components trained from each flyby are not identical.

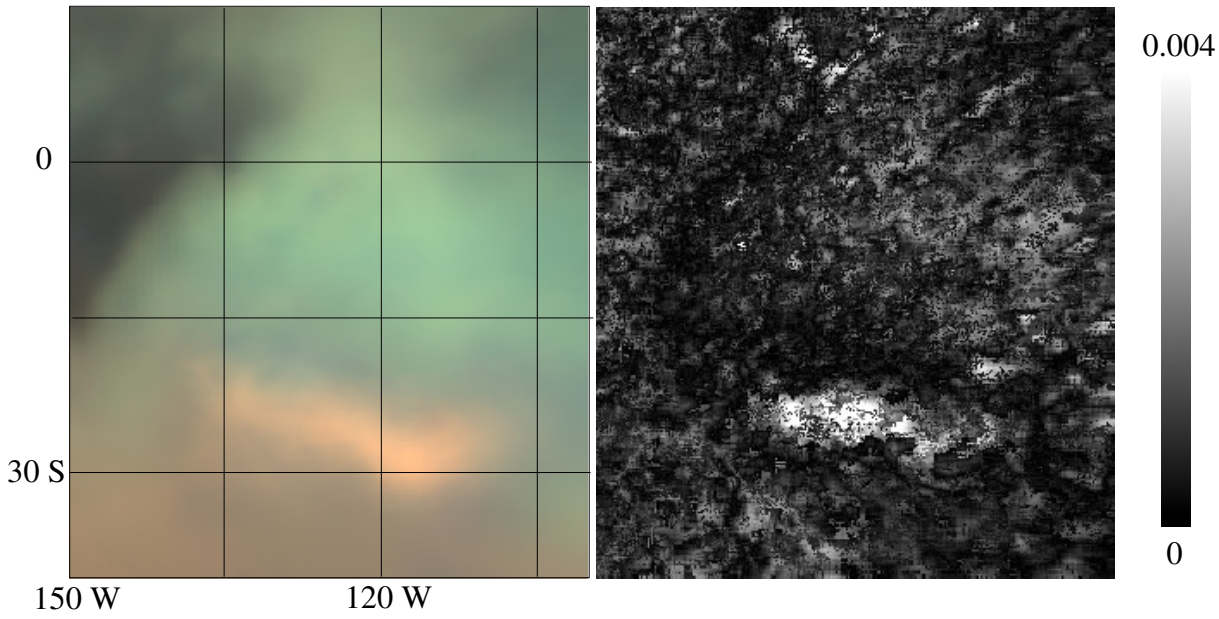

Figure 3.8: Correlation of the spatial extent of Tui Regio and the absorption feature at 4.92 μm. (left) Tui Regio is the bright pink feature in the VIMS data from Ta, Tb, and T8 shown here as a coadded, cylindrically projected map where north is up (R = 5 μm, G = 2 μm , B = 1.3 μm). Xanadu is the green-blue region to the north of Tui. (right) We plot the difference between the equivalent width calculated at 4.92 μm and the average of the equivalent width of any other dips/peaks in the coadded spectrum of each pixel. Larger difference values (whiter color in the plot) indicate the extent to which the equivalent width of an absorption feature is larger than the effective noise level.

geometries and exhibit the 4.92 μm absorption in Tui's spectra.

We include the coadded VIMS cylindrical map at the left of Figure 3.8. The right image plots the difference between the equivalent width calculated at 4.92 μm and the average equivalent width of any other dips or peaks in the pixel's spectrum. The larger the difference (whiter values), the more the 4.92 μm dip is above the pixel's effective noise level, which we estimate as the extent of the second smallest dip or peak of the spectrum. Comparing the two images reveals that the 5-μm-bright spectral unit at Tui and the large regions of 4.92 μm absorption spatially correlate. Xanadu, the blue-green region north of Tui, does not demonstrate the same correlation.

We show the equivalent width of the 4.92 μm feature at Tui, Hotei, and Xanadu as a function of flyby in Figure 3.9 and as a function of phase, incidence, and emission angles in Figure 3.10. The data are colored according to feature (Tui is black, Hotei is green, Xanadu is blue) and grouped by principal component basis vectors (circles are the flyby in question, squares are T8, and triangles are T49). The bars in Figures 3.9-3.11 represent the random error arising from the spread in color-only I/F for pixels spanning a surface feature. The standard deviation of the mean calculated from the original selection of pixels is propagated through the calculation of the equivalent widths.

The variance in pixel color-only I/F is small for all cases– often "error" bars barely clear the size of the point plotted. This indicates that the random error is relatively negligible thanks to the coaddition

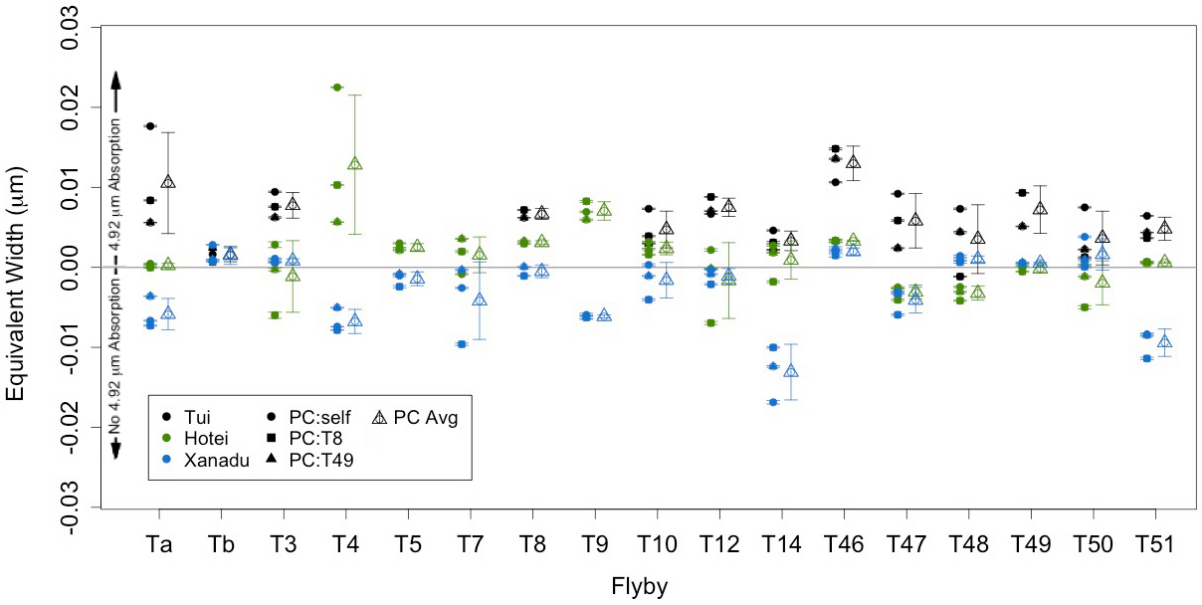

Figure 3.9: Equivalent width of the absorption feature at 4.92 μm as a function of flyby for Tui (black), Hotei (green), and Xanadu (blue). Each shape represents which eigenvector was used to project the data: from the flyby in question (circle), from T8 (square), and from T49 (triangle). The error bars are derived from the standard deviation of the mean for each pixel's color-only I/F at a particular wavelength. For the average from the three equivalent widths, the error bars are derived from the standard deviation of the mean from the three principal component values.

of pixels in our PCA-correction method. However, this does not take into account the systematic error. If all geometry and viewing effects were accounted for by subtracting the first principal component, then we might expect that differences between the equivalent widths derived from different basis vectors would be insignificant. As they are not, we know that the systematic error is not perfectly accounted for with this method. The average equivalent width between the values calculated with different basis vectors is shown to the right of the eigenvectors as a circle-filled triangle; the standard deviations of each set are normally distributed with the peak frequency at zero. When comparing the overall behavior of basis vector-derived equivalent widths as a function of flyby, the trends are the same. We thus discuss our results in light of the average behavior and the standard deviation of each eigenvector from this mean.

A linear regression fit through the average equivalent width values for Tui and Hotei reveals that it is reasonable to model the equivalent width as time-independent. The same cannot be said for Xanadu, as we expect for our control feature; the data is randomly distributed around the proposed model. The fit equivalent width is 0.0071$\pm$0.002 for Tui. A Bonferroni-adjusted test reveals no outliers, but according to our criteria, Tui shows the absorption feature in all but two (Tb and T50) of the thirteen flybys in which it is observed. In flybys Tb and T50, the calculated equivalent widths for Tui are of the same order as that of Xanadu, our control feature, and are thus too close to definitively call absorption cases. Note that our analysis agrees with that of McCord et al. (2008), as we observe an absorption feature in the T3 data.

Fitting the average equivalent widths for Hotei as independent of flyby gives a value of 0.0046$\pm$0.002.

As with Tui, no statistical outliers are present, though we exclude six flybys where Hotei's calculated equivalent width is below that of Xanadu's (T3,T12,T47,T48,T49,T50). Thus, Hotei only shows the absorption feature in eight of its sixteen observations (T4,T5, T7,T8, T9, T10, T14, and T46), with two flybys significantly above the time-independent average (T4 and T9). Two flybys have equivalent widths of near zero (Ta and T51).

When plotted as a function of viewing geometry (Figure 3.10), we do not observe any obvious trend to explain why the absorption feature is different from the time-independent average in some flybys and not others. Comparing each viewing angle with equivalent width via a Kendall tau test reveals no correlation. (With coefficients ≤ 0.1 for each, we cannot reject the null hypothesis.) For example, the two flybys during which the equivalent width for Tui Regio is significantly above the average, Ta and T46, are both near specular, but otherwise not similar in geometry. Ta is low phase with medium incidence and emission while T46 is high phase with medium incidence and emission. Furthermore, the flyby during which Tui's equivalent width is significantly below the average, T14, has almost identical viewing geometry to T46. Hotei's significant cases, Ta and T51 below the average and T4 and T9 above, are also near specular. But, as with Tui Regio, T51 and T4 are high phase while Ta and T9 are low phase. Therefore, our results do not support that any one value of phase, incidence, emission either independently or cumulatively is responsible for controlling equivalent width. We discuss possible explanations for this behavior and future analyses in Section 3.6.

3.5.2 Evaporites

We plot equivalent width as a function of flyby for evaporites in Figure 3.11 with the same shape scheme as we used in Figure 3.9. As it is difficult to see the most northern features in the cylindrical projection of Figure 3.2, we show in Figure 3.12 a labeled orthographic projection of the best VIMS data (T93-T97) of Titan's north pole in the same color scheme as Figure 3.2. The inset of Figure 3.12 shows the equivalent width-to-noise calculation of Figure 3.8 for Woytchugga Lacuna and MacKay Lacus[2]. (There are enough data from T96-T98 of similar viewing geometry for these two features to construct images of the necessary SNR per pixel.) Woytchugga, whose positive equivalent widths at 4.92 μm stand out above the noise level as an absorption feature, appears white in the inset. The region surrounding MacKay Lacus, which is also 5-μm-bright, also shows an absorption feature when coadding pixels from across the feature, but individually, no one pixel is above the noise level. Thus, it is indistinguishable in the inset.

It is less useful to conduct the linear regression analysis described above for Tui and Hotei with these evaporite cases, as most do not have overlapping error bars and have only a handful of observations. It is interesting to note, however, that the spread between values derived from different basis vectors is much smaller for the evaporites than for Tui, Hotei, and Xanadu. The evaporites with the largest spread are those with the largest surface area– Woytchugga, Flensborg Sinus, and south of Kraken. Thus, we interpret that another source of unaccounted error is the spectral blending unavoidable at km/pixel resolution. For example, in the higher resolution data of Hotei in T48 and T49, Soderblom et al. (2009) identify patches of dark blue spectral units. The polygons used to define the extent of Hotei for our pixel selection was drawn on these higher resolution maps, but this cannot fix coarser resolution data.

[2] *Lacuna* refers to a dried or potentially ephemerally filled lakebed while a *lacus* is a filled lake.

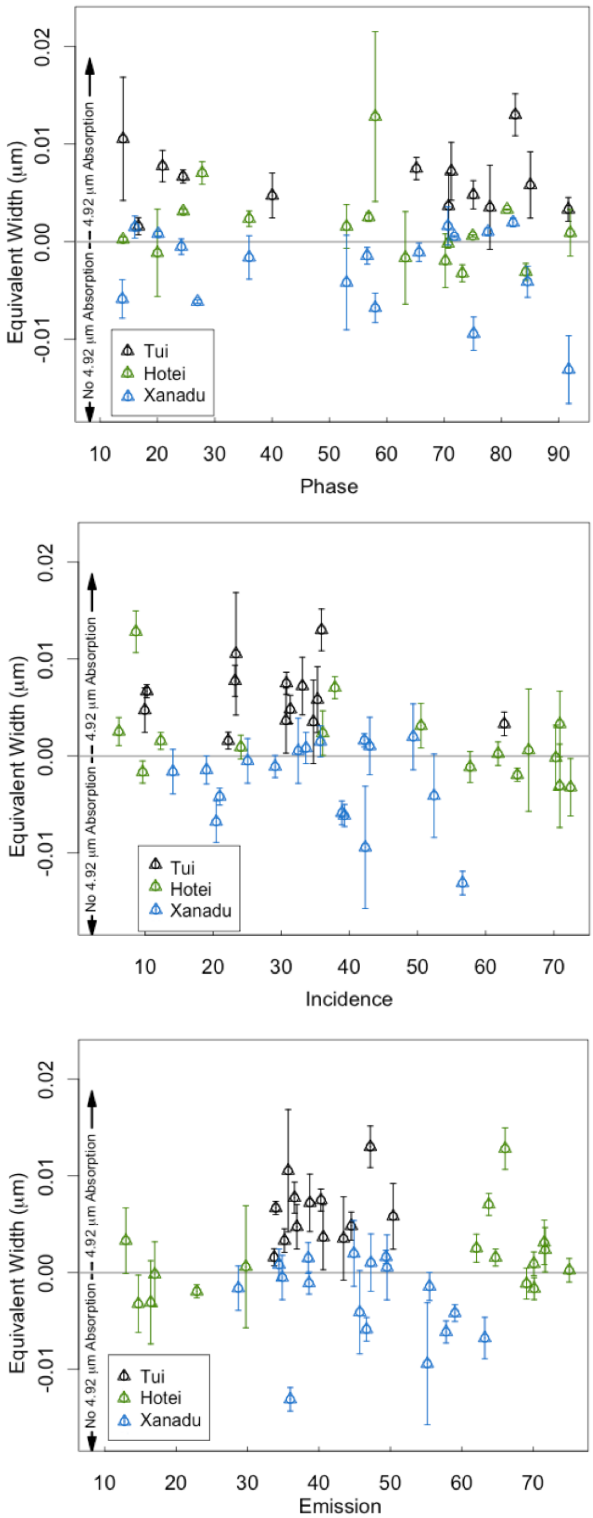

Figure 3.10: Equivalent width as a function of viewing geometry: phase (top), incidence (middle), emission(bottom) with the same color and shape scheme as Figure 3.9. We only plot the average of the three basis vectors for ease of interpretation; the bars represent the standard deviation from the mean of the equivalent widths calculated with each basis vector.

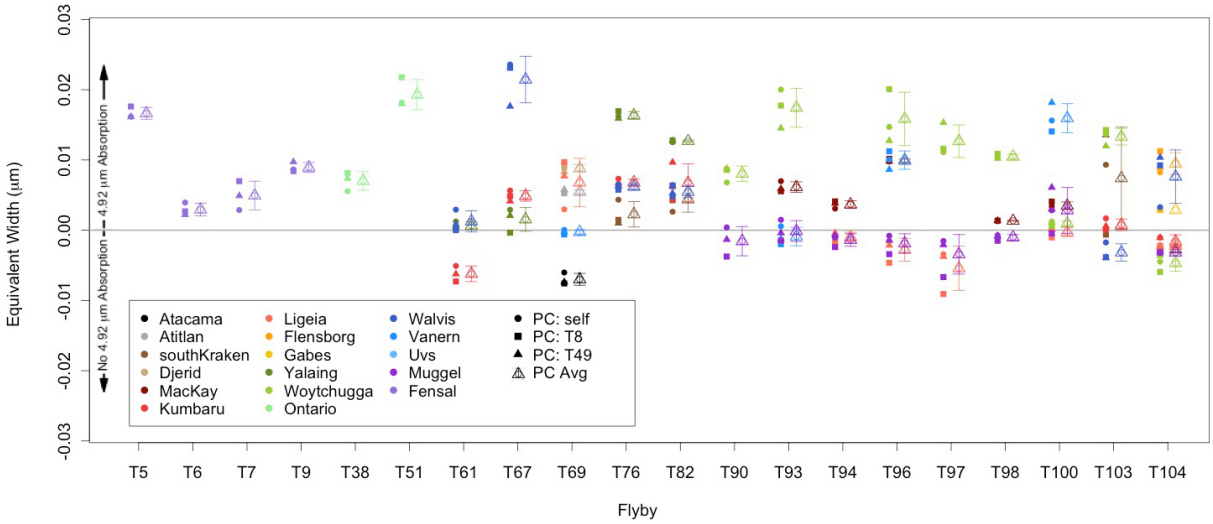

Figure 3.11: Equivalent width as a function of flyby for evaporites. Shapes correspond to which flyby the eigenvector for the PCA was derived from: the flyby in question (circle), T8 (square), or T49 (triangle). The error bars for each particular principal component are not shown as they are smaller than the point size. For the average from the three equivalent widths, the error bars are derived from the standard deviation of the mean from the three principal component values.

According to the calculated equivalent widths shown in Figure 3.11, we can group our results into three groups: evaporites that show the absorption feature in all observations, in most observations, and in at most one observation. There are eight evaporite deposits that demonstrate the absorption feature in every observation: deposits located in west Fensal (4 flybys); Ontario Lacus's shoreline deposits (2); Kraken Mare's Flensborg Sinus[3] and Gabes Sinus (both only observed once); Djerid Lacuna (1); Atitlan Lacus (1); Uvs Lacus (1); and MacKay Lacus (5).

In all but one of observation, Woytchugga Lacuna (7/8 flybys) and Walvis Sinus (5/6) demonstrate the 4.92 μm absorption feature, while Kumbaru Sinus (4/6) shows it in all but two observations. The 5-μm-bright deposit at the north end of Yalaing Terra and the deposits south of Kraken Mare both demonstrate absorption features at 4.92 μm in two out of the four observations of each feature. Whether these differences between flyby are due to viewing geometry, surface roughness, evaporite composition, etc. cannot be addressed by the methods used here and is thus beyond the scope of this paper. It is instead further evidence for the complexity of the problem evident in the results for Tui and Hotei. There are also evaporites that do not exhibit the absorption feature in a majority of their observations: Muggel Lacus, Vanern Lacus, Ligeia Mare shoreline deposits, and Atacama Lacuna.

3.6 Discussion and Conclusions

Not all 5-μm-bright terrains demonstrate the absorption feature at 4.92 μm, nor do those that do show the absorption show it in all observations. Our results cannot detail what physical characteristics set this behavior (i.e. relative abundances, micro-scale surface structure, etc.). To do so, more rigorous modeling

[3] *Sinus* is the International Astronomical Union designation for bays on Titan.

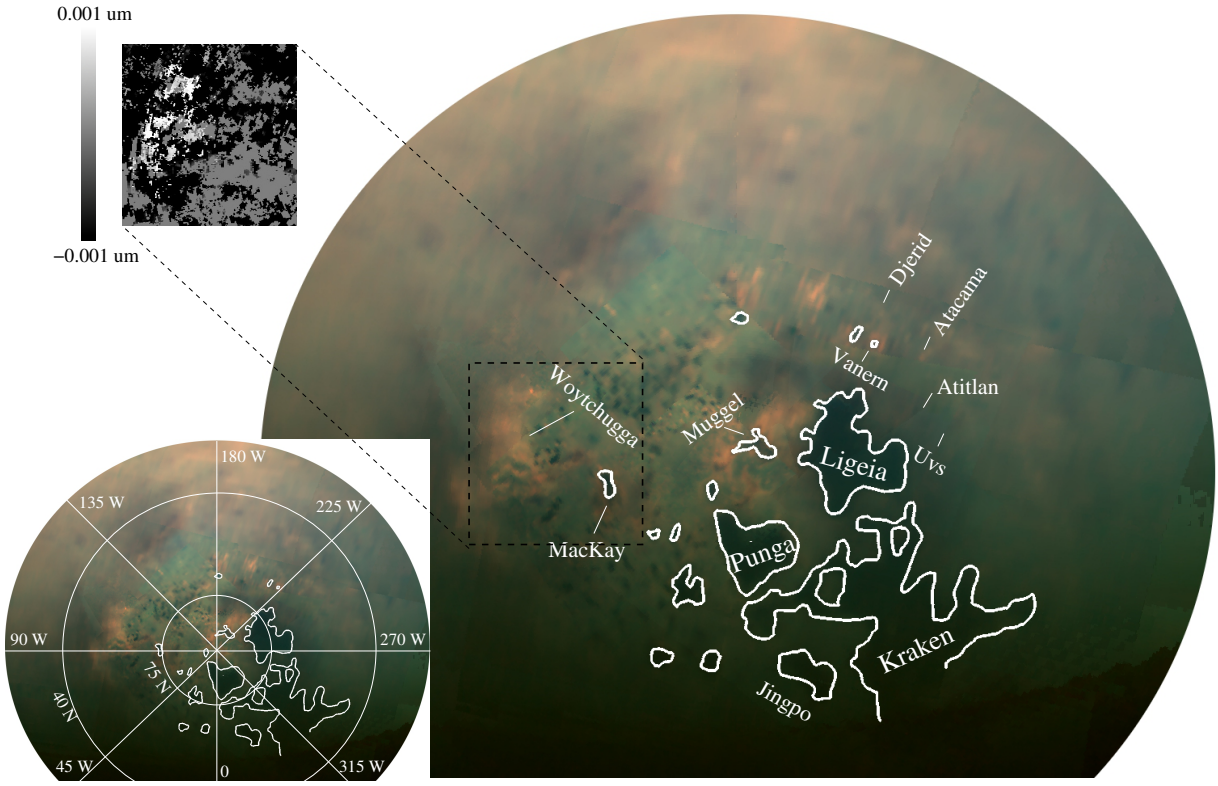

Figure 3.12: Orthographic projection of Titan's north pole in VIMS data (T93, T94, T96, and T97) with color scheme R = 5 μm, G = 2 μm, and B = 1.3 μm. The inset is the difference between the equivalent width at each pixel and the effective noise level of a coadded image of Woytchugga Lacuna and MacKay Lacus (created with coadded data from T96, T97, and T98), similar to the right panel of Figure 3.8. The extent of 5-μm-bright Woytchugga spatially correlates with positive equivalent widths at 4.92 μm well above the noise level (white values of the inset). We expect that the patches of dark within Woytchugga are a sampling effect.

of each feature's phase function will require a full radiative transfer correction for the atmosphere, our next project. However, our data, if true, do illuminate bulk spectral behavior, which we discuss below: what factors probably play in our results for Tui, why Hotei is different, and the heterogeneity of evaporite deposits.

3.6.1 Tui Regio

The equivalent widths of the 4.92 μm absorption feature in the spectra of Tui Regio are probably a function of viewing geometry, exposure time, the VIMS pipeline flat-field calibration, particle size, scattering properties of the grains of absorbent material, as well as the optical properties of surrounding materials. Generally, mid incidence angle observations yield a "stronger" absorption for Tui Regio, though if our estimated errors are robust, there is little difference between the extent of the absorption feature between flybys.

Titan evaporites could be crystalline like Earth evaporites as the end result of their similar formation process; such a structure would help explain why the 5-μm-bright material is bright at all wavelengths. As such, evaporites could have a preferred viewing geometry at which the absorption feature could appear stronger due to increased internal scattering before the light refracts out of the crystal and returns to the detector. Such an effect would be complicated by surrounding material and different particle sizes.

3.6.2 Differences between Hotei and Tui

The equivalent widths of the 4.92 μm absorption at Hotei Regio are generally smaller than those at Tui for the same flyby. Interestingly, Hotei does not show the same angular dependence as Tui: Hotei's absorption features are wider at smaller incidence and larger emission angles. However, the averages for both features in the flyby analysis are close enough to be within the estimated error of the fit, what we might expect if these features contain the same material responsible for the 4.92 μm absorption.

If the material responsible for this absorption is present at both Tui and Hotei, why might it demonstrate different spectral behavior in flybys where we observe both features? Our analysis of the influence of viewing geometry is not sufficient to explain this behavior– there must be other driving factors. For example, it has been shown by Shkuratov et al. (1999) that absorption depths for regolith-like surface material are strongly dependent on particle size; larger particles yielded a stronger absorption for the lunar soils of that study. Thus, it could be that the 4.92 μm absorbing grains are of different sizes at Tui Regio and Hotei Regio. Or, if Hotei's 4.92 μm absorbent material is covered by, say, larger grains not present or not of the same size than at Tui, the depth of the absorption feature might be dampened in different viewing geometries (i.e. flybys) for the different basins. Work by Pilorget et al. (2015) demonstrated that the overall phase curve behavior is largely controlled by the brightest, most abundant, and least isotropically scattering particles in a material. Of course it also could be that the albedo subtraction doesn't work as seamlessly as we have assumed, but the results for the evaporite cases demonstrate that material variability is not an unreasonable explanation.

3.6.3 Evaporites

What distinguishes evaporite deposits that do show the 4.92 μm absorption feature from those that don't? There is no simple, common geomorphological characteristic. Woytchugga Lacuna is a large (66,700 km^2), completely dry lakebed. Ontario Lacus is a lake with exposed evaporite along its eastern shorelines. MacKay Lacus is a partially-filled lake at $\sim 75^\circ$ N. Vanern Lacus is a 400 km^2 partially-filled lake south of Ligeia Mare with a bathtub ring of evaporite and Djerid Lacuna is a nearby dry lakebed of similar size. Yet all of these features demonstrate an absorption at 4.92 μm in most of their observations.

Recent work by Cordier et al. (2016) shows that for solutions with several solutes (each of different solubility in a Titan liquid), the evaporites will precipitate out in layers based on their solubilities; compounds with the largest solubilities will stay in solution the longest. In Figure 3.13 we show an example of this process on Earth in a wet interdune in Liwa, UAE (top photo). The inset shows thin sheets of gypsum evaporites along the edges of the receding shoreline while cubed halite is at the bottom of the liquid. This separation is due to the respective solubilities of the two compounds as well as the saturation of the solution.

Thus, it could be that each of these evaporite locations that do show the absorption are far enough along in the drying-out stage to have precipitated out the more soluble 4.92 μm absorbent material. Djerid and Woytchugga are at the end point of drying out (i.e. there is not enough liquid left to be detectable by VIMS). While, based on comparing the areas of liquid-covered surface and evaporite covered surface, Vanern and Ontario have receded by 90% and 15% their original areas, respectively. If our results are indicating that the evaporite deposits demonstrating the 4.92 μm absorption feature have reached some endpoint where the most soluble material has precipitated out, then the work of Cordier et al. (2016) would point to butane and acetylene as candidates for the material responsible for the 4.92 μm absorption.

Of course it could also be that the non-absorption cases (Muggel Lacus, Ligeia Mare shorelines, and Atacama Lacuna) have a different solution composition. At 83° N, Muggel is nearer to the north pole than the other deposits considered here. Lorenz (2014) discuss how more frequent rains at the northern-most parts of the pole might be responsible for a "salinity" dichotomy between the more northern Ligeia Mare and more southern Kraken Mare. Perhaps, then, Muggel and MacKay only precipitate out the least soluble sediments (and thus those that do not exhibit the 4.92 μm absorption), as before the 4.92-μm-absorbent material falls out of solution, a new influx of methane halts evaporite formation. Or it could be that the Ligeia watershed washes different sediments or even different amounts of sediments into the sea than Kraken's.

As for the less straightforward evaporite deposits that behave more like Hotei (Walvis Sinus, Kumbaru Sinus, Flensborg Sinus, south of Kraken deposits, Yalaing, and deposits located in west Fensal), it is again difficult to pull out viewing geometry dependence of extent of absorption feature depth without more rigorous modeling. Indeed, there are some inconsistencies in the cases we consider as demonstrating the absorption feature, like Woytchugga Lacuna which does not show an appreciable equivalent width in the most recent observations (T104). While we attribute these ambiguities to deficiencies in our current method, we cannot exclusively rule out the possibility that the 4.92 μm absorption in the studied evaporites might be lost in noise or highly variable due to dynamic surface processes.

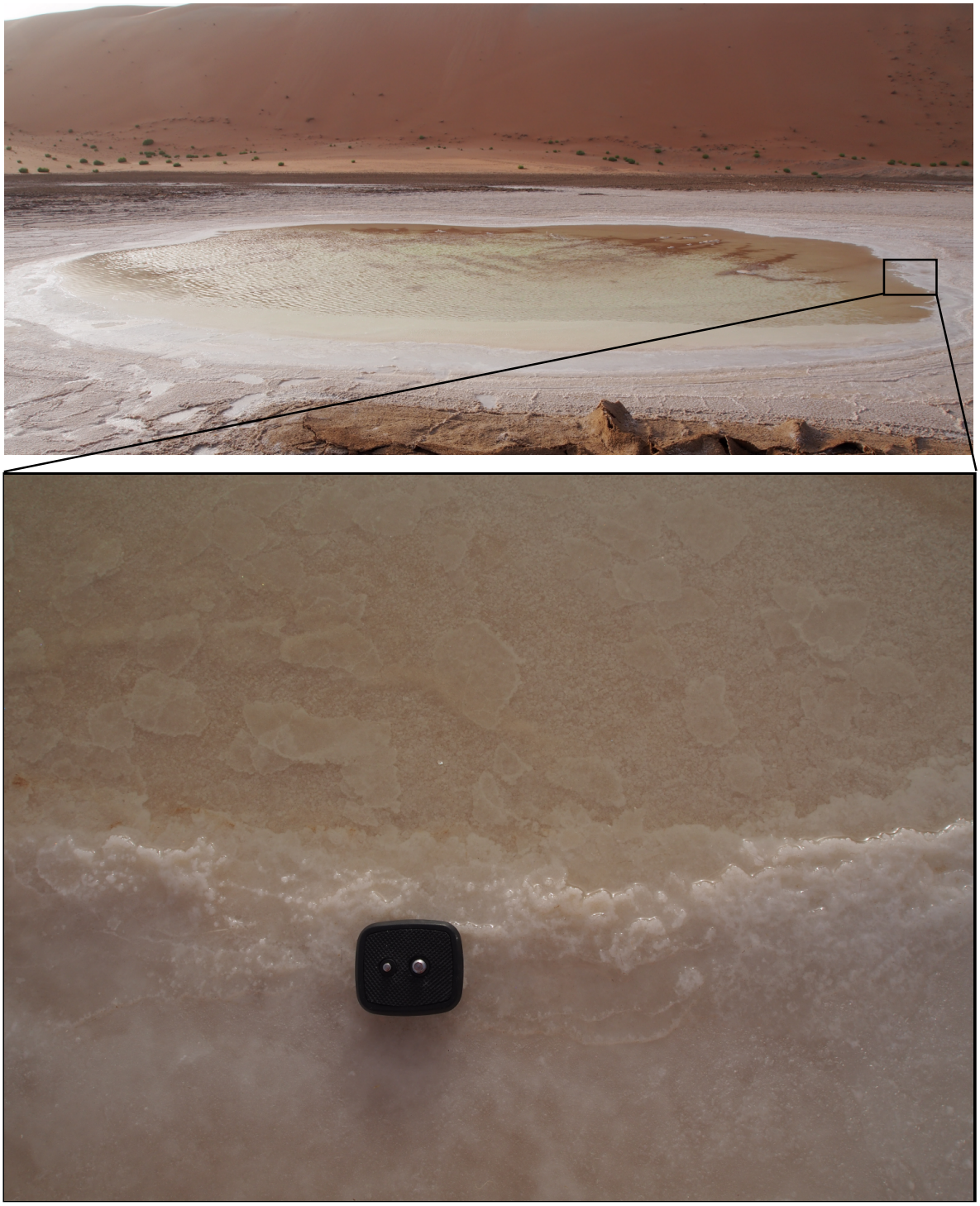

Figure 3.13: Earth evaporites forming in an interdune at Liwa, UAE. The extent of the liquid-filled sabkha is shown at top. In the inset, gypsum evaporite falls out as thin sheets at the shoreline while the bottom of the pond is covered by cubic halite structures. The camera mount included for scale is 5.5 cm across.

For example, as documented by Barnes et al. (2013a), there are VIMS observations of north Yalaing before, during, and after a wetting event. During T61-T67, Yalaing appears 5-μm-bright, but does not consistently show the absorption feature (note the disagreement between the different eigenvector samples in T67). In VIMS data from T76, during the wetting event, Yalaing Terra appears brighter at 2 μm, is no longer 5-μm-bright, and exhibits the absorption. With a thin enough layer, VIMS could still be sampling surface material beneath the 2-μm-bright covering. Then, after the wetting event (T82) the deposit returns to the 5-μm-bright spectral unit and, in our results, shows the absorption feature, though to a lesser extent than that observed in T76. Barnes et al. (2013a) propose that the spectral change was probably due to the presence of a transient layer: either volatile frost that sublimes away or a deposition of fine-grained particles that blow away to reveal the original material underneath. Sintering driven by the first scenario could create larger grain sizes that might thus explain the increased absorption feature at flybys during and after the wetting event. Or, it could be that this wetting event instigated a removal process of some surrounding material that promoted detection of the 4.92 μm feature.

Other evaporite candidates exhibit different values for equivalent width depending on flyby. While it is not clear that our analysis has removed all sources of systematic error, it is also a possibility that these other cases have experienced some change similar to that observed at Yalaing Terra. Unfortunately, there is no evidence in the ISS or VIMS cloud coverage maps to support such an explanation for the dramatic changes in equivalent width for Fensal (Rodriguez et al., 2009, 2011; Turtle et al., 2011a). Clouds have frequently been observed at the higher latitudes where the north polar evaporites are, but VIMS data provides no benchmarks for what the surface looked like beforehand. Surprisingly, there have been relatively few clouds at the north pole in our latest observations, despite global circulation model predictions of a pick up in seasonal weather activity (e.g. Rannou et al., 2006; Mitchell, 2012). Thus, there are no observed weather events able to explain, for example, the change between Vanern observed in T93 and T100.

Evaporites probably form on larger timescales than the lifetime of the *Cassini* mission, however. Thus, it is useful to also consider the results of general circulation models, which, for Titan, largely predict greater rainfall at the poles and a relative dearth at the equator (Rannou et al., 2006; Mitchell, 2008). That is not to say that it is impossible for rain to occur there—as demonstrated by the VIMS observations detailed above by (Barnes et al., 2013a) and ISS observations (Turtle et al., 2011b). Some GCM results suggest that perhaps this isn't as much of a problem for the evaporites found away from Titan's poles as previously thought. For example, in the model of Lora et al. (2015), pockets of equatorial and midlatitudes experienced surface liquid and drying periods (the conditions necessary for evaporite formation). This model's initial conditions included a 4 m deep methane reservoir with deeper, localized areas to represent the seas and Ontario Lacus. Interestingly, the evolution of such a Titan results in areas of surface liquid change in locations where we observe evaporites (namely, at Woytchugga Lacuna, Tui Regio, Hotei Regio, and Fensal; see Figure 14 of Lora et al. (2015)).

3.6.4 Conclusions

We report the observation of the same 4.92 μm absorption described by McCord et al. (2008) in the spectrum of Tui Regio in later observations of that surface feature, as well as in some observations of Hotei

Regio, another equatorial basin covered in 5-μm-bright material. Though we explore the dependence of this absorption feature on viewing geometry, we find that the phase function will require full radiative transfer treatment to solve completely. We also look for the 4.92 μm absorption in the spectra of several evaporites identified by Barnes et al. (2011) and MacKenzie et al. (2014) and find that while some do, not all evaporites have the spectral feature. We propose that this variance could be due to differences in solution composition, different states of drying, or different surface roughnesses. Our analysis is not able to definitively discern between which of these possibilities could best explain the variable behavior of the 4.92 μm absorption feature.

3.7 Acknowledgments

This work was supported by NASA Headquarters under the NASA Earth and Space Science Fellowship Program- Grant NNX14AO30H to SMM and the NASA *Cassini* Data Analysts and Participating Scientists (CDAPS) Grant NNX12AC28G to JWB. We gratefully acknowledge Sebastien Rodriguez for the helpful comments in his review.

Chapter 4: Phantom lakes: evidence for surface changes at Titan's north pole

When looking at the north polar evaporites, I noticed an interesting phenomenon that may be evidence for seasonal surface changes at Titan?s north pole, at a corner of Titan?s lake district. If true, this last work provides some of the first evidence for shoreline change at Titan's north pole, providing a glimpse into the seasonal dynamics of Titan's wettest region.

Titan, Saturn's largest moon, hosts lakes and seas of liquid hydrocarbons at its polar regions thanks to a hydrological cycling of methane between the surface and atmosphere. SpectroscopicBarnes et al. (2011); MacKenzie et al. (2014) and geomorphologicHayes et al. (2008, 2011); Hayes (2016) evidence suggest some degree of emptying, changing the distribution of liquids across Titan's surfaceAharonson et al. (2009b); Lora et al. (2014) on geological timescales. The seasonal timescales for shoreline change are less well understood. Shoreline change has not been observed yet at Titan's north pole where most of the lakes are found today. We identify three features at Titan's north pole that resemble shallow bodies of liquid in *Cassini* RADAR observations in 2006 but not in subsequent observations by infrared instruments starting in 2013. We investigate these "phantom lakes" (designated A, B, and C) to establish why they seem to disappear between observations. Phantom lakes A and C could be liquid bodies covered in a thin layer of scatterers, but we prefer the interpretation similar to that of B: removal of surface liquids to within at least a few microns of the surface. Our findings represent the first evidence for shoreline changes at the north pole at comparable timescales (6 months - 7 years) to that observed for lakes at the south poleHayes et al. (2011) of similar size.

Shallow lakes may be easier targets for identifying shoreline change as predicted evaporation or infiltration rates (centimeters-meters per year)Mitri et al. (2007); Hayes et al. (2008) would result in a more dramatic change than at the $>$ 100 m deep seasMastrogiuseppe et al. (2014) or the $\sim$ 100 m deep steep-sided lakesHayes (2016). The difficulty in observing shoreline change lies in establishing a long enough baseline in time between images: no single *Cassini* instrument has repeat coverage at sufficient spatial sampling to resolve change at the small lakes (Figure 4.1). By combining data from RADAR, the Imaging Science Subsystem (ISS), and Visual and Infrared Mapping Spectrometer (VIMS), we can take advantage of *Cassini*'s 13 years of Titan-targeted flybys at the cost of some complexity. Each surface imaging instrument's dataset is unique in spatial and temporal resolution and coverage, making precise comparison between them nontrivial. Furthermore, these three instruments probe different properties of the surface. VIMS and ISS are sensitive to composition and grain size on the scale of a few microns while Synthetic Aperture RADAR (SAR) images convey information about dielectric properties and surface roughness on the centimeter scale.

A single VIMS image cube shows a portion of Titan's lake district at fine enough spatial sampling (Figure 4.1) to resolve many of the small lakes, thus offering a temporal and spectral counterpart to the earlier RADAR observations. Here, tens of lakes are identifiable in RADAR, VIMS, and ISS due to their characteristic darkness in each dataset.

Because of their smoothness, light specularly reflects off the surface of the lakesSoderblom et al. (2012); often away from the direction of *Cassini*. At 2.14 cm, the reflected RADAR signal is unaffected

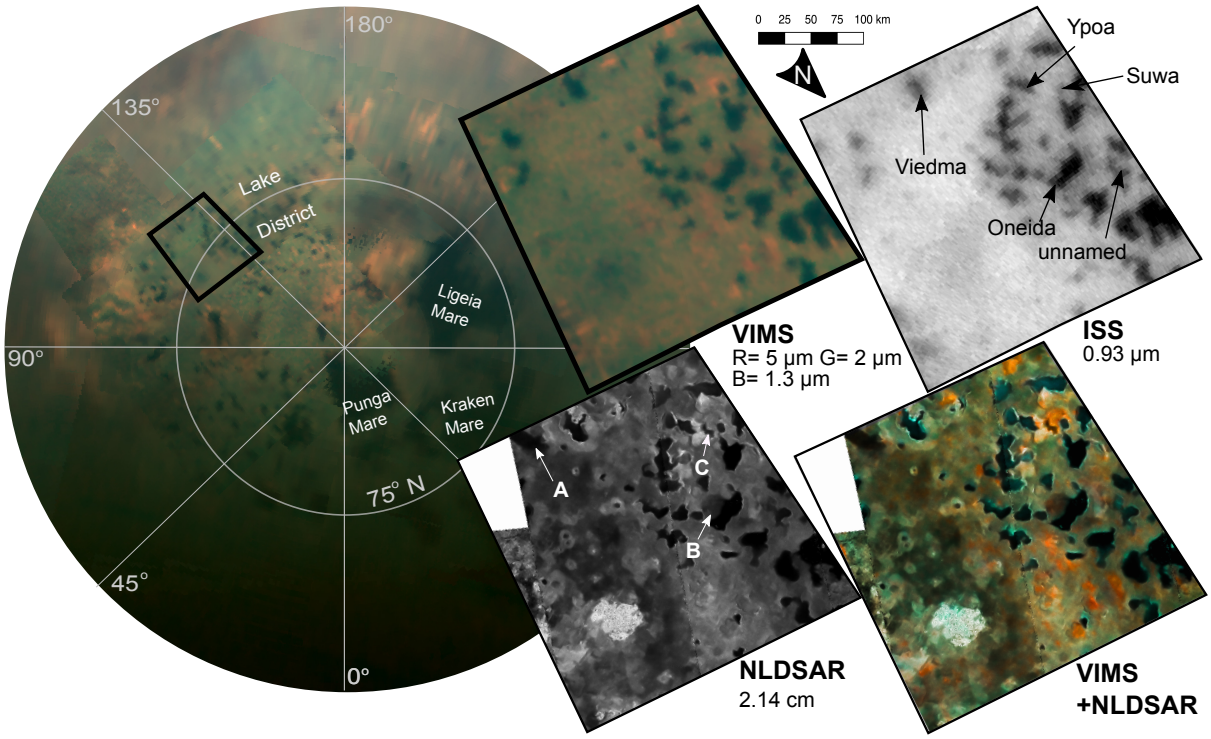

Figure 4.1: (left) Azimuthal stereographic projection of Titan's north pole as observed by *Cassini* VIMS on December 13, 2013. Titan's hydrocarbon seas (maria) lie opposite the lake district and at lower elevationHayes (2016); Birch et al. (2017). (insets) Eastern edge of the lake district as seen by VIMSBrown et al. (2004) (up to 4 km/pixel), ISSPorco et al. (2004) (map scale at 4 km/pixel), and Non-Localized DenoisedLucas et al. (2014) SARElachi et al. (2004) (350 m/pixel). These instruments observed the eastern half of the lake district at different wavelengths and seasons (northern winter and northern spring).

by atmospheric scattering and controlled by the dielectric properties of the surface: materials with a dielectric constant closer to that of air, such as liquid hydrocarbons, reflect less than those of higher dielectric constant, like the solid, organic-covered surface. Lakes therefore appear dark to RADAR. In the infrared (IR), diffuse scattering off haze in the atmosphere also illuminates the lake surfaces, making them appear dark grey to ISS (0.93 μm) and dark blue to VIMS (0.9 μm - 5 μm) in the color scheme presented in Figures 4.1 and 4.2. Each instrument is sensitive to liquid depths of at least a few wavelengths; thus, the IR instruments detect even a few tens microns of liquid while RADAR senses only tens of centimeters. Identification of lakes and seas represents some of the best agreement between RADAR, VIMS, and ISS datasets, with the exception of the three "phantom lakes" that appear liquid-covered to RADAR in 2009 and early 2013 but not in later IR observations.

RADAR observed the three phantom lakes in SAR mode on July 22 and October 9 of 2006Stofan et al. (2007) (top panel, Figure 4.2). Both the denoisedLucas et al. (2014) images (Figure 4.1) and uncorrected images (Figure 4.2) show the phantom lakes' normalized radar cross sections (σ^0) as consistent with those of nearby lakes (plotted as grey circles of Figure 4.3), a model for partially filled lakesHayes et al. (2011) (blue fit), and an unnamed lake with specular returns in altimetry data (U). This agreement suggests that liquid cover is a plausible explanation for the RADAR dark features, be it a shallow surface liquidPaillou et al. (2008) or a wetted regolith. Neighboring lakes may be much deeperHayes et al. (2017). Viedma Lacus near phantom lake A, for example, exhibits the sharp edges consistent with the deep "cookie cutter" lakesHayes (2016).

Phantom Lake B differs from A and C in that it nestles alongside Oneida Lacus. An altimetry pass shows a raised rim on the northern shore of Oneida but the track ends in the middle of the lake. Overlap between SAR swaths T19 and T91 indicates that the rim extends partially along the southern shore, separating the phantom lake terrain from the liquid of Oneida. A second observation on May 23, 2013 (T91; Figure 4.2 inset) shows the phantom lake area remained dark enough to agree with the partially-filled model, but was brighter than predicted.

Because the ISS and VIMS cameras rely upon reflected light, they could not observe Titan's north pole until the Sun rose with northern spring (2009) and the winter clouds dissipatedLe Mouélic et al. (2012b). ISS first glimpsed the lake district in October 13, 2013. In that image, Phantom Lake A was not dark like a lake while Phantom Lakes B and C were not resolved. Later, on November 30, 2013 (Figure 4.2 middle), Phantom Lakes A and C appear bright, inconsistent with the presence of surface liquids. The observation of Phantom Lake B is less conclusive due to its proximity to Oneida Lacus.

VIMS followed up on December 1, 2013 (Figure 4.2 bottom). At as fine as 4 km/pixel, at least four spectral units–surface materials with similar reflectance properties in the IR–are evident. EvaporitesBarnes et al. (2011); MacKenzie et al. (2014) appear bright pink/orange in our infrared color images because of their diagnostic brightness at 5 μm; they surround some of the dark blue lakes. (The blue and green materials are spectrally distinct but not yet geomorphologically interpreted.) VIMS pixels covering Phantom Lakes A and B do not behave as a single unit as they do in RADAR. In Figure 4.4 we show that the northern pixels of A (grey square) are darker than the southern pixels (black square). Similarly, the eastern half of B (grey star) is darker than the western (black star). These bright western pixels of B parallel the raised rim of Oneida Lacus. Though the outline of the phantom lakes is unmistakeable

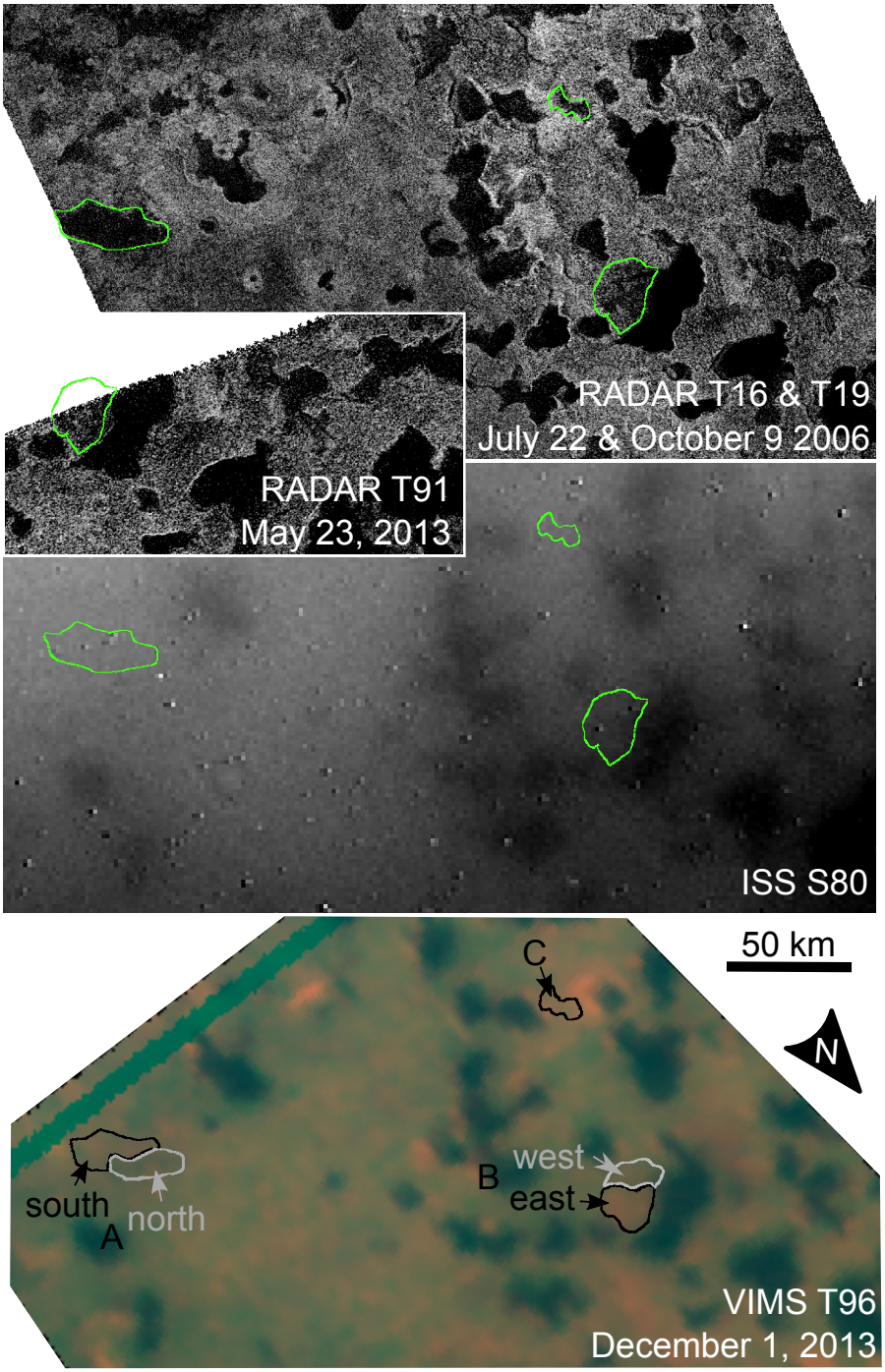

Figure 4.2: Sequence of observations of the phantom lakes, outlined in each dataset. SAR coverage from T16 and T19 (top) and T91 (top inset) show the phantom lakes as dark. But later, the same areas appear bright in ISS (middle) and VIMS (bottom) images. Normally, lakes appear dark in all three datasets. Because our temporal coverage relies on three datasets that probe different surface properties, we consider both liquid level change and physical phenomena as possible explanations.

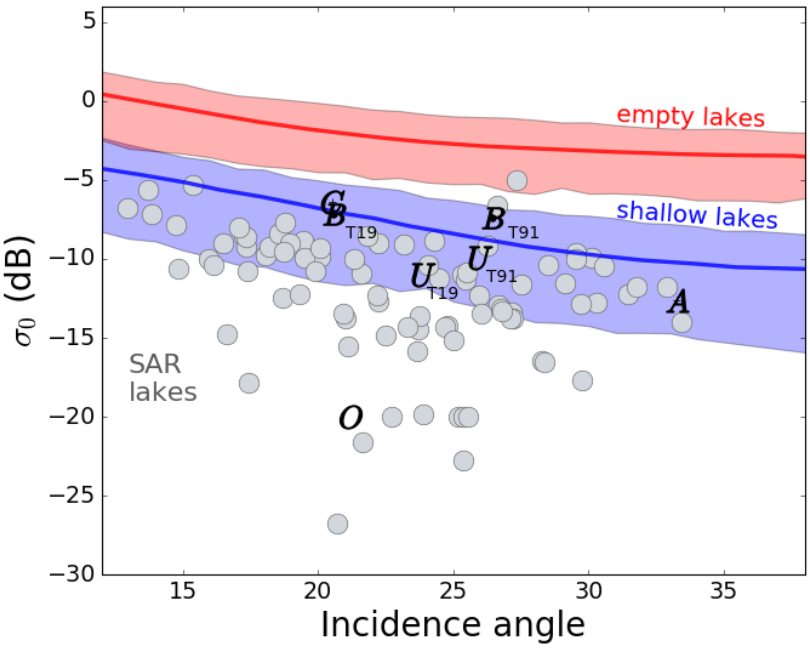

Figure 4.3: Normalized radar cross sections (σ^0) calculated from SAR swaths as a function of incidence angle for the phantom lakes (labels A,B,C), lakes (grey circles), and the model predictions (shading represents 95% confidence interval) for partially filled lakes (blue) and empty lakes (red)Hayes et al. (2011). O and U represent the σ^0 of Oneida Lacus and an unnamed adjacent lake that have altimetry returns consistent with a specular reflection off a smooth, presumably liquid surface. σ^0 is a measure of the microwave reflectivity of the surface. All standard deviations from the population mean are smaller than the size of plotted points.

in RADAR, A and C do not show these boundaries in VIMS. Phantom lake C's spectrum most closely resembles the evaporites of Ypoa and Suwa Lacus, nearby lakes that appear liquid filled in all datasets.

Subsequent VIMS observations are too coarse for in-depth analysis but appear consistent with a lack of surface liquids. ISS images from February 2014 and July 2017 show that the phantom lakes are bright even in the final *Cassini* glimpses of the lake district.

Thus, the phantom lakes scatter like nearby solid surfaces in the infrared. They cannot be open bodies of liquid at the time of VIMS or ISS observations. How then can we reconcile the liquid RADAR darkness with an IR bright surface? We put forth three possible explanations for the phantom lake observations: (1) a RADAR-invisible "scum" layer on a shallow liquid layer or saturated regolith, (2) an IR-bright "scum" developing between observations, and (3) liquid removal from at least the top few microns of the surface.

Given the right circumstances, the difference between the RADAR and IR observations could stem from the difference in wavelengths observed by the RADAR mapper and the IR imagers rather than from a change of surface properties. For example, according to effective medium theoryBohren and Huffman (2008), a sufficiently thin layer of scatterers (i.e. much smaller than a RADAR wavelength) does not change the loss of signal at the first reflection off the air-liquid boundary. Furthermore, there are also

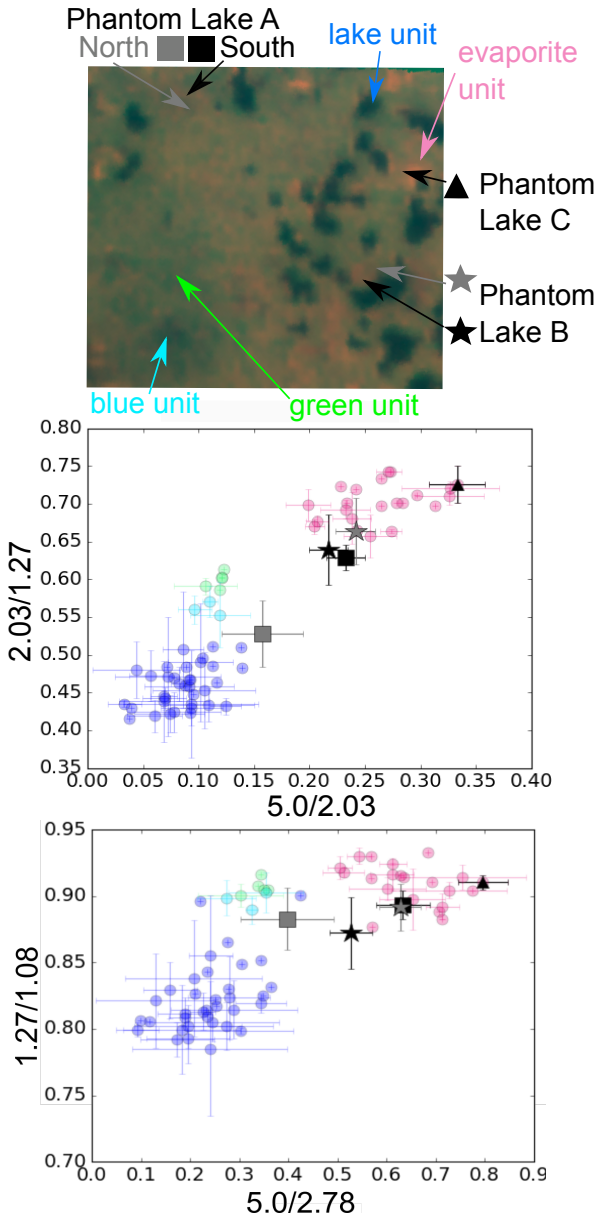

Figure 4.4: Behavior of phantom lakes relative to other VIMS spectral units within the spectral windows. Because VIMS can only see down to Titan's surface in seven windows (0.93 μm, 1.0 μm, 1.3 μm, 1.6 μm, 2.0 μm, 2.7 μm, 2.8 μm, and 5 μm), we group surface materials into spectral units defined by the relative reflectance at these wavelengths. In the T96 VIMS image (CM_1764550739_16), we identify four units (lake, evaporite, green, and blue) as endmembers to which we compare phantom lake pixels (examples labeled in top image). The ratios have been corrected for atmospheric effects using an empirical correctionLe Mouélic et al. (2012a). Error bars signify standard deviation of the mean.

scenarios in which diffuse scattering off particles suspended in an upper liquid layer contributes a small enough σ^0 to be consistent with the RADAR observations of the phantom lakes. If we approximate this signal as due to Rayleigh scatterers (particles much smaller in radii than a RADAR wavelength)Hofgartner et al. (2016), for example, a 2 cm thick layer of 1-4 mm radius particles with dielectric constants 1.5-2 (near that of liquid methane Paillou et al. (2008)) increases the signal less than the observed σ^0 of phantom lake A. To remain consistent with the later IR observations, however, the layer of scatterers would need to be thick enough (a few mm) to obscure any liquid methane or ethane absorptions in the spectraClark et al. (2010). Therefore, in scenario (1), no surface change occurs: some layer of scatters (1 mm $\lesssim$ thickness $\lesssim$ 2.14 cm) is present during all observations but is visible only to the IR instruments. Possible scatterers within a liquid layer include bubbles, haze fallout, or suspended sediment. For a liquid saturated regolith, the top IR-bright surface layer would need to be dry.

Alternatively, in scenario (2), the scattering layer could develop in the time between the RADAR and IR observations. In this case, the IR bright material (bubbles, fallout, suspended sediment, or dry surface) need only be at least millimeters thick.

The problem with any "scum" layer, however, is that the phantom lakes do not exhibit the same boundaries in VIMS as they do in RADAR. If a froth of bubbles acted as the scatterers, for example, then we would expect some lake outline in the VIMS data delineating where the unique properties of the scum covered lake ended and the rest of the surface began. If haze fallout creates the layer, then the surrounding surface and the lake might look the same to VIMS, but it is difficult to invoke a case of fallout so isolated as to not affect nearby lakes tens of kilometers away. Furthermore, Phantom Lakes A and B do not show the same spectral unit across the boundaries defined by the RADAR observations. Thus, the properties of the bubbles or haze layer would need to differ across the surface of the lakes. If the liquids of Phantom Lake B are an extension of Oneida Lacus, then the scums responsible for the different VIMS units would be sequestered to the side behind the raised rim and furthest from the liquid inlet.

We therefore prefer scenario (3) in which the liquid responsible for the dark σ^0 observed by RADAR disappears by the time VIMS and ISS observe the phantom lakes. A freshly exposed solid surface could explain both the IR brightness and the similarity between the phantom lakes' VIMS units and those of the surrounding terrain. Processes for emptying a lake on Titan include draining by channels, infiltration into a porous regolith, and evaporation. *Cassini* could not resolve any channels feeding into the phantom lakes; if any such features exist they must be subpixel in size ($<$ 175 m). Infiltration can happen on relatively short timescales: even the least permeable regoliths hypothesized on Titan can drain lakes of 10 m to a methane table a few centimeters below the surface within several yearsHayes et al. (2011). Evaporation rates at the north pole are poorly constrained by the empirical data of *Huygens*–given that the local wind speeds and humidities at the lake-dominated pole likely differ from the desert equatorial landing site of the probe–but models offer some insight. Mitri et al. (2007) predict that at expected north polar regional temperatures, evaporation rates vary between 0.3-10 m/yr as a function of windspeed.

For Phantom Lakes A and C, the emptying process would have to take place within the seven years between observations, a timescale that easily fits within the estimates for emptying either by infiltration or evaporation (in reality, it could be a combination of the two). In this scenario, we might expect other

lakes in the vicinity to empty or show some signs of shoreline change; none do. Differences in local permeability or local distance to the "water table" of subsurface methane can drive different infiltration rates. Evaporation would empty a shallow lake more quickly than a nearby deep lake, creating more easily resolvable shoreline change.

Phantom Lake B, on the other hand, would have a much shorter timescale. Though brief, the six months between observations may be enough time to remove liquid from the shallow depths the IR instruments probe. Phantom lake B appears brighter to RADAR at higher incidence angles than would be expected for a shallow lake. Scattering off suspended particles can increase σ^0, but so can looking through less liquid, i.e. a decrease in the amount of liquid at Phantom Lake B. Furthermore, B is situated along the shoreline of Oneida Lacus, enhancing the likelihood of a shallow deposition of liquid (e.g. lake overflow) or draining into a nearby reservoir (e.g. deeper into the subsurface). As a raised rim separates the western half of Phantom Lake B from Oneida Lacus, it is more likely for liquid to overflow on the eastern half.

Together, the phantom lakes make the case that observable change may have occurred at Titan's north pole during the *Cassini* mission at comparable timescales (6 months - 7 years) than that observed for lakes at the south poleHayes et al. (2011) of similar size. This may be consistent with global circulation models that predict liquid removal in the winter months, but not with predictions for liquid filling post-northern equinox.

4.1 Methods

All data presented here are available from the NASA Planetary Data System (PDS). After calibration (described below), we imported images into QGIS, an open-source GIS, for projection and mapping.

4.1.1 RADAR

In Synthetic Aperture Radar (SAR) mode, the Cassini RADAR instrument mapped the surface at resolutions of $\sim$ 350 m/pixel at 2.14 cm. We use incidence angle, noise-subtracted, and NLDSAR swaths from T16, T19, and T91Lucas et al. (2014). Incidence and NRCS values were then extracted via polygon mapping tools and averaged with QGIS.

4.1.2 ISS

ISS imaged Titan at 0.938 μmPorco et al. (2004). At this wavelength, haze particles in the atmosphere scatter most of the light before it reaches the surface. However, the shape of the haze phase scattering function (as derived by Tomasko et al. (2008c)) actually facilitates observation of the surface because some of that light forward scatters to the ISS detector. The resulting ISS maps are generally 1 km per pixel. Thus, ISS data have been used to identify the presence of liquid on Titan's surfaceTurtle et al. (2009, 2011b,c) as well as monitor cloud activity in the atmosphereTurtle et al. (2009, 2011a). For this work, we use the mosaic map available from the USGS [1]. Additionally, we use data from October 13,

[1] `https://astrogeology.usgs.gov/search/map/Titan/Cassini/Global-Mosaic/Titan_ISS_Globe_65Sto45N_450M_AvgMos`

2013 to February 2, 2014 available on the PDS. These images are calibrated and mosaicked using USGS Integrated Software for Imagers and Spectrometers (ISIS).

4.1.3 VIMS

VIMS observed Titan in the near infrared windows at which methane absorption (and that of trace gases) is weak enough to allow light to penetrate through the atmosphere and interact with the surfaceBaines et al. (2005); Brown et al. (2006a): 0.93 μm, 1.0 μm, 1.3 μm, 1.6 μm, 2.0 μm, 2.7μm, 2.8 μm, and 5 μm. Though specific chemical composition is difficult to identifyMcCord et al. (2008); MacKenzie and Barnes (2016), the diverse surface can be divided by spectral reflectance properties into spectral unitsBarnes et al. (2007b).

VIMS data were calibratedBarnes et al. (2008b) and coloredBarnes et al. (2007b) for initial identification of spectral units, R=5 μm, G= 2.0 μm, B=1.3 μm. To remove some of the atmospheric influence on the spectra, we also used an empirical correction Le Mouélic et al. (2012a); Cornet et al. (2012c). We identified five spectral units in the high resolution cube–lake, evaporite, blue, green, and purple–based on the unique behavior of the band ratio plots shown in Figure 4.4. These endmember representative spectra were created by averaging over pixels within the identified units.

There are many IR bright phenomena in VIMS observations of Titan. Specular reflections off smooth surfaces Stephan et al. (2010); Barnes et al. (2011); Soderblom et al. (2012) are bright at all wavelengths (especially 5 μm) but are only observed when *Cassini* images the surface at the same angle at which the light is incident. None of our phantom lakes were imaged at this geometry. Broad specular reflections from wavy surfaces can occur further from the specular point but are also much brighter than the reflectance of the phantom lakes Barnes et al. (2014). Furthermore, no specular reflections have been identified in ISS data to date, as the the high optical depth at 0.93 μm makes direct surface scattering unlikely even at favorable geometries. Thus, neither direct nor broad specular reflections can explain the brightness of the phantom lake features to ISS. Clouds are also bright but have a distinct spectrum (e.g. a high ratio between 5.0 μm and 2.75 μm Rodriguez et al. (2009, 2011)) that is inconsistent with that of the phantom lakes. Clouds would also have to appear in the same locations several times to obscure dark lakes in ISS images from October 2013- July 2017. The adjacency effect can artificially brighten dark surfaces when photons reflected from nearby bright surfaces get scattered into the cone of acceptance of the pixel imaging the dark material. However, this effect dominates at shorter distances with increasing optical depthMinomura et al. (2001) and we observe the opposite. The phantom lakes appear brighter at the longer wavelengths. The brightness of the phantom lakes is therefore most likely due to compositional and grain size properties of the surface and not some observational or atmospheric phenomenon.

Chapter 5: THEO Concept Mission: Testing the Habitability of Enceladus's Ocean

"THEO Concept Mission: Testing the Habitability of Enceladus's Ocean" *Advances in Space Research* 58.6 (2016): 1117-1137.

This work represents the culmination of the 10 week Planetary Science Summer School hosted by the Jet Propulsion Laboratory during which a group of about twenty graduate students and post docs design a mission concept to a New Frontiers (∼1 billion) mission. This process involved crafting the scope of the mission during the first nine weeks over telecons. The final week was spent at JPL, collaborating with the team of scientists and engineers specially trained in concurrent engineering to create mission designs, Team X.

I chose to pursue writing our findings as a published work (following the precedent set by some other years, (Duffard et al., 2011; Diniega et al., 2013; Bocanegra-Bahamón et al., 2015)) to make our findings available to the community: that solar power isn't impossible at Saturn and that providing context to any biosignatures search is critical for advancing the field forward. (This message became particularly relevant with the addition of Enceladus and Titan to the New Frontiers 4 target list in January 2016.)

5.1 ABSTRACT

Saturn's moon Enceladus offers a unique opportunity in the search for life and habitable environments beyond Earth, a key theme of the National Research Council's 2013-2022 Decadal Survey. A plume of water vapor and ice spews from Enceladus's south polar region. *Cassini* data suggest that this plume, sourced by a liquid reservoir beneath the moon's icy crust, contain organics, salts, and water-rock interaction derivatives. Thus, the ingredients for life as we know it– liquid water, chemistry, and energy sources– are available in Enceladus's subsurface ocean. We have only to sample the plumes to investigate this hidden ocean environment. We present a New Frontiers class, solar-powered Enceladus orbiter that would take advantage of this opportunity, Testing the Habitability of Enceladus's Ocean (THEO). Developed by the 2015 Jet Propulsion Laboratory Planetary Science Summer School student participants under the guidance of TeamX, this mission concept includes remote sensing and *in situ* analyses with a mass spectrometer, a sub-mm radiometer-spectrometer, a camera, and two magnetometers. These instruments were selected to address four key questions for ascertaining the habitability of Enceladus's ocean within the context of the moon's geological activity: (1) How are the plumes and ocean connected? (2) Are the abiotic conditions of the ocean suitable for habitability? (3) How stable is the ocean environment? (4) Is there evidence of biological processes? By taking advantage of the opportunity Enceladus's plumes offer, THEO represents a viable, solar-powered option for exploring a potentially habitable ocean world of the outer solar system.

5.2 Introduction

Since the discovery of Enceladus's subsurface ocean (e.g. Porco et al., 2006; Spencer et al., 2006; Schmidt et al., 2008; Postberg et al., 2011; Iess et al., 2014; Thomas et al., 2016), the small moon of Saturn has been considered a potentially habitable world in the solar system (e.g. McKay et al., 2008; Parkinson et al., 2008; McKay et al., 2014). Subsequent observations and investigations by *Cassini* have revealed that Enceladus's ocean depths are not only liquid, but also warm (e.g Matson et al., 2007; Sekine et al., 2015; Hsu et al., 2015), salty (e.g. Postberg et al., 2009; Sekine et al., 2015), and host to a range of interesting organic compounds (e.g. Waite et al., 2006, 2009). As such, the subsurface ocean is already known to have the three elements identified as necessary for life– liquid water, chemistry, and energy. Enceladus is therefore of crucial importance to the search for life in our solar system, the study of how habitable environments develop, and defining what "habitable" might mean. What makes Enceladus most unique, however, are the vents that connect the ocean to the surface, releasing water ice and vapor in geyser-like plumes (e.g. Dougherty et al., 2006; Spencer et al., 2006; Porco et al., 2006; Hansen et al., 2006; Waite et al., 2006; Spahn et al., 2006). This readily available ocean material makes testing whether Enceladus's hidden ocean world is habitable both possible and relatively easy with today's technology on a medium-sized mission budget.

While water ice is an abundant resource in the outer solar system, liquid water is more unusual. Enceladus's water plumes and subsurface ocean were two of the great discoveries of the *Cassini* mission; a true team effort with lines of evidence from the magnetometer suite (Dougherty et al., 2006), the Composite InfraRed Spectrometer (CIRS) (Spencer et al., 2006), the Imaging Science Subsystem camera (ISS) (Porco et al., 2006), the Ultraviolet and Visible Imaging Spectrometer (UVIS) (Hansen et al., 2006), the Ion Neutral Mass Spectrometer (INMS) (Waite et al., 2006), the Cosmic Dust Analyzer (CDA) (Spahn et al., 2006), the Visual and Infrared Mapping Spectrometer (VIMS) (Brown et al., 2006b), and the Radio Science Subsystem (Iess et al., 2014). The plumes emanating from Enceladus's south polar region were directly sampled by INMS and CDA and observed in occultation by UVIS. The results indicated that the plumes are mostly water vapor and ice. The source of that water was identified to be a subsurface ocean using the derived gravity field (Iess et al., 2014), libration observations (Thomas et al., 2016), stress field analysis (Patthoff and Kattenhorn, 2011), and the detection of potassium salts (Postberg et al., 2011) in plume-derived (e.g. Baum et al., 1981; Spahn et al., 2006; Hillier et al., 2007; Juhász et al., 2007; Kempf et al., 2008, 2010) E-ring material. The crust of Enceladus is thought to be pure water ice (Brown et al., 2006b; Zolotov, 2007) and therefore cannot be the sole source of a salty plume. The plumes thus provide a unique opportunity to understand the internal processes of an icy body with a subsurface ocean. Be they hydrothermal, geochemical, or perhaps even biological, such processes are relatively easy to explore at Enceladus from orbit without the need to land, drill, or rove.

Sampling the plumes has also indicated that a rich chemistry is in the subsurface ocean. Trace amounts of organics– such as methane, ethane, butane, and pentane– are present in the plume vapor, according to the data from INMS. (See Table 1 of Waite et al. (2009) for a comprehensive list.) During higher-velocity flybys, the mass spectrometer observed higher percentages of carbon compounds. This is consistent with longer chain organics breaking into smaller compounds upon impact in the instrument,

thus fortuitously facilitating their detection within the limited mass range of INMS (Perry et al., 2015). Biologically available nitrogen (nitrogen bearing compounds other than N_2) and salts (NaCl, $NaHCO_3$, Na_2CO_3, and potassium salts) have also been detected (e.g. Waite et al., 2006, 2009; Hansen et al., 2011; Postberg et al., 2011).

There are several avenues from which energy can be produced and made available to Enceladus's ocean, including hydrothermal, chemical, and geothermal processes. Silica spherules were identified by Hsu et al. (2015) in the E-ring. This discovery strongly supports a warm oceanic environment driven by hydrothermal reactions between the liquid and rocky core. The inventory of organic molecules and other oxidizable species identified by INMS (Waite et al., 2006, 2009) indicates that redox reactions are also a potential energy source. CIRS has observed that most of the 15 GW of thermal emission from the south polar terrain is localized on the "tiger stripes" (Howett et al., 2011), the ∼130 km long fissures (Nahm and Kattenhorn, 2015) from which the plumes erupt, though exactly what processes drive this geothermal activity is not yet clear.

Cassini has revealed Enceladus to be a world of true astrobiological potential with evidence for liquid water, chemistry, and energy. However, these results have only scratched the surface. We do not yet fully understand how the ocean is connected to the surface or what drives that activity. Hence, the extent to which sampling the plumes is equivalent to sampling the ocean is unclear. Nor do we know if and how Enceladus could sustain enough heat production to maintain an ocean. It is thus difficult to quantify the lifetime of this liquid reservoir, dramatically affecting which Earth extremophiles would be considered good Enceladus analogs. We do not have a complete inventory of higher order organics, heavy compounds, isotopes, or noble gases present in the plumes. Without this, it is difficult to thoroughly characterize what kind of environment the ocean represents and impossible to quantify whether life is presently at Enceladus. Therefore, we have yet to capitalize on the full scientific potential of sampling Enceladus's plumes.

The most exciting question surrounding Enceladus is whether extant life exists. We propose, however, that answering that question alone wouldn't give the complete picture of Enceladus's astrobiological potential. If life is there, what conditions support that biology? How long have conditions been suitable for this life to evolve? What Earth organisms are found in similar habitats? Or, if life isn't there, why not? Could it have been supported in the past? Did the environment change? Fully characterizing this ocean world to answer these fundamental questions about life and where it can develop or survive require a dedicated mission with the latest technology.

We therefore present here a concept study for a mission to Enceladus that would follow up on the discoveries of *Cassini*. This paper summarizes how a solar-powered Enceladus orbiter called THEO, Testing the Habitability of Enceladus's Ocean, could specifically determine the state of biologically favorable conditions and search for evidence of biological activity at the small moon. THEO is the result of the 2015 Planetary Science Summer School hosted by the Jet Propulsion Laboratory (JPL) at the California Institute of Technology, the purpose of which is to offer the participants an authentic but primarily educational experience of the mission proposal process. The concept mission was vetted during an intensive week of collaboration with JPL TeamX, resulting in a viable mission adhering to the 2009 New Frontiers

Announcement of Opportunity[1]. We report here our findings of this exercise, that important science (as identified by the planetary community[2]) is possible with a solar powered mission at Saturn, to contribute to the discussion of future missions.

In Section 5.3, we discuss the science mission of THEO, the hypotheses THEO would test and the data THEO would acquire to do so. We then describe the mission architecture (instrument payload, mission design, and spacecraft design) in Section 5.4 and include a discussion of key trades our team considered. Cost and risk assessment are detailed in Section 5.5 and we conclude with how Enceladus science can be accomplished with a medium class mission in Section 5.6.

5.3 Mission Goals

THEO would address unanswered questions that directly relate to establishing what kind of environment lies beneath Enceladus's icy crust. There are, of course, countless scientific objectives that *could* be investigated at Enceladus, but success as a medium-sized mission requires limiting our concept mission's scope. Therefore, the overarching theme of THEO seeks to characterize the Enceladus ocean and plumes to determine if lifeforms like those found on Earth could survive or evolve in such an environment. To do this, we must answer the following questions: (1) How are the plumes connected to the subsurface ocean? (2) Are the abiotic conditions habitable? (3) How stable is the ocean environment? and (4) Is there evidence of biological processes?

Figure 5.1 illustrates the direct connections between these four questions and the themes and areas of interest highlighted in the 2013 Decadal Survey. Our concept mission focuses on one goal: assessing Enceladus's habitability. However, as demonstrated by Figure 5.1, this one goal addresses many of the outstanding questions identified as important by the planetary science community.

The proposed mission design approaches the key questions with five instruments as the spacecraft would be equipped with a mass spectrometer, sub-mm instrument, camera, magnetometers, and a radio science instrument. Figure 5.2, the concept mission's science traceability matrix, describes the experiments that would be performed, expected observations from each instrument, and how the results address the mission's four fundamental questions.

The linchpin of THEO's mission strategy is providing context for all *in situ* sampling regimes. Proper interpretation of plume samples, including their implications for biological activity and the abiotic conditions of the reservoir, requires knowledge of how material from Enceladus's ocean is driven through the crust to the surface and whether any unique processes take place within the vents. To place these results in the proper timescale, we would investigate the stability of the ocean itself: why it is liquid now, and how it might remain so. By completing these objectives, THEO would form a more complete picture of whether Enceladus could support life.

This section further details how THEO would address each of the four key questions listed in Figure 5.2. We describe the proposed science experiments and the data produced, outlining how the results would allow us to discern between hypotheses and models relating to Enceladus's habitability.

[1]NASA Science Mission Directorate, New Frontiers Announcement of Opportunity 2009; Solicitation NNH09ZDA007O
[2]Vision and Voyages for Planetary Science in the Decade 2013-2022. National Academies Press, 2012.

Decadal Survey			THEO Key Questions			
Themes	Icy Satellite Questions (Ch. 8)		How are the plumes and subsurface ocean connected?	Is the abiotic environment suitable for life?	How stable is the ocean environment?	Is there evidence of biological processes?
Planetary Habitats- Searching for the requirements for life	What are the processes that result in habitable environments?	Is there evidence for life on the satellites?		X		X
		Where are the subsurface bodies of liquid water located, and what are their characteristics and histories?	X	X	X	X
		What energy sources are available to sustain life?		X	X	
Building New Worlds- Understanding solar system beginnings	How did the satellites of the outer solar system form and evolve?	What were the conditions during satellite formation?	X		X	
		What determines the abundance and composition of satellite volatiles?	X	X	X	X
		How are satellite thermal and orbital evolution and internal structure related?	X		X	
		What is the diversity of geologic activity and how has it changed over time?	X		X	
Workings of the Solar System - Revealing planetary processes through time	What processes control the present-day behavior of these bodies?	How do active endogenic processes shape the satellites' surfaces and influence their interiors?	X		X	

Figure 5.1: Relationship between THEO data and the 2013 Decadal Survey. THEO's main goal, of establishing the habitability of Enceladus's ocean, directly addresses the planetary habitats theme. However, the data from THEO would also address questions from at least two other themes of the 2013 Decadal Survey.

Theme	Science Questions	Science Tasks	Science Measurements	Instrument	Deliverables
Is Enceladus habitable?	1. How are the plumes connected to the subsurface ocean?	A. Determining the relative abundance of phases of water in the plumes	Ice particle abundance: constrained by images over 200 orbits at 500 km	DRIPS (Camera)	images of plumes with <10 km/px spatial resolution
			Water vapor abundance: constrained by spectral radial profiles over 200 orbits at 500 km	WAVES (Sub-mm)	spectral line strength of the H216O molecular transition at 556936.002 MHz with spatial resolution 1.1 km
		B: Constrain the thermochemical conditions at the vent source	Evidence of larger-chain (>C3) organics in the vapor phase in 300 orbits at 30 km	SWAMP (Mass Spectrometer)	mass spectra with mass range 36:1000 amu with 1 amu sensitivity
			Measurement of surface temperature at the fracture zones in 300 orbits at 30 km and 30 orbits at 100 km	WAVES (Sub-mm)	radiometric measurements of brightness temperature in mm/sub-mm continuum channels with sensitivity < 1K, spatial resolution 692/217 m at 100 km and 207/65 m at 30 km
			Plasma environment near plume the plume by time sampling of 1Hz for 600 orbits 30km	OSMOSIS (Magnetometer)	three component B field with 1.0 nT field strength resolution; fed into fluid models for ion flux derivation
		C: Constrain the temperature of the internal ocean	16O/17O/18O isotope ratios constrained by spectral radial profiles over 200 orbits at 500 km	WAVES (Sub-mm)	spectral line strengths of the H216O H217O H218O molecular transitions at 556936.002 MHz, 552020.960 MHz and 547676.440 MHz respectively
			Abundances of volatiles CO2, CO, H2O, CH4, N2, NH3, and OH from samples over 200 orbits at 500 km, 30 orbits at 100 km, and 300 orbits at 30 km	SWAMP (Mass Spectrometer)	mass spectra with mass range up to 44 amu with 30,000 M/dM
		D: Determine the rate of transport of vapor and particles from the subsurface ocean to the surface	Physical distribution of plume particles from high phase images of the plume over 200 orbits at 500km	DRIPS (Camera)	images of plumes with <20 km/px spatial resolution
			Mass flux of vapor from spectral radial profiles over 200 orbits at 500 km	WAVES (Sub-mm)	spectral line strength of the H216O molecular transition at 556936.002 MHz with spatial resolution 1.1 km at 500km
		E: Determine the chemical and physical mechanisms driving plume material transport	Ice particle abundance and extent as a function of orbital position in observations of plume at increments of 4 deg of mean anomaly at 500 km	DRIPS (Camera)	images of plumes with <20 km/px spatial resolution
			Vapor abundance and extent as a function of orbital position from observations of plume at increments of 4 deg of mean anomaly at 500 km	WAVES (Sub-mm)	spectral line strength of the H216O molecular transition at 556936.002 MHz with spatial resolution 1164 m at 500km.
			Abundance of gas species CO2, N2, CO, CH4, NH3, and H2O by vapor sampling 300 orbits at 30 km, 30 orbits at 100 km, and 100 orbits at 500 km.	SWAMP (Mass Spectrometer)	mass spectra in mass range up to 44 amu with 30,000 M/dM
	2. Is the abiotic environment suitable for life?	A: Determine the pH of the subsurface ocean	Abundance of CO2 constrained by vapor sampling over 300 orbits at 30 km, 30 orbits at 100 km, and 100 orbits at 500 km	SWAMP (Mass Spectrometer)	mass spectra with 30,000 M/dM sensitivity
			Temperature of the plume source by mapping the brightness temperature in 300 orbits at 30 km and 100 orbits at 500 km	WAVES (Sub-mm)	radiometric measurements of brightness temperature in both mm & sub-mm continuum channels with sensitivity < 1K
		B: Determine the salinity of the subsurface ocean	Abundance of Na, Cl, K, N determined from vapor sampling over 300 orbits at 30 km	SWAMP (Mass Spectrometer)	mass spectra with 30,000 M/dM sensitivity
			Conductivity of the subsurface ocean from sampling magnetic field at a rate >5,000 samples/sec in 30 orbits at 30 km	OSMOSIS (Magnetometer)	Three component periodic B field with 1.0 nT resolution.
		C: Determine the state of hydrothermal activity of the subsurface ocean.	Relative abundances of noble gases 40/38/36Ar, 4/3He, 20/22Ne, Kr, 128-136Xe via vapor sampling regime Relative concentrations of N, NH3, HCN via vapor sampling regime	SWAMP (Mass Spectrometer)	mass spectra with >5,000 M/dM sensitivity
			Resolve D/H and 16O/17O/18O isotope ratios from spectra of resolution of v/δv ~ 10^7	WAVES (Sub-mm)	spectral line strengths of the H216O H217O H218O molecular transitions at 556936.002 MHz, 552020.960 MHz and 547676.440 MHz respectively
	3. How stable is the ocean environment?	A: Determine the extent and thickness of Enceladus' liquid ocean	Longitudinal extent of librations due to 1.37 day and 3.7 year perturbations detected in surface images	DRIPS (Camera)	Images of the limb with <15 m/px spatial resolution
			Conductivity of the subsurface ocean constrained by magnetic field sampling sampling at 1 Hz in 30 orbits at 30 km	OSMOSIS (Magnetometer)	Three component periodic B field with 1.0 nT resolution.
		B: Constrain the radial structure of Enceladus' interior and the magnitude and spatial distribution of tidal dissipation within the ice shell	Moment of inertia, tidal love number, and quality factor derived from Doppler tracking of spacecraft to determine gravity field to degree 4+ in 30 orbits at 30 km	GEISER (Radio Science)	Deviations from nominal orbital path determined to the 10^-5 m/s resolution
			Determine non-hydrostatic part of gravity field in 30 orbits at 30 km		
		C: Determine the thermal history of the ice shell to constrain the longevity of the subsurface ocean	Radiometric temperature of the near tiger-stripe terrain from radiance temperature maps from 100 km and 30 km	WAVES (Sub-mm)	radiometric measurements of brightness temperature in both mm & sub-mm continuum channels with sensitivity < 1K and resolution 692 & 218 m/pix at 100 km and 208 & 65 m/pix at 30 km
			Measure the relaxation of simple craters in the near-SPT terrain from images over 300 orbits at 30 km	DRIPS (Camera)	topographic map with ~10m vertical resolution and 10 m/px spatial resolution
	4. Is there evidence of biological processes?	A: Determine resources available for biological processes, including those necessary for redox	Abundances of C,H,N,O,P,S and shorter chain organics constrained by vapor sampling in 300 orbits at 30 km	SWAMP (Mass Spectrometer)	mass spectra with 30,000 M/dM sensitivity
			CH3D abundance constrained by vapor sampling in 300 orbits at 30 km, 30 orbits at 100 km, and 100 orbits at 500 km.		
		B: Determine whether the isotopic ratio of C is indicative of biological processes	Relative abundances of 12C and 13C by vapor sampling constrained by 300 orbits at 30 km, 30 orbits at 100 km, and 100 orbits at 500 km	SWAMP (Mass Spectrometer)	mass spectra with 30,000 M/dM sensitivity
		C: Distinguish biomarkers present in the plumes and determine their abundances	Abundances of amino acids, lipids, and nucleic acids constrained by sampling over 300 orbits at 30 km		

Figure 5.2: The science traceability matrix for the proposed mission. This table lists the science mission theme and questions, the supporting experiments, and what data would be produced to answer the questions.

5.3.1 How are the plumes connected to the subsurface ocean?

Unlike other icy satellites with subsurface oceans whose thick crusts prohibit direct sampling with today's technology, Enceladus's plumes offer the unique opportunity for *in situ* exploration from orbit. In order to take full advantage of the plumes, however, it is necessary to identify the mechanisms that transport ice grains and vapor from the ocean to the surface. Understanding this plume-ocean connection would allow us to disambiguate any compounds that are a byproduct of or altered during transport when interpreting plume composition.

Several hypotheses have been put forth to explain how the water is delivered from the subsurface ocean to the surface. For example, the thermodynamic model of Bouquet et al. (2015) predicts that clathrates at the ice/ocean boundary of Enceladus's subsurface could participate in plume mechanics. Other models employ an equilibrium boundary between the liquid reservoir and ice grains and vapor at the bottom of the fractures (Schmidt et al., 2008; Porco et al., 2014). Because the vent structure, wall temperature, and gas densities are largely unknown, the predictions of the plume mechanics models for observable quantities– such as the abundances and velocities of ejected ice and vapor– vary. Thus, the THEO mission would address the connection between plume and ocean by measuring the ice-vapor ratio, the chemical composition of the vapor, the spatial distribution and velocities of plume ice grains, and the structure and temperature of the plume vents.

The ice-vapor ratio of the plumes is a function of the eruptive process. Clathrate decomposition predicts smaller ratios while equilibrium at a liquid boundary would result in higher ratios. Results from *Cassini* for the ice-vapor content in the plume are inconclusive; the ratio has been reported as 0.42 (Porco et al., 2006), 0.21 (Kieffer et al., 2009), and 0.35-0.71 (Ingersoll and Ewald, 2011). (See Ingersoll and Ewald (2011) for a comprehensive discussion of the different analyses.) The camera and sub-mm instrument onboard the THEO spacecraft would capture concurrent images and spectra of the plumes. These combined data sets would yield a more precise measurement of the ice-vapor abundance than has been possible with *Cassini*. Furthermore, the mission design includes repeat coupled observations, ensuring that any spatial and/or temporal differences in the abundance could be observed. Thus, by measuring the ice-vapor ratio and comparing spatial and temporal column abundances, THEO would help identify the mechanism driving Enceladus's eruptions.

Vent models rely on the observed plume characteristics (e.g. velocity and size distributions) to investigate rates and mechanics of transport from ocean to surface. For example, vents with smaller volume relative to the surface area in contact with the ocean would erupt gas with higher velocities (Spitale et al., 2015). The velocities of the vapor have been estimated by fitting UVIS data (Hansen et al., 2006; Tian et al., 2007) to be ∼300-500 m/s. Schmidt et al. (2008) used these values (and other parameters) to model vapor condensation and particle growth within the vents. THEO would provide better constraints to such investigations by conducting direct, repeat measurements of the vapor velocity with the sub-mm instrument, which is sensitive to the Doppler shift of the H_2O spectra.

The spatial distribution of the plume material also reflects the plume-ocean connection. Discrete jets, for example, are inconsistent with a brittle ice shell, while curtain-like eruptions would be indicative of a deep reservoir with a surface area of liquid to chamber ratio large enough to allow the particles and gas

enough time to interact (Spitale et al., 2015). Jets of high velocity ejecta have been documented in ISS data by Porco et al. (2006); Hansen et al. (2006); Spitale and Porco (2007); and Hansen et al. (2008). UVIS observations have also been interpreted as observing discrete areas of higher water density when compared to the broader plume (Hansen et al., 2011). Recently, however, a jets-only interpretation was questioned by Spitale et al. (2015) who reproduced ISS images of the backlit plumes by modeling plume material as curtains of particles and vapor. These authors argued that the fine structure of a plume curtain can appear as discrete sources in superposition. By taking high phase images of the plumes taken over hundreds of orbits, THEO would be able to map the physical structure of the plumes in higher spatial and temporal detail, allowing the research community to discern between jet- or curtain-like eruptions. Two hundred observations, taken at ∼100 m resolution at about the same time of year as the data analyzed by Spitale et al. (2015), would represent a seven-fold increase in data over that produced by *Cassini* thus far. Additionally, as Hedman et al. (2013) observed a correlation between plume brightness and predicted tidal stresses, these images would be spread over various points along Enceladus's eccentric orbit. Different models (e.g. Běhounková et al., 2015) for the size and structure of plume vents predict different responses to time-varying tidal stresses.

The composition of the plumes could also be constrained by THEO's magnetometer. The deceleration and deflection of the impinging magnetospheric plasma near the plume of Enceladus leaves a measurable imprint on the magnetic field configuration (Dougherty et al., 2006). Numerical simulations have already been generated to study this behavior (Saur et al., 2008). Indications to the quantity and behavior of both ions and neutrals near the plume have been made by comparing these simulations with *Cassini* magnetometer data (Kriegel et al., 2011; Simon et al., 2011). Data from THEO's magnetometers could be used to better characterize these complex interactions with the magnetic field. The B field components (as a function of time and space) are an important input into models like that of Kriegel et al. (2011) that predict quantities and behavior of ions and neutrals near the plume. These models, in turn, would better our understanding of plume composition and dynamics, necessary for putting other sampling results in the context as either unique to plumes or reflective of the subsurface ocean.

While characterizing the content and structure of the plumes themselves, THEO would also investigate the locations from which the plumes erupt. The temperature of the fissures where the plumes originate is a critical parameter in models describing the system. For example, Ingersoll and Pankine (2010) and Goguen et al. (2013) predict mass loss rates and calculate radiated power based on observed surface temperatures, the most precise of which comes from a single, high-resolution measurement by *Cassini* VIMS. These data estimate a vent temperature of 197 ± 20 K. To discern the thermal budget at the plume source, THEO's sub-mm would map the brightness temperature of the south polar terrain with thermal resolution < 1K at a best spatial resolution of 217 m. At this resolution, THEO would not resolve the width of individual vents, which are likely on the order of ten meters (Goguen et al., 2013), but would complement the CIRS data set (Howett et al., 2011) with similar, if not better, resolution and temperature sensitivity, as well as providing temporal context not possible with *Cassini* data. Measurements taken by THEO would greatly improve the results of thermodynamic modeling by more accurately determining the temperature, monitoring any change over time, and quantifying differences and similarities between fissure temperatures.

The temperature of the ocean is also a critical parameter for thermal modeling the ocean-to-plume vents. An inventory of volatiles like CO_2, CO, H_2O, CH_4, N_2, NH_3, and OH can illuminate conditions at this boundary. The relative abundances of these species indicate the chemical equilibrium at the ocean which depends on temperature. For example, the detection of SiO_2 by Hsu et al. (2015) suggests that geothermal activity at the ocean-core boundary drives hydrothermal reactions and that thermally buoyant liquid may interact there. The abundances of numerous other species in the subsurface ocean, including hydrocarbons, ammonia, methane, carbon dioxide, carbon monoxide, and nitrogen, are also determined by temperature (Matson et al., 2007). Oxygen isotopes can also indicate thermal conditions of the ocean as high temperatures favor the formation of certain oxygen-bearing minerals, leading to relatively depleted levels of ^{18}O in the water vapor produced at the plumes. THEO would be able to address each of these factors using the mass spectrometer and sub-mm instruments. The mass spectrometer would determine abundances for the above mentioned species at three altitudes– heavier species are thought to fall out of the plume faster, necessitating measurements at high-and low-altitudes to generate a more complete picture of plume composition (Perry et al., 2015). The sub-mm instrument would take spectra at sufficient resolution to distinguish between the oxygen isotopes ^{16}O, ^{17}O, and ^{18}O.

With the data provided by the experiments outlined here– namely, quantifying the abundance and distribution of the plume constituents and the thermal budget of the vents– thermodynamic models would be able to more accurately explain the behavior of the plumes and predict what alteration might occur during the journey from ocean to surface. Defining precisely how sampling the plumes is related to sampling the ocean would be a crucial insight from the THEO mission. Without it, it would be difficult to determine the habitability of the ocean from the remainder of our experiments that rely on interpreting samples gathered from the plume.

5.3.2 Is the abiotic environment suitable for life?

Here on Earth, organisms have been found to inhabit a broad range of environmental conditions– e.g. pH, salinity, and temperature. Quantifying these abiotic characteristics of the ocean environment is therefore necessary for understanding what kind of life might evolve or survive in Enceladus's subsurface ocean or why terrestrial-like lifeforms cannot. These characteristics also reveal the possible thermal, chemical, and geological processes at work under Enceladus's icy crust.

pH indicates the acidity or alkalinity of the aqueous environment. While most biological processes take place at circum-neutral pH (5-8), there are unicellular organisms that thrive in highly acidic environments (pH<1) and others that prefer very basic environments (pH>9) (Rothschild and Mancinelli, 2001). Current estimates of the pH of Enceladus's subsurface ocean are between 5.7 and 13.5 (Zolotov, 2007; Postberg et al., 2009; Marion et al., 2012; Glein et al., 2015; Hsu et al., 2015) and were derived from modeling the thermodynamics of species observed in the plumes and E-ring particles by *Cassini*. This range is too large to constrain the ionic potential of the ocean or the sort of life that might inhabit it.

Two important inputs for thermodynamic modeling of the ocean's pH are the amount of dissolved CO_2 and the temperature. The amount of CO_2 dissolved in the ocean affects its acidity; increasing

the effective concentration of CO_2 available for reactions decreases pH. The concentration of CO_2 in the plumes– and, hence, in the ocean– is thus a critical indicator of chemical potentials in the ocean. Bouquet et al. (2015) and Glein et al. (2015) use only data from low-velocity flybys of *Cassini* (a few km/s) to fit the mixing ratio of CO_2 to H_2O at 0.006 ± 0.00016 as these measurements are thought to give more accurate gas compositions (Waite et al., 2009; Glein et al., 2015). With even lower orbital velocities (between 126-206 m/s), THEO would thus create mass spectra of higher fidelity than any previously obtained. pH is also a temperature-dependent variable, so pH models depend on the ocean temperature and the surface temperature of the vents. Combined with maps of surface temperature from our sub-mm radiometric data, THEO would pave the way for more accurate calculations of the pH of Enceladus's ocean, and therefore a better understanding of what kinds of life might inhabit it.

The ocean's salt inventory also provides important insights into biological and geochemical activity. Salts often provide the ions necessary for transportation across cell membranes, but high salinity solutions may negatively impact microbial metabolic processes (Stevenson et al., 2015). The salinity of Enceladus's subsurface ocean will therefore determine the range of habitable conditions and the types of microorganisms that could evolve there (e.g. Norton and Grant, 1988; Rothschild et al., 1994; Kamekura, 1998; Seckbach, 2013). Salt content also indicates which rock-water interactions occur. Of particular interest is hydrothermal activity as it affects the temperature of the ocean and can constrain the amount of dissolution and precipitation taking place at the water-rock boundary. *Cassini*'s CDA has observed salt-rich ice particles in the E-ring (Postberg et al., 2009) and in the plumes (Postberg et al., 2011). Ground-based observations constrain the salt content in the plume vapor to be at most $0.5\text{-}1.0 \times 10^8$ atoms/cm^2 (Schneider et al., 2009). THEO's mass spectrometer would establish the amount of sodium in the vapor with multi-altitude sampling and temporal context to provide more accurate inputs for the Enceladus interior models.

Indirect evidence of the ocean's salinity is also obtainable with THEO's magnetometers. The saltiness of the ocean relates directly to its conductivity, a key parameter of the induced electric and magnetic fields that form as Enceladus orbits Saturn. Because Saturn's magnetic field is aligned with its spin axis, the variations in Saturn's magnetic field are not as dramatic as those at Jupiter. Any induced fields at Enceladus would thus be different from those those observed at Jovian ocean worlds (e.g. Kivelson et al., 1997). The precision and quantity of data collected by THEO's proposed orbiting magnetometer would be sufficient to constrain the induced magnetic field and predict the conductivity, and thus salinity, of the ocean.

Hydrothermal alteration, with its associated implications for the ocean's temperature, can also be inferred from the abundances of radiogenically-derived isotopes in the plumes. Enrichment in ^{40}Ar, for example, would indicate that hydrothermal activity has persisted for sufficiently long times to allow the isotope to leach from the rock. Unfortunately, ^{40}Ar was not well resolved by *Cassini* (Waite et al., 2009). THEO's mass spectrometer would be able to identify the isotopic ratios of noble gases, especially ^{40}Ar/^{38}Ar/^{36}Ar, Kr, ^{4}He/^{3}He, ^{22}Ne/^{20}Ne, ^{128}Xe/^{136}Xe. These improved measurements would constrain what hydrothermal activity occurs at the water-rock boundary.

Hydrogen and oxygen isotopes can also be used to search for evidence of hydrothermal alteration. The relative abundance of deuterium in methane and oxygen isotopes in carbon dioxide isotopologues

is affected by whether the species are produced via serpentinization, the addition of water into the rock structure (Mousis et al., 2009). The mass spectra compiled by THEO's mass spectrometer would be sensitive enough to distinguish between D/H isotopes in CH_4 and oxygen isotopes in CO_2, thus shedding light on whether abiotic processes play a role in the formation of molecules of biological interest. The proposed sub-mm data would be able to determine the D/H ratio. Combined with radiogenically-derived isotope measurements, THEO would thus provide two independent means of investigating whether hydrothermal activity occurs at the water-rock interface.

Finally, the abundance of molecular hydrogen in the plumes can also be used to infer the state of hydrothermal reactions. Hydrothermal systems like Earth's Lost City (Kelley et al., 2001) are rampant with molecular hydrogen as a byproduct of several serpentinization reactions (Kelley et al., 2005). It is difficult to discern molecular hydrogen in the mass spectra of INMS as the source of molecular hydrogen detected is degenerate: it is unclear to what extent the mass abundance observed is from the material sampled in a given flyby is affected by H_2O interacting with the titanium of the instrument walls (Perry et al., 2015). The mass spectrometer on-board THEO would conduct sampling at high enough resolution to resolve the abundance of H_2 without the complication of water-titanium interactions, thanks to low relative velocity sampling. The observed value could be compared to models (e.g. Glein et al., 2016) that predict the production rate of H_2 as a function of geochemical and geophysical conditions.

THEO's inventory of molecules and isotopes present in the plumes would also shed light on the thermal conditions in the ocean. Because NH_3 depresses the freezing point of water, its abundance in the plume vapor (as well as that of N_2, a decomposition product of NH_3) would offer another constraint on the ocean temperature (Matson et al., 2007; Waite et al., 2009; Sekine et al., 2015). Another example of how species abundances can provide constraints on the temperature of the ocean is studying the HCN abundance. HCN quickly reacts in warm water to produce formic acid and ammonia, the rate of which is in part a function of temperature (Miyakawa et al., 2002). Thus, as noted by Waite et al. (2009), comparing the abundances of HCN and N_2 can shed light on whether this kind of reaction is happening now or happened in the past.

Together, THEO's investigation of abiotic environmental factors like acidity, salinity, and temperature would improve the current characterization of Enceladus's ocean by reducing uncertainties on these parameters that are presently too large to make definitive statements on habitability. While characteristics like pH, salinity, and temperature are not tell-tale signs of life, these data would constrain which analog terrestrial environments could guide the search for bio-signatures at Enceladus (Preston and Dartnell, 2014). Understanding the present conditions of the ocean is also an essential starting point for investigating whether Enceladus's ocean maintains these conditions and thus over what timescales life might have to evolve.

5.3.3 How stable is the ocean environment?

Critical to the habitability of Enceladus's ocean is its longevity. The energy source powering geologic activity on Enceladus has been investigated since *Voyager* revealed a young surface on the small moon (Smith et al., 1982), but *Cassini*'s discovery of the plumes has exacerbated the problem. The observed heat flux from the south polar region is significantly greater than predicted by models for Enceladus's

evolution. *Cassini* CIRS measurements indicate that the endogenic power of the south polar terrain is 15.8 ± 3.1 GW (Howett et al., 2011). Radiogenic heating, however, is estimated to provide only 0.3 GW (Schubert et al., 2007) and tidal heating has not yet been shown to accommodate the difference. Several models have been proposed to explain the discrepancy between observed and predicted heat flux such as episodic activity at Enceladus with alternating periods of net energy accumulation and expulsion (e.g. Běhounková et al., 2012; Spencer and Nimmo, 2013). Before firm predictions can be made, however, more information is required. Understanding the energy sources powering Enceladus's plumes and maintaining its ocean is necessary for determining the ocean stability. This in turn provides context for any biological findings, or lack thereof (perhaps the ocean hasn't been liquid long enough for life to evolve, etc.). To this end, THEO would conduct imaging, thermal mapping, and radio science campaigns over the south polar terrain to explore ice shell properties as they relate to heat production and the current extent of the liquid ocean.

A variety of mechanisms have been put forth to explain Enceladus's heat flux. Decoupling the ice shell from the silicate interior, for example, increases the amount of heat generated by tidal dissipation (Roberts and Nimmo, 2008a; Tobie et al., 2008; Běhounková et al., 2010). Iess et al. (2014) found a gravitational anomaly at the south pole consistent with a large body of liquid that would decouple the south polar terrain, while recent work by Thomas et al. (2016) identified evidence of librations (longitudinal oscillations of the surface) in the ISS data set that are consistent with a fully decoupled ice shell. These results were surprising considering calculations that a global ocean would freeze in 100 Myr without transient heating events (e.g. Roberts and Nimmo, 2008b). Thomas et al. (2016) were able to place an upper bound on the amplitude of the libration, but greater imaging resolution is required to fully constrain the libration and therefore the structure of the ice shell and extent of the ocean layer. THEO would address this need through imaging observations. Rambaux et al. (2010) predict minimum libration amplitudes on the order of 100 m in the case of full ice-rock coupling, with significant increases in amplitude if the ice shell is fully decoupled. Such amplitudes would be measurable by comparing observations from THEO's camera. Thus, the mission would be capable of confirming the existence of a global ocean and better constraining its structure and the ocean lifetime.

The thermal history of the ice shell can also be explored through its rheology. Consider a warmer, less-viscous shell. It is more likely to undergo convection and cool rapidly, but a less-viscous ice shell dissipates more tidal energy to heat the interior. THEO would distinguish between these different possibilities with a variety of methods. Topographic maps would be derived from high-resolution stereo imaging of Enceladus's south polar terrain. These maps would facilitate models of viscous relaxation of observed features that would provide a proxy for the viscosity of the ice shell and thus its thermal history. For example, Bland et al. (2012) examined crater relaxation in two regions of Enceladus's northern hemisphere and found that the viscous relaxation indicated an average heat flux of 150 mW/m^2. Barr and Preuss (2010) estimated the age and viscosity of a folding layer in the south polar terrain from the fold wavelength, but the scope of that study was limited by the available image resolution. THEO's images (with a best spatial resolution of 10 m/pixel) would be used to validate these estimates and investigate whether shorter wavelength folds are present. Thus, THEO's proposed image data set would allow exploration of the spatial and, in some cases, temporal evolution of the thermal budget of Enceladus's ice shell,

illuminating the conditions contributing to maintaining Enceladus's ocean.

Finally, geophysical properties such as moment of inertia, tidal Love number, and quality factor are integral to determining the thermal budget of Enceladus. The tidal Love number and quality factor are important parameters required for modeling tidal dissipation, but are not well constrained for Enceladus, leaving the amount of heat generated by tidal dissipation a crucial unknown. Precise measurement of the moment of inertia, for example, would reveal the size and density of the core. A low density core made of hydrated silicates, for example, could suggest that heat-producing ^{40}K leached into the overlying ocean (e.g. Engel et al., 1994). Additionally, determining the hydration state of the core would provide major constraints on whether rock is currently available for hydrothermal reactions. (e.g. Glein et al., 2016).

Mass distribution within Enceladus can be explored via radio science. Variations from a uniform distribution affect the moon's gravity field, slightly perturbing the spacecraft's orbital velocity. These Doppler shifts are measurable by tracking the signal from the spacecraft's high gain antenna with the Deep Space Network. As *Cassini* could only conduct flyby observations, the current estimate for Enceladus's gravity field is determined to degree 3 (Iess et al., 2014). Spacecraft interactions with the plume and the lack of spherical symmetry of Enceladus complicate the interpretation of gravity data. But because THEO would be an orbital mission, the frequency and coverage of measurements would complement and improve our understanding of Enceladus's gravity field to at least degree 4. Additionally, frequent measurements of the plume gas velocity by the sub-mm instrument and density by the camera would better constrain the neutral particle drag on the spacecraft, making derivations of the changes in the spacecraft's line-of-sight velocity more accurate. Solving for a higher degree, more precise gravity field would provide more accurate parameters to models like those of Iess et al. (2014) and Baland et al. (2016) which produce estimates for the tidal Love number, quality factor, and principal moments of inertia.

By quantifying the ice shell characteristics and thermal flux at unprecedented resolution in space and time, THEO could offer a better understanding of just how long the ocean has been and will remain liquid. This is a critical parameter for putting the results of biological and environmental ocean characterization into context. First, as Enceladus is one of several icy ocean worlds in our solar system, these findings would be of interest with respect to formation timescales of other potentially habitable oceans, such as at Europa or Titan. Second, if THEO were to detect life, constraining the time scale of Enceladus's ocean offers an important comparison with how long it took life to evolve on Earth. Or, if we do not detect any biomarkers, the stability of the ocean might explain such an important, albeit null, result.

5.3.4 Is there evidence of biological processes?

Evidence from *Cassini* suggests that Enceladus is a good candidate for a habitability study, but these data cannot reveal if Enceladus is currently inhabited. A new mission is required to search for evidence of biological processes. With improved resolution and sensitivity, the THEO mass spectrometer would be able to follow up on the insights gained from INMS to do exactly that. THEO has several experiments to test for biological activity, including identifying the presence of biomarkers in the vapor and the relative abundances of C, H, N, O, P, S, organics, and C isotopes.

Some of the simplest biomarkers for terrestrial life are amino acids, lipids, and nucleotides. These polymers are essential for biological processes and their presence within the plumes would be strong

evidence for life within Enceladus's ocean. These biomarkers are also extremely large, with masses of over 100 amu (∼100 amu for amino acids, > 200 amu for lipids, and > 400 amu for nucleotides). *Cassini*'s INMS is only sensitive up to 100 amu and therefore unable to resolve any of these biomarkers. THEO's mass spectrometer, sensitive to masses > 1000 amu, would not only detect the mass signature of amino acids, lipids, and nucleotides, but also distinguish them from other macromolecules, if they are present.

For THEO to sense these polymers, however, they must be present in the vapor component of the plumes. As of yet, there is no evidence to exclude the possibility of complex organics in the vapor. Recently, however, the mass signatures in CDA data indicate the presence of these target molecules in the ice grains (Postberg, 2015). With relatively slow orbital velocities, THEO would not have enough kinetic energy to break apart ice grains upon impact within the mass spectrometer as INMS did in several flybys (Perry et al., 2015). In Section 5.4.1.1, we discuss how to expand the sample range. However, if biomarkers are present in the plume vapor at the same abundances identified in meteorite samples (amino acids at 60 ppm; adenine, guanine, and uracil at 1.3 ppm in the Murchison meteorite (Cronin and Pizzarello, 1986)), the planned plume sampling (see Figure 5.5 and Section 5.4.2) would be sufficient to characterize their abundances.

Even if these "smoking gun" biomarkers are not observed, there are less direct lines of evidence that THEO could investigate. Life on Earth has developed using a small set of chemical building blocks: C, H, N, O, P, and S (McKay, 2004). Thus, in an environment with active biological processes, these "legos" are sequestered at greater concentrations in specific molecules than if only abiotic processes were responsible (McKay, 2004; McKay et al., 2014). Specifically, when abiotic processes are responsible, the distribution of the six elements would be more uniform across possible molecules. Consistently high abundances of bio-relevant molecules with C, H, N, O, P, and S would thus be evidence for Earth-similar life processes. Or, if other element combinations are found at high abundances within specific molecules, this may indicate biological processes analogous, not identical to, terrestrial biology.

Data from THEO would vastly improve the available inventory of material in the plume vapor. The mass spectrometer on-board THEO would catalog species of atomic mass between 0-1000 amu with 30,000 M/dM resolving power, a larger and therefore more complete sampling than presently available of the full range of species present in the plume. Species of larger masses than CO_2 and H_2O are more likely to be observed at the lowest observing altitude of our mission (30 km) at some <1% abundance (Waite et al., 2009) as mass is a driving factor in the distribution of ice grains in the plume (Perry et al., 2015). INMS observed species with as low as one in 10^6 abundance (Waite et al., 2006) during a flyby with closest approach to the plumes of ∼ 400 km. With 300 orbits near this altitude (500 km), THEO would collect data over the extent of the tiger stripes, the densest part of the plume (Waite et al., 2006) for over 430 hours. At the highest sampling rate, this would translate to over 10^8 samples. At lower altitudes not sampled by INMS, the density of the plumes is likely orders of magnitude larger. If plume density roughly falls off as $1/r^2$, at 30 km, water abundance should be on the order of $10^{20}m^{-3}$ and higher order organics observed by INMS would be at least $10^{14}m^{-3}$, well within the 1 ppb sensitivity of SWAMP.

To put the observed inventory of higher-order organics into proper context, it is necessary that THEO discern whether the observed species are biologically-derived products. We know that not all organics are the result of biology. A plethora of exotic, long-chained organic species are formed in the photolytic

processes of Titan's upper atmosphere, while Fischer-Tropsch synthesis and thermal degradation create methane from the decomposition of other organic material on Earth and elsewhere in the solar system (e.g. Hindermann et al., 1993; McCollom and Simoneit, 1999a; McCollom, 1999; Hill and Nuth, 2003). Biological methanogenisis has been proposed for the methane observed in Enceladus's plumes (McKay et al., 2014), though other works propose that the methane is thermogenic in origin (Matson et al., 2007). While not entirely conclusive (see, for example, the work of Allen et al. (2006) and Horita and Berndt (1999)), isotopes offer a potential means of distinguishing between the two processes. Work by McCollom and Simoneit (1999b), Sassen et al. (2004) and Proskurowski et al. (2008) demonstrates that abiotic processes produce a power-law relationship between the concentrations of C_1 relative to C_2+C_3 and the isotope ratio in CH_4. Biological and abiotic processes produce similar concentrations of C_1 isotopes, but orders-of-magnitude difference in the concentrations of higher-order C isotopes in methane.

Thus, an inventory of hydrocarbons of sufficient resolution to distinguish between C isotopes would inform our understanding of where Enceladus's methane comes from: abiotic chemical reactions, biotic processes, or a mixture of both. THEO's mass resolution would be sufficient to distinguish between $^{13}CH_2D$, $^{13}CH_4$, and CH_3D, as well as C and H isotopologues. The sub-mm instrument would also be able to distinguish between H isotopologues, enabling inter-instrument comparison in real time and adding redundancy and reliability to our science measurements.

Should any biomarkers be found in the plume vapor, these proposed experiments would offer the first direct evidence of another inhabited world in our solar system. However, even if amino acids, lipids, or nucleotides are not observed, THEO would constrain the likelihood of biological activity from isotope and C, H, N, O, P, and S abundances. These two results alone would address the very heart of one of the 2013 Decadal Survey themes: searching for the requirements for life and life itself.

5.4 Mission Architecture

The THEO mission architecture was designed via the concurrent systems engineering process of JPL TeamX that facilitates real-time trades between mass, power, volume, cost, and data transfer rates for mission development. Through this process, the JPL Planetary Science Summer School produces mission concept studies of similar caliber to competed missions. We developed an architecture for THEO that best enables the science goals described in the previous section. This New Frontiers class mission would include a five-instrument suite on a solar-powered bus and would conduct an altitude-dependent observing campaign during nearly 1000 orbits of Enceladus ($\sim$ 6 months).

5.4.1 Instruments

THEO's suite of instruments would conduct remote sensing and *in situ* experiments. The proposed mission design uses heritage instruments (hardware that has been proven on previous missions or has been selected to fly on missions in the near future) to reduce cost and development time. All estimates for cost, mass, and power are based on the heritage instruments, summarized in Table 5.1.

Acronym	Name	Instrument	Data (Gb)	Mass (kg)	Power (W)	Heritage
SWAMP	Space-borne Water Analysis by Molecule Pulverization	Mass spectrometer	12	15.3	50	MASPEX
WAVES	WAter Vapor Emissions Sub-mm	Sub-mm	6	22.9	59	MIRO
DRIPS	Dynamic Resolution Imaging of the Plumes and Surface	Camera	186	1.53	12	Malin Space Science Systems
OSMOSIS	Ocean Sensing Magnetometer Orbital Salinity Induction Science	Magnetometers	1	6.12	3	numerous
GEISER	Gravity Engaging Investigation Sensing Enceladus with Radio	Doppler tracking	-	-	-	numerous

Table 5.1: Summary of the proposed instrument suite of THEO. Each instrument would contribute to the science objectives via the tasks listed in Figure 5.2, but here we list the mission architecture characteristics of each.

5.4.1.1 Mass Spectrometer

The mass spectrometer, Space-borne Water Analysis by Molecule Pulverization (SWAMP), would measure element and isotope ratios as well as molecule abundances. SWAMP is modeled after MASPEX, the mass spectrometer selected for the Europa flagship and proposed as a part of ELF (Lunine et al., 2015). With an extended mass range (>1000 amu), mass resolution (>30,000 M/dM), and sensitivity (1 ppt), the capabilities of this instrument are sufficient to complete the science tasks of our mission. For comparison, *Cassini*'s INMS is sensitive to a mass range of up to 100 amu at 100 M/dM resolution. SWAMP thus represents a significant enhancement over the capability of our most recent exploration of Enceladus.

In situ sampling would be accomplished by flying THEO through the plumes with SWAMP pointed in the ram direction. In this orientation, vapor would fly into the open and closed sources of SWAMP before being ionized and directed towards the detector to record the time of flight. Because time-of-flight is a function of mass, the data would then be converted into charge versus mass distributions (e.g. Waite et al., 2004; Hässig et al., 2015) and used to determine abundances of elements and compounds of interest, including isotopic ratios.

In orbit, THEO would be able to take an unprecedented amount of data at three altitudes for a comprehensive sampling of the plume vapor content with a state-of-the-art, high resolution mass spectrometer. The relatively slow orbital velocities would remove the problems known to affect INMS of molecules dissociating within the instrument (Perry et al., 2015). However, this also means that the spacecraft does not have enough relative kinetic energy to passively break down, and thus sample, ice grains in the plume. Thus, SWAMP (as currently designed) is limited to sampling only the vapor component of the plumes. The instrument on which we based our mass spectrometer is not specifically equipped to actually "pulverize" ice grains in the plume, but modifications (such as the addition of a filament) may be added to actively break down ice grains before they enter SWAMP. Such modifications (or investigations into other modes of passive breakdown) were beyond the scope of this study, but we note that

this would be an important avenue for research to prepare for a THEO-like mission. Regardless, THEO's observing schedule is more than sufficient to resolve and characterize any salts, amino acids, and larger order hydrocarbons found in the plume vapor.

5.4.1.2 Sub-mm

The sub-mm instrument, WAter Vapor Emissions Sub-mm (WAVES), would analyze the water vapor content in the plumes at resolutions high enough to distinguish H and O isotopes. The instrument would be sensitive to the molecular transitions of H_2O isotopologues at 556936.002 MHz, 552020.960 MHz, and 547676.440 MHz. Additionally, this instrument is sensitive to Doppler shifts in water spectra, allowing for the determination of ice grain velocities in the plumes. WAVES is modeled after MIRO flown on Rosetta, a 30-cm diameter telescope and two receivers operating at frequencies of 190 GHz (1.6 mm, the "mm" component) and 562 GHz (0.5mm, the "sub-mm" component) (Gulkis et al., 2007). These components have 6.9 μrad and 2.1 μrad fields of view, respectively, in the spectra-collecting mode. WAVES data could be used to map the spatial extent and strength of the water content in plumes and thus be used to derive vapor content and velocity. Based on the spectral resolving power of MIRO ($2x10^6$, Gulkis et al. (2007)), WAVES should be able to resolve differences in ice grain velocities on the order of 200 m/s, similar to estimates of the bulk vapor velocity (300-500 m/s, Hansen et al., 2006; Tian et al., 2007) and twice that for ice grains (80-180 m/s, Hedman et al., 2009) derived from VIMS data, though this observed range is not sensitive to larger velocities due to the resolution and field of view.

In the thermal mapping mode, WAVES would measure the thermal emission of the south polar terrain at 218 m/pixel (orbiting at 100 km) and 65 m/pixel (at 30 km) and cover the entirety of the south polar terrain with $<$ 1K resolution. Blackbody emission curves would then be fit to the data to derive temperature maps and heat production rates. The thermal maps would be two orders of magnitude higher resolution than those made by *Cassini* CIRS, which covered the entire south pole at 6-10 km/pixel at $\pm$ 20 K.

5.4.1.3 Camera

The Dynamic Resolution Imaging of Plumes and Surface (DRIPS) is THEO's camera, the proposed roles of which include both science tasks and optical navigation. With a design based on previous cameras produced by Malin Space Science Systems, DRIPS would collect data essential to determining the plume ice-vapor ratio, constraining libration amplitudes, and investigating the thermal history of the ice shell. By imaging the plumes at high phase in the visible band at an order of magnitude higher resolution than possible with ISS, THEO would create a data set of radiance images that would be converted to I/F maps. Porco et al. (2006) and Ingersoll and Ewald (2011) have demonstrated that the scattering at visible wavelengths from the plume ice grains with a mean radius of 3.1 $\pm$ 0.5 μm (Ingersoll and Ewald, 2011) is sufficient to inverse model the reflectance as a function of particle size-frequency distribution, yielding the column abundance. *Cassini* measured the total mass of the plume to be 1.45 $\pm$ 0.5 $x10^5$kg (Ingersoll and Ewald, 2011). By increasing the integration time and optimizing the phase angle (which is possible with the large number of planned observations), THEO would be capable of detecting a plume many orders of magnitude less massive than observed by *Cassini.*

These data, taken at a spacing of about 4° true anomaly, also represent an improvement in the frequency of observation to characterize plume particle distribution dependence on Enceladus's eccentric orbit. While observing at 30 km, the camera would map the south polar terrain up to 50°S with 10 m/px spatial resolution. *Cassini* ISS created regional maps of 110 m/pixel, with select south polar terrain images at up to 7 m/pixel. Repeat imaging with DRIPS would be used to generate stereo maps of the surface with up to ∼10 m vertical resolution (on the order of the vertical resolution of ISS, but with more complete coverage of the south polar terrain). These data sets would be used to identify librations of the surface and investigate surface geology.

5.4.1.4 Magnetometers

Ocean Sensing Magnetometer Orbital Salinity Induction Science (OSMOSIS) includes two magnetometers, each located at the end of a solar array wing. These instruments would measure B fields in the Enceladus environment by sampling at a rate of 1 Hz. OSMOSIS would determine the three component periodic magnetic field with 1.0 nT resolution, a significant improvement over *Cassini* MAG in terms of resolution (40 nT) and spatial and temporal frequency of data collection (30 orbits of data with OSMOSIS; 22 flybys with MAG). Processing these data would disambiguate unique fields of the Enceladus environment, such as those of plume interactions and the conducting ocean. The strengths of these components could then be used to determine the conductivity and depth of Enceladus's ocean as well as serve as important inputs to fluid models that predict the ion flux in the plumes (Kriegel et al., 2011).

5.4.1.5 Gravity Science

As used on many missions, THEO's high gain antenna (HGA) would also serve as a science instrument by conducting Doppler tracking of the radio signal during contact with the Deep Space Network and is thus known as Gravity Engaging Investigation Sensing Enceladus with Radio (GEISER). The data taken during these experiments would include line-of-sight velocity changes with precision 10^{-5} m/s from which the gravity field could be derived. Despite having the same absolute precision as *Cassini*, THEO would be roughly an order-of-magnitude more sensitive to velocity perturbations induced by Enceladus because of its relatively slow orbital velocities. For example, the velocity perturbations associated with the degree-3 zonal harmonic coefficient J_3 are estimated as 6 mm/s at an orbital altitude of 100 km, compared to 0.2 mm/s during a *Cassini* flyby (Iess et al., 2014). While the HGA's operations role would be continuous through the mission, we only list those orbits when the instrument would be used for its scientific tasks in Figure 5.5.

5.4.2 Mission Design

The THEO spacecraft would launch on an Atlas V 541. As a Jupiter gravity assist was not available during the proposed timeframe of the mission (summarized in Figure 5.3), the spacecraft would first complete an inner solar system tour, summarized in Figure 5.3, to gain the necessary Δv to reach Saturn's orbit. The suggested flight path includes one gravity assist from Venus and two from Earth. In

	1: Launch	2: Venus	3: Earth	4: Earth	5: Saturn
Date	4/1/2026	4/13/2027	11/3/2028	7/20/2031	4/10/2036
Time of Flight (days)	0	377.8	947.2	1936.1	3662.0
Flyby Altitude (km)	-	638	3940	1641	-
Accumulated Δv (km/s)	-	0.001	0.01	0.029	0.044
V_∞ (km/s)	3.64	7.14	12.75	12.79	6.03

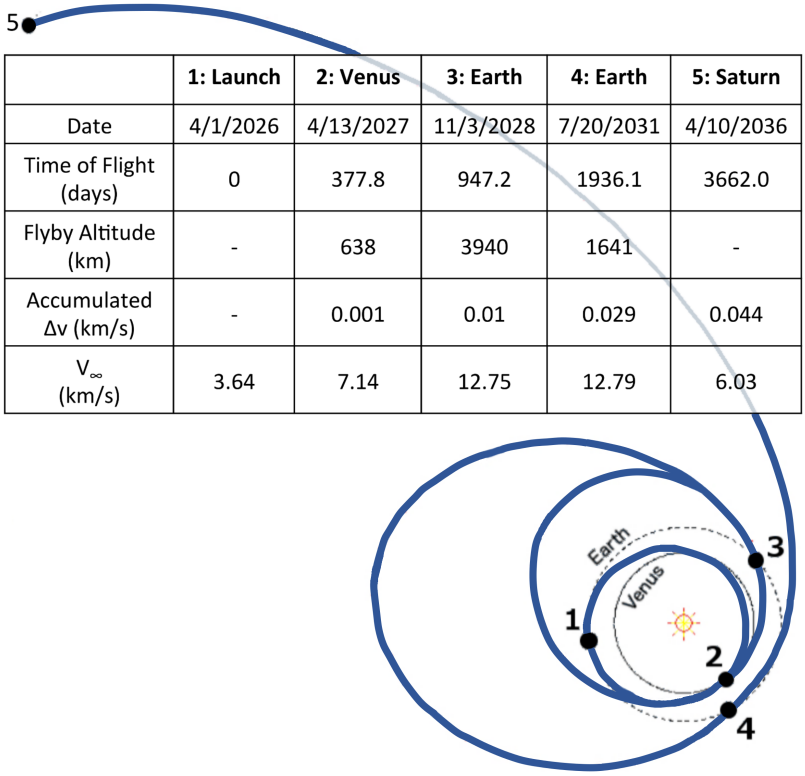

Figure 5.3: Possible inner solar system tour schedule. With no Jupiter gravity assist available, THEO would make use of one Venus and two Earth flybys to get the spacecraft. While in the inner solar system, the spacecraft would operate in standby mode to reduce communications and staffing costs. The potential heating concerns during THEO's proximity to the Sun would be addressed by using the high gain antenna as a heat shield (see Section 5.5.2). Time of flight is listed in Earth days. V_∞ is the hyperbolic velocity of the spacecraft, i.e. as if it were orbiting at an infinite distance from the target.

total, the journey to the Saturnian system would take ten years, during which no science collection is planned.

The spacecraft would be inserted into Saturn's orbit with a Δv of 712 m/s. Because of Enceladus's low mass and the location of its orbit deep within Saturn's gravity well, designing a Δv-efficient rendezvous with Enceladus is a challenge. To reduce the spacecraft's kinetic energy to that appropriate for Enceladus orbit insertion, THEO would conduct a 2.7 year tour of the Saturn system, making a total of 62 flybys of several other Saturnian moons (e.g. Strange et al., 2009; Campagnola et al., 2010). The schedule is shown in Figure 5.4 and includes flybys of Titan (3), Rhea (15), Dione (10), Tethys (12), and Enceladus (12). The costed mission plan does not budget for science operations during this phase, but it does not preclude opportunities for mission enhancement post-selection.

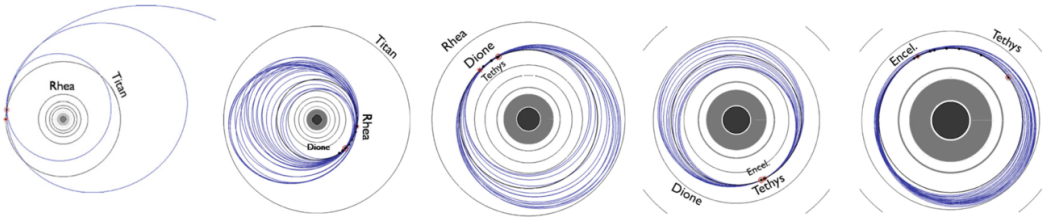

	Titan Tour	Rhea Tour	Dione Tour	Tethys Tour	Enceladus Tours
Event End Date	12/9/2036	07/12/2037	06/15/2038	10/20/2038	07/10/2039
Time of Flight (days)	53	363	190	158	233
Δv (m/s)	29	126	26	12	102

Figure 5.4: Proposed flybys at the Saturn system necessary for Enceladus orbit insertion. No science operations are proposed during this tour of Saturn moons. Though they could increase scientific return, such operations are not within the scope of the proposed mission and would have to be evaluated post-selection.

5.4.2.1 Observation Schedule

To ensure timely completion of all science objectives and to reconcile our science objectives with the power and data constraints of operating under solar power at Saturn, THEO would have a specific observing schedule, summarized in Figure 5.5. High-altitude orbits would be used to conduct the high-phase (backlit) plume imaging campaign from far enough away to catch the plumes at a sufficiently wide field of view. As it is also easier to do Enceladus orbit insertion at higher altitudes, we would begin our science mission at 500 km with 200 orbits of remote sensing with WAVES and DRIPS, the sub-mm instrument and the camera. This would be a unique set of observations in our schedule because the spacecraft would be oriented such that the instrument bus would be pointed in the ram direction. These observations would also be the only ones conducted with orbit nodes at midnight and noon to ensure proper lighting conditions for the high-phase images.

Such a configuration, however, is not sustainable power-wise; the solar panels would spend too much time in shadow. In the subsequent observation campaigns, the spacecraft would be oriented such that its orbit nodes are at 6pm and 6am– this modification is key to meeting the solar power requirements and comes at no cost to the science mission. The instrument bus would also point in the nadir direction. In this new orientation, THEO would conduct an additional 100 orbits with SWAMP, the mass spectrometer, at an altitude of 500 km to determine the plume composition at this distance from Enceladus's surface.

The spacecraft would then descend to an altitude of 100 km for only 10 orbits. This brief sampling time is enough to establish baseline measurements with SWAMP for what species make it to this lower altitude and for WAVES to make thermal emission maps of broader coverage to put the high resolution maps of later observations in the correct context.

The bulk of our observation campaign would be spent at 30 km, 18 km closer than the closest *Cassini* flyby of over Enceladus's south polar region. The highest priority science, making an inventory of the species within the plumes, would be conducted in the first 300 orbits. WAVES would operate in the

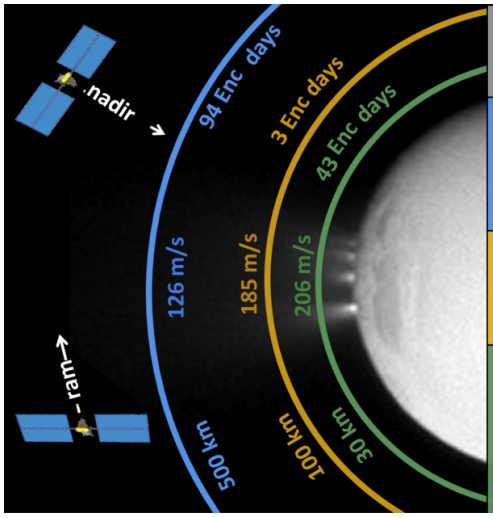

Altitude	# of orbits	SWAMP	WAVES	DRIPS	OSMOSIS	GEISER	Science task	Orbit nodes
500 km	200	-	ram	ram	-	-	Ice/vapor relative abundance	12am-12pm
	100	ram	-	-	-	-	Vapor sampling	6am-6pm
100 km	10 (entry) 20 (exit)	ram	nadir	-	-	on	Vapor sampling, thermal mapping	6am-6pm
30 km	300	ram	nadir	-	on	on	Vapor sampling, thermal mapping, ion flux, gravity field	6am-6pm
	300	-	-	nadir	on	on	Geological mapping, ion flux, gravity field	6am-6pm

Figure 5.5: Proposed THEO observing schedule. The altitude, spacecraft velocity, and total time spent in orbit at that altitude (in Enceladus days, 1 Enceladus day is 1.3 Earth days) are shown above each orbit level with corresponding color scheme in the operations schedule table. "Ram" indicates that the instrument bus is pointed in the ramming direction relative to the plumes; for "nadir" observations, instruments are pointed at Enceladus's surface. This observation schedule would allow THEO to conduct all the necessary science while complying with the solar power budget.

thermal mapping mode in high resolution strips. As the data collected by both instruments is relatively small in number of bits, SWAMP and WAVES would concurrently conduct their observations. On the next 300 orbits, DRIPS would map the south polar terrain, up to 50° S. OSMOSIS, the magnetometer suite, would operate for 10 orbits at 30 km and GEISER would conduct the Doppler-tracking experiment for 10 orbits at the 30 km altitude.

In the final stages of the proposed science mission, the spacecraft must exit Enceladus orbit to comply with planetary protection protocol [3]. As the spacecraft climbs out of Enceladus orbit, SWAMP and WAVES would conduct an additional 20 orbits of observation at 100 km. The proposed fuel budget ensures enough fuel to de-orbit Enceladus and subsequently impact Tethys at the end of mission, thus eliminating any potential contamination of the THEO spacecraft crashing into Enceladus.

5.4.3 Spacecraft Design

5.4.3.1 Mechanical and Configuration

The THEO spacecraft would be an orbiter in the family of JUNO and is shown in Figure 5.6. The main bus would be a standard cylindrical body of 4.5 m in height, 1.5 m in diameter, made of metal and metallic honeycomb. Dry mass of the proposed spacecraft is estimated at 1153.3 kg; wet mass is estimated at 4187 kg. As such, THEO would fit on the Atlas V 541 with the standard launch vehicle adapter and a mass margin of 2%. A HGA would sit atop the cylinder and, as it is attached via a gimbal, have 2 degrees of motion. A medium gain antenna and two low gain antennae would be located at the top

[3] NASA. "Planetary protection provisions for robotic extraterrestrial missions." (2005).

of the HGA. The bus would hold three spherical tanks: one for the oxidizer and two for fuel. The main engine would be located opposite the HGA. The instrument suite with the mass spectrometer, sub-mm, and camera would be on the nadir-pointing side of the bus. To account for the relative velocity of the vapor, the mass spectrometer would be mounted at a 80° from nadir-pointing.

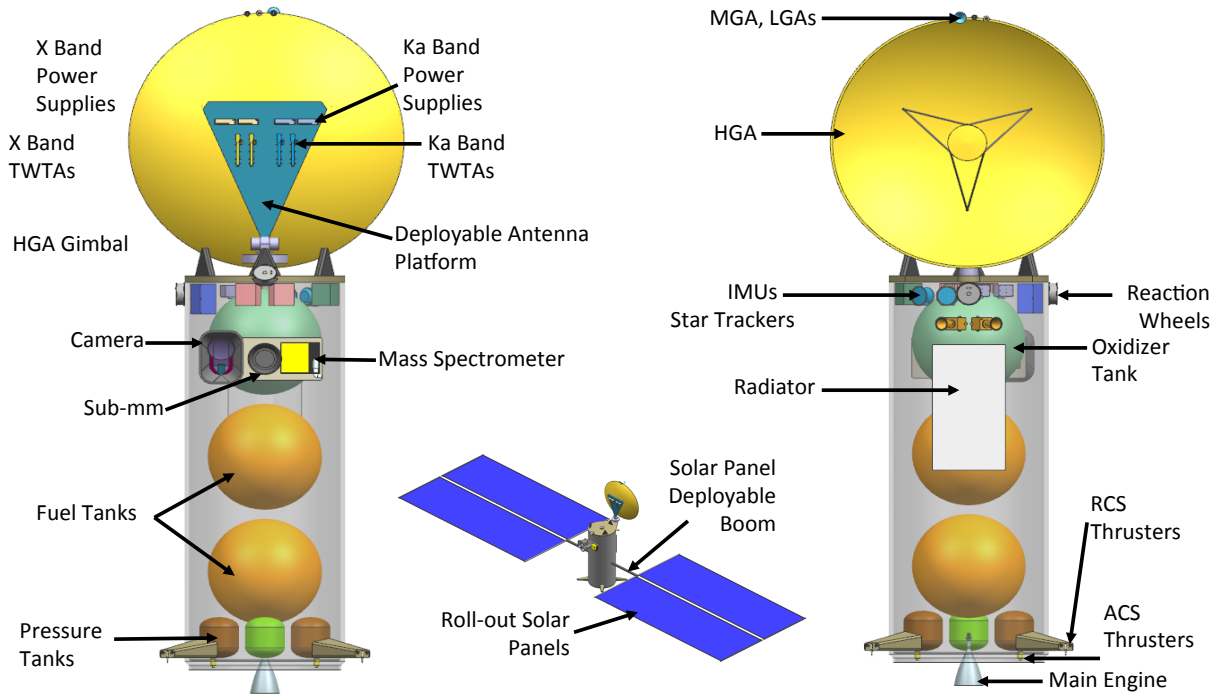

Figure 5.6: CAD model for the THEO spacecraft. The solar arrays would roll out, an important characteristic for enabling the mission. Before deployment, the spacecraft is small enough to fit on an Atlas V for launch. Operationally, the higher packing density and larger panels would specifically enable the use of solar power at 10 AU.

5.4.3.2 Solar Panels

Two wings of two Roll-Out Solar Array (ROSA) solar panels each would also attach to the main bus with 1 axis gimbals, allowing the flexible arrays to track the sunlight. Each wing would be made of two panels that are 36 m^2 in area. Once released from the rocket capsule, the solar arrays would be deployed in an accordion unfolding, similar to the deployment planned for NASA's Surface Water Ocean Topography mission. The cumulative estimated power output is 44.2 kW at beginning-of-life and 594 W at end-of-life operations at Saturn (a value consistent with the empirically-based predictions of Lorenz (2015) for the energy needed to transmit data back to Earth).

5.4.3.3 Propulsion

A dual-mode bi-propellant system with a 445 N main engine would provide spacecraft propulsion. Orbit changing maneuvers would be powered by N_2H_4 fuel and N_2O_4 oxidizer. N_2H_4 monopropellant would fuel the four 22 N RCS thrusters and twelve 0.9 N ACS thrusters. The proposed thrusters and propellant tanks are commercially available, minimizing development costs. The primary function of the RCS thrusters is to correct for misalignment in maneuvers executed by the main engine. It is assumed that the main engine thrust can only be aligned to within 1%. Thus, the RCS thrusters are assigned approximately 23 m/s of Δv (1% of the total Δv allocated to the main engine) to perform these corrections. These designs are flexible enough to accommodate mass growth up to the launch vehicle capability.

5.4.3.4 Attitude Control

THEO's proposed attitude control subsystem (ACS) components consist of commercial, off-the-shelf sensors and actuators whose operations would be within the required pointing, stability, and slewing margins. The 12 ACS thrusters provide contingency attitude control of up to 50 m/s of Δv for maneuvers such as momentum dumping and fast slewing. The sensor suite for determining position and pointing would include two Galileo AA-STAR star trackers, two Honeywell MIMU internal measurement units, and eight Adcole course grain sun sensors. Four RSI 4-33 reaction wheels would serve as THEO's actuators. THEO's predicted pointing ability is accurate to within 0.05°, smaller than the 0.15° required. Pointing stability is predicted to be 1.7 arcsec/sec, a margin of 0.3 arcsec/sec. The predicted slewing velocity, important for our sub-mm plume observations at 500 km in the ram direction is three times greater than the minimum required.

5.4.3.5 Thermal

At Enceladus orbit, 10 AU, the spacecraft must maintain its own operational temperature (-40 °C for the main bus). The spacecraft fuel, for example, must be warm enough to maintain its liquid phase and is therefore the driving factor in the thermal-related power requirements. Without the heat generated from a radioisotope thermoelectric generator power source, the main bus's temperature would be regulated by a suite of thermal hardware including mechanical thermostats, platinum resistance thermometers, Kapton film resistive heaters, multilayer insulation, and louvers. While the temperature at the location where instruments attach to the spacecraft would be maintained by this system, instruments would provide their own independent thermal systems based on their appropriate operating temperatures. The spacecraft would also be covered with multi-layered insulation.

5.4.3.6 Telecommunications

THEO's communications operations related to spacecraft health and safety tracking as well as navigation would be sent using the X band and the high gain antenna. During all critical events, like Saturn Orbit Insertion and Enceladus Orbit Insertion, THEO would be in contact with operations control through continuous X band communications.

Power constraints and operational costs would prohibit the spacecraft from continuously sending back data. Therefore, the proposed spacecraft telecommunications operations includes storing and transmitting/receiving modes. To accommodate all data collected in our observational schedule, data compression would be used to limit data buildup on the spacecraft computer to 6 Gbits/ Earth day. The computer hardware would consist of a dual-string Rad-750 with 786 Gbits of mass storage with redundant 1553 buses for interfacing the main computer and other systems. During downlink with the 34 m arrays of the Deep Space Network, the high gain antenna would send these data at 40 kbps via the Ka band (7.5 mm - 1 cm) for four hours each day. Thus, THEO would send back 0.5 Gbits per day during data collecting modes. Upon receipt and timely validation, the data would be archived on the Planetary Data System.

5.4.4 Key Trades

Using solar power instead of a radioisotope thermoelectric generator (RTG) was a key decision in our concept study. As is discussed in Section 5.5.2, solar power has not been demonstrated at 10 AU and thus represents some level of risk. However, the demonstrated ability and power output of an RTG system did not balance the mass and financial costs associated with it. Furthermore, RTGs did not specifically enable additional or better science. In terms of solar power architecture, the most challenging science tasks are those involving eclipse geometries, the number and duration of which limit solar charging capabilities. We designed THEO to easily accommodate these difficulties with the observing schedule summarized in Figure 5.5. With a little planning, therefore, THEO would operate within the power constraints of a solar powered spacecraft without sacrificing any of the science tasks outlined in Figure 5.2.

Another key trade explored in the development of THEO's mission architecture was the choice between a flyby mission or an orbiter. The Δv difference between achieving orbit and a multiple flyby configuration was on the order of a few 100 m/s (less than 10% of the mission total) and as the mission design was largely the same for either architecture, the difference in operations cost was also minimal. The difference in science capabilities, however, was significant. Twelve flybys simply could not gather enough data to meet the science goals outlined in Section 2, whereas the 930 orbits of data collection over three altitudes of an orbiter configuration could. The biggest disadvantage to an orbiter configuration is the slower orbital velocity– it is insufficient to pulverize ice grains with kinetic energy alone. However, as discussed above, lower velocities present advantages to measuring the plume vapor (such as preserving larger molecules). Therefore, we chose to conduct our investigation with the mass spectrometer as designed, meeting the science objectives listed in Section 5.3. Future investigations could address the possibility of adding a pulverizing mechanism to the mass spectrometer.

5.5 Management

The THEO mission would be a "standard" New Frontiers mission. The spacecraft, as designed, incorporates only technology at high technology readiness level, minimizing obstacles in technology development. THEO's development timeline would therefore be consistent with other New Frontiers missions. The spacecraft design is also of low enough mass to take advantage of launch vehicle incentives, which provide a cost credit that allows THEO to fit comfortably within the New Frontiers cost cap. Thus, the

Table 5.2: Total cost estimates for the concept mission. Current best estimates are calculated without reserves; predicted best estimates add reserves to the current best estimate. Dollar amounts are listed in millions for each phase of the mission, from development through operations.

	Current Best Estimate ($M)	Reserve	Predicted Best Estimate ($M)
Phase A	2.1	20%	2.5
Phase B	54.2	30%	70.4
Phase C-D	541.9	30	704.2
Operations Cost (Phases E-F)	206.2	13	233.9

assessment of Enceladus's habitability is possible with modest investment and minimal risk.

5.5.1 Cost

The nominal 2009 New Frontiers mission cost cap is set at $1000 M (excluding the cost of the launch vehicle). The THEO spacecraft, however, is sufficiently light to fit within a smaller launch vehicle, the Atlas V 541. This would activate a cost incentive and raise the cost cap to $1046.9 M. In Table 5.2, the current and predicted best estimate costs for each development phase are listed. The current best estimate includes project, development, and operating costs, excluding the cost of the launch vehicle. The predicted best estimate is calculated by adding reserves to the current best estimate. These figures were derived using Team-X Institutional (JPL) cost models. The total proposed mission cost is estimated to be $1011.1 M, 3.4% below the cap.

There are no reductions in mission scope (instrument payload or mission schedule) that would result in worthwhile savings in cost, mass, power, data, or time without significantly undermining the science mission. Thus, the threshold mission is the baseline mission for THEO. There is no descope-related cost model for the mission.

During the developmental phases (A-D), the payload and flight systems represent the largest portions of the $777.1 M total at 14% and 38% respectively. 33% of the flight systems cost is budgeted for the power system, including the manufacturing and installation related to the solar panels. $178.9 M (23%) is retained as development reserves. Operations costs (E-F) are estimated to total $233.9 M. As mission operations– DSN tracking; personnel for monitoring, navigation, and mission planning; etc. – represents the largest portion of these phases's cost at 54%, we budget an additional 13% for phases E-F as reserves.

5.5.2 Risk

Risk assessment was conducted in association with Team X using the risk assessment matrix per subsystem outlined in Hihn et al. (2010). The most significant risks identified in our study reflect the novelty of our proposed mission design. THEO would utilize solar panels and a mass spectrometer whose heritages are, at the time of mission design, not proven on a successfully flown mission. (That's not to say that solar power hasn't been proposed for Saturn before– see, for example, the Enceladus Life Finder

mission concept of Lunine et al. (2015).) In addition to these technological risks, we find two low level risks associated with the proposed mission: the thermal environment of the inner solar system trajectory and the reliability of plume activity at Enceladus.

We consider the primary risk in this mission concept to be the utilization of solar cells at Saturn– i.e., at an unprecedented distance from the Sun. This risk is accepted in lieu of the programmatic risks of nuclear power systems as the mass savings of solar power enables the scope of our science mission. Several mitigation strategies are built into the mission concept. The array design incorporates a 43% margin to accommodate array degradation or unforeseen operational constraints, and meets spacecraft power requirements at solar incidence angles of 10° (though gimbaled arrays will track the sunlight, providing significantly higher levels of insolation). THEO utilizes ROSA technology currently being developed under contract to NASA's Space Technology Mission Directorate. Missions currently in development (e.g. the Asteroid Redirect Robotic Mission) are expected to advance the flight-readiness of the hardware and establish test and fabrication practices that would be used by THEO. Though engineering and operational challenges can be overcome, the THEO mission cannot be flown as a New Frontiers class mission with the science payload slated without ROSA technology. Thus, dependence on this not-yet-flown array poses a critical risk to the THEO mission concept.

The readiness level of the mass spectrometer proposed for THEO depends upon successful development of the MASPEX instrument currently slated to fly aboard NASA's Europa mission. Should MASPEX not be successfully flown prior to THEO development, THEO's mass spectrometer could instead be modeled after ROSINA, the mass spectrometer onboard Rosetta. The ROSINA instrument is smaller, less expensive, and uses less power than MASPEX. However, ROSINA is not capable of resolving nucleotides and other organic molecules >300 amu (Balsiger et al., 2007). There is thus a science cost to this strategy: we can establish habitability, but not life. Because there are a number of important science tasks still possible with a ROSINA-equivalent model, we consider the science loss an acceptable one and therefore designate the risk to THEO as low.

The Earth-Venus-Earth-Earth trajectory proposed for THEO incurs significant variations in thermal environment as the spacecraft initially travels in closer to the Sun for a Venus gravity assist. The risk to the spacecraft would be mitigated operationally by using the high-gain antenna as a sun shield, a technique successfully used by the *Cassini* spacecraft (Matson et al., 2003).

As our proposed mission relies on the *in situ* sampling opportunity offered by Enceladus's plumes, we must address the risk of the plumes not being active. The likelihood of sustained activity is high based on several lines of evidence. Plume activity has persisted throughout the *Cassini* mission and has been shown to be the source of Saturn's E-ring, consistently observed since its discovery in 1967 (Feibelman, 1967). (Particle lifetimes in the E-ring are estimated at most to be ∼50 years due to sputtering from energetic particles in the Saturnian system (Jurac et al., 2001).) Additionally, water in the magnetosphere (Hansen et al., 2008) constrains activity to at least within the last 15 years. Tectonic features away from Enceladus's currently active south polar region suggest that venting of the subsurface ocean may have occurred throughout Enceladus's history (Thomas et al., 2016). Therefore, the plumes are not expected

to cease within the geologically near future.

However, in the worst-case scenario that upon Saturn system arrival Enceladus is no longer active, THEO could still achieve meaningful science. The THEO instrument package is capable of alternative scientific investigations in the Saturn system which could be implemented in the event that Earth-based observations revealed cessation of plume activity during THEO's cruise. Detailed descriptions of these alternatives are beyond the scope of this work. The spacecraft Δv budget would be sufficient to modify the trajectory and enter Saturn-orbit, or to take advantage of the numerous flybys that would otherwise be used to pump-down the vehicle's velocity before entering Enceladus orbit. Alternatively, exploring a newly inactive Enceladus might also provide valuable insight into the mechanics of plume activity and shutoff. Though the resulting science investigation would be drastically different from that proposed here, we emphasize that the proposed instrument package is inherently flexible; the spacecraft would not "go to waste" in the unlikely event that the plumes mysteriously cease.

5.6 Conclusions

As *Cassini* approaches its end of mission in 2017, it is increasingly important that the community consider the next phase of exploring the dynamic worlds revealed by the Saturnian flagship. Enceladus is one such world– its plumes offer a unique opportunity to sample a potentially habitable subsurface ocean with relative ease. Other proposed missions have recognized the astrobiological potential of Enceladus, including sample return (Tsou et al., 2012), joint Titan-Enceladus investigations (Coustenis et al., 2009; Sotin et al., 2011; Tobie et al., 2014), and plume-sampling on a Discovery-class budget (Lunine et al., 2015). Like these other mission concepts, THEO was specifically designed for exploring Enceladus to answer questions uncovered by *Cassini* discoveries.

THEO would meet a preponderance of Enceladus science goals laid out by the 2013 Decadal Survey by conducting experiments that would elucidate both whether the moon's hidden ocean is habitable and the factors that affect that answer. We think that these two questions– whether life exists somewhere and why it does or does not– are both necessary questions when seeking life in the solar system and are thus the driving motivation for THEO. The proposed science mission (the logo for which is shown in Figure 5.7) would address how Enceladus's plumes are connected to its subsurface ocean, what mechanisms might be keeping the ocean liquid, whether the abiotic conditions of the ocean are suitable for Earth-analogue life forms, and whether there is evidence of biological processes active at the time of sampling. The THEO mission concept demonstrates that a medium-class mission of a solar-powered orbiter can take full advantage of Enceladus's plumes to explore a potentially habitable ocean world of the outer solar system.

5.7 Acknowledgments

Disclaimer: The cost information contained in this document is of a budgetary and planning nature and is intended for informational purposes only. It does not constitute a commitment on the part of JPL and/or Caltech.

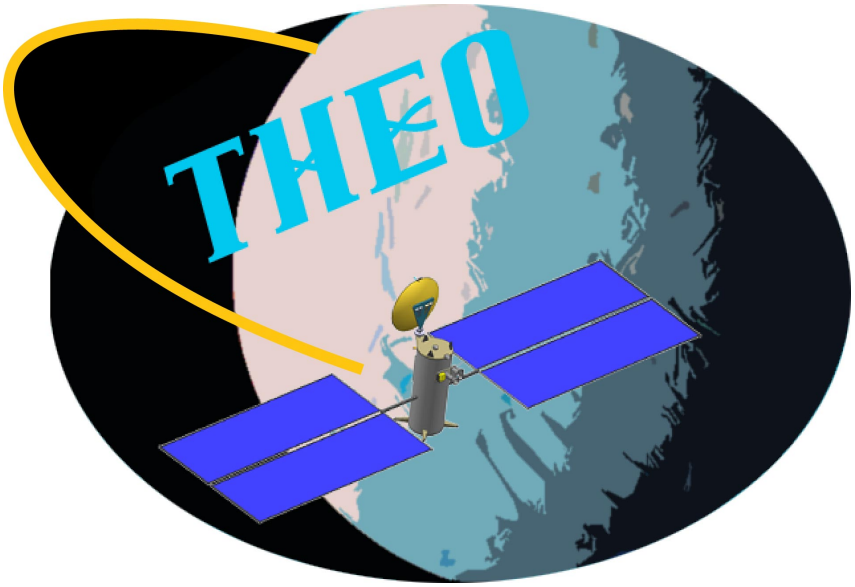

Figure 5.7: Mission logo for Testing the Habitability of Enceladus's Ocean. The proposed patch highlights the three key characteristics of THEO: solar-paneled spacecraft (featured center), in orbit around Enceladus (yellow trajectory), seeking to answer questions related to habitability and therefore biology (double strands in the acronym lettering).

This work was carried out at JPL/Caltech under a contract with NASA.

We thank Chris McKay and an anonymous reviewer for their helpful comments as well as Hunter Waite for his generous insight into the MASPEX instrument.

The THEO team would like to thank the Planetary Science Summer School mentoring team and staff whose efforts made the experience possible: Anita M. Sohus, Leslie L. Lowes, Jessica Parker, and Greg Baerg. We also gratefully acknowledge the TeamX members for their patience, expertise, and insight: Pamela Clark, Alfred Nash, Timothy Koch, Matt Bennett, Austin Lee, Roger Klemm, Enrique Baez, Brian Bairstow, Adam Nelessen, Gregory Welz, Melissa Vick, Morgan Henry, Ted Sweetser, Ron Hall, Jarius Hihn, Masashi Mizukami, Bill Smythe, Michael Sekerak, Vaughn Cable, Eric Sunada, Daniel Forgette, Jennifer Miller, Yogi Krikorian, Try Lam, Dhack Muthulingham, and Patrick Ward. As the culminating event of our summer school, the following volunteers served on a review panel: Farah Alibay, Luther Beegle, Richard Bennett, Ramon P. DePaula, Kevin Hand, Keith Grogan, Young Lee, and Rob Sherwood. We thank the panel for their time and constructive critiques that strengthened our "proposal" and thus the results presented in this paper. Thanks also to task managers J. Cutts, M. Viotti, and R. Zimmerman-Brachman. Finally, we express our gratitude to NASA HQ Science Mission Directorate, the NASA Planetary Science Division, and the NASA Radioisotope Power Systems Program for providing continued financial support for JPL's Planetary Science Summer school.

Shannon M. MacKenzie acknowledges support from the NASA Earth and Space Science Fellowship Program– Grant NNX14AO30H.

5.7.1 Author Contributions

Shannon M. MacKenzie led the mission as Principal Investigator and wrote the manuscript. Tess E. Caswell served as Project Manager and played a primary role in writing the manuscript. Charity M. Phillips-Lander served as the risk and programmatics chair, geochemistry team lead, and provided revisions to the manuscript. E. Natasha Stavros was the systems engineer, co-lead for the sub-mm instrument, and assisted with manuscript reorganization and revisions. Jason D. Hofgartner was the Deputy PI, geology team lead, telecommunications subsystems chair, co-lead on the imaging camera, and assisted with manuscript revisions. Vivian Z. Sun served as Deputy System Engineer, co-lead on the imaging camera, and assisted with manuscript revisions. Katheryn E. Powell led the command and data handling subsystem and assisted with manuscript revisions. Casey J. Steuer served as the attitude control subsystem chair, the magnetometer suite lead, and provided revisions to the manuscript. Joseph G. O'Rourke was as the science chair, led the geophysics team, and assisted with manuscript revisions. Jasmeet K. Dhaliwal served as the ground systems chair, lead of the Plumes team, and co-lead for the mass spectrometer. Cecilia W.S. Leung served as the mission design chair, led the sub-mm instrument, and assisted with manuscript revisions. Elaine M. Petro was in charge of propulsion chair and assisted with manuscript revisions. J. Judson Wynne led the thermal control subsystem and provided revisions to the manuscript. Samson Phan was in charge of the power design, served as co-lead for the mass spectrometer, and assisted with manuscript revisions. Matteo Crismani served as the instruments lead and assisted with manuscript revisions. Kristen K. John was in charge of spacecraft configuration and assisted with manuscript revisions. Akshata Krishnamurthy served as the cost chair and assisted with manuscript revisions. Kevin DeBruin was in charge of mechanical design. Charles J. Budney and Karl L. Mitchell were the coordinators of the JPL Planetary Science Summer School.

Chapter 6: Conclusions

After 13 years orbiting the gas giant, *Cassini* was purposefully flown into Saturn. The spacecraft continued to take data up until it could no longer keep itself pointed at Earth to send the bits home, a fittingly dramatic end for the spacecraft that revolutionized our understanding of Saturn, the rings, and the icy moons. Part of *Cassini*'s legacy is undoubtedly the discoveries revealing Titan and Enceladus as potentially habitable ocean worlds with vast liquid water reservoirs and, in the case of Titan, atmospheric and surface hydrocarbon reservoirs.

In this work I demonstrated that liquid hydrocarbons were not always only found at Titan's poles (Chapter 2). The evaporites left behind by some receding lakes probably vary in composition and grain size, though we cannot discern exactly how from *Cassini* data (Chapter 3). Some lakes at the north pole either emptied over the course of the *Cassini* mission or experienced some kind of surface processing (Chapter 4). Together, our findings provide more evidence that the plethora of organic species in Titan's atmosphere are further modified and moved across Titan's surface.

Of course the question I do not answer is one of, if not the, most pressing Titan mysteries post-*Cassini*: what compounds sit on the surface of Titan? Cataloging the exact composition, diversity, and complexity of the solid hydrocarbons available to interact with liquid water in transient liquid water environments like impact melt and cryovolcanic flow is crucial to constraining the possibilities for biochemistry of water-based life on Titan. Or, should any surface hydrocarbons make it through the ice crust to the ocean (perhaps through impact processes that also bring silicates, Fortes (2000)), the compounds could feed a habitat within Titan's subsurface ocean. (Alternatively, Fortes (2000) describes how methanogenic biota within the subsurface ocean could provide the replenishing mechanism for the methane in Titan's atmosphere, which should be drained by photolysis in the upper atmosphere in about 50 million years.)

Titan also offers the opportunity to also test the assumption that habitability requires liquid *water* (e.g. Chyba and Hand, 2005; McKay and Smith, 2005; McKay, 2016). Titan's lakes and seas provide a solution for chemistry unique from that on Earth, but could some opportunistic biota take advantage of it? Predicting the habitability of this "weird life" remains difficult. For example, life on Earth sequesters nutrients from and maintains conditions independent of the surrounding environment in cells by taking advantage of water's polarity. A double sheet of phospholipids organizes itself such that the hydrophilic heads (phosphate) point outward and the hydrophobic ends (fatty acids) attract to the opposite sheet's hydrophobic ends through van Der Waals forces (e.g. Tanford et al., 1978). This membrane creates an effective barrier behind which aqueous conditions can be regulated independent of the surrounding environment. Recent theoretical work, however, showed that the nonpolar nature of the liquid hydrocarbons does not preclude compartmentalization (Stevenson et al., 2015) (and therefore cellular life) within Titan's seas. Exploiting the polarity of nitrogen-rich heads, compounds like acrylonitrile (CH_2CHCN) can self-organize into layers in nonpolar, cryogenic solutions.

Sampling previously melted water ice and how the organics mixed in differ from the other surface components would constrain how far prebiotic chemistry can proceed before biochemistry takes over. The Earth formed 4.5 Ga (billion years ago) and the discovery of stromatolites in the Pilbara craton of Western Australia (see Figure 6.1) places the earliest definitive evidence for life at 3.4 Ga (Lowe, 1980; Walter et al., 1980; Allwood et al., 2006). Increased abundance of light carbon isotopes provides indirect

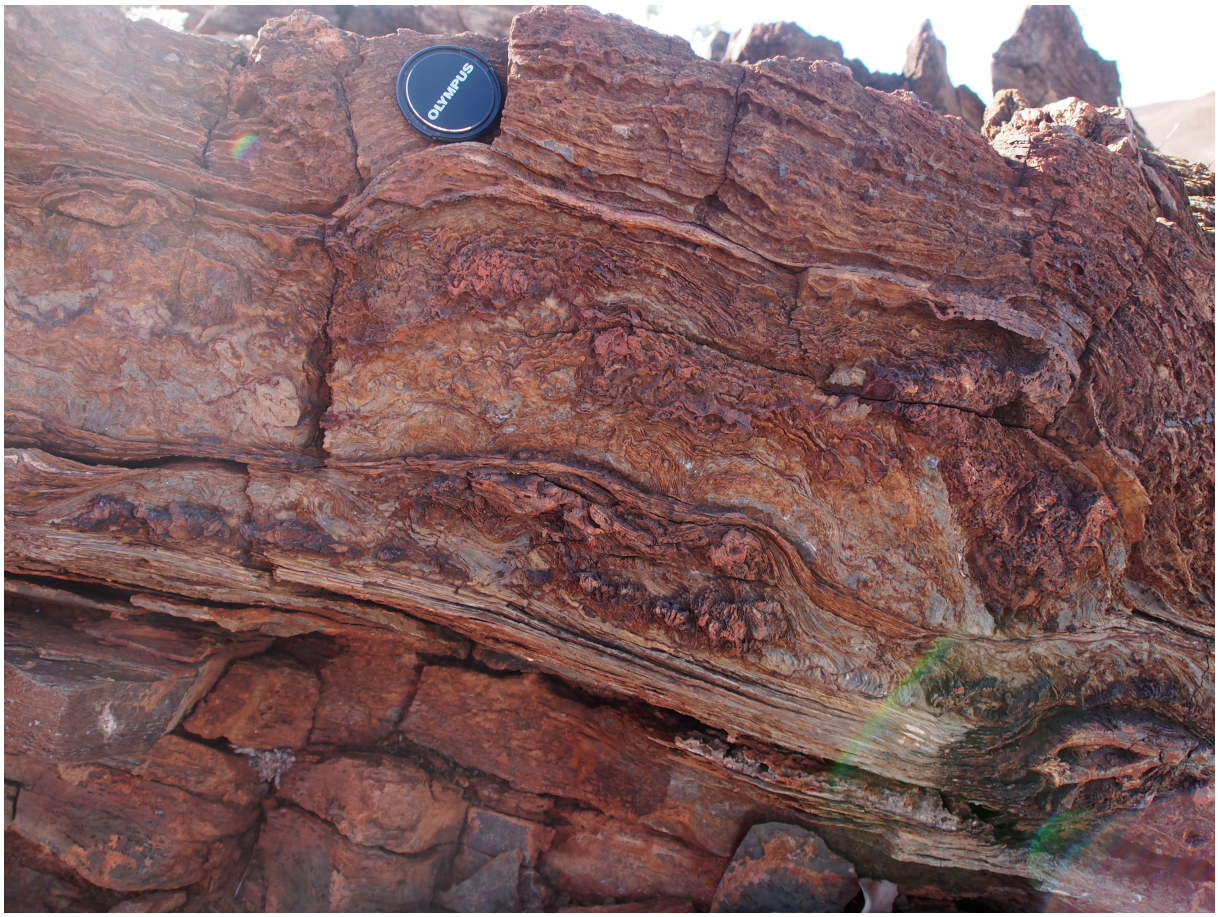

Figure 6.1: Archean stromatolite outcrop on the Pilbara Craton taken July 10, 2017 by the author (Western Australia, Australia). Camera lens cap for scale is 5 cm in diameter. Populations of cyanobacteria grow in mats in shallow waters and soils (e.g. Wright, 1989). Each growth episode results in a lamination (the thin lines of the pictured outcrop), undulations of which come from the upward growth of tower-like structures in response to light availability. Some abiotic processes can form similar structures, but Allwood et al. (2006) find that the diverse morphologies found on the Pilbara Craton are more consistent with biogenetic origin. Once a prolific form of life on Earth's surface, stromatolite growth cannot compete with the grazing rate of modern fauna and are now found mostly in hypersaline environments where they are less likely to be eaten.

isotopic evidence for 3.8 Ga (Schidlowski, 2001). More recently, Dodd et al. (2017) discovered evidence for hydrothermal activity as early as 4.28 Ga in the fossil record and interpret this as evidence for life based on the plethora of biological activity found at modern hydrothermal vents (e.g. Kelley et al., 2001; Kelley et al., 2005).

Orgel (1998), however, demonstrates the difficulty in determining exactly *when* life began because *how* life began still remains a mystery. Does the first appearance of bacteria mark the beginning of life? Or is it some other signature like sequestration of light elements? Is life bound to begin and develop quickly as soon as the "right" conditions (whatever those are) are met? Or is the spark an inherently improbable event? Attempts to estimate the lower limit timescale based on the time necessary to synthesize certain chemical compounds Lazcano and Miller (e.g. 1994) rely on the incorrect assumptions that even simple molecule's synthesis requires a large number of events that are not well understood and that the time for self-replication equals the time for initial development. Orgel (1998) conclude with

> We do not understand how a self replicating system originated on the primitive earth, so it is impossible, on the basis of chemical arguments, to set upper or lower limits on the time that would be required. Hopefully, further research will clarify the nature of the chemical steps involved. Then we might be able to offer some meaningful estimates about the time needed for the transition from an abiotic to a biotic world.

Titan's atmosphere, transient liquid environments, and potentially the hydrocarbon lakes are natural laboratories for properly deriving such estimates for the first time.

Even if Titan proves inhospitable to water- or hydrocarbon-based life, its surface chemical inventory would still provide critical insight into prebiotic chemistry—abiotic, organic-producing processes (Domagal-Goldman et al., 2016)—on Earth. The difference in isotopic abundances between Earth and the Sun suggests that while Earth probably accreted gases as it assembled from the planetary nebula, that atmosphere was removed and replaced with what would eventually become the modern atmosphere (Russell and Menzel, 1933); this secondary formation process is unknown. The rock record suggests that the second atmosphere was anoxic between 3.8-1.5 billion years ago (the Archean geological era), but otherwise the state of the early atmosphere remains controversial (Farquhar et al., 2000). One possible scenario paints Earth's early atmosphere like modern Titan: highly reduced where methane photolysis creates an organic haze layer (Trainer, 2013) in order to help maintain a greenhouse effect strong enough to balance the decreased insolation early in Earth's history (the Faint Young Sun paradox (Sagan and Mullen, 1972; Sagan and Chyba, 1997)). The analogy is not perfect, however (Trainer, 2013): early Earth was likely much warmer (276 K) and had a higher abundance of CO_2 (Kasting, 1993). Laboratory studies can shed light on the kinds of organic chemistries possible in Early Earth's hazy atmosphere, but Titan offers the unique opportunity to investigate an atmosphere that has been highly reduced for at least the age of the modern atmosphere (perhaps 60-1600 Myr ago, if the only removal mechanism is photolysis; Nixon et al. (2012)). If life is truly not present on Titan's surface, then this planetary-wide experiment is the control counterpart to what happened on Earth. All we have to do is gather the results.

The study of exoplanet atmospheres would also benefit from understanding Titan's. Worlds with atmospheres replete with haze, like Titan, may be quite common (Lunine, 2010). Telescopes like James

Web Space Telescope will allow astronomers collect transit spectra of exoplanet atmospheres (e.g. Deming et al., 2009; Shabram et al., 2011); properly interpreting these results will rely on an understanding of archetypical hazy world within our back yard where haze composition, particle sizes, and scattering properties have been studied both in occultation (Hayne et al., 2014; Maltagliati et al., 2015) and *in situ* (Grard et al., 2006; Niemann et al., 2005; Tomasko et al., 2005, 2008c,a,b; Niemann et al., 2010; Doose et al., 2016). Robinson et al. (2014) demonstrate how occultation spectra taken by *Cassini* VIMS can be treated as transit spectra comparable to exoplanet observations.

Clearly, a new mission to Titan would revolutionize our understanding of prebiotic chemistry; the timescales necessary for life; and what makes an environment habitable, thus providing critical context for other searches for habitable worlds, be they in our own solar system or light years away. Ideally the spacecraft would determine the full heterogeneity of surface compounds. Since these are not found all found in one location, an *in situ* sampling spacecraft would need to be mobile. How do you design wheels for a world where the sand is sticky and the topography unknown? You don't. You fly.

Dragonfly is a rotorcraft lander proposed for selection in the New Frontiers 4 announcement of opportunity (Turtle et al., 2017). Taking advantage of Titan's low gravity and high atmospheric pressure, Dragonfly's octocopter design would allow the spacecraft to hop to desired sampling sites. The rotorcraft would run off a battery charged during the eight Earth day Titanian night by a radio isotope power generator. Dragonfly would sample both the dune sands (organic sediments) and water-ice rich interdunes with a sophisticated chemical laboratory capable of discerning prebiotic molecules and potential biomarkers. Complementary investigations of nearby surface geology, weather, and crustal properties would provide the necessary context of what we sample, where it came from, and where it might go.

Alternatively, Sotin et al. (2017) proposed Oceanus, a Titan orbiter whose imaging, altimetry, and gravity science campaigns would map out the distribution of organic sediments and liquids and sites of potential transient liquid environments (cryovolcanoes and impact craters). Oceanus would also taste Titan's atmosphere at higher mass resolution than possible with *Cassini*, better informing the haze and aerosol formation models that feed our understanding of what falls out on Titan's surface.

Cassini hinted at higher order hydrocarbons in Enceladus's plumes, but a new mission could further our understanding of the complexity and abundance of biologically-important compounds. We detailed one way to return to do so in Chapter 5. Note that the advantages of exploring Titan do not necessarily apply to Enceladus. A "null" result (i.e., no biomolecules or "lego" signatures in the elemental abundances identified in the plume samples) does not by itself offer much new information. Would this mean that there is no life in Encealdus's ocean? Or was the sample size not large enough? THEO was designed to provide some of the necessary context by conducting measurements to constrain vent mechanisms as well as the longevity of the ocean. While THEO would probably overrun the cost cap in an actual proposal (rather than a student exercise), our emphasis on collecting as much contextual evidence as possible to complement the *in situ* sampling remains an important message to consider in future mission designs.

Other approaches to returning to Enceladus include the Life Investigation for Enceladus (LIFE, Tsou et al. (2012)) and the Enceladus Life Finder (ELF, Lunine et al. (2015)). The former would return plume samples to Earth, as the chemical assays required to fully analyze samples may require follow-up investigations difficult to plan for when designing a multi-year (perhaps over a decade) long mission (McKay et al.,

2008). ELF makes use of two high resolution mass spectrometers (Srama et al., 2015; Brockwell et al., 2016) to survey the plumes in multiple flybys. Recent estimates of biomolecule abundance–assuming similarity to Earth's hydrothermal vents (Hsu et al., 2015; Postberg, 2015; Sekine et al., 2015; Waite et al., 2017) and a specific mechanism for vent mechanics (direct connection to the surface)–suggest that multiple flybys may be sufficient with a single transect at 50 km to collect 1 organism, though collection speeds would have to be less than 2 km/s (Porco et al., 2017). Processes like bubble scrubbing may be at work to concentrate the number of biota in the plume material by a few orders of magnitude. Microbes and organic material tend to adhere to the film created by a bubble (Walls et al., 2014); when the bubble breaks, the small droplets produced then contain a higher concentration than the bulk ocean content. The likelihood of such scenarios is difficult to constrain with *Cassini* data.

Cassini identified the water and the carbon. To follow either, we need new missions to the Saturn system. In the meantime, a vast dataset from over a decade at Saturn offers us the opportunity to learn as much as possible about the ocean worlds Titan and Enceladus before we visit them again to establish whether Earth no longer solely holds the title of "inhabited".

References

Adams, W. S., Dunham, T., 1932. Absorption bands in the infra-red spectrum of venus. Publications of the Astronomical Society of the Pacific 44 (260), 243–245.

Aharonson, O., Hayes, A. G., Lunine, J. I., Lorenz, R. D., Allison, M. D., Elachi, C., Dec. 2009a. An asymmetric distribution of lakes on Titan as a possible consequence of orbital forcing. Nature Geoscience 2, 851–854.

Aharonson, O., Hayes, A. G., Lunine, J. I., Lorenz, R. D., Allison, M. D., Elachi, C., Dec. 2009b. An asymmetric distribution of lakes on Titan as a possible consequence of orbital forcing. Nature Geoscience 2, 851–854.

Ahlers, J. P., Barnes, J. W., Barnes, R., 2015. Spin–orbit misalignment of two-planet-system koi-89 via gravity darkening. The Astrophysical Journal 814 (1), 67.

Allen, M., Sherwood Lollar, B., Runnegar, B., Oehler, D. Z., Lyons, J. R., Manning, C. E., Summers, M. E., 2006. Is Mars Alive? Eos, Transactions American Geophysical Union 87 (41), 433–439.

Allwood, A. C., Walter, M. R., Kamber, B. S., Marshall, C. P., Burch, I. W., 2006. Stromatolite reef from the early archaean era of australia. Nature 441 (7094), 714.

Archinal, B. A., A'Hearn, M. F., Bowell, E., Conrad, A., Consolmagno, G. J., Courtin, R., Fukushima, T., Hestroffer, D., Hilton, J. L., Krasinsky, G. A., et al., 2011. Report of the IAU working group on cartographic coordinates and rotational elements: 2009. Celestial Mechanics and Dynamical Astronomy 109 (2), 101–135.

Baines, K. H., Drossart, P., Momary, T. W., Formisano, V., Griffith, C., Bellucci, G., Bibring, J. P., Brown, R. H., Buratti, B. J., Capaccioni, F., Cerroni, P., Clark, R. N., Coradini, A., Combes, M., Cruikshank, D. P., Jaumann, R., Langevin, Y., Matson, D. L., McCord, T. B., Mennella, V., Nelson, R. M., Nicholson, P. D., Sicardy, B., Sotin, C., Jun. 2005. The Atmospheres of Saturn and Titan in the Near-Infrared First Results of Cassini/vims. Earth Moon and Planets 96, 119–147.

Baines, K. H., Smith, W. H., 1990. The atmospheric structure and dynamical properties of neptune derived from ground-based and iue spectrophotometry. Icarus 85 (1), 65–108.

Baland, R.-M., Yseboodt, M., Van Hoolst, T., Apr. 2016. The obliquity of Enceladus. Icarus 268, 12–31.

Balsiger, H., Altwegg, K., Bochsler, P., et al., 2007. Rosina–Rosetta orbiter spectrometer for ion and neutral analysis. Space Science Reviews 128 (1-4), 745–801.

Barnes, J. W., Bow, J., Schwartz, J., Brown, R. H., Soderblom, J. M., Hayes, A. G., Vixie, G., Le Mouélic, S., Rodriguez, S., Sotin, C., Jaumann, R., Stephan, K., Soderblom, L. A., Clark, R. N., Buratti, B. J., Baines, K. H., Nicholson, P. D., Nov. 2011. Organic sedimentary deposits in Titan's dry lakebeds: Probable evaporite. Icarus 216, 136–140.

Barnes, J. W., Brown, R. H., Radebaugh, J., Buratti, B. J., Sotin, C., Le Mouelic, S., Rodriguez, S., Turtle, E. P., Perry, J., Clark, R., Baines, K. H., Nicholson, P. D., Aug. 2006. Cassini observations of flow-like features in western Tui Regio, Titan. Geophysical Research Letters 33, L16204.

Barnes, J. W., Brown, R. H., Soderblom, J. M., Soderblom, L. A., Jaumann, R., Jackson, B., Le Mouélic, S., Sotin, C., Buratti, B. J., Pitman, K. M., Baines, K. H., Clark, R. N., Nicholson, P. D., Turtle, E. P., Perry, J., May 2009a. Shoreline features of Titan's Ontario Lacus from Cassini/VIMS observations. Icarus 201, 217–225.

Barnes, J. W., Brown, R. H., Soderblom, J. M., Soderblom, L. A., Jaumann, R., Jackson, B., Le Mouélic, S., Sotin, C., Buratti, B. J., Pitman, K. M., Baines, K. H., Clark, R. N., Nicholson, P. D., Turtle, E. P., Perry, J., May 2009b. Shoreline features of Titan's Ontario Lacus from Cassini/VIMS observations. Icarus 201, 217–225.

Barnes, J. W., Brown, R. H., Soderblom, L., Buratti, B. J., Sotin, C., Rodriguez, S., Le Mouèlic, S., Baines, K. H., Clark, R., Nicholson, P., Jan. 2007a. Global-scale surface spectral variations on Titan seen from Cassini/VIMS. Icarus 186, 242–258.

Barnes, J. W., Brown, R. H., Soderblom, L., Buratti, B. J., Sotin, C., Rodriguez, S., Le Mouèlic, S., Baines, K. H., Clark, R., Nicholson, P., Jan. 2007b. Global-scale surface spectral variations on Titan seen from Cassini/VIMS. Icarus 186, 242–258.

Barnes, J. W., Brown, R. H., Soderblom, L., Sotin, C., Le Mouèlic, S., Rodriguez, S., Jaumann, R., Beyer, R. A., Buratti, B. J., Pitman, K., et al., 2008a. Spectroscopy, morphometry, and photoclinometry of Titan's dunefields from Cassini/VIMS. Icarus 195 (1), 400–414.

Barnes, J. W., Brown, R. H., Soderblom, L., Sotin, C., Le Mouèlic, S., Rodriguez, S., Jaumann, R., Beyer, R. A., Buratti, B. J., Pitman, K., et al., 2008b. Spectroscopy, morphometry, and photoclinometry of titan's dunefields from cassini/vims. Icarus 195 (1), 400–414.

Barnes, J. W., Brown, R. H., Turtle, E. P., McEwen, A. S., Lorenz, R. D., Janssen, M., Schaller, E. L., Brown, M. E., Buratti, B. J., Sotin, C., Griffith, C., Clark, R., Perry, J., Fussner, S., Barbara, J., West, R., Elachi, C., Bouchez, A. H., Roe, H. G., Baines, K. H., Bellucci, G., Bibring, J.-P., Capaccioni, F., Cerroni, P., Combes, M., Coradini, A., Cruikshank, D. P., Drossart, P., Formisano, V., Jaumann, R., Langevin, Y., Matson, D. L., McCord, T. B., Nicholson, P. D., Sicardy, B., Oct. 2005. A 5-Micron-Bright Spot on Titan: Evidence for Surface Diversity. Science 310, 92–95.

Barnes, J. W., Buratti, B. J., Turtle, E. P., Bow, J., Dalba, P. A., Perry, J., Brown, R. H., Rodriguez, S., Mouélic, S. L., Baines, K. H., Sotin, C., Lorenz, R. D., Malaska, M. J., McCord, T. B., Clark, R. N., Jaumann, R., Hayne, P. O., Nicholson, P. D., Soderblom, J. M., Soderblom, L. A., Jan. 2013a. Precipitation-induced surface brightenings seen on Titan by Cassini VIMS and ISS. Planetary Science 2, 1.

Barnes, J. W., Clark, R. N., Sotin, C., Ádámkovics, M., Appéré, T., Rodriguez, S., Soderblom, J. M., Brown, R. H., Buratti, B. J., Baines, K. H., Le Mouélic, S., Nicholson, P. D., Nov. 2013b. A Trans-

mission Spectrum of Titan's North Polar Atmosphere from a Specular Reflection of the Sun. The Astrophysical Journal 777, 161.

Barnes, J. W., Lorenz, R. D., Radebaugh, J., Hayes, A. G., Arnold, K., Chandler, C., 2015. Production and global transport of Titan's sand particles. Planetary Science 4 (1), 1.

Barnes, J. W., MacKenzie, S. M., Young, E. F., Trouille, L. E., Rodriguez, S., Cornet, T., Jackson, B. J., Ádámkovics, M., Sotin, C., Soderblom, J. M., accepted. Spherical Radiative Transfer in C++ (SRTC++): A Parallel Monte-Carlo Radiative Transfer Model for Titan. The Astrophysical Journal.

Barnes, J. W., Radebaugh, J., Brown, R. H., Wall, S., Soderblom, L., Lunine, J., Burr, D., Sotin, C., Le Mouélic, S., Rodriguez, S., Buratti, B. J., Clark, R., Baines, K. H., Jaumann, R., Nicholson, P. D., Kirk, R. L., Lopes, R., Lorenz, R. D., Mitchell, K., Wood, C. A., Nov. 2007c. Near-infrared spectral mapping of Titan's mountains and channels. JGR Planets 112, 11006.

Barnes, J. W., Soderblom, J. M., Brown, R. H., Buratti, B. J., Sotin, C., Baines, K. H., Clark, R. N., Jaumann, R., McCord, T. B., Nelson, R., Le Mouélic, S., Rodriguez, S., Griffith, C., Penteado, P., Tosi, F., Pitman, K. M., Soderblom, L., Stephan, K., Hayne, P., Vixie, G., Bibring, J.-P., Bellucci, G., Capaccioni, F., Cerroni, P., Coradini, A., Cruikshank, D. P., Drossart, P., Formisano, V., Langevin, Y., Matson, D. L., Nicholson, P. D., Sicardy, B., Dec. 2009c. VIMS spectral mapping observations of Titan during the Cassini prime mission. Planetary and Space Science 57, 1950–1962.

Barnes, J. W., Soderblom, J. M., Brown, R. H., Soderblom, L. A., Stephan, K., Jaumann, R., Le Mouélic, S., Rodriguez, S., Sotin, C., Buratti, B. J., et al., 2011. Wave constraints for Titan's Jingpo Lacus and Kraken Mare from VIMS specular reflection lightcurves. Icarus 211 (1), 722–731.

Barnes, J. W., Sotin, C., Soderblom, J. M., Brown, R. H., Hayes, A. G., Donelan, M., Rodriguez, S., Le Mouélic, S., Baines, K. H., McCord, T. B., 2014. Cassini/VIMS observes rough surfaces on Titan's Punga Mare in specular reflection. Planetary science 3 (1), 3.

Barr, A. C., Preuss, L. J., jul 2010. On the origin of south polar folds on Enceladus. Icarus 208, 499–503.

Barth, E. L., Nov. 2010. Cloud formation along mountain ridges on Titan. Planetary and Space Science 58, 1740–1747.

Baum, W. A., Kreidl, T., Westphal, J. A., et al., jul 1981. Saturn's E ring. Icarus 47, 84–96.

Bellucci, G., Pinori, S., Formisano, V., 1998. Imaging spectroscopy of the moon: data reduction-analysis techniques and compositional variability of the mare serenitatis-tranquillitatis region. Planetary and space science 46 (4), 377–390.

Birch, S., Hayes, A., Dietrich, W., Howard, A., Bristow, C., Malaska, M., Moore, J., Mastrogiuseppe, M., Hofgartner, J., Williams, D., et al., 2017. Geomorphologic mapping of Titan's polar terrains: Constraining surface processes and landscape evolution. Icarus 282, 214–236.

Birch, S., Hayes, A., Howard, A., Moore, J., Radebaugh, J., 2016. Alluvial fan morphology, distribution and formation on titan. Icarus 270, 238–247.

Bishop, J., Atreya, S. K., Romani, P. N., Sandel, B. R., Herbert, F., 1992. Voyager 2 ultraviolet spectrometer solar occultations at neptune: Constraints on the abundance of methane in the stratosphere. Journal of Geophysical Research: Planets 97 (E7), 11681–11694.

Bland, M. T., Singer, K. N., McKinnon, W. B., Schenk, P. M., sep 2012. Enceladus' extreme heat flux as revealed by its relaxed craters. Geophysical Research Letters 39, 17204.

Bocanegra-Bahamón, T., Bracken, C., Sitjà, M. C., Dirkx, D., Gerth, I., Konstantinidis, K., Labrianidis, C., Laneuville, M., Luntzer, A., MacArthur, J. L., et al., 2015. Muse–mission to the uranian system: Unveiling the evolution and formation of ice giants. Advances in Space Research 55 (9), 2190–2216.

Bohren, C. F., Huffman, D. R., 2008. Absorption and scattering of light by small particles. John Wiley & Sons.

Bouquet, A., Mousis, O., Waite, J. H., Picaud, S., mar 2015. Possible evidence for a methane source in Enceladus' ocean. Geophysical Research Letters 42, 1334–1339.

Brockwell, T. G., Meech, K. J., Pickens, K., Waite, J. H., Miller, G., Roberts, J., Lunine, J. I., Wilson, P., 2016. The mass spectrometer for planetary exploration (maspex). In: Aerospace Conference, 2016 IEEE. IEEE, pp. 1–17.

Brossier, J. e. a., under review. Titan's Equatorial Belt: Composition and Geomorphology from Cassini/VIMS and RADAR data. Journal of Geophysical Research.

Brossier, J. F., Rodriguez, S., Maltagliati, L., Cornet, T., Lucas, A., Le Mouélic, S., Solomonidou, A., Coustenis, A., Hirtzig, M., Jaumann, R., et al., 2017. Equatorial belt of Titan revisited using a comprehensive radiative transfer model.

Brown, M., Smith, A., Chen, C., Ádámkovics, M., 2009. Discovery of fog at the south pole of titan. The Astrophysical Journal Letters 706 (1), L110.

Brown, M. E., Roberts, J. E., Schaller, E. L., 2010. Clouds on titan during the cassini prime mission: A complete analysis of the vims data. Icarus 205 (2), 571–580.

Brown, R. H., Baines, K. H., Bellucci, G., Bibring, J.-P., Buratti, B. J., Capaccioni, F., Cerroni, P., Clark, R. N., Coradini, A., Cruikshank, D. P., Drossart, P., Formisano, V., Jaumann, R., Langevin, Y., Matson, D. L., McCord, T. B., Mennella, V., Miller, E., Nelson, R. M., Nicholson, P. D., Sicardy, B., Sotin, C., Dec. 2004. The Cassini Visual And Infrared Mapping Spectrometer (Vims) Investigation. Space Science Reviews 115, 111–168.

Brown, R. H., Baines, K. H., Bellucci, G., Buratti, B. J., Capaccioni, F., Cerroni, P., Clark, R. N., Coradini, A., Cruikshank, D. P., Drossart, P., Formisano, V., Jaumann, R., Langevin, Y., Matson, D. L., McCord, T. B., Mennella, V., Nelson, R. M., Nicholson, P. D., Sicardy, B., Sotin, C., Baugh, N., Griffith, C. A., Hansen, G. B., Hibbitts, C. A., Momary, T. W., Showalter, M. R., Feb. 2006a. Observations in the Saturn system during approach and orbital insertion, with Cassini's visual and infrared mapping spectrometer (VIMS). Astronomy and Astrophysics 446, 707–716.

Brown, R. H., Clark, R. N., Buratti, B. J., Cruikshank, D. P., Barnes, J. W., Mastrapa, R. M. E., Bauer, J., Newman, S., Momary, T., Baines, K. H., Bellucci, G., Capaccioni, F., Cerroni, P., Combes, M., Coradini, A., Drossart, P., Formisano, V., Jaumann, R., Langevin, Y., Matson, D. L., McCord, T. B., Nelson, R. M., Nicholson, P. D., Sicardy, B., Sotin, C., Mar. 2006b. Composition and Physical Properties of Enceladus' Surface. Science 311, 1425–1428.

Brown, R. H., Soderblom, L. A., Soderblom, J. M., Clark, R. N., Jaumann, R., Barnes, J. W., Sotin, C., Buratti, B., Baines, K. H., Nicholson, P. D., Jul. 2008. The identification of liquid ethane in Titan's Ontario Lacus. Nature 454, 607–610.

Buratti, B., Veverka, J., 1984. Voyager photometry of rhea, dione, tethys, enceladus and mimas. Icarus 58 (2), 254–264.

Burr, D. M., 2010. Palaeoflood-generating mechanisms on earth, mars, and titan. Global and Planetary Change 70 (1), 5–13.

Burr, D. M., Drummond, S. A., Cartwright, R., Black, B. A., Perron, J. T., 2013. Morphology of fluvial networks on titan: Evidence for structural control. Icarus 226 (1), 742–759.

Burr, D. M., Jacobsen, R. E., Roth, D. L., Phillips, C. B., Mitchell, K. L., Viola, D., Nov. 2009. Fluvial network analysis on Titan: Evidence for subsurface structures and west-to-east wind flow, southwestern Xanadu. Geophysical Research Letters 36, 22203.

Burr, D. M., Perron, T., Lamb, M. P., Irwin, R. P., Collins, G. C., Howard, A. D., Sklar, L. S., Moore, J. M., , Ádámkovics, M., Baker, V. R. Drummond, S., Black, B. A., 2013. Fluvial features on Titan: Insights from morphology and modeling. Bulletin of the Geological Society of America 125, 229 – 321. URL http://www.sciencedirect.com/science/article/pii/S0019103513002728

Běhounková, M., Tobie, G., Choblet, G., Čadek, O., sep 2010. Coupling mantle convection and tidal dissipation: Applications to Enceladus and Earth-like planets. Journal of Geophysical Research (Planets) 115, 9011.

Běhounková, M., Tobie, G., Choblet, G., Čadek, O., jun 2012. Tidally-induced melting events as the origin of south-pole activity on Enceladus. Icarus 219, 655–664.

Běhounková, M., Tobie, G., Čadek, O., Choblet, G., Porco, C., Nimmo, F., aug 2015. Timing of water plume eruptions on Enceladus explained by interior viscosity structure. Nature Geoscience 8, 601–604.

Cable, M. L., Hörst, S. M., Hodyss, R., Beauchamp, P. M., Smith, M. A., Willis, P. A., 2011. Titan tholins: simulating Titan organic chemistry in the Cassini-Huygens era. Chemical Reviews 112 (3), 1882–1909.

Čadek, O., Tobie, G., Van Hoolst, T., Massé, M., Choblet, G., Lefèvre, A., Mitri, G., Baland, R.-M., Běhounková, M., Bourgeois, O., et al., 2016. Enceladus's internal ocean and ice shell constrained from cassini gravity, shape, and libration data. Geophysical Research Letters 43 (11), 5653–5660.

Campagnola, S., Strange, N. J., Russell, R. P., Oct. 2010. A fast tour design method using non-tangent v-infinity leveraging transfer. Celestial Mechanics and Dynamical Astronomy 108, 165–186.

Carr, M. H., Belton, M. J., Chapman, C. R., Davies, M. E., et al., 1998. Evidence for a subsurface ocean on europa. Nature 391 (6665), 363.

Cartwright, R., Burr, D., 2017. Using synthetic aperture radar data of terrestrial analogs to test for alluvial fan formation mechanisms on titan. Icarus 284, 183–205.

Chevrel, S. D., Pinet, P. C., Head, J. W., 1999. Gruithuisen domes region: A candidate for an extended nonmare volcanism unit on the moon. Journal of Geophysical Research: Planets 104 (E7), 16515–16529.

Chyba, C. F., Hand, K. P., 2005. Astrobiology: the study of the living universe. Annu. Rev. Astron. Astrophys. 43, 31–74.

Clark, R. N., Cruikshank, D. P., Jaumann, R., Brown, R. H., Stephan, K., Dalle Ore, C. M., Livo, K. E., Pearson, N., Curchin, J. M., Hoefen, T. M., et al., 2012. The surface composition of iapetus: Mapping results from cassini vims. Icarus 218 (2), 831–860.

Clark, R. N., Curchin, J. M., Barnes, J. W., Jaumann, R., Soderblom, L., Cruikshank, D. P., Brown, R. H., Rodriguez, S., Lunine, J., Stephan, K., Hoefen, T. M., Le Mouélic, S., Sotin, C., Baines, K. H., Buratti, B. J., Nicholson, P. D., Oct. 2010. Detection and mapping of hydrocarbon deposits on Titan. JGR Planets 115 (E14), 10005.

Cook-Hallett, C., Barnes, J. W., Kattenhorn, S. A., Hurford, T., Radebaugh, J., Stiles, B., Beuthe, M., 2015. Global contraction/expansion and polar lithospheric thinning on titan from patterns of tectonism. Journal of Geophysical Research: Planets 120 (6), 1220–1236.

Cordier, D., Barnes, J. W., Ferreira, A. G., Nov. 2013. On the chemical composition of Titan's dry lakebed evaporites. Icarus 226, 1431–1437.

Cordier, D., Cornet, T., Barnes, J., MacKenzie, S., Le Bahers, T., Nna-Mvondo, D., Rannou, P., Ferreira, A., 2016. Structure of Titan's evaporites. Icarus 270, 41–56.

Cordier, D., Mousis, O., Lunine, J., Lebonnois, S., Rannou, P., Lavvas, P., Lobo, L., Ferreira, A., 2012. Titan's lakes chemical composition: sources of uncertainties and variability. Planetary and Space Science 61 (1), 99–107.

Cordier, D., Mousis, O., Lunine, J. I., Lavvas, P., Vuitton, V., Dec. 2009. An Estimate of the Chemical Composition of Titan's Lakes. ApJ-L 707, L128–L131.

Cornet, T., Bourgeois, O., Le Mouélic, S., Rodriguez, S., Lopez Gonzalez, T., Sotin, C., Tobie, G., Fleurant, C., Barnes, J. W., Brown, R. H., Baines, K. H., Buratti, B. J., Clark, R. N., Nicholson, P. D., Apr. 2012a. Geomorphological significance of Ontario Lacus on Titan: Integrated interpretation of Cassini VIMS, ISS and RADAR data and comparison with the Etosha Pan (Namibia). Icarus 218, 788–806.

Cornet, T., Bourgeois, O., Le Mouélic, S., Rodriguez, S., Sotin, C., Barnes, J. W., Brown, R. H., Baines, K. H., Buratti, B. J., Clark, R. N., Nicholson, P. D., Jul. 2012b. Edge detection applied to Cassini images reveals no measurable displacement of Ontario Lacus' margin between 2005 and 2010. JGR Planets 117, 7005.

Cornet, T., Bourgeois, O., Le Mouélic, S., Rodriguez, S., Sotin, C., Barnes, J. W., Brown, R. H., Baines, K. H., Buratti, B. J., Clark, R. N., Nicholson, P. D., Jul. 2012c. Edge detection applied to Cassini images reveals no measurable displacement of Ontario Lacus' margin between 2005 and 2010. JGR Planets 117, 7005.

Cornet, T., Cordier, D., Bahers, T. L., Bourgeois, O., Fleurant, C., Mouélic, S. L., Altobelli, N., 2015. Dissolution on Titan and on Earth: Toward the age of Titan's karstic landscapes. Journal of Geophysical Research: Planets 120 (6), 1044–1074.

Coustenis, A., Achterberg, R. K., Conrath, B. J., Jennings, D. E., Marten, A., Gautier, D., Nixon, C. A., Flasar, F. M., Teanby, N. A., Bézard, B., et al., 2007. The composition of titan's stratosphere from cassini/cirs mid-infrared spectra. Icarus 189 (1), 35–62.

Coustenis, A., Atreya, S. K., Balint, T., Brown, R. H., Dougherty, M. K., et al., mar 2009. TandEM: Titan and Enceladus mission. Experimental Astronomy 23, 893–946.

Coustenis, A., Jennings, D., Nixon, C., Achterberg, R., Lavvas, P., Vinatier, S., Teanby, N., Bjoraker, G., Carlson, R., Piani, L., et al., 2010. Titan trace gaseous composition from cirs at the end of the cassini–huygens prime mission. Icarus 207 (1), 461–476.

Cronin, J. R., Pizzarello, S., 1986. Amino acids of the Murchison meteorite. III. Seven carbon acyclic primary α-amino alkanoic acids1. Geochimica et cosmochimica acta 50 (11), 2419–2427.

Cruikshank, D., Pilcher, C., Morrison, D., 1976. Pluto-evidence for methane frost. Science 194, 835–837.

Cruikshank, D. P., Meyer, A. W., Brown, R. H., Clark, R. N., Jaumann, R., Stephan, K., Hibbitts, C. A., Sandford, S. A., Mastrapa, R. M., Filacchione, G., et al., 2010. Carbon dioxide on the satellites of saturn: Results from the cassini vims investigation and revisions to the vims wavelength scale. Icarus 206 (2), 561–572.

Davies, A. G., Sotin, C., Choukroun, M., Matson, D. L., Johnson, T. V., Aug. 2016. Cryolava flow destabilization of crustal methane clathrate hydrate on Titan. Icarus 274, 23–32.

De Sanctis, M., Raponi, A., Ammannito, E., Ciarniello, M., Toplis, M., McSween, H., Castillo-Rogez, J., Ehlmann, B., Carrozzo, F., Marchi, S., et al., 2016. Bright carbonate deposits as evidence of aqueous alteration on (1) ceres. Nature 536 (7614), 54–57.

Delitsky, M., McKay, C., 2010. The photochemical products of benzene in titan's upper atmosphere. Icarus 207 (1), 477–484.

Deming, D., Seager, S., Winn, J., Miller-Ricci, E., Clampin, M., Lindler, D., Greene, T., Charbonneau, D., Laughlin, G., Ricker, G., et al., 2009. Discovery and characterization of transiting super earths using an all-sky transit survey and follow-up by the james webb space telescope. Publications of the Astronomical Society of the Pacific 121 (883), 952.

Diez-y Riega, H., Camejo, D., Rodriguez, A. E., Manzanares, C. E., 2014. Unsaturated hydrocarbons in the lakes of titan: Benzene solubility in liquid ethane and methane at cryogenic temperatures. Planetary and Space Science 99, 28–35.

Diniega, S., Sayanagi, K. M., Balcerski, J., Carande, B., Diaz-Silva, R. A., Fraeman, A. A., Guzewich, S. D., Hudson, J., Nahm, A. L., Potter-McIntyre, S., et al., 2013. Mission to the trojan asteroids: Lessons learned during a jpl planetary science summer school mission design exercise. Planetary and Space Science 76, 68–82.

Dobrea, E. N., Bell, J., Wolff, M., Noll, K., Lubenow, A., Million, C., 2008. Global-scale near infrared variability on mars: Analysis of 2003 mars opposition observations from hst/nicmos. Icarus 193 (1), 112–124.

Dodd, M. S., Papineau, D., Grenne, T., Slack, J. F., Rittner, M., Pirajno, F., O'Neil, J., Little, C. T., 2017. Evidence for early life in Earth's oldest hydrothermal vent precipitates. Nature 543 (7643), 60–64.

Domagal-Goldman, S. D., Wright, K. E., Adamala, K., Arina de la Rubia, L., Bond, J., Dartnell, L. R., Goldman, A. D., Lynch, K., Naud, M.-E., Paulino-Lima, I. G., et al., 2016. The astrobiology primer v2. 0. Astrobiology 16 (8), 561–653.

Doose, L. R., Karkoschka, E., Tomasko, M. G., Anderson, C. M., 2016. Vertical structure and optical properties of Titan's aerosols from radiance measurements made inside and outside the atmosphere. Icarus 270, 355–375.

Dougherty, M. K., Khurana, K. K., Neubauer, F. M., Russell, C. T., Saur, J., Leisner, J. S., Burton, M. E., mar 2006. Identification of a Dynamic Atmosphere at Enceladus with the Cassini Magnetometer. Science 311, 1406–1409.

Douté, S., Schmitt, B., Quirico, E., Owen, T., Cruikshank, D. P., De Bergh, C., Geballe, T., Roush, T., 1999. Evidence for methane segregation at the surface of pluto. Icarus 142 (2), 421–444.

Duffard, R., Kumar, K., Pirrotta, S., Salatti, M., Kubínyi, M., Derz, U., Armytage, R., Arloth, S., Donati, L., Duricic, A., et al., 2011. A multiple-rendezvous, sample-return mission to two near-earth asteroids. Advances in Space Research 48 (1), 120–132.

Elachi, C., Allison, M., Borgarelli, L., Encrenaz, P., Im, E., Janssen, M., Johnson, W., Kirk, R., Lorenz, R., Lunine, J., et al., 2004. Radar: the cassini titan radar mapper. Space Science Reviews 115 (1), 71–110.

Elachi, C., Wall, S., Janssen, M., Stofan, E., Lopes, R., Kirk, R., Lorenz, R., Lunine, J., Paganelli, F., Soderblom, L., Wood, C., Wye, L., Zebker, H., Anderson, Y., Ostro, S., Allison, M., Boehmer, R.,

Callahan, P., Encrenaz, P., Flamini, E., Francescetti, G., Gim, Y., Hamilton, G., Hensley, S., Johnson, W., Kelleher, K., Muhleman, D., Picardi, G., Posa, F., Roth, L., Seu, R., Shaffer, S., Stiles, B., Vetrella, S., West, R., Jun. 2006. Titan Radar Mapper observations from Cassini's T3 fly-by. Nature 441, 709–713.

Elliot, J., Veverka, J., Goguen, J., 1975. Lunar occultation of Saturn. I. The diameters of Tethys, Dione, Rhea, Titan, and Iapetus. Icarus 26 (4), 387–407.

Engel, M. H., Macko, S., 1997. Isotopic evidence for extraterrestrial non-racemic amino acids in the Murchison meteorite. Nature 389 (6648), 265.

Engel, S., Lunine, J. I., Norton, D. L., 1994. Silicate interactions with ammonia-water fluids on early Titan. Journal of Geophysical Research: Planets (1991–2012) 99 (E2), 3745–3752.

Farquhar, J., Bao, H., Thiemens, M., 2000. Atmospheric influence of earth's earliest sulfur cycle. Science 289 (5480), 756–758.

Farrand, W. H., Bell, J. F., Johnson, J. R., Rice, M. S., Hurowitz, J. A., 2013. Vnir multispectral observations of rocks at cape york, endeavour crater, mars by the opportunity rover's pancam. Icarus 225 (1), 709–725.

Feibelman, W. A., may 1967. Concerning the "D" Ring of Saturn. Nature 214, 793–794.

Flasar, F., 1983. Oceans on Titan? Science 221 (4605), 55–57.

Flasar, F., Achterberg, R., Conrath, B., Gierasch, P., Kunde, V., Nixon, C., Bjoraker, G., Jennings, D., Romani, P., Simon-Miller, A., et al., 2005. Titan's atmospheric temperatures, winds, and composition. Science 308 (5724), 975–978.

Fortes, A., 2000. Exobiological implications of a possible ammonia–water ocean inside Titan. Icarus 146 (2), 444–452.

Fouchet, T., Lellouch, E., Bézard, B., Feuchtgruber, H., Drossart, P., Encrenaz, T., 2000. Jupiter's hydrocarbons observed with iso-sws: vertical profiles of c2h6 and c2h2, detection of ch3c2h. arXiv preprint astro-ph/0002273.

Fulchignoni, M., Ferri, F., Angrilli, F., Ball, A. J., Bar-Nun, A., Barucci, M. A., Bettanini, C., Bianchini, G., Borucki, W., Colombatti, G., Coradini, M., Coustenis, A., Debei, S., Falkner, P., Fanti, G., Flamini, E., Gaborit, V., Grard, R., Hamelin, M., Harri, A. M., Hathi, B., Jernej, I., Leese, M. R., Lehto, A., Lion Stoppato, P. F., López-Moreno, J. J., Mäkinen, T., McDonnell, J. A. M., McKay, C. P., Molina-Cuberos, G., Neubauer, F. M., Pirronello, V., Rodrigo, R., Saggin, B., Schwingenschuh, K., Seiff, A., Simões, F., Svedhem, H., Tokano, T., Towner, M. C., Trautner, R., Withers, P., Zarnecki, J. C., Dec. 2005. In situ measurements of the physical characteristics of Titan's environment. Nature 438, 785–791.

Gasnault, O., Taylor, G. J., Karunatillake, S., Dohm, J., Newsom, H., Forni, O., Pinet, P., Boynton, W. V., 2010. Quantitative geochemical mapping of martian elemental provinces. Icarus 207 (1), 226–247.

Gibbard, S., de Pater, I., Macintosh, B., Roe, H., Max, C., Young, E., McKay, C., 2004. Titan's 2 μm surface albedo and haze optical depth in 1996–2004. Geophysical research letters 31 (17).

Gladstone, G. R., Allen, M., Yung, Y., 1996. Hydrocarbon photochemistry in the upper atmosphere of jupiter. Icarus 119 (1), 1–52.

Glein, C. R., Baross, J. A., Waite, J. H., aug 2015. The pH of Enceladus' ocean. Geochimica et Cosmochimica Acta 162, 202–219.

Glein, C. R., Shock, E. L., Aug. 2013. A geochemical model of non-ideal solutions in the methane-ethane-propane-nitrogen-acetylene system on Titan. Geochimica et Cosmochimica Acta 115, 217–240.

Glein, C. R., Shock, E. L., 2013. PA geochemical model of non-ideal solutions in the methane–ethane–propane–nitrogen–acetylene system on Titan. Geochimica et Cosmochimica Acta 115, 217–240.

Glein, C. R., Waite, J. H., Lunine, J. I., Mar. 2016. How Much Hydrothermal Hydrogen Might We Find in Enceladus' Plume? In: Lunar and Planetary Science Conference. Vol. 47 of Lunar and Planetary Science Conference. p. 2885.

Goguen, J. D., Buratti, B. J., Brown, R. H., et al., sep 2013. The temperature and width of an active fissure on Enceladus measured with Cassini VIMS during the 14 April 2012 South Pole flyover. Icarus 226, 1128–1137.

Grard, R., Hamelin, M., López-Moreno, J., Schwingenschuh, K., Jernej, I., Molina-Cuberos, G., Simões, F., Trautner, R., Falkner, P., Ferri, F., et al., 2006. Electric properties and related physical characteristics of the atmosphere and surface of titan. Planetary and Space Science 54 (12), 1124–1136.

Grasset, O., Castillo-Rogez, J., Guillot, T., Fletcher, L., Tosi, F., 2017. Water and volatiles in the outer solar system. Space Science Reviews, 1–41.

Griffith, C., Penteado, P., Rannou, P., Brown, R., Boudon, V., Baines, K., Clark, R., Drossart, P., Buratti, B., Nicholson, P., et al., 2006. Evidence for a polar ethane cloud on Titan. Science 313 (5793), 1620–1622.

Griffith, C. A., 2009. Storms, polar deposits and the methane cycle in Titan's atmosphere. Philosophical Transactions of the Royal Society of London A: Mathematical, Physical and Engineering Sciences 367 (1889), 713–728.

Griffith, C. A., Lora, J. M., Turner, J., Penteado, P. F., Brown, R. H., Tomasko, M. G., Doose, L., See, C., 2012. Possible tropical lakes on titan from observations of dark terrain. Nature 486 (7402), 237–239.

Griffith, C. A., Owen, T., Miller, G. A., Geballe, T., Oct. 1998. Transient clouds in Titan's lower atmosphere. Nature 395, 575–578.

Griffith, C. A., Owen, T., Wagener, R., 1991. Titan's surface and troposphere, investigated with ground-based, near-infrared observations. Icarus 93 (2), 362–378.

Griffith, C. A., Penteado, P., Baines, K., Drossart, P., Barnes, J., Bellucci, G., Bibring, J., Brown, R., Buratti, B., Capaccioni, F., et al., 2005. The evolution of titan's mid-latitude clouds. Science 310 (5747), 474–477.

Grundy, W., Binzel, R., Buratti, B., Cook, J., Cruikshank, D., Dalle Ore, C., Earle, A., Ennico, K., Howett, C., Lunsford, A., et al., 2016. Surface compositions across pluto and charon. Science 351 (6279), aad9189.

Gulkis, S., Frerking, M., Crovisier, J., et al., feb 2007. MIRO: Microwave Instrument for Rosetta Orbiter. Space Science Reviews 128, 561–597.

Hanel, R., Conrath, B., Flasar, F., Kunde, V., Maguire, W., Pearl, J., Pirraglia, J., Samuelson, R., Cruikshank, D., Gautier, D., et al., 1982. Infrared observations of the saturnian system from voyager 2. Science 215 (4532), 544–548.

Hansen, C. J., Esposito, L., Stewart, A. I. F., et al., mar 2006. Enceladus' Water Vapor Plume. Science 311, 1422–1425.

Hansen, C. J., Esposito, L. W., Stewart, A. I. F., et al., nov 2008. Water vapour jets inside the plume of gas leaving Enceladus. Nature 456, 477–479.

Hansen, C. J., Shemansky, D. E., Esposito, L. W., et al., jun 2011. The composition and structure of the Enceladus plume. Geophysical Research Letters 38, 11202.

Hapke, B., 2012. Theory of reflectance and emittance spectroscopy. Cambridge university press.

Hässig, M., Libardoni, M., Mandt, K., Miller, G., Blase, R., nov 2015. Performance evaluation of a prototype multi-bounce time-of-flight mass spectrometer in linear mode and applications in space science. Planetary and Space Science 117, 436–443.

Hayes, A., Aharonson, O., Callahan, P., Elachi, C., Gim, Y., Kirk, R., Lewis, K., Lopes, R., Lorenz, R., Lunine, J., Mitchell, K., Mitri, G., Stofan, E., Wall, S., May 2008. Hydrocarbon lakes on Titan: Distribution and interaction with a porous regolith. Geophysical Research Letters 35, L9204.

Hayes, A., Michaelides, R., Turtle, E., Barnes, J., Soderblom, J., Masrtogiuseppe, M., Lorenz, R., Kirk, R., Lunine, J., 2014. The distribution and volume of Titan's hydrocarbon lakes and seas. In: Lunar and Planetary Science Conference. Vol. 45. p. 2341.

Hayes, A. G., 2016. The lakes and seas of Titan. Annual Review of Earth and Planetary Sciences 44, 57–83.

Hayes, A. G., Aharonson, O., Lunine, J. I., Kirk, R. L., Zebker, H. A., Wye, L. C., Lorenz, R. D., Turtle, E. P., Paillou, P., Mitri, G., Wall, S. D., Stofan, E. R., Mitchell, K. L., Elachi, C., the Cassini RADAR Team, Jan. 2011. Transient surface liquid in Titan's polar regions from Cassini. Icarus 211, 655–671.

Hayes, A. G., Birch, S. P. D., Dietrich, W. E., Howard, A. D., Kirk, R. L., Poggiali, V., Mastrogiuseppe, M., Michaelides, R. J., Corlies, P. M., Moore, J. M., Malaska, M. J., Mitchell, K. L., Lorenz, R. D., Wood, C. A., 2017. Topographic Constraints on the Evolution and Connectivity of Titan's Lacustrine Basins. Geophysical Research Letters, n/a–n/a2017GL075468.
URL http://dx.doi.org/10.1002/2017GL075468

Hayes, A. G., Wolf, A. S., Aharonson, O., Zebker, H., Lorenz, R., Kirk, R. L., Paillou, P., Lunine, J., Wye, L., Callahan, P., Wall, S., Elachi, C., Sep. 2010. Bathymetry and absorptivity of Titan's Ontario Lacus. Journal of Geophysical Research (Planets) 115, 9009.

Hayne, P. O., McCord, T. B., Sotin, C., Nov. 2014. Titan's surface composition and atmospheric transmission with solar occultation measurements by Cassini VIMS. Icarus 243, 158–172.

He, C., Smith, M. A., 2015. NMR study of the potential composition of Titan's lakes. Planetary and Space Science 109, 149–153.

Head, J., Neukum, G., Jaumann, R., Hiesinger, H., et al., 2005. Tropical to mid-latitude snow and ice accumulation, flow and glaciation on mars. Nature 434 (7031), 346.

Hedman, M. M., Gosmeyer, C. M., Nicholson, P. D., et al., aug 2013. An observed correlation between plume activity and tidal stresses on Enceladus. Nature 500, 182–184.

Hedman, M. M., Nicholson, P. D., Showalter, M. R., Brown, R. H., Buratti, B. J., Clark, R. N., mar 2009. Spectral Observations of the Enceladus Plume with Cassini-Vims. ApJ 693, 1749–1762.

Hibbitts, C., Pappalardo, R., Hansen, G., McCord, T., 2003. Carbon dioxide on ganymede. Journal of Geophysical Research: Planets 108 (E5).

Hihn, J., Chattopadhyay, D., Hanna, R., Port, D., Eggleston, S., 2010. Identification and classification of common risks in space science missions. In: Proc. AIAA Space 2010 Conference and Exposition, Anaheim, CA.

Hill, H. G. M., Nuth, J. A., 2003. The catalytic potential of cosmic dust: implications for prebiotic chemistry in the solar nebula and other protoplanetary systems. Astrobiology 3 (2), 291–304.

Hillier, J. K., Green, S. F., McBride, N., et al., jun 2007. The composition of Saturn's E ring. Monthly Notices of the Royal Astronomical Society 377, 1588–1596.

Hindermann, J. P., Hutchings, G. J., Kiennemann, A., 1993. Mechanistic aspects of the formation of hydrocarbons and alcohols from CO hydrogenation. Catalysis Reviews Science and Engineering 35 (1), 1–127.

Hirtzig, M., Tokano, T., Rodriguez, S., Le Mouélic, S., Sotin, C., 2009. A review of Titan's atmospheric phenomena. The Astronomy and Astrophysics Review 17 (2), 105–147.

Hofgartner, J., Hayes, A. G., Lunine, J., Zebker, H., Stiles, B., Sotin, C., Barnes, J., Turtle, E., Baines, K., Brown, R., et al., 2014. Transient features in a titan sea. Nature geoscience.

Hofgartner, J. D., Hayes, A. G., Lunine, J. I., Zebker, H., Lorenz, R. D., Malaska, M. J., Mastrogiuseppe, M., Notarnicola, C., Soderblom, J. M., 2016. Titan's "Magic Islands": Transient features in a hydrocarbon sea. Icarus 271, 338–349.

Horita, J., Berndt, M. E., 1999. Abiogenic methane formation and isotopic fractionation under hydrothermal conditions. Science 285 (5430), 1055–1057.

Hörst, S. M., 2017. Titan's atmosphere and climate. Journal of Geophysical Research: Planets 122 (3), 432–482.

Howett, C. J. A., Spencer, J. R., Pearl, J., Segura, M., mar 2011. High heat flow from Enceladus' south polar region measured using 10-600 cm^{-1} Cassini/CIRS data. Journal of Geophysical Research (Planets) 116, 3003.

Hsu, H.-W., Postberg, F., Sekine, Y., et al., mar 2015. Ongoing hydrothermal activities within Enceladus. Nature 519, 207–210.

Hubbard, G. S., Naderi, F. M., Garvin, J. B., 2002. Following the water, the new program for mars exploration. Acta Astronautica 51 (1), 337–350.

Hussmann, H., Choblet, G., Lainey, V., Matson, D. L., Sotin, C., Tobie, G., Van Hoolst, T., 2010. Implications of rotation, orbital states, energy sources, and heat transport for internal processes in icy satellites. Space science reviews 153 (1-4), 317–348.

Hussmann, H., Sohl, F., Spohn, T., 2006. Subsurface oceans and deep interiors of medium-sized outer planet satellites and large trans-neptunian objects. Icarus 185 (1), 258–273.

Iess, L., Jacobson, R. A., Ducci, M., Stevenson, D. J., Lunine, J. I., Armstrong, J. W., Asmar, S. W., Racioppa, P., Rappaport, N. J., Tortora, P., 2012. The tides of Titan. Science 337 (6093), 457–459.

Iess, L., Stevenson, D. J., Parisi, M., Hemingway, D., Jacobson, R. A., Lunine, J. I., Nimmo, F., Armstrong, J. W., Asmar, S. W., Ducci, M., Tortora, P., apr 2014. The Gravity Field and Interior Structure of Enceladus. Science 344, 78–80.

Ingersoll, A. P., Ewald, S. P., dec 2011. Total particulate mass in Enceladus plumes and mass of Saturn's E ring inferred from Cassini ISS images. Icarus 216, 492–506.

Ingersoll, A. P., Pankine, A. A., apr 2010. Subsurface heat transfer on Enceladus: Conditions under which melting occurs. Icarus 206, 594–607.

Janssen, M. A., Le Gall, A., Lopes, R. M., Lorenz, R. D., Malaska, M. J., Hayes, A. G., Neish, C., Solomonidou, A., Mitchell, K., Radebaugh, J., et al., 2016. Titan's surface at 2.18-cm wavelength imaged by the Cassini RADAR radiometer: Results and interpretations through the first ten years of observation. Icarus 270, 443–459.

Jaumann, R., Brown, R. H., Stephan, K., Barnes, J. W., Soderblom, L. A., Sotin, C., Le Mouélic, S., Clark, R. N., Soderblom, J., Buratti, B. J., Wagner, R., McCord, T. B., Rodriguez, S., Baines, K. H., Cruikshank, D. P., Nicholson, P. D., Griffith, C. A., Langhans, M., Lorenz, R. D., Oct. 2008. Fluvial erosion and post-erosional processes on Titan. Icarus 197, 526–538.

Johnson, P. E., Smith, M. O., Adams, J. B., 1985. Quantitative analysis of planetary reflectance spectra with principal components analysis. Journal of Geophysical Research: Solid Earth 90 (S02).

Jones, E. G., Lineweaver, C. H., 2010. To what extent does terrestrial life "follow the water"? Astrobiology 10 (3), 349–361.

Juhász, A., Horányi, M., Morfill, G. E., may 2007. Signatures of Enceladus in Saturn's E ring. Geophysical Research Letters 34, 9104.

Jurac, S., Johnson, R. E., Richardson, J. D., feb 2001. Saturn's E Ring and Production of the Neutral Torus. Icarus 149, 384–396.

Kamekura, M., 1998. Diversity of extremely halophilic bacteria. Extremophiles 2 (3), 289–295.

Kasting, J. F., 1993. Earth's early atmosphere. Science, 920–926.

Kelley, D. S., Karson, J. A., Blackman, D. K., FruÈh-Green, G. L., Butterfield, D. A., Lilley, M. D., Olson, E. J., Schrenk, M. O., Roe, K. K., Lebon, G. T., et al., 2001. An off-axis hydrothermal vent field near the mid-atlantic ridge at 30 n. Nature 412 (6843), 145–149.

Kelley, D. S., Karson, J. A., Früh-Green, G. L., Yoerger, D. R., Shank, T. M., Butterfield, D. A., Hayes, J. M., Schrenk, M. O., Olson, E. J., Proskurowski, G., Jakuba, M., Bradley, A., Larson, B., Ludwig, K., Glickson, D., Buckman, K., Bradley, A. S., Brazelton, W. J., Roe, K., Elend, M. J., Delacour, A., Bernasconi, S. M., Lilley, M. D., Baross, J. A., Summons, R. E., Sylva, S. P., Mar. 2005. A Serpentinite-Hosted Ecosystem: The Lost City Hydrothermal Field. Science 307, 1428–1434.

Kempf, S., Beckmann, U., Moragas-Klostermeyer, G., Postberg, F., Srama, R., Economou, T., Schmidt, J., Spahn, F., Grün, E., feb 2008. The E ring in the vicinity of Enceladus. I. Spatial distribution and properties of the ring particles. Icarus 193, 420–437.

Kempf, S., Beckmann, U., Schmidt, J., apr 2010. How the Enceladus dust plume feeds Saturn's E ring. Icarus 206, 446–457.

Khare, B., Thompson, W., Cheng, L., Chyba, C., Sagan, C., Arakawa, E., Meisse, C., Tuminello, P., 1993. Production and optical constants of ice tholin from charged particle irradiation of (1: 6) c2h6/h2o at 77 k. Icarus 103 (2), 290–300.

Khurana, K., Kivelson, M., Stevenson, D., Schubert, G., et al., 1998. Induced magnetic fields as evidence for subsurface oceans in europa and callisto. Nature 395 (6704), 777.

Kieffer, S. W., Lu, X., McFarquhar, G., Wohletz, K. H., sep 2009. A redetermination of the ice/vapor ratio of Enceladus'plumes: Implications for sublimation and the lack of a liquid water reservoir. Icarus 203, 238–241.

Kivelson, M., Khurana, K., Russell, C., Walker, R., et al., 1996. Discovery of ganymede's magnetic field by the galileo spacecraft. Nature 384 (6609), 537.

Kivelson, M. G., Khurana, K. K., Joy, S., Russell, C. T., Southwood, D. J., Walker, R. J., Polanskey, C., 1997. Europa's magnetic signature: Report from Galileo's pass on 19 December 1996. Science 276 (5316), 1239–1241.

Kriegel, H., Simon, S., Motschmann, U., Saur, J., Neubauer, F. M., Persoon, A. M., Dougherty, M. K., Gurnett, D. A., oct 2011. Influence of negatively charged plume grains on the structure of Enceladus' Alfvén wings: Hybrid simulations versus Cassini Magnetometer data. Journal of Geophysical Research (Space Physics) 116 (A15), A10223.

Langhans, M., Jaumann, R., Stephan, K., Brown, R. H., Buratti, B., Clark, R., Baines, K. H., Nicholson, P. D., Lorenz, R. D., Soderblom, L., et al., 2012. Titan's fluvial valleys: Morphology, distribution, and spectral properties. Planetary and Space Science 60 (1), 34–51.

Lazcano, A., Miller, S. L., 1994. How long did it take for life to begin and evolve to cyanobacteria? Journal of Molecular Evolution 39 (6), 546–554.

Le Mouélic, S., Cornet, T., Rodriguez, S., Sotin, C., Barnes, J. W., Baines, K. H., Brown, R. H., Lefèvre, A., Buratti, B. J., Clark, R. N., et al., 2012a. Global mapping of Titan's surface using an empirical processing method for the atmospheric and photometric correction of Cassini/VIMS images. Planetary and Space Science 73 (1), 178–190.

Le Mouélic, S., Paillou, P., Janssen, M. A., Barnes, J. W., Rodriguez, S., Sotin, C., Brown, R. H., Baines, K. H., Buratti, B. J., Clark, R. N., et al., 2008. Mapping and interpretation of Sinlap crater on Titan using Cassini VIMS and RADAR data. Journal of Geophysical Research: Planets 113 (E4).

Le Mouélic, S., Rannou, P., Rodriguez, S., Sotin, C., Griffith, C. A., Le Corre, L., Barnes, J. W., Brown, R. H., Baines, K. H., Buratti, B. J., et al., 2012b. Dissipation of Titan's north polar cloud at northern spring equinox. Planetary and Space Science 60 (1), 86–92.

Lebonnois, S., Toublanc, D., Hourdin, F., Rannou, P., 2001. Seasonal variations of titan's atmospheric composition. Icarus 152 (2), 384–406.

Lellouch, E., Coustenis, A., Sebag, B., Cuby, J.-G., López-Valverde, M., Schmitt, B., Fouchet, T., Crovisier, J., 2003. Titan's 5-μm window: observations with the Very Large Telescope. Icarus 162 (1), 125–142.

Lindal, G. F., Lyons, J., Sweetnam, D., Eshleman, V., Hinson, D., Tyler, G., 1987. The atmosphere of uranus: Results of radio occultation measurements with voyager 2. Journal of Geophysical Research: Space Physics 92 (A13), 14987–15001.

Lodders, K., 2003. Solar system abundances and condensation temperatures of the elements. The Astrophysical Journal 591 (2), 1220.

Lopes, R., Stofan, E., Peckyno, R., Radebaugh, J., Mitchell, K., Mitri, G., Wood, C., Kirk, R., Wall, S., Lunine, J., et al., 2010. Distribution and interplay of geologic processes on Titan from Cassini radar data. Icarus 205 (2), 540–558.

Lopes, R. M. C., Kirk, R. L., Mitchell, K. L., Legall, A., Barnes, J. W., Hayes, A., Kargel, J., Wye, L., Radebaugh, J., Stofan, E. R., Janssen, M. A., Neish, C. D., Wall, S. D., Wood, C. A., Lunine, J. I., Malaska, M. J., Mar. 2013. Cryovolcanism on Titan: New results from Cassini RADAR and VIMS. JGR Planets 118, 416–435.

Lora, J. M., Lunine, J. I., Russell, J. L., Apr. 2015. GCM simulations of Titan's middle and lower atmosphere and comparison to observations. Icarus 250, 516–528.

Lora, J. M., Lunine, J. I., Russell, J. L., Hayes, A. G., 2014. Simulations of Titan's paleoclimate. Icarus 243, 264–273.

Lorenz, R. D., Aug. 2014. The flushing of Ligeia: Composition variations across Titan's seas in a simple hydrological model. Geophysical Research Letters 41, 5764–5770.

Lorenz, R. D., 2015. Energy Cost of Acquiring and Transmitting Science Data on Deep-Space Missions. Journal of Spacecraft and Rockets, 1–5.

Lorenz, R. D., Kirk, R. L., Hayes, A. G., Anderson, Y. Z., Lunine, J. I., Tokano, T., Turtle, E. P., Malaska, M. J., Soderblom, J. M., Lucas, A., Özgür Karatekin, Wall, S. D., 2014. A radar map of Titan Seas: Tidal dissipation and ocean mixing through the throat of Kraken . Icarus 237 (0), 9 – 15. URL http://www.sciencedirect.com/science/article/pii/S0019103514001973

Lorenz, R. D., Lopes, R. M., Paganelli, F., Lunine, J. I., Kirk, R. L., Mitchell, K. L., Soderblom, L. A., Stofan, E. R., Ori, G., Myers, M., et al., 2008. Fluvial channels on titan: initial cassini radar observations. Planetary and Space Science 56 (8), 1132–1144.

Lorenz, R. D., Lunine, J. I., Jul. 1996. Erosion on Titan: Past and Present. Icarus 122, 79–91.

Lorenz, R. D., Lunine, J. I., 2005. Titan's surface before cassini. Planetary and Space Science 53 (5), 557–576.

Lorenz, R. D., Mitchell, K. L., Kirk, R. L., Hayes, A. G., Aharonson, O., Zebker, H. A., Paillou, P., Radebaugh, J., Lunine, J. I., Janssen, M. A., Wall, S. D., Lopes, R. M., Stiles, B., Ostro, S., Mitri, G., Stofan, E. R., Jan. 2008. Titan's inventory of organic surface materials. Geophysical Research Letters 35, 2206.

Lorenz, R. D., Radebaugh, J., Feb. 2009. Global pattern of Titan's dunes: Radar survey from the Cassini prime mission. Geophysical Research Letters 36, 3202.

Lorenz, R. D., Stiles, B. W., Aharonson, O., Lucas, A., Hayes, A. G., Kirk, R. L., Zebker, H. A., Turtle, E. P., Neish, C. D., Stofan, E. R., Barnes, J. W., Jul. 2013. A global topographic map of Titan. Icarus 225, 367–377.

Lowe, D. R., 1980. Stromatolites 3,400-myr old from the Archean of Western Australia. Nature 284 (5755), 441–443.

Lucas, A., Aharonson, O., Deledalle, C., Hayes, A. G., Kirk, R., Howington-Kraus, E., 2014. Insights into titan's geology and hydrology based on enhanced image processing of cassini radar data. Journal of Geophysical Research: Planets 119 (10), 2149–2166.

Lunine, J., Elachi, C., Wall, S., Janssen, M., Allison, M., Anderson, Y., Boehmer, R., Callahan, P., Encrenaz, P., Flamini, E., et al., 2008. Titan's diverse landscapes as evidenced by cassini radar's third and fourth looks at titan. Icarus 195 (1), 415–433.

Lunine, J. I., 1993. The atmospheres of uranus and neptune. Annual review of astronomy and astrophysics 31 (1), 217–263.

Lunine, J. I., 2010. Titan and habitable planets around m-dwarfs. Faraday discussions 147, 405–418.

Lunine, J. I., Stevenson, D. J., Yung, Y. L., 1983. Ethane ocean on titan. Science 222 (4629), 1229–1230.

Lunine, J. I., Waite, J. H., Postberg, F., Spilker, L., Clark, K., mar 2015. Enceladus Life Finder: The Search for Life in a Habitable Moon. In: Lunar and Planetary Science Conference. Vol. 46 of Lunar and Planetary Science Conference. p. 1525.

Luspay-Kuti, A., Chevrier, V., Cordier, D., Rivera-Valentin, E., Singh, S., Wagner, A., Wasiak, F., 2015. Experimental constraints on the composition and dynamics of titan's polar lakes. Earth and Planetary Science Letters 410, 75–83.

Luspay-Kuti, A., Chevrier, V. F., Wasiak, F. C., Roe, L. A., Welivitiya, W. D. D. P., Cornet, T., Singh, S., Rivera-Valentin, E. G., Dec. 2012. Experimental simulations of CH_4 evaporation on Titan. Geophysical Research Letters 39, 23203.

MacKenzie, S., Barnes, J. W., 2016. Compositional similarities and distinctions between titan's evaporitic terrains. The Astrophysical Journal 821 (1), 17.

MacKenzie, S. M., Barnes, J. W., Sotin, C., Soderblom, J. M., Le Mouélic, S., Rodriguez, S., Baines, K. H., Buratti, B. J., Clark, R. N., Nicholson, P. D., McCord, T. B., Nov. 2014. Evidence of Titan's climate history from evaporite distribution. Icarus 243, 191–207.

Malaska, M. J., Hodyss, R., 2014. Dissolution of benzene, naphthalene, and biphenyl in a simulated Titan lake. Icarus 242, 74–81.

Maltagliati, L., Bézard, B., Vinatier, S., Hedman, M. M., Lellouch, E., Nicholson, P. D., Sotin, C., de Kok, R. J., Sicardy, B., Mar. 2015. Titan's atmosphere as observed by Cassini/VIMS solar occultations: CH_4, CO and evidence for C_2H_6 absorption. Icarus 248, 1–24.

Mandt, K. E., Waite, J. H., Teolis, B., Magee, B. A., Bell, J., Westlake, J. H., Nixon, C. A., Mousis, O., Lunine, J. I., 2012. The 12c/13c ratio on titan from cassini inms measurements and implications for the evolution of methane. The Astrophysical Journal 749 (2), 160.

Marion, G. M., Kargel, J. S., Catling, D. C., Lunine, J. I., aug 2012. Modeling ammonia-ammonium aqueous chemistries in the Solar System's icy bodies. Icarus 220, 932–946.

Marty, B., Alexander, C. M., Raymond, S. N., 2013. Primordial origins of Earth's carbon. Reviews in Mineralogy and Geochemistry 75 (1), 149–181.

Mastrapa, R., Sandford, S., Roush, T., Cruikshank, D., Dalle Ore, C., 2009. Optical constants of amorphous and crystalline h2o-ice: 2.5-22 μm (4000-455 cm–1) optical constants of h2o-ice. The Astrophysical Journal 701 (2), 1347.

Mastrogiuseppe, M., Poggiali, V., Hayes, A., Lorenz, R., Lunine, J., Picardi, G., Seu, R., Flamini, E., Mitri, G., Notarnicola, C., et al., 2014. The bathymetry of a titan sea. Geophysical Research Letters 41 (5), 1432–1437.

Matson, D. L., Castillo, J. C., Lunine, J., Johnson, T. V., apr 2007. Enceladus' plume: Compositional evidence for a hot interior. Icarus 187, 569–573.

Matson, D. L., Spilker, L. J., Lebreton, J.-P., 2003. The cassini/huygens mission to the saturnian system. In: The Cassini-Huygens Mission. Springer, pp. 1–58.

McCollom, T. M., 1999. Methanogenesis as a potential source of chemical energy for primary biomass production by autotrophic organisms in hydrothermal systems on Europa. Journal of Geophysical Research: Planets (1991–2012) 104 (E12), 30729–30742.

McCollom, T. M., Simoneit, B. R. T., 1999a. Abiotic formation of hydrocarbons and oxygenated compounds during thermal decomposition of iron oxalate. Origins of Life and Evolution of the Biosphere 29 (2), 167–186.

McCollom, T. M., Simoneit, B. R. T., mar 1999b. Abiotic Formation of Hydrocarbons and Oxygenated Compounds During Thermal Decomposition of Iron Oxalate. Origins of Life and Evolution of the Biosphere 29, 167–186.

McCord, T. B., Hansen, G. B., Hibbitts, C. A., 2001. Hydrated salt minerals on ganymede's surface: evidence of an ocean below. Science 292 (5521), 1523–1525.

McCord, T. B., Hayne, P., Combe, J.-P., Hansen, G. B., Barnes, J. W., Rodriguez, S., Le Mouélic, S., Baines, E. K. H., Buratti, B. J., Sotin, C., Nicholson, P., Jaumann, R., Nelson, R., the Cassini VIMS Team, Mar. 2008. Titan's surface: Search for spectral diversity and composition using the Cassini VIMS investigation. Icarus 194, 212–242.

McKay, C., Smith, H., 2005. Possibilities for methanogenic life in liquid methane on the surface of Titan. Icarus 178 (1), 274–276.

McKay, C. P., 2004. What is life-and how do we search for it in other worlds? PLoS Biology 2, 1260–1262.

McKay, C. P., 2016. Titan as the Abode of Life. Life 6 (1), 8.

McKay, C. P., Anbar, A. D., Porco, C., Tsou, P., apr 2014. Follow the Plume: The Habitability of Enceladus. Astrobiology 14, 352–355.

McKay, C. P., C., P. C., Altheide, T., Davis, W. L., Kral, T. A., oct 2008. The Possible Origin and Persistence of Life on Enceladus and Detection of Biomarkers in the Plume. Astrobiology 8, 909–919.

McKay, C. P., Porco, C. C., Altheide, T., Davis, W. L., Kral, T. A., 2008. The possible origin and persistence of life on enceladus and detection of biomarkers in the plume. Astrobiology 8 (5), 909–919.

Minomura, M., KUzE, H., Takeuchi, N., 2001. Adjacency effect in the atmospheric correction of satellite remote sensing data: evaluation of the influence of aerosol extinction profiles. Optical review 8 (2), 133–141.

Mitchell, J. L., Aug. 2008. The drying of Titan's dunes: Titan's methane hydrology and its impact on atmospheric circulation. Journal of Geophysical Research (Planets) 113, 8015.

Mitchell, J. L., Sep. 2012. Titan's Transport-driven Methane Cycle. The Astrophysical Journal Letters 756, L26.

Mitchell, J. L., Pierrehumbert, R. T., Frierson, D. M., Caballero, R., 2009. The impact of methane thermodynamics on seasonal convection and circulation in a model titan atmosphere. Icarus 203 (1), 250–264.

Mitchell, K. L., Barmatz, M. B., Jamieson, C. S., Lorenz, R. D., Lunine, J. I., 2015. Laboratory measurements of cryogenic liquid alkane microwave absorptivity and implications for the composition of ligeia mare, titan. Geophysical Research Letters 42 (5), 1340–1345.

Mitri, G., Showman, A. P., Lunine, J. I., Lorenz, R. D., Feb. 2007. Hydrocarbon lakes on Titan. Icarus 186, 385–394.

Miyakawa, S., Cleaves, H. J., Miller, S. L., 2002. The cold origin of life: A. Implications based on the hydrolytic stabilities of hydrogen cyanide and formamide. Origins of Life and Evolution of the Biosphere 32 (3), 195–208.

Moore, J. M., Howard, A. D., Nov. 2010. Are the basins of Titan's Hotei Regio and Tui Regio sites of former low latitude seas? Geophysical Research Letters 37, L22205.

Moore, M. H., Ferrante, R. F., Moore, W. J., Hudson, R., 2010. Infrared spectra and optical constants of nitrile ices relevant to titan's atmosphere. The Astrophysical Journal Supplement Series 191 (1), 96.

Moses, J., Fouchet, T., Bézard, B., Gladstone, G., Lellouch, E., Feuchtgruber, H., 2005. Photochemistry and diffusion in jupiter's stratosphere: constraints from iso observations and comparisons with other giant planets. Journal of Geophysical Research: Planets 110 (E8).

Moses, J. I., Bézard, B., Lellouch, E., Gladstone, G. R., Feuchtgruber, H., Allen, M., 2000. Photochemistry of saturn's atmosphere: I. hydrocarbon chemistry and comparisons with iso observations. Icarus 143 (2), 244–298.

Mousis, O., Lunine, J. I., Waite, J. H., Magee, B., Lewis, W., Mandt, K. E., Marquer, D., Cordier, D., 2009. Formation conditions of Enceladus and origin of its methane reservoir. The Astrophysical Journal Letters 701 (1), L39.

Nahm, A. L., Kattenhorn, S. A., sep 2015. A unified nomenclature for tectonic structures on the surface of Enceladus. Icarus 258, 67–81.

Neish, C., Somogyi, A., Imanaka, H., Lunine, J., Smith, M., 2008. Rate measurements of the hydrolysis of complex organic macromolecules in cold aqueous solutions: implications for prebiotic chemistry on the early earth and titan. Astrobiology 8 (2), 273–287.

Neish, C. D., Somogyi, Á., Lunine, J. I., Smith, M. A., 2009. Low temperature hydrolysis of laboratory tholins in ammonia-water solutions: Implications for prebiotic chemistry on Titan. Icarus 201 (1), 412–421.

Neish, C. D., Somogyi, Á., Smith, M. A., 2010. Titan's primordial soup: formation of amino acids via low-temperature hydrolysis of tholins. Astrobiology 10 (3), 337–347.

Niemann, H., Atreya, S., Bauer, S., Carignan, G., et al., 2005. The abundances of constituents of titan's atmosphere from the gcms instrument on the huygens probe. nature 438 (7069), 779.

Niemann, H., Atreya, S., Demick, J., Gautier, D., Haberman, J., Harpold, D., Kasprzak, W., Lunine, J., Owen, T., Raulin, F., 2010. Composition of titan's lower atmosphere and simple surface volatiles as measured by the cassini-huygens probe gas chromatograph mass spectrometer experiment. Journal of Geophysical Research: Planets 115 (E12).

Nimmo, F., Hamilton, D., McKinnon, W., Schenk, P., Binzel, R., Bierson, C., Beyer, R., Moore, J., Stern, S., Weaver, H., et al., 2016. Reorientation of sputnik planitia implies a subsurface ocean on pluto. Nature 540 (7631), 94–96.

Nixon, C., Temelso, B., Vinatier, S., Teanby, N., Bézard, B., Achterberg, R., Mandt, K., Sherrill, C., Irwin, P., Jennings, D., et al., 2012. Isotopic ratios in titan's methane: measurements and modeling. The Astrophysical Journal 749 (2), 159.

Noe Dobrea, E., Bell, J., McConnochie, T., Malin, M., 2006. Analysis of a spectrally unique deposit in the dissected noachian terrain of mars. Journal of Geophysical Research: Planets 111 (E6).

Norton, C. F., Grant, W. D., 1988. Survival of halobacteria within fluid inclusions in salt crystals. Journal of General Microbiology 134 (5), 1365–1373.

O'Brien, D. P., Lorenz, R. D., Lunine, J. I., 2005. Numerical calculations of the longevity of impact oases on Titan. Icarus 173 (1), 243–253.

Orgel, L. E., 1998. The origin of life–how long did it take? Origins of Life and Evolution of the Biosphere 28 (1), 91–96.

Paillou, P., Mitchell, K., Wall, S., Ruffié, G., Wood, C., Lorenz, R., Stofan, E., Lunine, J., Lopes, R., Encrenaz, P., 2008. Microwave dielectric constant of liquid hydrocarbons: Application to the depth estimation of titan's lakes. Geophysical Research Letters 35 (5).
URL http://onlinelibrary.wiley.com/doi/10.1029/2007GL032515/full

Parkinson, C. D., Liang, M.-C., Yung, Y. L., Kirschivnk, J. L., 2008. Habitability of Enceladus: planetary conditions for life. Origins of Life and Evolution of Biospheres 38 (4), 355–369.

Patthoff, D. A., Kattenhorn, S. A., Sep. 2011. A fracture history on Enceladus provides evidence for a global ocean. Geophysical Research Letters 38, L18201.

Perry, M. E., Teolis, B. D., Hurley, D. M., et al., sep 2015. Cassini INMS measurements of Enceladus plume density. Icarus 257, 139–162.

Pieters, C. M., Stankevich, D., Shkuratov, Y. G., Taylor, L., 2002. Statistical analysis of the links among lunar mare soil mineralogy, chemistry, and reflectance spectra. Icarus 155 (2), 285–298.

Pilorget, C., Fernando, J., Ehlmann, B., Douté, S., 2015. Photometry of particulate mixtures: What controls the phase curve? Icarus 250, 188–203.

Poggiali, V., Mastrogiuseppe, M., Hayes, A., Seu, R., Birch, S., Lorenz, R., Grima, C., Hofgartner, J., 2016. Liquid-filled canyons on titan. Geophysical Research Letters 43 (15), 7887–7894.

Porco, C., DiNino, D., Nimmo, F., sep 2014. How the Geysers, Tidal Stresses, and Thermal Emission across the South Polar Terrain of Enceladus are Related. The Astrophysical Journal 148, 45.

Porco, C. C., Dones, L., Mitchell, C., 2017. Could it be snowing microbes on Enceladus? Assessing conditions in its plume and implications for future missions. Astrobiology 17 (9), 876–901.

Porco, C. C., Helfenstein, P., Thomas, P. C., et al., mar 2006. Cassini Observes the Active South Pole of Enceladus. Science 311, 1393–1401.

Porco, C. C., West, R. A., Squyres, S., McEwen, A., Thomas, P., Murray, C. D., Del Genio, A., Ingersoll, A. P., Johnson, T. V., Neukum, G., Veverka, J., Dones, L., Brahic, A., Burns, J. A., Haemmerle, V., Knowles, B., Dawson, D., Roatsch, T., Beurle, K., Owen, W., Dec. 2004. Cassini Imaging Science: Instrument Characteristics And Anticipated Scientific Investigations At Saturn. Space Science Reviews 115, 363–497.

Postberg, F., 2015. Refractory organic compounds in enceladus' ice grains and hydrothermal activity. In: 2015 AGU Fall Meeting. Agu.

Postberg, F., Kempf, S., Schmidt, J., Brilliantov, N., Beinsen, A., Abel, B., Buck, U., Srama, R., jun 2009. Sodium salts in E-ring ice grains from an ocean below the surface of Enceladus. Nature 459, 1098–1101.

Postberg, F., Schmidt, J., Hillier, J., et al., jun 2011. A salt-water reservoir as the source of a compositionally stratified plume on Enceladus. Nature 474, 620–622.

Preston, L. J., Dartnell, L. R., 2014. Planetary habitability: lessons learned from terrestrial analogues. International Journal of Astrobiology 13 (01), 81–98.

Proskurowski, G., Lilley, M. D., Seewald, J. S., Früh-Green, G. L., Olson, E. J., Lupton, J. E., Sylva, S. P., Kelley, D. S., 2008. Abiogenic hydrocarbon production at Lost City hydrothermal field. Science 319 (5863), 604–607.

Protopapa, S., Grundy, W., Reuter, D., Hamilton, D., Dalle Ore, C., Cook, J., Cruikshank, D., Schmitt, B., Philippe, S., Quirico, E., et al., 2017. Pluto's global surface composition through pixel-by-pixel hapke modeling of new horizons ralph/leisa data. Icarus 287, 218–228.

Radebaugh, J., Lorenz, R., Wall, S., Kirk, R., Wood, C., Lunine, J., Stofan, E., Lopes, R., Valora, P., Farr, T., et al., 2011. Regional geomorphology and history of Titan's Xanadu province. Icarus 211 (1), 672–685.

Radebaugh, J., Lorenz, R. D., Kirk, R. L., Lunine, J. I., Stofan, E. R., Lopes, R. M., Wall, S. D., et al., 2007. Mountains on titan observed by cassini radar. Icarus 192 (1), 77–91.

Radebaugh, J., Lorenz, R. D., Lunine, J. I., Wall, S., Boubin, G., Reffet, E., Kirk, R. L., Lopes, R. M., Stofan, E. R., Soderblom, L., et al., 2008. Dunes on titan observed by cassini radar. Icarus 194 (2), 690–703.

Radebaugh, J., Ventra, D., Lorenz, R. D., Farr, T., Kirk, R., Hayes, A., Malaska, M. J., Birch, S., Liu, Z. Y.-C., Lunine, J., et al., 2016. Alluvial and fluvial fans on Saturn's moon Titan reveal processes, materials and regional geology. Geological Society, London, Special Publications 440, SP440–6.

Rambaux, N., Castillo-Rogez, J. C., Williams, J. G., Karatekin, Ö., feb 2010. Librational response of Enceladus. Geophysical Research Letters 37, 4202.

Rannou, P., Cours, T., Le Mouélic, S., Rodriguez, S., Sotin, C., Drossart, P., Brown, R., 2010. Titan haze distribution and optical properties retrieved from recent observations. Icarus 208 (2), 850–867.

Rannou, P., Hourdin, F., McKay, C., Luz, D., 2004. A coupled dynamics-microphysics model of titan's atmosphere. Icarus 170 (2), 443–462.

Rannou, P., McKay, C., Lorenz, R., 2003. A model of titan's haze of fractal aerosols constrained by multiple observations. Planetary and Space Science 51 (14), 963–976.

Rannou, P., Montmessin, F., Hourdin, F., Lebonnois, S., Jan. 2006. The Latitudinal Distribution of Clouds on Titan. Science 311, 201–205.

Ribas, I., Guinan, E. F., Güdel, M., Audard, M., 2005. Evolution of the solar activity over time and effects on planetary atmospheres. i. high-energy irradiances (1-1700 å). The Astrophysical Journal 622 (1), 680.

Roberts, J. H., Nimmo, F., may 2008a. Near-surface heating on Enceladus and the south polar thermal anomaly. Geophysical Research Letters 35, 9201.

Roberts, J. H., Nimmo, F., 2008b. Near-surface heating on Enceladus and the south polar thermal anomaly. Geophysical Research Letters 35 (9).

Robinson, T. D., Maltagliati, L., Marley, M. S., Fortney, J. J., 2014. Titan solar occultation observations reveal transit spectra of a hazy world. Proceedings of the National Academy of Sciences 111 (25), 9042–9047.

Robuchon, G., Nimmo, F., 2011. Thermal evolution of pluto and implications for surface tectonics and a subsurface ocean. Icarus 216 (2), 426–439.

Rodriguez, S., Garcia, A., Lucas, A., Appéré, T., Le Gall, A., Reffet, E., Le Corre, L., Le Mouélic, S., Cornet, T., Courrech du Pont, S., Narteau, C., Bourgeois, O., Radebaugh, J., Arnold, K., Barnes, J. W., Stephan, K., Jaumann, R., Sotin, C., Brown, R. H., Lorenz, R. D., Turtle, E. P., Feb. 2014. Global mapping and characterization of Titan's dune fields with Cassini: Correlation between RADAR and VIMS observations. Icarus 230, 168–179.

Rodriguez, S., Le Mouélic, S., Rannou, P., Sotin, C., Brown, R. H., Barnes, J. W., Griffith, C. A., Burgalat, J., Baines, K. H., Buratti, B. J., Clark, R. N., Nicholson, P. D., Nov. 2011. Titan's cloud seasonal activity from winter to spring with Cassini/VIMS. Icarus 216, 89–110.

Rodriguez, S., Le Mouélic, S., Rannou, P., Tobie, G., Baines, K. H., Barnes, J. W., Griffith, C. A., Hirtzig, M., Pitman, K. M., Sotin, C., Brown, R. H., Buratti, B. J., Clark, R. N., Nicholson, P. D., Jun. 2009. Global circulation as the main source of cloud activity on Titan. Nature 459, 678–682.

Rodriguez, S., Le Mouélic, S., Sotin, C., Clénet, H., Clark, R. N., Buratti, B., Brown, R. H., McCord, T. B., Nicholson, P. D., Baines, K. H., the VIMS Science Team, Dec. 2006. Cassini/VIMS hyperspectral observations of the HUYGENS landing site on Titan. Planetary and Space Sciences 54, 1510–1523.

Roe, H. G., 2012. Titan's methane weather. Annual Review of Earth and Planetary Sciences 40, 355–382.

Rothschild, L. J., Giver, L. J., White, M. R., Mancinelli, R. L., 1994. Metabolic activity of microorganisms in evaporites. Journal of Phycology 30 (3), 431–438.

Rothschild, L. J., Mancinelli, R. L., 2001. Life in extreme environments. Nature 409 (6823), 1092–1101.

Russell, H. N., Menzel, D. H., 1933. The terrestrial abundance of the permanent gases. Proceedings of the National Academy of Sciences 19 (12), 997–1001.

Sagan, C., Chyba, C., 1997. The early faint sun paradox: Organic shielding of ultraviolet-labile greenhouse gases. Science 276 (5316), 1217–1221.

Sagan, C., Khare, B., 1978. Tholins: Organic chemistry of interstellar grains and gas. NASA STI/Recon Technical Report N 79.

Sagan, C., Mullen, G., 1972. Earth and mars: evolution of atmospheres and surface temperatures. Science 177 (4043), 52–56.

Sassen, R., Roberts, H. H., Carney, R., Milkov, A. V., et al., 2004. Free hydrocarbon gas, gas hydrate, and authigenic minerals in chemosynthetic communities of the northern Gulf of Mexico continental slope: relation to microbial processes. Chemical Geology 205 (3), 195–217.

Saur, J., Schilling, N., Neubauer, F. M., Strobel, D. F., Simon, S., Dougherty, M. K., Russell, C. T., Pappalardo, R. T., oct 2008. Evidence for temporal variability of Enceladus' gas jets: Modeling of Cassini observations. Geophysical Research Letters 35, L20105.

Schidlowski, M., 2001. Carbon isotopes as biogeochemical recorders of life over 3.8 ga of earth history: evolution of a concept. Precambrian Research 106 (1), 117–134.

Schmidt, J., Brilliantov, N., Spahn, F., Kempf, S., feb 2008. Slow dust in Enceladus' plume from condensation and wall collisions in tiger stripe fractures. Nature 451, 685–688.

Schneider, N. M., Burger, M. H., Schaller, E. L., Brown, M. E., Johnson, R. E., Kargel, J. S., Dougherty, M. K., Achilleos, N. A., 2009. No sodium in the vapour plumes of Enceladus. Nature 459 (7250), 1102–1104.

Schneider, T., Graves, S. D. B., Schaller, E. L., Brown, M. E., Jan. 2012. Polar methane accumulation and rainstorms on Titan from simulations of the methane cycle. Nature 481, 58–61.

Schubert, G., Anderson, J. D., Travis, B. J., Palguta, J., 2007. Enceladus: Present internal structure and differentiation by early and long-term radiogenic heating. Icarus 188 (2), 345–355.

Schulze-Makuch, D., Grinspoon, D. H., 2005. Biologically enhanced energy and carbon cycling on Titan? Astrobiology 5 (4), 560–567.

Seckbach, J., 2013. Enigmatic microorganisms and life in extreme environments. Vol. 1. Springer Science & Business Media.

Sekine, Y., Shibuya, T., Postberg, F., et al., oct 2015. High-temperature water-rock interactions and hydrothermal environments in the chondrite-like core of Enceladus. Nature Communications 6, 8604.

Shabram, M., Fortney, J. J., Greene, T. P., Freedman, R. S., 2011. Transmission spectra of transiting planet atmospheres: model validation and simulations of the hot neptune gj 436b for the james webb space telescope. The Astrophysical Journal 727 (2), 65.

Shkuratov, Y., Starukhina, L., Hoffmann, H., Arnold, G., 1999. A model of spectral albedo of particulate surfaces: Implications for optical properties of the Moon. Icarus 137 (2), 235–246.

Simon, S., Saur, J., Kriegel, H., Neubauer, F. M., Motschmann, U., Dougherty, M. K., apr 2011. Influence of negatively charged plume grains and hemisphere coupling currents on the structure of Enceladus' Alfvén wings: Analytical modeling of Cassini magnetometer observations. Journal of Geophysical Research (Space Physics) 116, A04221.

Singh, S., Combe, J.-P., Cordier, D., Wagner, A., Chevrier, V., McMahon, Z., 2017. Experimental determination of acetylene and ethylene solubility in liquid methane and ethane: Implications to Titan's surface. Geochimica et Cosmochimica Acta 208, 86–101.

Smith, B. A., Soderblom, L., Batson, R., Bridges, P., Inge, J., Masursky, H., Shoemaker, E., Beebe, R., Boyce, J., Briggs, G., et al., 1982. A new look at the saturn system: The voyager 2 images. Science 215 (4532), 504–537.

Smith, B. A., Soderblom, L., Batson, R. M., et al., jan 1982. A new look at the Saturn system - The Voyager 2 images. Science 215, 504–537.

Soderblom, J. M., Barnes, J. W., Soderblom, L. A., Brown, R. H., Griffith, C. A., Nicholson, P. D., Stephan, K., Jaumann, R., Sotin, C., Baines, K. H., et al., 2012. Modeling specular reflections from hydrocarbon lakes on titan. Icarus 220 (2), 744–751.

Soderblom, J. M., Brown, R. H., Soderblom, L. A., Barnes, J. W., Jaumann, R., Mouélic, S. L., Sotin, C., Stephan, K., Baines, K. H., Buratti, B. J., Clark, R. N., Nicholson, P. D., Aug. 2010. Geology of the Selk crater region on Titan from Cassini VIMS observations. Icarus 208, 905–912.

Soderblom, L. A., Brown, R. H., Soderblom, J. M., Barnes, J. W., Kirk, R. L., Sotin, C., Jaumann, R., MacKinnon, D. J., Mackowski, D. W., Baines, K. H., Buratti, B. J., Clark, R. N., Nicholson, P. D., Dec. 2009. The geology of Hotei Regio, Titan: Correlation of Cassini VIMS and RADAR. Icarus 204, 610–618.

Soderblom, L. A., Kirk, R. L., Lunine, J. I., Anderson, J. A., Baines, K. H., Barnes, J. W., Barrett, J. M., Brown, R. H., Buratti, B. J., Clark, R. N., Cruikshank, D. P., Elachi, C., Janssen, M. A., Jaumann, R., Karkoschka, E., Mouélic, S. L., Lopes, R. M., Lorenz, R. D., McCord, T. B., Nicholson, P. D., Radebaugh, J., Rizk, B., Sotin, C., Stofan, E. R., Sucharski, T. L., Tomasko, M. G., Wall, S. D., Nov. 2007. Correlations between Cassini VIMS spectra and RADAR SAR images: Implications for Titan's surface composition and the character of the Huygens Probe Landing Site. Planetary and Space Sciences 55, 2025–2036.

Solomonidou, A., Hirtzig, M., Coustenis, A., Bratsolis, E., Le Mouélic, S., Rodriguez, S., Stephan, K., Drossart, P., Sotin, C., Jaumann, R., Brown, R. H., Kyriakopoulos, K., Lopes, R. M. C., Bampasidis, G., Stamatelopoulou-Seymour, K., Moussas, X., Aug. 2014. Surface albedo spectral properties of geologically interesting areas on Titan. Journal of Geophysical Research (Planets) 119, 1729–1747.

Solomonidou, A., Hirtzig, M., Coustenis, A., Bratsolis, E., Le Mouélic, S., Rodriguez, S., Stephan, K., Drossart, P., Sotin, C., Jaumann, R., et al., 2014. Surface albedo spectral properties of geologically interesting areas on Titan. Journal of Geophysical Research: Planets 119 (8), 1729–1747.

Sotin, C., Altwegg, K., Brown, R. H., Hand, K., Lunine, J. I., Soderblom, J., Spencer, J., Tortora, P., JET Team, mar 2011. JET: Journey to Enceladus and Titan. In: Lunar and Planetary Science Conference. Vol. 42 of Lunar and Planetary Inst. Technical Report. p. 1326.

Sotin, C., Brown, R. H., Baines, K. H., Barnes, J., Buratti, B. J., Clark, R. N., Jaumann, R., LeMouelic, S., Nicholson, P. D., Rodriguez, S., Soderblom, J., Soderblom, L., Stephan, K., Apr. 2014. 10 years of Cassini/VIMS observations at Titan. European Planetary Science Congress 2014, EPSC Abstracts, Vol. 9, id. EPSC2014-697 9, EPSC2014–697.

Sotin, C., Hayes, A., Malaska, M., Nimmo, F., Trainer, M., Mastrogiuseppe, M., Soderblom, J., Tortora, P., Hofgartner, J., Aharonson, O., Barnes, J. W., Hodyss, R., Iess, L., Kirk, R., Lavvas, P., Lorenz, R., Lunine, J. I., Mazarico, E., McEwen, A., Neish, C., Nixon, C., Turtle, E., Vuitton, V., Yelle, R., Mar. 2017. Oceanus: A New Frontiers Orbiter to Study Titan's Potential Habitability. In: Lunar and Planetary Science Conference. Vol. 48 of Lunar and Planetary Science Conference. p. 2306.

Sotin, C., Jaumann, R., Buratti, B., Brown, R., et al., 2005. Release of volatiles from a possible cryovolcano from near-infrared imaging of Titan. Nature 435 (7043), 786.

Sotin, C., Lawrence, K. J., Reinhardt, B., Barnes, J. W., Brown, R. H., Hayes, A. G., Le Mouélic, S., Rodriguez, S., Soderblom, J. M., Soderblom, L. A., Baines, K. H., Buratti, B. J., Clark, R. N., Jaumann, R., Nicholson, P. D., Stephan, K., Nov. 2012. Observations of Titan's Northern lakes at 5 μm: Implications for the organic cycle and geology. Icarus 221, 768–786.

Spahn, F., Schmidt, J., Albers, N., et al., mar 2006. Cassini Dust Measurements at Enceladus and Implications for the Origin of the E Ring. Science 311, 1416–1418.

Spencer, J. R., Nimmo, F., may 2013. Enceladus: An Active Ice World in the Saturn System. Annual Review of Earth and Planetary Sciences 41, 693–717.

Spencer, J. R., Pearl, J. C., Segura, M., et al., mar 2006. Cassini Encounters Enceladus: Background and the Discovery of a South Polar Hot Spot. Science 311, 1401–1405.

Spitale, J. N., Hurford, T. A., Rhoden, A. R., Berkson, E. E., Platts, S. S., may 2015. Curtain eruptions from Enceladus' south-polar terrain. Nature 521, 57–60.

Spitale, J. N., Porco, C. C., oct 2007. Association of the jets of Enceladus with the warmest regions on its south-polar fractures. Nature 449, 695–697.

Srama, R., Ahrens, T. J., Altobelli, N., Auer, S., Bradley, J., Burton, M., Dikarev, V., Economou, T., Fechtig, H., Görlich, M., et al., 2004. The cassini cosmic dust analyzer. In: The Cassini-Huygens Mission. Springer, pp. 465–518.

Srama, R., Postberg, F., Henkel, H., Klopfer, T., Li, Y., Simolka, J., Bugiel, S., Kempf, S., Hillier, J., Khawaja, N., et al., 2015. Enceladus icy jet analyzer (enija): Search for life with a high resolution tof-ms for in situ characterization of high dust density regions. Eur. Planet. Sci. Congr 10.

Stephan, K., Hibbitts, C., Hoffmann, H., Jaumann, R., 2008. Reduction of instrument-dependent noise in hyperspectral image data using the principal component analysis: Applications to galileo nims data. Planetary and Space Science 56 (3), 406–419.

Stephan, K., Jaumann, R., Brown, R. H., Soderblom, J. M., Soderblom, L. A., Barnes, J. W., Sotin, C., Griffith, C. A., Kirk, R. L., Baines, K. H., et al., 2010. Specular reflection on titan: liquids in kraken mare. Geophysical Research Letters 37 (7).

Stevenson, A., Burkhardt, J., Cockell, C. S., et al., 2015. Multiplication of microbes below 0.690 water activity: implications for terrestrial and extraterrestrial life. Environmental microbiology 17 (2), 257–277.

Stevenson, J., Lunine, J., Clancy, P., 2015. Membrane alternatives in worlds without oxygen: Creation of an azotosome. Science advances 1 (1), e1400067.

Stiles, B. W., Hensley, S., Gim, Y., Bates, D. M., Kirk, R. L., Hayes, A., Radebaugh, J., Lorenz, R. D., Mitchell, K. L., Callahan, P. S., Zebker, H., Johnson, W. T. K., Wall, S. D., Lunine, J. I., Wood, C. A., Janssen, M., Pelletier, F., West, R. D., Veeramacheneni, C., Cassini RADAR Team, Aug. 2009. Determining Titan surface topography from Cassini SAR data. Icarus 202, 584–598.

Stofan, E. R., Aharonson, O., Hayes, A., Kirk, R., Lopes, R., Lorenz, R., Lucas, A., Lunine, J., Malaska, M., Radebaugh, J., et al., 2012. Searching for the remnants of southern seas: Cassini observations of the south pole of Titan. In: AAS/Division for Planetary Sciences Meeting Abstracts. Vol. 44.

Stofan, E. R., Elachi, C., Lunine, J. I., Lorenz, R. D., Stiles, B., Mitchell, K. L., Ostro, S., Soderblom, L., Wood, C., Zebker, H., Wall, S., Janssen, M., Kirk, R., Lopes, R., Paganelli, F., Radebaugh, J., Wye, L., Anderson, Y., Allison, M., Boehmer, R., Callahan, P., Encrenaz, P., Flamini, E., Francescetti, G., Gim, Y., Hamilton, G., Hensley, S., Johnson, W. T. K., Kelleher, K., Muhleman, D., Paillou, P., Picardi, G., Posa, F., Roth, L., Seu, R., Shaffer, S., Vetrella, S., West, R., Jan. 2007. The lakes of Titan. Nature 445, 61–64.

Strange, N. J., Campagnola, S., Russell, R. P., 2009. Leveraging flybys of low mass moons to enable an enceladus orbiter. Advances in the Astronautical Sciences 135 (3), 2207–2225.

Strobel, D. F., 1983. Photochemistry of the reducing atmospheres of jupiter, saturn and titan. International reviews in physical chemistry 3 (2), 145–176.

Tanford, C., et al., 1978. The hydrophobic effect and the organization of living matter. Science 200 (4345), 1012–1018.

Teanby, N. A., Irwin, P. G., Nixon, C. A., de Kok, R., Vinatier, S., Coustenis, A., Sefton-Nash, E., Calcutt, S. B., Flasar, F. M., 2012. Active upper-atmosphere chemistry and dynamics from polar circulation reversal on titan. Nature 491 (7426), 732.

Thomas, P. C., Tajeddine, R., Tiscareno, M. S., Burns, J. A., Joseph, J., Loredo, T. J., Helfenstein, P., Porco, C., jan 2016. Enceladus's measured physical libration requires a global subsurface ocean. Icarus 264, 37–47.

Tian, F., Stewart, A. I. F., Toon, O. B., Larsen, K. W., Esposito, L. W., may 2007. Monte Carlo simulations of the water vapor plumes on Enceladus. Icarus 188, 154–161.

Tobie, G., Teanby, N. A., Coustenis, A., Jaumann, R., Raulin, F., Schmidt, J., Carrasco, N., Coates, A. J., Cordier, D., De Kok, R., Geppert, W. D., Lebreton, J.-P., Lefevre, A., Livengood, T. A., Mandt, K. E., Mitri, G., Nimmo, F., Nixon, C. A., Norman, L., Pappalardo, R. T., Postberg, F., Rodriguez,

S., Schulze-Makuch, D., Soderblom, J. M., Solomonidou, A., Stephan, K., Stofan, E. R., Turtle, E. P., Wagner, R. J., West, R. A., Westlake, J. H., dec 2014. Science goals and mission concept for the future exploration of Titan and Enceladus. Planetary and Space Science 104, 59–77.

Tobie, G., Čadek, O., Sotin, C., aug 2008. Solid tidal friction above a liquid water reservoir as the origin of the south pole hotspot on Enceladus. Icarus 196, 642–652.

Tokano, T., 2005. Meteorological assessment of the surface temperatures on titan: constraints on the surface type. Icarus 173 (1), 222–242.

Tokano, T., 2009. Impact of seas/lakes on polar meteorology of titan: Simulation by a coupled gcm-sea model. Icarus 204 (2), 619–636.

Tomasko, M. G., Archinal, B., Becker, T., Bézard, B., Bushroe, M., Combes, M., Cook, D., Coustenis, A., de Bergh, C., Dafoe, L. E., Doose, L., Douté, S., Eibl, A., Engel, S., Gliem, F., Grieger, B., Holso, K., Howington-Kraus, E., Karkoschka, E., Keller, H. U., Kirk, R., Kramm, R., Küppers, M., Lanagan, P., Lellouch, E., Lemmon, M., Lunine, J., McFarlane, E., Moores, J., Prout, G. M., Rizk, B., Rosiek, M., Rueffer, P., Schröder, S. E., Schmitt, B., See, C., Smith, P., Soderblom, L., Thomas, N., West, R., Dec. 2005. Rain, winds and haze during the Huygens probe's descent to Titan's surface. Nature 438, 765–778.

Tomasko, M. G., Bézard, B., Doose, L., Engel, S., Karkoschka, E., Apr. 2008a. Measurements of methane absorption by the descent imager/spectral radiometer (DISR) during its descent through Titan's atmosphere. Planetary and Space Science 56, 624–647.

Tomasko, M. G., Bézard, B., Doose, L., Engel, S., Karkoschka, E., Vinatier, S., Apr. 2008b. Heat balance in Titan's atmosphere. Planetary and Space Science 56, 648–659.

Tomasko, M. G., Doose, L., Engel, S., Dafoe, L. E., West, R., Lemmon, M., Karkoschka, E., See, C., Apr. 2008c. A model of Titan's aerosols based on measurements made inside the atmosphere. Planetary and Space Sciences 56, 669–707.

Trainer, M. G., 2013. Atmospheric prebiotic chemistry and organic hazes. Current organic chemistry 17 (16), 1710–1723.

Tsou, P., Brownlee, D. E., McKay, C. P., Anbar, A. D., Yano, H., Altwegg, K., Beegle, L. W., Dissly, R., Strange, N. J., Kanik, I., aug 2012. LIFE: Life Investigation For Enceladus A Sample Return Mission Concept in Search for Evidence of Life. Astrobiology 12, 730–742.

Tsou, P., Brownlee, D. E., McKay, C. P., Anbar, A. D., Yano, H., Altwegg, K., Beegle, L. W., Dissly, R., Strange, N. J., Kanik, I., 2012. LIFE: Life investigation for Enceladus a sample return mission concept in search for evidence of life. Astrobiology 12 (8), 730–742.

Turtle, E. P., Barnes, J. W., Trainer, M. G., Lorenz, R. D., MacKenzie, S. M., Hibbard, K. E., Adams, D., Bedini, P., Langelaan, J. W., Zacny, K., Dragonfly Team, Mar. 2017. Dragonfly: Exploring Titan's Prebiotic Organic Chemistry and Habitability. In: Lunar and Planetary Science Conference. Vol. 48 of Lunar and Planetary Science Conference. p. 1958.

Turtle, E. P., Del Genio, A. D., Barbara, J. M., Perry, J. E., Schaller, E. L., McEwen, A. S., West, R. A., Ray, T. L., Feb. 2011a. Seasonal changes in Titan's meteorology. Geophysical Research Letters 38, 3203.

Turtle, E. P., Perry, J. E., Hayes, A. G., Lorenz, R. D., Barnes, J. W., McEwen, A. S., West, R. A., Del Genio, A. D., Barbara, J. M., Lunine, J. I., Schaller, E. L., Ray, T. L., Lopes, R. M. C., Stofan, E. R., Mar. 2011b. Rapid and Extensive Surface Changes Near Titan's Equator: Evidence of April Showers. Science 331, 1414–.

Turtle, E. P., Perry, J. E., Hayes, A. G., McEwen, A. S., Apr. 2011c. Shoreline retreat at Titan's Ontario Lacus and Arrakis Planitia from Cassini Imaging Science Subsystem observations. Icarus 212, 957–959.

Turtle, E. P., Perry, J. E., McEwen, A. S., Del Genio, A. D., Barbara, J., West, R. A., Dawson, D. D., Porco, C. C., Jan. 2009. Cassini imaging of Titan's high-latitude lakes, clouds, and south-polar surface changes. Geophysical Research Letters 36, L2204.

Ventura, B., Notarnicola, C., Casarano, D., Posa, F., Hayes, A. G., Wye, L., 2012. Electromagnetic models and inversion techniques for Titan's Ontario Lacus depth estimation from Cassini RADAR data. Icarus 221 (2), 960–969.

Vinatier, S., Bézard, B., Lebonnois, S., Teanby, N. A., Achterberg, R. K., Gorius, N., Mamoutkine, A., Guandique, E., Jolly, A., Jennings, D. E., et al., 2015. Seasonal variations in Titan's middle atmosphere during the northern spring derived from Cassini/CIRS observations. Icarus 250, 95–115.

Vixie, G., Barnes, J. W., Bow, J., Le Mouélic, S., Rodriguez, S., Brown, R. H., Cerroni, P., Tosi, F., Buratti, B., Sotin, C., et al., 2012. Mapping Titan's surface features within the visible spectrum via Cassini VIMS. Planetary and Space Science 60 (1), 52–61.

Vixie, G., Barnes, J. W., Jackson, B., Rodriguez, S., Le Mouélic, S., Sotin, C., MacKenzie, S., Wilson, P., 2015. Possible temperate lakes on titan. Icarus 257, 313–323.

Von Zahn, U., Kumar, S., Niemann, H., Prinn, R., 1983. 13. composition of the venus atmosphere. Venus, 299.

Vuitton, V., Dutuit, O., Smith, M., Balucani, N., 2014. Chemistry of titan's atmosphere. Titan, by Ingo Müller-Wodarg, Caitlin A. Griffith, Emmanuel Lellouch, Thomas E. Cravens, Cambridge, UK: Cambridge University Press, 2014, p. 224, 224.

Vuitton, V., Yelle, R., Anicich, V., 2006. The nitrogen chemistry of titan's upper atmosphere revealed. The Astrophysical Journal Letters 647 (2), L175.

Vuitton, V., Yelle, R., Cui, J., 2008. Formation and distribution of benzene on titan. Journal of Geophysical Research: Planets 113 (E5).

Wahlund, J.-E., Galand, M., Müller-Wodarg, I., Cui, J., Yelle, R., Crary, F., Mandt, K., Magee, B., Waite, J., Young, D., et al., 2009. On the amount of heavy molecular ions in titan's ionosphere. Planetary and Space Science 57 (14), 1857–1865.

Waite, J., Young, D., Cravens, T., Coates, A., Crary, F., Magee, B., Westlake, J., 2007. The process of tholin formation in titan's upper atmosphere. Science 316 (5826), 870–875.

Waite, J. H., Combi, M. R., Ip, W. H., et al., mar 2006. Cassini Ion and Neutral Mass Spectrometer: Enceladus Plume Composition and Structure. Science 311, 1419–1422.

Waite, J. H., Glein, C. R., Perryman, R. S., Teolis, B. D., Magee, B. A., Miller, G., Grimes, J., Perry, M. E., Miller, K. E., Bouquet, A., et al., 2017. Cassini finds molecular hydrogen in the enceladus plume: Evidence for hydrothermal processes. Science 356 (6334), 155–159.

Waite, J. H., Lewis, W. S., Kasprzak, W. T., et al., 2004. The Cassini ion and neutral mass spectrometer (INMS) investigation. In: The Cassini-Huygens Mission. Springer, pp. 113–231.

Waite, J. H., Lewis, W. S., Magee, B. A., et al., jul 2009. Liquid water on Enceladus from observations of ammonia and ^{40}Ar in the plume. Nature 460, 487–490.

Wall, S., Hayes, A., Bristow, C., Lorenz, R., Stofan, E., Lunine, J., Le Gall, A., Janssen, M., Lopes, R., Wye, L., et al., 2010. Active shoreline of ontario lacus, titan: A morphological study of the lake and its surroundings. Geophysical Research Letters 37 (5).

Walls, P. L., Bird, J. C., Bourouiba, L., 2014. Moving with bubbles: A review of the interactions between bubbles and the microorganisms that surround them.

Walter, M., Buick, R., Dunlop, J., 1980. Stromatolites 3,400–3,500 Myr old from the North Pole area, Western Australia. Nature 284 (5755), 443–445.

Wasiak, F. C., Androes, D., Blackburn, D. G., Tullis, J. A., Dixon, J., Chevrier, V. F., Aug. 2013. A geological characterization of Ligeia Mare in the northern polar region of Titan. Planetary and Space Sciences 84, 141–147.

Wood, C., Stofan, E., Hayes, A., Kirk, R., Lunine, J., Radebaugh, J., Malaska, M., 2013. Morphological evidence for former seas near titan's south pole. In: Lunar and Planetary Science Conference. Vol. 44. p. 1764.

Wright, V. P., 1989. Terrestrial stromatolites and laminar calcretes: a review. Sedimentary Geology 65 (1-2), 1–13.

Young, E. F., Rannou, P., McKay, C. P., Griffith, C. A., Noll, K., Jun. 2002. A Three-dimensional Map of Titan's Tropospheric Haze Distribution Based on Hubble Space Telescope Imaging. The Astrophysical Journal 123, 3473–3486.

Zolotov, M. Y., dec 2007. An oceanic composition on early and today's Enceladus. Geophysical Research Letters 34, L23203.

Appendix A: Further Information

A.1 Cartographic Coordinates

On Earth, the prime meridian was chosen to run through Greenwich, UK[1]. But without a naval empire to bully an arbitrary standard on other planetary bodies, the International Astronomical Union (IAU) selects a location on the surface by which to set the cartographic coordinates (Archinal et al., 2011). For tidally locked moons like Titan and Enceladus the sub-planet point defines 0° longitude and the anti-planet point at 180°. Figure A.1 shows a cylindrical map of Titan labeled with two of the conventions used in the Titan community (panels A and C). The leading hemisphere of Titan, shown in panel B, points in the direction of Titan's orbit (thus "leading" the motion); the opposite hemisphere "trails" behind. There advantages to both longitude schemes. Panel A's scheme is more intuitive for the orbital motion of Titan but inconveniently cuts through important features, including Ontario Lacus, the first lake identified on Titan. Panel C's scheme adheres to the convention defined by the IAU: the values positive westward for a prograde planet in the direction that would increase in time for an observer in a fixed inertial system (Archinal et al., 2011). While perhaps less intuitive, this definition centers the map such that the *Huygens* probe landing site lies in the center of the map, along with Ontario Lacus. For the works in this dissertation, the IAU convention is the most convenient as a region of numerous small lakes and evaporite deposits also plot at the map's center.

A.2 Shape of Titan's surface spectrum

Titan's surface spectrum typically shows higher I/F at shorter wavelengths than long. Figure 2.1 shows how there is some variation between surface units in brightness at each window, but the generally "blue" slope (i.e. higher reflectance at shorter wavelengths) remains. There are several factors at work.

The atmosphere too plays a role. Using Spherical Radiative Transfer in C++ (SRTC++, Barnes et al. (accepted)), I modeled Titan's atmosphere with the optical depths and single scattering albedos derived by (Tomasko et al., 2008c) and illuminated the surface with one million photons, treating each surface albedo case separately. The synthetic images produced were coadded according to scattering group; Figure A.2 shows these results. The black line represents the total I/F observed. One advantage of SRTC++ lies in the ability to distinguish the sequence of scattering events responsible for the signal observed. The blue line in Figure A.2 traces the I/F from photons that scatter only off the surface; only the longer wavelengths have small enough optical depths to allow an appreciable signal from such photons. The opposite case, photons that scatter only in the atmosphere, is depicted by the green line. Photons that scatter in the atmosphere before hitting the surface then directly hitting the detector (red) effectively add more signal than would be observed if no atmosphere were present. Conversely, photons that scatter in the atmosphere after hitting the surface (purple) add more noise in that these photons lose some of their spatial information. Finally, multiply scattered photons (black dash and cyan) also add more I/F to the shorter wavelengths due to the higher optical depths there.

[1]Though 22 other countries agreed on an international standard for the prime meridian at a conference in Washington, D.C. in October of 1884, France continued to use a Parisian prime meridian until 1911.

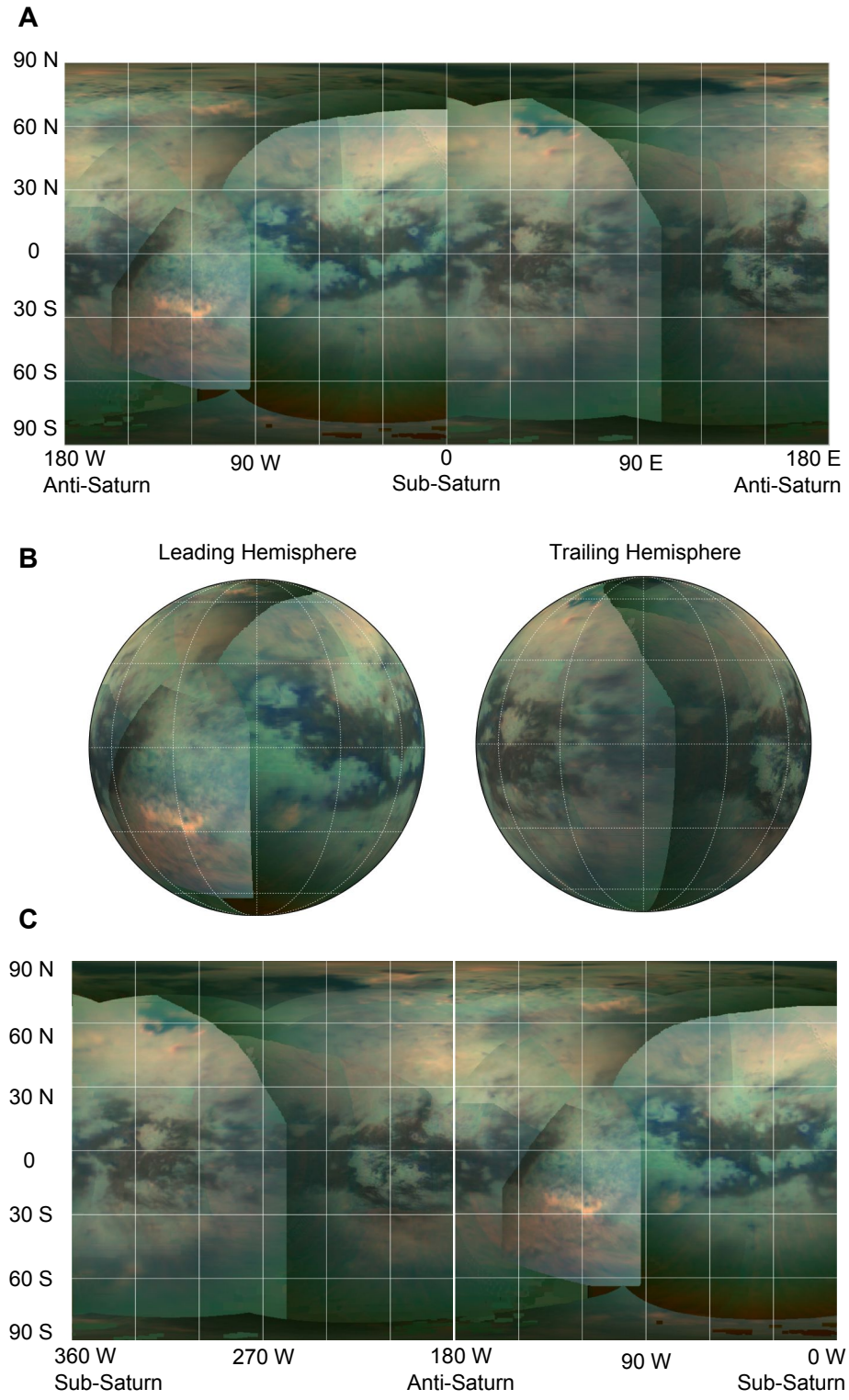

Figure A.1: (A) Cylindrical projection of Titan as seen by *Cassini* VIMS with the longitude convention used by some of the Titan community (e.g. Barnes et al., 2007b). (B) Orthographic projection of *Cassini* VIMS data of the leading and trailing hemispheres. (C) Cylindrical projection using the longitude convention of the IAU. All graticules delineate 30° in longitude or latitude. The color scheme maps 1.3 μm to blue, 2 μm to green, and 5 μm to red.

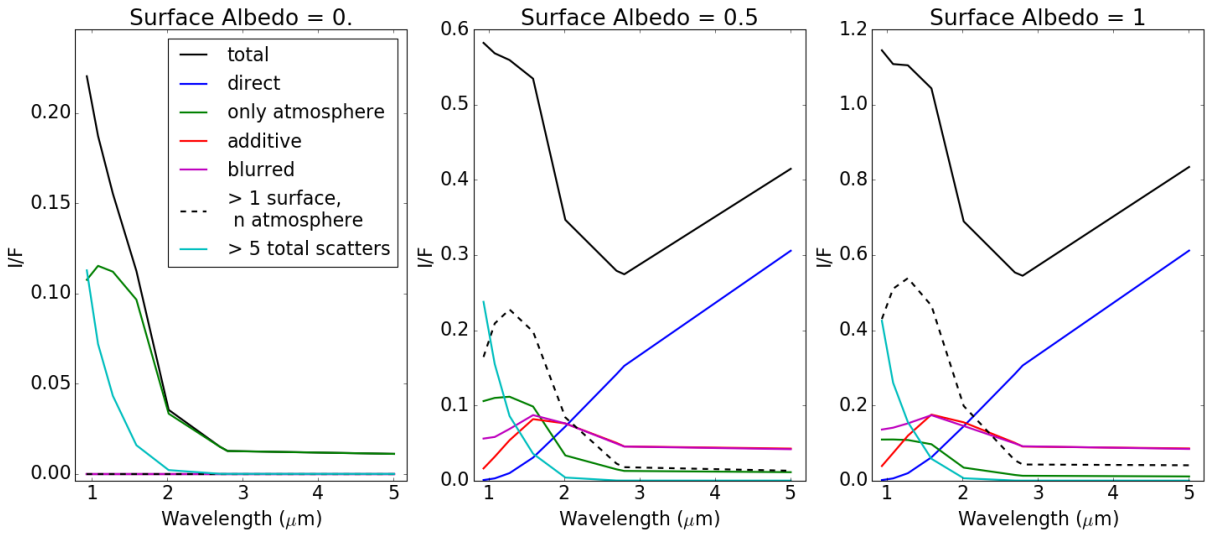

Figure A.2: Relative contribution of different scattering cases to the total I/F for three surface albedos: total I/F (black); direct photons that experience no scattering (blue); photons only scatter in the atmosphere (green), photons that scatter in the atmosphere before hitting the surface and directly reaching the detector (red); photons that scatter off the surface and scatter in the atmosphere before intercepting the detector (purple); photons that scatter n times in the atmosphere and more than once of the surface (black dash); and photons that scatter in the atmosphere and/or off the surface more than 5 times (cyan).

However, this model uses the same number of photons at each wavelength. To explore the effect of the Sun's emission, the Sun can be modeled as a blackbody emitter

$$B_\lambda(\lambda, T) = \frac{2hc^2}{\lambda^5 e^{\frac{hc}{\lambda k_B T}} - 1} \tag{A.1}$$

where λ is the wavelength, T is the temperature, h is Planck's constant, c is the speed of light, and k_B is Boltzman's constant. B_λ thus represents the amount of light incident on Titan's surface as a function of wavelength, shown in the left panel of Figure A.3 as relative to the irradiance at 5 μm. The Sun emits 200 times more at 0.93 μm than it does at 5μm. Less than a percent of those photons make it out of the atmosphere unscattered as discussed above. That is, there are both more scattering events and more photons available to scatter at shorter wavelengths, providing diffuse illumination both to the surface and to the detector.

It is important to note that SRTC++ only accounts for scattering extinction, which can largely explain the relative brightness observed at each surface window. To fully model the shape of Titan's surface spectrum, the effects of gaseous absorption must also be included (see, for example, Figure 5 of Clark et al. (2010)).

A.3 Effects of grain size on reflectance spectra

The reflectance properties of materials of different composition often uniquely identify that material. Incident electromagnetic radiation at energies that excite rotations and vibrations within the atomic

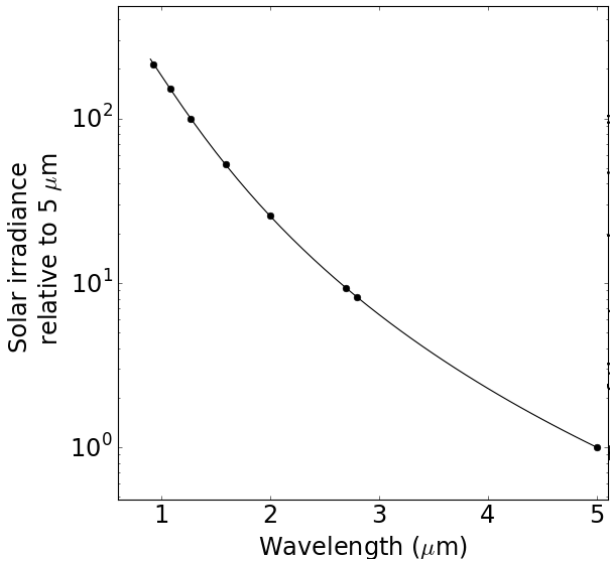

Figure A.3: Irradiance at Titan in the IR relative to the 5 μm window calculated from Planck's law for black body emission.

structure is absorbed rather than reflected, the degree to which depends on the path length through the material. According to the Beer-Lambert law, the incident energy (I_0) exponentially diminishes with distance travelled through the medium (z) based on the likelihood of absorption (k): $I = I_0 e^{-kz}$. Thus, smaller grained materials, whose maximum possible z is thus smaller, absorption features in reflectance spectra cannot be as deep as larger grain sizes.

The synthetic spectra shown in Figure A.4 demonstrate this grain size effect for three kinds of components thought to be present on Titan's surface: water ice, hydrocarbons, and nitriles. These spectra were derived from the model of Shkuratov et al. (1999). This simple, geometrical optics approach models reflectance of materials based on their optical constants by treating the reflection and transmission through a material as a sequence of Fresnel reflections and transmissions. The model explicitly depends on the scattering path length through a medium, a good proxy for grain size, thus allowing us to explore the effects of changing this parameter for any material with defined optical constants. On airless bodies, surface properties like grain size or porosity can be estimated by comparing the observed reflectance to synthetic spectra created with models like that of Shkuratov et al. (1999) or Hapke (2012) where those properties are known. Titan's atmosphere makes spectral fitting like this less straightforward, but thanks to recent improvements in radiative transfer corrections, such investigations are beginning to be more robustly explored (e.g. Brossier et al., 2017).

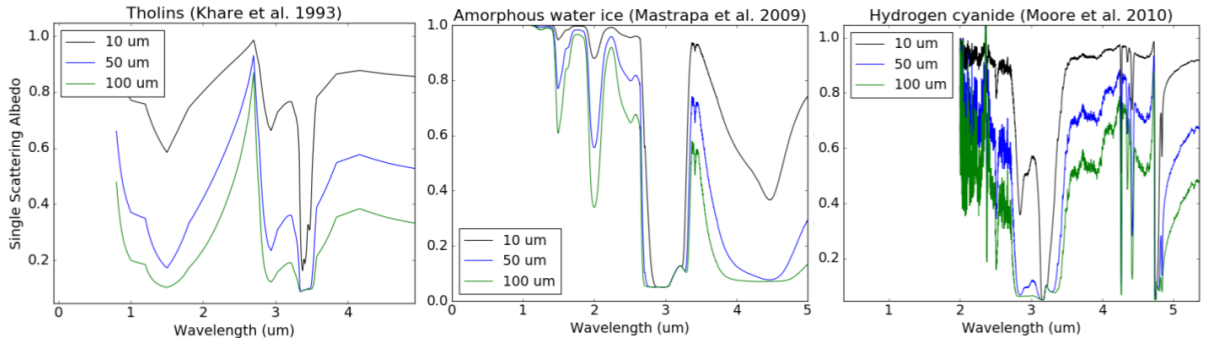

Figure A.4: Synthetic spectra as calculated from optical constants using a Shkuratov model of three compounds representative of what might make up Titan's surface: laboratory analogs for Titan haze particles called tholins (Khare et al., 1993), water ice (Mastrapa et al., 2009), and hydrogen cyanide (Moore et al., 2010).